ENERGY CALIBRATION OF THE SUDBURY NEUTRINO OBSERVATORY USING MONOENERGETIC GAMMA-RAY SOURCES

By

Alan Wing Pok Poon

B.Sc. (Hons. Physics), The University of British Columbia, 1991

A THESIS SUBMITTED IN PARTIAL FULFILLMENT OF
THE REQUIREMENTS FOR THE DEGREE OF
DOCTOR OF PHILOSOPHY

in

THE FACULTY OF GRADUATE STUDIES
DEPARTMENT OF PHYSICS AND ASTRONOMY

We accept this thesis as conforming
to the required standard

. . . .

. . . .

. . . .

THE UNIVERSITY OF BRITISH COLUMBIA

April 1998

Department of Physics and Astronomy
The University of British Columbia
6224 Agricultural Road
Vancouver, Canada
V6T 1Z1

Date:

Abstract

The Sudbury Neutrino Observatory (SNO) is a new 1000-tonne D_2O Čerenkov detector. It will shed some light on the long-standing solar neutrino problem by detecting all flavours of neutrinos originating from the Sun. A high energy gamma-ray source is needed to calibrate SNO beyond the ^{8}B solar neutrino endpoint of 15 MeV. This source must have a gamma-ray yield of > 0.2 s^{-1}, a neutron yield of $< 10^4$ s^{-1}, and an operational lifetime of > 60 hours. To be compatible with the deployment hardware, it must be less than 30 cm in diameter and 75 cm in length.

This thesis describes the design and construction of a source that generates 19.8-MeV gamma rays using the ^{3}H$(p,\gamma)^4$He reaction ("pT"), and demonstrates that the source meets all the physical, operational and lifetime requirements for calibrating SNO. An ion source was built into this unit to generate and to accelerate protons up to 30 keV, and a high purity scandium tritide target with a scandium-to-triton atomic ratio of 1:2.0±0.2 was included. The techniques that were developed for fabricating this target are useful for producing pure tritiated films needed in commercial applications. This pT source is the first self-contained, compact, and portable high energy gamma-ray source (E_γ >10 MeV) ever built.

The usefulness of this source was demonstrated by measuring with it the gamma-ray angular distribution in ^{3}H$(p,\gamma)^4$He at a beam energy of 29 keV, which is more than an order of magnitude lower in energy than all previous measurements. The data were fitted to the form: $W(\theta) = A + B\sin^2\theta$. The results are consistent with the picture of E1 capture of p-wave protons in this reaction, as evidenced by the predominantly $\sin^2\theta$ angular distribution. The ratio A/B is less than 0.35 at the 90% confidence level.

Monte Carlo simulations were used to investigate how monoenergetic gamma-ray sources like the pT source could be used to understand the energy response of SNO. Finally, algorithms were developed to correct for the dependencies of the energy response on various event parameters using calibration data from these sources. These algorithms are essential for establishing an accurate energy scale in the detector response.

Table of Contents

List of Tables

List of Figures

Acknowledgements

When I first started the experimental work for this doctoral thesis project at the Los Alamos National Laboratory (LANL) back in spring 1993, the pT 19.8-MeV gamma-ray energy calibration source was just an idea. Much help was provided at various institutions where parts of this project were done. I have incurred many debts of gratitude in the course of bringing this source to reality, and I want to acknowledge the people who have helped me in so many different ways in the past few years.

First and foremost, special thanks go to my advisors of this project: Prof. Chris Waltham of the University of British Columbia (UBC) and Prof. R. G. Hamish Robertson of the University of Washington (UW) for their patient guidance and their eagerness to help me solve my problems, whether they are administrative, personal, technical or scientific. Thanks, Chris and Hamish, for your unwavering faith in my ability during all those difficult times even when I had doubts about myself. Graduate education is a form of apprenticeship, and I have certainly benefited a lot from working with two of the greatest masters around.

I am especially indebted to Dr. Rob Komar of UBC for helping me in many technical aspects, and the data taking in this project. Thanks, Rob, for all those extra mileage you had to travel/hitchhike, and for coping with all my whinings when things were not going well.

I thank the faculty and the technical staff at the Nuclear Physics Laboratory (NPL) at UW where a significant amount of the technical work was done. In particular, I thank the Sudbury Neutrino Observatory (SNO) collaborators at NPL for all those laughters and fruitful discussions: Mr. Jim Beck, Mr. Charles Duba, Prof. Peter Doe, Dr. Joe

Germani, Mr. Karsten Heeger, Dr. Reena Meijer Drees, Mr. Miles Smith, and Prof. John Wilkerson. Prof. Ludwig DeBraeckeleer, Prof. Kurt Snover, and Dr. Zhiping Zhao also provided many stimulating ideas to this project. Prof. Bob Vandenbosch's administrative help in importing the tritium source for testing at NPL is appreciated. Many technical staffers at NPL have contributed to my project, most notably Mr. Tom Burritt, Mr. Allan Myers, Mr. Dick Seymour, Mr. Tim Van Wechel, Mr. Doug Will, Mr. John Wootress, and Mr. Steve Zsitvay. Mr. Hank Simons's superb craftsmanship in machining and welding the delicate parts used in the tritium source is very much admired. I thank Ms. Barb Fulton for her tremendous help in keeping my visiting graduate student status at UW in good standing during the past four years. I want to express my gratitude to Dr. Diane Markoff. We shared a lot of our experience and problems in thesis writing, job hunting and...etc. at our daily "peer support group" meetings during the last months of our graduate studies. Thanks, everyone, for putting up with the "Poon-ster" over the past few years.

Much support was provided by the former P-3 group at LANL during the early phase of this project. I thank Mr. J. Mel Anaya, Prof. Tom Bowles, Dr. Andrew Hime, Dr. Gabe Luther, and Dr. Jeff Nico for their help during my stay in Los Alamos.

The tritium target used in this project was fabricated at the tritium facility in collaboration with the Process Development Unit of Ontario Hydro Technologies (OHT) in Toronto. I am grateful to OHT for its hospitality. In particular, my gratitude goes to Mr. Mark Hooper, Dr. Nazir Kherani and Mr. Clive Morton for their help.

Mrs. Winnie Lee's hospitality is very much appreciated whilst I was struggling with a ruptured achilles tendon in Toronto.

Preliminary testing of the tritium source was performed at Queen's University at Kingston. I want to express my appreciation to Prof. Aksel Hallin for dealing with tritium licensing and shipping logistics for the source at Queen's. I must also thank Prof.

Hay-Boon Mak for his help in testing the source. Thanks, Mak, for the soothing words (the encouragement, and the very much needed beer) after the initial dud.

Several SNO collaborators at Oxford University have contributed to this project. I thank Dr. Steve Brice and Dr. Nick West for their help in SNOMAN. On a different front, Dr. George Doucas has given a lot of insights to various aspects of the ion source design and operation at the early stage of this project. I must also thank all the Oxford collaborators for their hospitality, and for staging the High Street thriller, during my brief visit in spring 1995.

I thank all those who kept me away from complete solitude during the past few years, especially Michael C. "M.F. Rainier" Browne. Thanks, Mike, for all your help in the project, and for the Rainier, Armish,...etc. on all those rainy Tuesday nights in Seattle. The Burritt "Burrittos" household , Ivy "Sis" Chan, Hunter and Rowena Cheng, Steve "Two-Tees" Elliott, Karin "Catia" Hendrikson, Mohammad "the Great" Kermani, Chris "Big Old Chief" König, Rita "Scouter" Kwan, Nina Lujan and her puppy Licorice, Sheila "Shatsie" McFarland, Helen Ng, Monica Ngan, Christina "Rocket Girl" Scovel, Tom "Edgar" Steiger, John "Canucks Fan" Tong, and Jacqueline "Minnie" Wu have all contributed significantly to shaping me into a more personable character. I must also acknowledge the occasional financial support from the UW SNO Poker Club.

And I express my deepest appreciation to my parents, my sister Doris, my uncle Paul and aunt Monica for their encouragement and caring throughout these years.

It has taken many seasons to complete this project. I am sure that I have left out some people whom I should acknowledge, and I apologise to them for this inadvertent omission.

To my parents

I grew up with an ambition and determination without which I would have been a good deal happier. I thought a lot and developed the faraway look of a dreamer, for it was always the distant heights which fascinated me and drew me to them in spirit. I was not sure what could be accomplished by means of tenacity and little else, but the target was set high and each rebuff only saw me more determined to see at least one major dream through to its fulfillment.

Earl Denman
Alone to Everest (1954)

Chapter 1

Neutrinos and the Solar Neutrino Problem

> *From man or angel the great Architect*
> *Did wisely to conceal, and not divulge*
> *His secrets to be scanned by them who ought*
> *Rather admire; or if they list to try*
> *Conjecture, he his fabric of the heav'ns*
> *Hath left to their disputes, perhaps to move*
> *His laughter at their quaint opinions wide*
> *Hereafter, when they come to model heav'n*
> *And calculate the stars, how they will wield*
> *The mighty frame, how build, unbuild, contrive*
> *To save appearances, how gird the sphere*
> *With centric and eccentric scribbled o'er,*
> *Cycle and epicycle, orb in orb.*
>
> John Milton
> Paradise Lost, Bk. 8 (1674)

In 1914, James Chadwick, working at the *Physikalisch Technische Reichsanstalt* in Berlin, found that the β-ray energy spectra of "radium-B" and "radium-C,"[1] apart from several discrete lines arising from the internal conversion electrons, were continuous [1]. His finding of a continuous electron energy spectrum was confirmed by Ellis and Wooster in their calorimetric measurement of the total energy emitted in the "radium-E"[2] β-decay in 1927 [2]. Two years later, Meitner and Orthmann confirmed this experimental finding [3]. A continuous electron energy spectrum was troublesome as this would violate the energy conservation law in a two-body final state decay. In a desperate attempt to explain this

---

[1] This was the jargon used at the turn of the century. "Radium-B" is now identified as ^{214}Pb, and "radium-C" is now known as ^{214}Bi.

[2] "Radium-E" is known as ^{210}Bi today.

strange phenomenon, Niels Bohr proposed a violation of the energy principle in β-decays in 1930 [4].

In his open letter to the "radioactive ladies and gentlemen" gathered in Tübingen in 1930, Wolfgang Pauli proposed the existence of a *neutron* to share the energy released in β-decay with the electron and the daughter nucleus [5]. Fermi later called this particle a "neutrino" after Chadwick's discovery of the neutron in 1932. More than two decades passed before Cowan and Reines announced their first observation of electron antineutrino capture in inverse β-decay in 1956 [6].

Since the discovery of neutrinos, extensive efforts have been made to study the properties of this elusive particle on both theoretical and experimental fronts. It has been established experimentally that neutrinos interact in accord with the Standard Model of electroweak interactions of Glashow, Weinberg and Salam (GWS) [7]. In this model, the three flavours of neutrinos, ν_e, ν_μ and ν_τ, form the isospin $I_3=\frac{1}{2}$ component of a left-handed lepton doublet, and each of the right-handed charged leptons form a singlet. Fermions in the GWS model, which is based on the gauge group $SU(3)_C \otimes SU(2)_L \otimes U(1)_Y$, acquire a mass through the spontaneous symmetry breaking of the group. Unlike the charged leptons, neutrinos are massless in the Standard Model as they do not have a right-handed singlet to allow them to couple to the Higgs particle through Yukawa coupling.

However, there is no compelling reason why the neutrinos have to be massless. In fact, unified theories and other extended gauge groups with a mass scale M_X often predict that neutrinos acquire a seesaw-type mass. Typically in these models, the mass of the neutrino m_ν is related to M_X as

$$m_{\nu_l} \sim \frac{M_l^2}{M_X} \tag{1.1}$$

where M_l is the mass of the corresponding lepton in the same family. A non-zero neutrino mass has significant implications in cosmology; if the sum of the masses of the neutrinos in the three families exceeds 30 eV, the relic neutrinos from Big Bang nucleosynthesis will be massive enough to close the universe.

Nuclear fusion in stellar interiors produces an enormous flux of electron-type neutrinos. Complicated theoretical calculations have been performed to trace the evolution of the Sun in the past several billion years of main sequence burning. These "Standard Solar Models" predict, amongst many solar characteristics, the solar neutrino flux. Since the late 1960's, experimentalists have been monitoring this flux. However, theoretical predictions and experimental observations do not agree. Many proposals have been put forward as plausible solutions to this so-called "Solar Neutrino Problem." One of the most favourable solutions, the Mikheyev-Smirnov-Wolfenstein (MSW) effect [8] predicts a massive neutrino oscillating from one flavour to another in the presence of matter, thereby escaping detection by the terrestrial neutrino detectors. By observing this effect in solar neutrinos, the neutrino mass can be determined indirectly with a sensitivity several orders of magnitude better than the most sensitive direct laboratory mass measurement in tritium β-decay. Thus the study of solar neutrinos does not only allow us to probe the solar interior, it also provides an exciting arena for probing physics beyond the standard electroweak model.

In Section 1.1, we shall first describe the elements of the Standard Solar Model. We shall then summarise the present experimental status of the solar neutrino flux measurements in Section 1.2. A brief overview of the Solar Neutrino Problem is made in Section 1.3. Many plausible solutions to the Solar Neutrino Problem have been proposed, and some of these proposals will be discussed in Section 1.4. And we shall finish this chapter with a brief discussion of future solar neutrino experiments in Section 1.5.

1.1 The Standard Solar Model

1.1.1 Elements of the Solar Standard Models

In the late 1930's, pioneering work by Bethe, Critchfield, Gamow, von Weizsäcker and others provided the theoretical grounding in solar energy generation [9]. It is now believed that the fusion of protons into α particles is the only mechanism capable of sustaining the long-term energy production as constrained by geological and astronomical observations. The Sun has been in its main sequence, or hydrogen burning, phase for the last 4.6 billion years. In this quasistatic stage, the overall scheme for energy generation is the fusion of four protons to form a ^{4}He nucleus in the solar core:

$$4p + 2e \;\rightarrow\; {}^4\mathrm{He} + 2\nu_e + 26.7\ \mathrm{MeV}. \tag{1.2}$$

The so-called proton-proton (pp) chain, in which the whole energy generation process is initiated by two protons fusing together, generates about 98% of the total energy. The remaining 2% of the energy is produced from the carbon-nitrogen-oxygen (CNO) cycle. In this latter scheme, the overall conversion of four protons into a ^{4}He nucleus is facilitated by the presence of a spectator ^{12}C nucleus — the most abundant heavy isotope in a main sequence stellar environment. The solar pp chain and the CNO cycle are depicted in Figures 1.1 and 1.2 respectively.

On average only a small amount of the energy released in reaction (1.2) is carried away by the neutrinos. Therefore, one can estimate the total solar neutrino flux ϕ_ν to be

$$\phi_\nu \;\simeq\; \frac{L_\odot}{(13\,\mathrm{MeV})(4\pi D^2)} \;=\; 6.5\times 10^{10}\,\mathrm{cm}^{-2}\,\mathrm{s}^{-1}, \tag{1.3}$$

where $L_\odot$ (=3.85×10^{26} W) is the solar luminosity and D (=1.5×10^{11} m) is the Earth-Sun distance.

To obtain the neutrino flux from individual reactions in the pp chain, one needs to perform very complex numerical calculations. The Standard Solar Models are numerical

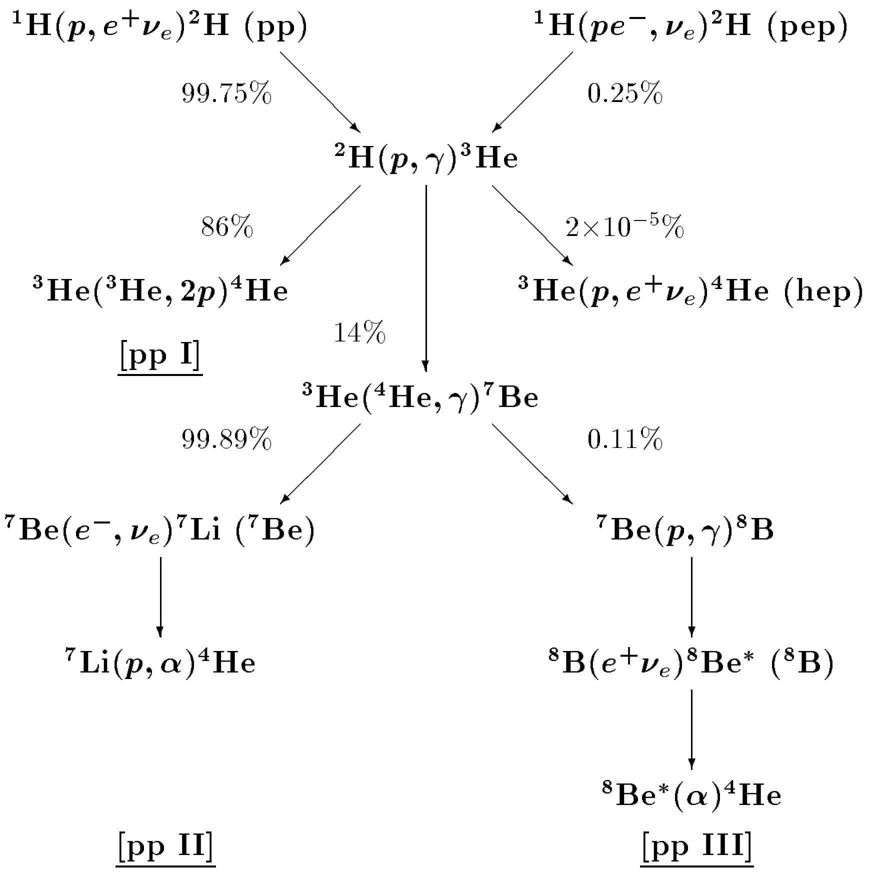

Figure 1.1: The solar proton-proton chain.

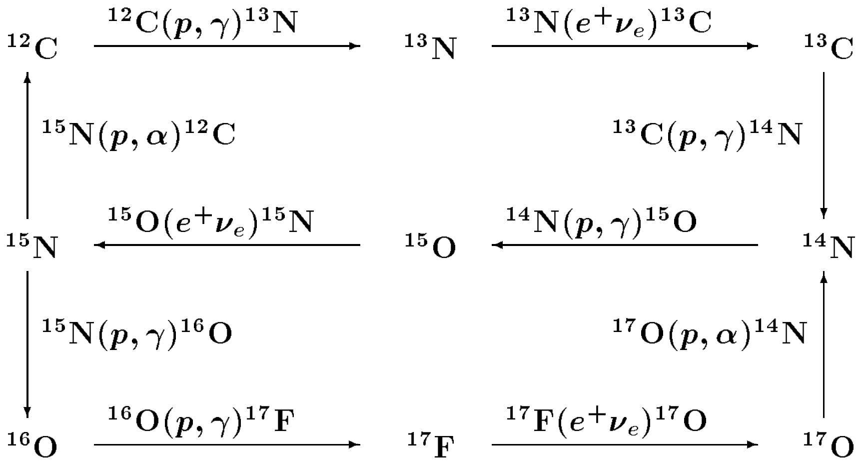

Figure 1.2: The solar CNO cycle.

calculations which track the development of the Sun since the hydrogen burning phase began 4.6 billion years ago. This chronology allows the prediction of the present-day solar core temperature and the neutrino fluxes from individual reactions in the *pp*-chain and the CNO cycle.

The Standard Solar Models require many input parameters and functions: solar age, solar luminosity, nuclear cross sections, initial chemical abundances, equation of state, and calculated radiative opacity. These models use the present-day solar surface chemical composition for heavy elements ($A > 5$) as the initial abundances, assuming that these have not been transformed by subsequent evolution since the Sun entered the main sequence phase. The models are then constrained to produce the present-day solar luminosity by adjusting the initial ^{4}He to ^{1}H ratio as the Sun evolves to the present epoch.

In the more recent solar model calculations, the effect of helium and heavy element diffusion is also included. Gravitational settling and temperature gradient diffusion mix the elements in the solar interior slowly over the lifetime of the Sun. The former effect tends to pull the heavier elements towards the solar core, whilst the latter effect pushes the light elements towards the solar surface. The combination of these effects causes helium and heavier element to diffuse towards the solar core, and hydrogen to diffuse towards the solar surface. As a result, the radiative opacity, hence the interior temperature, throughout the solar interior is somewhat different from a chemically homogeneous model. As we shall see in Section 1.1.2, the neutrino fluxes, especially the ^{8}B neutrino flux, depend critically on the core temperature. Very few model calculations include these diffusion effects as it was previously estimated that the elemental diffusion over a solar radius occurs on a time scale of 10^{13} years under solar conditions.

Bahcall and Pinsonneault [10] argue that the inclusion of the heavy element diffusion is necessary to reconcile the solar model predictions and helioseismological measurements of the present-day helium surface abundance Y_s and the depth of the solar convective zone. With this inclusion, the solar model predictions are indeed in excellent agreement with the helioseismological measurements. For instance, the computed depth of the convective zone with helium and heavy element diffusion is $R = 0.712 R_\odot$ (in units of the solar radius $R_\odot$), whilst that without any diffusion is $R = 0.726 R_\odot$. The former value is in better agreement with the observed value determined from the solar p-mode oscillation data of $R = 0.713 \pm 0.003 R_\odot$ [11].

1.1.2 Standard Solar Model Prediction of the Solar Neutrino Flux

Several Standard Solar Model predictions of neutrino fluxes have been published in the past few years [10, 12, 13, 14, 15, 16, 17, 18, 19, 20, 21, 22]. These models do predict somewhat different solar neutrino fluxes. Bahcall and Pinsonneault [12] argued that the differences amongst these models are attributed to the choice of input parameters, rather than the underlying physics. In Table 1.1, we summarise the neutrino flux prediction of the two most complete numerical calculations: the Bahcall-Pinsonneault [10, 12] and the Turck-Chièze-Lopes [13] models. The solar neutrino energy spectrum in the Bahcall-Pinsonneault model is shown in Figure 1.3.

In a recent paper by Bahcall and Ulmer [23], the authors refined the previous Monte Carlo analyses by Bahcall and Ulrich [16] and obtained the temperature dependence of the solar neutrino flux. Similar to the previous study, Bahcall and Ulmer analysed 1000 detailed solar models by sampling the nuclear cross sections and the elemental abundances within their ranges of uncertainty, thereby changing the solar core temperature. The temperature dependence of the solar neutrino flux was fitted to the form

$$\phi \propto T^m. \tag{1.4}$$

The fitted m-values from their analysis are summarised in Table 1.2.

		flux ($\mathrm{cm}^{-2}\mathrm{s}^{-1}$)		
Source	$E_{\nu_e}^{max}$ (MeV)	BP95 (diffusion)	BP95 (no diffusion)	TCL
${}^{1}\mathrm{H}(p, e^{+}\nu_e){}^{2}\mathrm{H}$	0.42	$5.91(1.00^{+0.01}_{-0.01})\times10^{10}$	6.01×10^{10}	6.03×10^{10}
${}^{13}\mathrm{N}(e^{+}\nu_e){}^{13}\mathrm{C}$	1.20	$6.18(1.00^{+0.17}_{-0.20})\times10^{8}$	4.07×10^{8}	3.83×10^{8}
${}^{15}\mathrm{O}(e^{+}\nu_e){}^{15}\mathrm{N}$	1.73	$5.45(1.00^{+0.19}_{-0.22})\times10^{8}$	3.45×10^{8}	3.18×10^{8}
${}^{17}\mathrm{F}(e^{+}\nu_e){}^{17}\mathrm{O}$	1.74	$6.48(1.00^{+0.15}_{-0.19})\times10^{6}$	4.02×10^{6}	
${}^{8}\mathrm{B}(e^{+}\nu_e){}^{8}\mathrm{Be}$	∼15	$6.62(1.00^{+0.14}_{-0.17})\times10^{6}$	4.85×10^{6}	4.43×10^{6}
${}^{3}\mathrm{He}(p, e^{+}\nu_e){}^{4}\mathrm{He}$	18.77	1.21×10^{3}	1.27×10^{3}	
${}^{7}\mathrm{Be}(e, \nu_e){}^{7}\mathrm{Li}$	0.86 (90%) 0.38 (10%)	$5.15(1.00^{+0.06}_{-0.07})\times10^{9}$	4.53×10^{9}	4.34×10^{9}
${}^{1}\mathrm{H}(p, e^{-}, \nu_e){}^{2}\mathrm{H}$	1.44	$1.40(1.00^{+0.01}_{-0.02})\times10^{8}$	1.44×10^{8}	1.39×10^{8}

Table 1.1: The solar neutrino fluxes as predicted by the Bahcall-Pinsonneault (BP95) and the Turck-Chièze-Lopes (TCL) standard solar models. The BP results are shown for calculations with and without the helium and heavy element diffusion effect. The uncertainties shown in the BP95 diffusion model are 1σ uncertainties. No error estimate was made for the *hep* neutrinos because of the large uncertainty in the *hep* reaction.

Neutrino Flux	Monte Carlo Exponent m
$\phi(\mathrm{pp})$, m'	13.0±0.7
$\phi(\mathrm{pp})$, m	-1.1±0.1
$\phi(\mathrm{pep})$	-2.4±0.9
$\phi({}^{7}\mathrm{Be})$	10±2
$\phi({}^{8}\mathrm{B})$	24±5
$\phi({}^{13}\mathrm{N})$	24.4±0.2
$\phi({}^{15}\mathrm{O})$	27.1±0.1
$\phi({}^{17}\mathrm{F})$	27.8±0.1

Table 1.2: Temperature dependence of the solar neutrino flux. Bahcall and Ulmer [23] recommended a new functional dependence for $\phi(\mathrm{pp})$, $\phi(\mathrm{pp}) \propto 1 - 0.08(T/T_{SSM})^{m'}$, where T_{SSM}=15.64×10^{6}K.

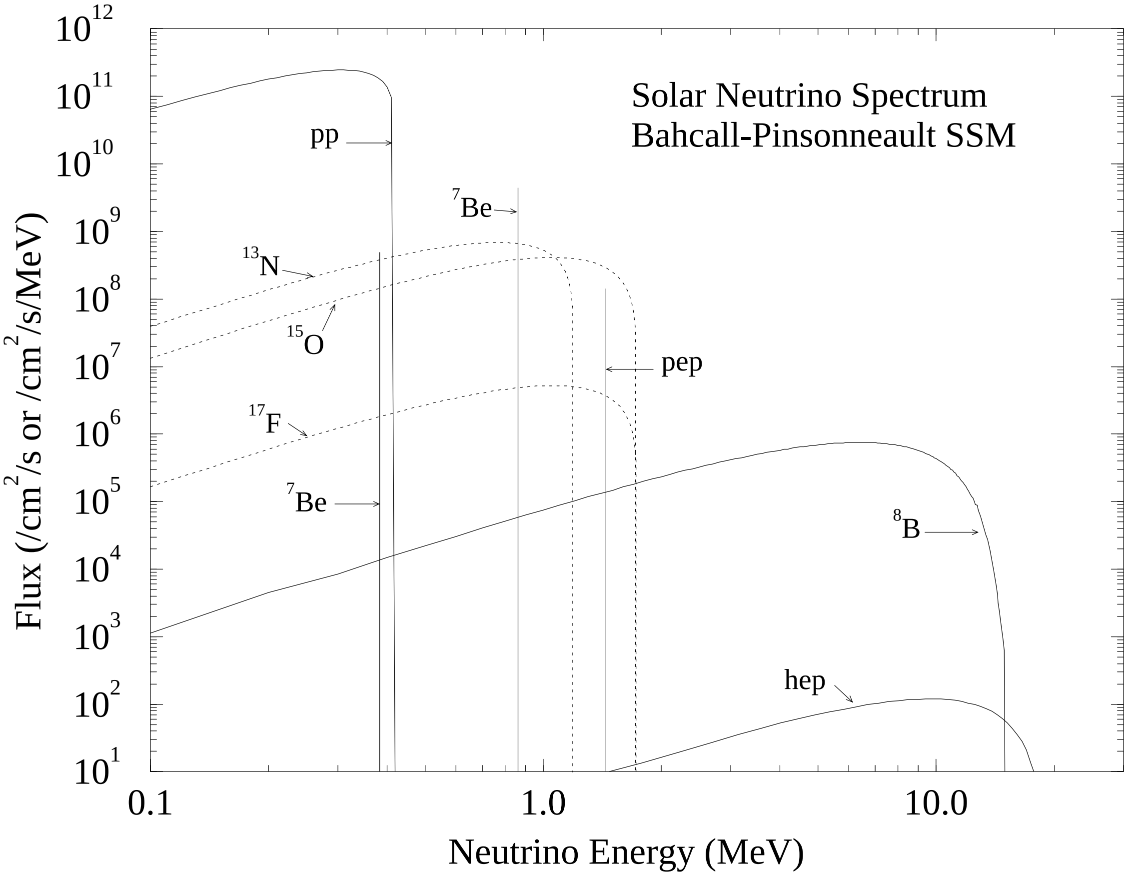

Figure 1.3: The solar neutrino energy spectrum calculated by Bahcall and Pinsonneault [12]. The dotted lines show the energy of neutrinos produced in the CNO cycle, whilst the solid lines show the corresponding spectra in the *pp* chain.

1.1.3 Standard Solar Model Uncertainties

Standard Solar Model calculations require a lot of experimental, observational and calculational input data. To understand the uncertainty inherent in the model calculation, one must examine the individual uncertainty associated with these input data. These uncertainties include the nuclear reaction cross sections for the *pp* chain and the CNO cycle, the solar age, the solar luminosity, the calculated solar radiative opacity, and the elemental abundances. A thorough review of all these uncertainties would take us beyond the scope of this thesis, though a brief discussion of some of the important issues is appropriate.

The *pp* chain consists of a series of non-resonant charged-particle reactions occurring at energies well below the Coulomb barrier potential. As a result, the reaction cross sections must be deduced from laboratory measurements by extrapolating from hundreds of keV to the thermal energy of a few keV. The most controversial nuclear reaction cross section is that of $^7\text{Be}(p,\gamma)^8\text{B}$ on which the high energy ^{8}B neutrino flux depends. The two laboratory measurements which quoted the smallest uncertainties (Kavanagh *et al.* [24] and Filippone *et al.* [25]) are shown to have their centroid values of $S_{17}(0)$[3], which is a parameter used in near threshold charged particle non-resonant cross section, in disagreement. However, this difference would only lead to an uncertainty of less than ~15% in the ^{8}B neutrino flux calculated by Bahcall and Pinsonneault [26].

Over the past several decades, many precision measurements of critical solar model input data have been performed. For instance, both the solar luminosity and the solar age are now thought to be known to an accuracy of about 0.4%. Although some input data, notably the heavy-element-to-hydrogen ratio Z/X, have higher intrinsic uncertainties, these uncertainties are adequate enough to constrain the calculated solar neutrino flux

---

[3] More detail on parameterisation of near threshold charged particle non-resonant cross sections can be found in Section 3.3.

to within a very tight range. In fact, Bahcall and Pinsonneault argued that "no single quantity dominates the uncertainties...in the individual neutrino fluxes. Therefore it seems likely that — despite continuing efforts to improve the input parameters — the net uncertainties in the computed neutrino fluxes will not be greatly reduced in the foreseeable future [10]."

1.2 Present Experimental Status

There are currently three solar neutrino experiments monitoring the solar neutrino flux. They are the ^{37}Cl detector in the Homestake Gold Mine in Lead, South Dakota, USA; the ^{71}Ga SAGE experiment in Baksan Valley, Russia; and the SuperKamiokande detector in Kamioka, Japan. Another ^{71}Ga experiment — Gallex at the Gran Sasso Underground Laboratory in Italy — is in the decommissioning phase after having monitored the solar neutrino flux since the early 1990s.

These detectors probe different regions of the neutrino energy spectrum. The ^{71}Ga experiments have a low enough threshold to allow the detection of the low energy *pp* neutrinos, the ^{37}Cl experiment is sensitive to the ^{7}Be and ^{8}B neutrinos, and the Kamiokande series of experiments detects only the ^{8}B neutrinos.

1.2.1 The ^{37}Cl Experiment

The ^{37}Cl detector is located at the Homestake Gold Mine in Lead, South Dakota, USA, at a depth of approximately 4,850 feet [4,900 metres water equivalent (m.w.e)]. Chlorine was chosen for this pioneering experiment in monitoring the solar neutrino flux because of its unique physical and chemical properties, which are favourable for building a relatively low-cost, large scale neutrino detector. The Homestake detector contains 615 tons of the cleaning fluid perchloroethylene C_2Cl_4.

Solar neutrinos are captured through the reaction

$$\nu_e + {}^{37}\mathrm{Cl} \rightarrow e^- + {}^{37}\mathrm{Ar} \tag{1.5}$$

with a relatively low threshold of 0.814 MeV for the transition to the ground state of ^{37}Ar. This capture process creates an ^{37}Ar atom with sufficient energy to break free of the parent perchloroethylene molecule. The ^{37}Ar nucleus has a half life of 35 days. Once every one to three months, these ^{37}Ar are removed by purging the liquid with helium gas, and the gas is then circulated through a charcoal trap cooled to liquid nitrogen temperature. About 95% of the ^{37}Ar in the tank is captured in this trap. The extracted ^{37}Ar atoms are then introduced into a small low-background proportional counter for counting of its decay back to ^{37}Cl.

The number of neutrinos captured at the ^{37}Cl detector has been lower than the Standard Solar Model prediction by a factor of three ever since the detector began operation. The capture rate predicted for the ^{37}Cl detector by the latest Bahcall-Pinsonneault Standard Solar Model [10] is $(9.3^{+1.2}_{-1.4})$ SNU [4], whereas only a capture rate of $(2.55\pm0.17(\mathrm{stat.})\pm0.18(\mathrm{syst.}))$ SNU was observed [27] after 25 years of measurement. In Table 1.3, we summarise the Bahcall-Pinsonneault model prediction of the signal for the chlorine detector.

1.2.2 Kamiokande and SuperKamiokande

The series of Kamiokande experiments in Japan began its operation in 1985. The Kamiokande-I detector was a Čerenkov nucleon decay experiment situated at about 1 km underground (2700 m.w.e.). Much effort was invested in converting this detector to a low-background solar neutrino detector Kamiokande-II by reducing the radon and other natural radioactivity background in the circulating water. These upgrades allowed the

---

[4] SNU: Solar Neutrino Unit. 1 SNU = 10^{-36} events per target atom per second.

Neutrino	Predicted Capture Rate (SNU)
pp	0.00
pep	0.22
hep	-
^{7}Be	1.24
^{8}B	7.36
^{13}N	0.11
^{15}O	0.37
^{17}F	-
Total	$9.3^{+1.2}_{-1.4}$

Table 1.3: Predicted solar neutrino capture rate at the ^{37}Cl detector. The predicted rates are taken from [10]. The quoted uncertainty in the total capture rate is a 3σ uncertainty.

Kamiokande-II detector to monitor the solar neutrino flux through the neutrino-electron elastic scattering process:

$$\nu + e^- \rightarrow \nu + e^-. \tag{1.6}$$

Although this reaction is sensitive to all neutrino flavours, it is dominated by the electron neutrinos with the cross section for the other types a factor of six lower. Because of the strong correlation between the direction of the scattered electron and the Sun, the results from the Kamiokande-II confirmed the origin of the detected neutrinos was indeed the Sun.

The Kamiokande-II detector contained 3,000 tons of water, and only the inner 680 tons was used as the fiducial volume for the solar neutrino experiment because of the stringent background requirements. A total of 948 50-cm-diameter photomultiplier tubes were installed in the detector, providing a 20% photocathode coverage of full solid angle. Further improvements were made in Kamiokande-III. These changes included improvements in electronics and the installation of wavelength shifters.

In April 1996, the SuperKamiokande detector began taking solar neutrino data. This detector contains 50,000 tons of water, out of which the innermost 22,500 tons is used as the fiducial volume for solar neutrino data runs. With 11,200 50-cm photomultiplier tubes installed, SuperKamiokande has a total photocathode coverage of 40%.

Recently, the SuperKamiokande collaboration announced their initial results for the first 101.9 days of data. With an analysis threshold of 7 MeV, the detector detected $2.51\pm0.14(\text{stat.})\pm0.18(\text{syst.})\times10^6$ ^{8}B ν_e cm^{-2} s^{-1} [28]. This is consistent with the combined results from the Kamiokande-II and Kamiokande-III data, which was $2.95^{+0.22}_{-0.21} \pm 0.36$ cm^{-2} s^{-1} [29]. In the Bahcall-Pinsonneault model [10], the ^{8}B neutrino flux is calculated to be $6.6(1.00^{+0.14}_{-0.17})\times10^6$ cm^{-2} s^{-1}.

1.2.3 The ^{71}Ga Experiments: SAGE and Gallex

The ^{71}Ga experiments capture solar electron neutrinos through the reaction

$$\nu_e + {}^{71}\text{Ga} \rightarrow e^- + {}^{71}\text{Ge}. \tag{1.7}$$

The threshold of this reaction is only 0.2332 MeV which permits the detection of the most abundant low energy *pp* neutrinos ($E_{pp} \leq 0.42$ MeV). The neutrino capture rate is determined experimentally by chemically extracting ^{71}Ge, which has a half life of 11.43 days.

The Russian (Soviet)-American Gallium Experiment (SAGE) began taking data in January, 1990, with 30 tons of metallic gallium. In May, 1991, an additional 30 tons was incorporated into the detector. This detector is located in the Baksan Neutrino Observatory in the Caucasus Mountain with an overhead shielding of approximately 4,700 m.w.e. The Gallex experiment was located in the Gran Sasso underground facility in Italy where the overhead shielding is approximately 3,300 m.w.e. This detector consisted of 30.3 tons of gallium in the form of a concentrated $GaCl_3$-HCl solution. In both experiments, ^{71}Ge was extracted chemically from the bulk gallium into the gaseous form

Neutrino	Predicted Capture Rate (SNU)
pp	69.7
pep	3.0
hep	-
^{7}Be	37.7
^{8}B	16.1
^{13}N	3.8
^{15}O	6.3
^{17}F	-
Total	137^{+8}_{-7}

Table 1.4: Predicted solar neutrino capture rate at the ^{71}Ga detectors. The predicted rates are taken from [10]. The quoted uncertainty in the total capture rate is a 3σ uncertainty.

of germane (GeH_4). The extracted germane was then mixed with xenon to form the counter gas for direct counting in a miniature proportional counter. The solar neutrino flux was then inferred by detecting the Auger electrons from ^{71}Ge decay [10.37 keV (K shell) and 1.17 keV (L shell)]. In the Bahcall-Pinsonneault Standard Solar Model [10], the predicted neutrino capture rate for the gallium experiments is 137^{+8}_{-7} SNU. However, the Gallex and the SAGE experiments have seen only 77.1±8.5(stat.)$^{+4.4}_{-5.4}$(syst.) SNU and 74^{+13}_{-12}(stat.)$^{+5}_{-7}$(syst.) SNU respectively. In Table 1.4, we summarise the Bahcall-Pinsonneault model prediction of the gallium detector signal.

Both the SAGE and the Gallex experiments have carried out at least one ^{51}Cr calibration run. In these runs, an intense ^{51}Cr source supplied the neutrinos with a spectrum that closely mimics the ^{7}Be neutrino lines in the solar neutrino spectrum. The ^{51}Cr nucleus decays by electron capture and produces neutrinos of 751 keV (90%) and 426 keV (10%). Both gallium experiments verified their ability to extract the decaying ^{71}Ge with high efficiency. The extraction efficiency was determined to be 0.97±0.11 and $0.93^{+0.15}_{-0.17}$ for the first Gallex and the SAGE ^{51}Cr irradiation [30, 31].

Experiment	Solar Model Prediction (3σ)	Measured Value (1σ)
^{37}Cl [SNU]	$9.3^{+1.2}_{-1.4}$	$2.55\pm0.17\pm0.18$
H_2O [$\times10^6$ cm^{-2} s^{-1}]	$6.6(1.00^{+0.14}_{-0.17})$	$2.51\pm0.14\pm0.18$
^{71}Ga (Gallex) [SNU]	$137\ ^{+8}_{-7}$	$77.1\pm8.5^{+4.4}_{-5.4}$
^{71}Ga (SAGE) [SNU]	$137\ ^{+8}_{-7}$	74^{+13+5}_{-12-7}

Table 1.5: Comparison between the Standard Solar Model calculated and the measured solar neutrino flux. For the Solar Model predictions, we have used the Bahcall-Pinsonneault calculation [10]. The H_2O flux is taken to be the latest SuperKamiokande results [28].

1.3 The Solar Neutrino Problem

In Table 1.5 we have summarised the present experimental status. It is clear that all the neutrino detectors are detecting fewer neutrinos than the Standard Solar Model prediction. Before the commissioning of the Kamiokande and the gallium detectors, this apparent deficit of solar neutrinos in the ^{37}Cl detector was the "original" Solar Neutrino Problem.

After the Kamiokande-II data became available, there were indications that the solar neutrino deficit might have an energy dependence as the amount of observed neutrinos differs for the chlorine and the Kamiokande data.

The results from the three classes of neutrino experiments form a coarse solar neutrino spectrum measurement because of their different energy thresholds. It is then possible to do a model independent study on the neutrino flux from the various reactions in the *pp*-chain subject to the solar luminosity constraint (for example, see [32, 33, 36]). In Figure 1.4, a fit of the ^{7}Be and the ^{8}B neutrino fluxes using the experimental results from all three classes of experiment is shown [32]. It is apparent from this fit that the ^{7}Be neutrino flux $\phi(^{7}\text{Be})$ is severely suppressed as the best fit occurs at <7% of the Standard Solar Model. In another study, Parke [33] shows that if one assumes standard neutrino properties, either the solar model calculations are ruled out at the 3σ level or at least two of the three types of experiments are incorrect. This strong suppression of the ^{7}Be neutrino flux represents a different statement than just "low flux."

1.4 Possible Solutions to the Solar Neutrino Problem

Many solutions to the Solar Neutrino Problem have been proposed. These solutions can be roughly divided into two broad categories: astrophysical solutions and particle physics solutions. Before the announcement of the ^{71}Ga results, solutions that fall into the former category propose different ways to lower the solar core temperature, thereby reducing the ^{8}B neutrino flux. With the ^{71}Ga results, it has been demonstrated in several model independent studies that ^{7}Be neutrinos are much more severely suppressed than the ^{8}B neutrinos. And astrophysical solutions seem to have fallen out of favour since then, as the ^{8}B neutrino flux has a much stronger temperature dependence.

In the particle physics category of proposed solutions to the Solar Neutrino Problem, the standard electroweak model is extended in various ways in order to adjust the observed ν_e flux. The solution favoured by most physicists is neutrino oscillation, in which a neutrino can be converted, or oscillated, to a neutrino of a different flavour. This requires an extension to the standard electroweak model as this is feasible only when at least one flavour of neutrinos has a non-zero mass.

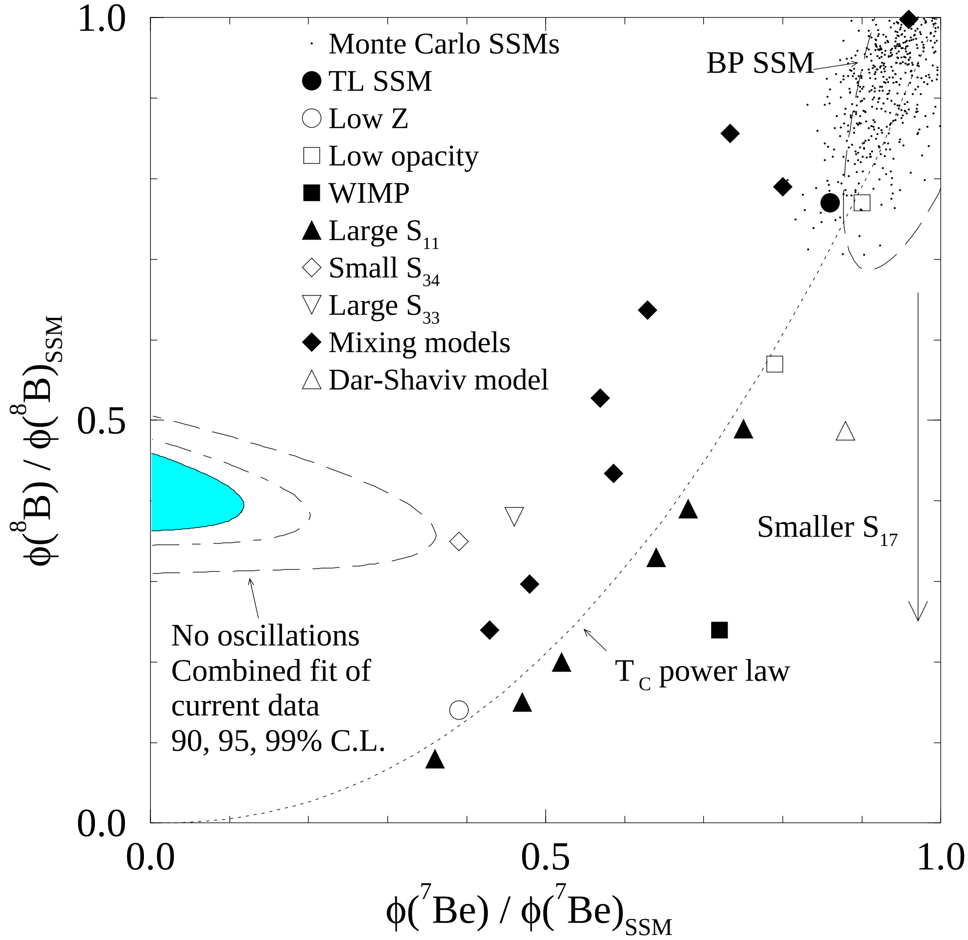

Figure 1.4: Combined fit for ^{7}Be and ^{8}B solar neutrino fluxes using data from all four neutrino experiments. Without invoking any new neutrino physics, the best fit occurs at $\phi(^7\text{Be})<7\%$ and $\phi(^8\text{B})=0.41\pm0.04$ relative to the Standard Solar Model. This fit has a rather poor reduced χ^2 of 3.3. Also shown are the predictions of the Bahcall-Pinsonneault model [12], and results from the 1000 Monte Carlo Standard Solar Model and various other models which reduce the core temperature (from [32]).

1.4.1 Astrophysical Solutions

A simple way to adjust solar neutrino flux in the solar model calculations is to tune the nuclear cross section for the various nuclear reactions in the *pp* chain. Therefore, one can envision the difference between the calculated and the measured neutrino flux to be the inaccuracy in the nuclear cross sections used in the calculation. Extrapolating the nuclear reaction cross section from the laboratory energies down to the thermal energies inside the solar core constitutes one of the largest uncertainties in the calculated solar neutrino flux. The uncertainties in the metallicity and in the opacity are the other major components. As we have mentioned in Section 1.1.3, these factors cannot be the only contributors to the Solar Neutrino Problem. However, one must also realise that the ^{7}Be neutrino flux $\phi(^7\mathrm{Be})$ is independent of the ^{8}B neutrino production rate. This is because the rate for the $^7\mathrm{Be}(\mathrm{p},\gamma)^8\mathrm{B}$ reaction, which subsequently generates the ^{8}B neutrino following the decay of ^{8}B, is very much slower than the electron capture process that gives rise to the ^{7}Be neutrinos [34]. Therefore, it seems unlikely that uncertainties of the nuclear cross section are the main contributor to the ^{7}Be neutrino problem.

One can also reduce the calculated solar neutrino flux by introducing mechanisms which reduce the core temperature of the Sun. Because of the strong temperature dependence of the solar neutrino flux, especially the ^{7}Be and the ^{8}B fluxes, these models seem to be able to accommodate the neutrino flux deficit without changing the core temperature significantly. But the solar luminosity puts a severe constraint on how much the core temperature can be reduced without contradicting existing observations. In fact, several analyses have come to the conclusion that one cannot account for the solar neutrino data by simply adjusting the core temperature, or other nuclear reaction cross sections (see [35] and references therein). Also many of these astrophysical solutions also make the helioseismological predictions in disagreement with recent precision measurements.

Finally, the ^{8}B neutrino flux should have been suppressed much more severely than the ^{7}Be neutrino flux with a reduced core temperature given the temperature dependence outlined in Table 1.2.

1.4.2 Neutrino Oscillation

Another class of proposed solutions to the Standard Solar Model introduces new physical properties to the neutrinos. Based on the current experimental results, Heeger and Robertson [36] concluded in a recent paper that the probability of a standard neutrino physics solution is less than 2% if one invokes the solar luminosity constraint in a model-independent study. Even with this constraint abandoned, the probability is still no more than 4%. Therefore, the experimental data strongly suggest new neutrino physics beyond the minimal standard model.

As we have seen in Section 1.3, the solar neutrino flux data show a strong hint of energy dependence. However, most of the proposed solutions to the Solar Neutrino Problem, whether astrophysical or particle physics solutions, do not have a mechanism to incorporate this energy dependence naturally. The exception is neutrino oscillation, in which the "disappearance" of electron type neutrinos is energy dependent. Neutrino oscillation can be categorised into two categories: in vacuum and in matter. In the following, we shall discuss both of these categories.

Vacuum Oscillation

The neutrino ν_l ($l = e, \mu, \tau$) emerging from weak decays is a superposition of fields ν_α (α=1,2,3) of mass m_α [5]:

$$|\nu_l\rangle = \sum_\alpha U_{l\alpha}|\nu_\alpha\rangle \tag{1.8}$$

---

[5] In the jargon of neutrino physics, $|\nu_l\rangle$ is called the flavour eigenstate and $|\nu_\alpha\rangle$ is called the mass eigenstate.

where U is an unitary matrix. After a time t, the beam is then described by

$$|\nu_l\rangle_t \;=\; \sum_\alpha e^{-iE_\alpha t} U_{l\alpha} |\nu_\alpha\rangle \tag{1.9}$$

where E_α, the energy of the mass eigenstate $|\nu_\alpha\rangle$, is given by[6]

$$E_\alpha \;=\; \sqrt{p^2 + m_\alpha^2} \;\approx\; p + \frac{m_\alpha^2}{2p} \tag{1.10}$$

for $p \gg m_\alpha$. Since the neutrinos are extremely relativistic, we can replace the time t by the distance R the neutrino beam has travelled. So, the probability $P_{\nu_l\nu_{l'}}(R)$ of finding a neutrino of flavour l' ($\nu_{l'}$) at a distance R is

$$\begin{aligned} P_{\nu_l\nu_{l'}}(R) \;&=\; |\langle \nu_{l'} | \nu_l \rangle_t|^2 && (1.11) \\ &=\; \sum_{\alpha,\beta} \left| U_{l\alpha} U^*_{l'\alpha} U^*_{l\beta} U_{l'\beta} \right| \cos \left[\left(\frac{2\pi R}{L_{\alpha\beta}} - \phi \right) \right] && (1.12) \end{aligned}$$

where

$$\phi \;=\; \arg \left(U_{l\alpha} U^*_{l'\alpha} U^*_{l\beta} U_{l'\beta} \right), \tag{1.13}$$

and $|L_{\alpha\beta}|$, the so-called oscillation length, which defines the distance scale of the vacuum oscillation effect, is given by

$$L_{\alpha\beta} \;=\; \frac{4\pi p}{\Delta_{\alpha\beta}} \tag{1.14}$$

with

$$\Delta_{\alpha\beta} \;=\; m_\alpha^2 - m_\beta^2. \tag{1.15}$$

We shall apply these general equations to a two-flavour problem. Let us consider only the two flavours ν_e and ν_μ. The unitary matrix U is just a rotation matrix in two dimensions:

$$U \;=\; \begin{pmatrix} \cos\theta_{\rm V} & \sin\theta_{\rm V} \\ -\sin\theta_{\rm V} & \cos\theta_{\rm V} \end{pmatrix} \tag{1.16}$$

---

[6] The sharp reader would realise that we have made an assumption of the neutrinos being monoenergetic, which of course is not true. Kayser [37] used a wave packet approach to treat this problem. The results obtained from this approximation agree with Kayser's.

where θ_{V} is called the vacuum mixing angle. Using Eqn.(1.11), we find that the probability of observing a ν_μ at a distance R given that the initial state is a ν_e of energy E is

$$P_{\nu_e\nu_\mu}(R) \;=\; \sin^2 2\theta_{\mathrm{V}}\, \sin^2\left(\frac{\pi R}{L_{\mathrm{V}}}\right) \tag{1.17}$$

where the vacuum oscillation length $|L_{\mathrm{V}}|$ in this case is given by

$$L_{\mathrm{V}} \;=\; \frac{4\pi E}{\Delta m^2} \tag{1.18}$$

with $\Delta m^2{=}m_2^2 - m_1^2$ which is the mass-squared difference between the two mass eigenstates $|\nu_1\rangle$ and $|\nu_2\rangle$. Similarly, the probability for a ν_e remaining a ν_e after traveling a distance R is

$$P_{\nu_e\nu_e}(R) \;=\; 1 \,-\, \sin^2 2\theta_{\mathrm{V}}\, \sin^2\left(\frac{\pi R}{L_{\mathrm{V}}}\right). \tag{1.19}$$

We can see that the magnitude of vacuum mixing is proportional to $\sin^2 2\theta_{\mathrm{V}}$, which is expected to be small by considering the analogous quark mixing. The smallness of this vacuum mixing angle makes vacuum oscillation a somewhat unattractive solution to the Solar Neutrino Problem because a large mixing angle is needed to explain the solar neutrino deficit.

The MSW Effect: Matter-Enhanced Neutrino Oscillation

In 1986, Mikheyev and Smirnov realised that one does not need a large mixing angle to solve the Solar Neutrino Problem if the oscillation takes place in the solar interior, i.e. in dense matter. This is now known as the Mikheyev-Smirnov-Wolfenstein (MSW) effect [8].

All flavours of neutrinos interact with matter through the exchange of the Z boson—the neutral-current interactions. However, the electron neutrino can also interact with the electrons in the solar interior through the charged-current interactions, i.e. with the exchange of a charged W boson. This channel is available only to the electron neutrino because the Sun is not hot enough to provide μ's and τ's in the background. And it is this unique feature of electron neutrino's interaction with matter that gives rise to resonant conversion in the MSW effect.

As before, we shall deal with a two-flavour problem of ν_e and ν_μ. The contribution of the charged-current interaction to the effective energy is

$$A_e \;=\; \langle \mathcal{M}^{\rm CC} \rangle \;=\; \langle e\nu_e | \mathcal{M}^{\rm CC} | e\nu_e \rangle \;=\; \sqrt{2} G_F n_e \tag{1.20}$$

where n_e is the number density of electrons and G_F is the Fermi constant. In this expression, we have assumed the electrons to be non-relativistic since the thermal energy of electrons in the solar interior is very low. Similarly the net neutral-current contribution A_n is

$$A_n \;=\; \langle e\nu_e | \mathcal{M}^{\rm NC} | e\nu_e \rangle \;=\; -\frac{1}{\sqrt{2}} G_F n_n \tag{1.21}$$

where n_n is the number density of neutrons.

In the ν_e-ν_μ flavour representation, the evolution equation is

$$i\frac{d}{dt}\begin{pmatrix} \nu_e(t) \\ \nu_\mu(t) \end{pmatrix} \;=\; H \begin{pmatrix} \nu_e(t) \\ \nu_\mu(t) \end{pmatrix} \tag{1.22}$$

where

$$H = \left(p + \frac{m_1^2 + m_2^2}{4p} - A_n \right) + \begin{pmatrix} -\frac{\Delta m^2}{4p}\cos 2\theta_{\rm V} + A_e & \frac{\Delta m^2}{4p}\sin 2\theta_{\rm V} \\ \frac{\Delta m^2}{4p}\sin 2\theta_{\rm V} & \frac{\Delta m^2}{4p}\cos 2\theta_{\rm V} - A_e \end{pmatrix}. \tag{1.23}$$

In this formalism, we have assumed that $m_2 > m_1$.

The diagonalising angle, or the effective mixing angle in matter, $\theta_{\rm M}$, is given by

$$\tan 2\theta_{\rm M} \;=\; \frac{\tan 2\theta_{\rm V}}{1 - \frac{L_{\rm V}}{L_e}\sec 2\theta_{\rm V}} \tag{1.24}$$

where L_{V} is the vacuum oscillation length in Eqn.(1.18) and L_e is given by

$$L_e = \frac{\sqrt{2}\pi}{G_F n_e}. \tag{1.25}$$

Clearly, Eqn.(1.24) shows that the MSW effect is a resonance effect with the resonance condition

$$\left(\frac{L_{\mathrm{V}}}{L_e}\right)_{\mathrm{res}} = \cos 2\theta_{\mathrm{V}}, \tag{1.26}$$

and hence the "MSW resonance electron density" is

$$n_{e,res} = \frac{\Delta m^2 \cos 2\theta_{\mathrm{V}}}{2\sqrt{2}G_F E}. \tag{1.27}$$

The reason why the MSW effect is now favoured by most physicists as the solution to the Solar Neutrino Problem is that even for a small vacuum mixing angle θ_{V}, it is still possible to have a significant conversion if the electron density satisfies Eqn.(1.27).

If the electron density changes sufficiently slowly, which is known as the adiabatic condition, the ν_e created in the solar core exits from the Sun essentially in a different flavour eigenstate ν_μ, which cannot be detected by the ^{37}Cl or the ^{71}Ga detectors. However, near the resonance electron density, the energy gap between the trajectories of the two mass eigenstates is minimal and there is a finite probability of level crossing—a transition from the one mass eigenstate to the other. This probability was calculated by various authors using different approximations. The reader is referred to Bahcall [40] for more details.

Finally, the probability that a ν_e created in the solar interior at a density n_e ($> n_{e,res}$) to remain a ν_e when arriving at a terrestrial detector is given by Parke [38] and is

$$|\langle \nu_e | \nu_e \rangle_t|^2 = \frac{1}{2} + \left(\frac{1}{2} - P_{\mathrm{jump}}\right) \cos 2\theta_{\mathrm{M}} \cos 2\theta_{\mathrm{V}} \tag{1.28}$$

where P_{jump} is the level crossing probability and θ_{M} is defined in Eqn.(1.24).

The solar neutrino experiments we discussed in Section 1.2 measure the neutrino flux spanning from the low energy *pp* neutrinos to the highest energy *hep* neutrinos, albeit

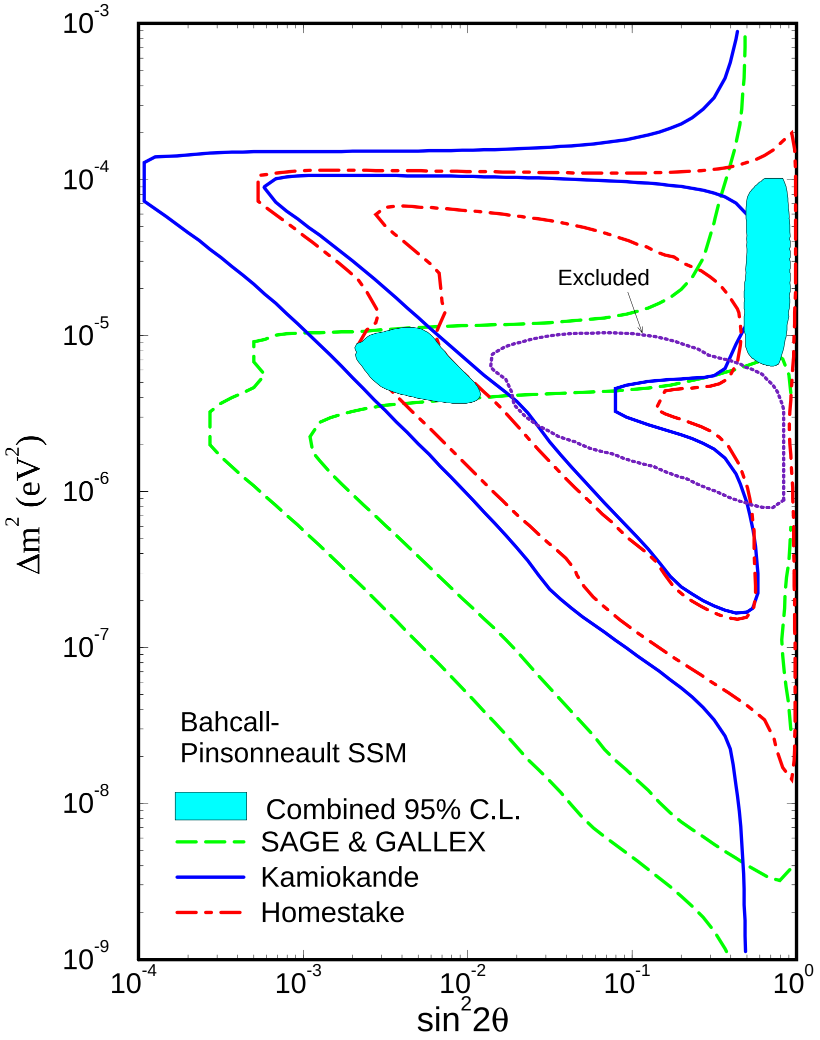

Figure 1.5: The MSW Δm^2-$\sin^2(2\theta)$ contour plot for the solar neutrino data taken by all the operating solar neutrino detectors is shown here. Based on the solar neutrino flux measured by the four operating detectors, and the theoretical predictions by Bahcall and Pinsonneault [12], two "allowed" regions for the MSW oscillation parameters can be found. The "allowed regions" shown above have a 95% confidence level (from [32]).

this latter signal is negligible because of its low flux. In Section 1.3, we saw that the ratio of the measured flux at each experiment differs. This energy dependence can be accounted for by the intrinsic energy dependence in the MSW effect. Given the measured solar neutrino flux at each detector, one can constrain the oscillation parameters: Δm^2 and $\sin^2 2\theta$. One such plot is shown in Figure 1.5.

1.5 Future Prospects

Existing solar neutrino data are insufficient to identify the origin of the Solar Neutrino Problem. In particular, one would want to verify or to falsify the MSW mechanism. This simple, yet elegant, mechanism can be tested by the SuperKamiokande experiment and the Sudbury Neutrino Observatory (SNO). SNO is a major topic of this thesis, and a detailed description of the detector is deferred until the next chapter.

Because of a significant increase in the fiducial volume for solar neutrino detection and an improved detector threshold, SuperKamiokande detects solar neutrinos through neutrino-electron elastic scattering at a rate two orders of magnitude higher than its predecessor. High statistics will enable the SuperKamiokande collaboration to detect the MSW mechanism by observing a distortion in the recoil electron energy spectrum. In Figure 1.6, the recoil electron energy spectrum at the SuperKamiokande detector for various neutrino oscillation scenarios is shown.

The Borexino experiment [41] is under construction at the Gran Sasso Laboratory in Italy. This detector is mainly sensitive to the ^{7}Be neutrino line through neutrino-electron scattering in 300 tonnes of liquid scintillator surrounded by 3000 tonnes of high purity water. Because the recoil electrons have very low energy, there are stringent requirements on the purity of the material used in the construction of the detector. For example, the acceptable limits for the natural radionuclides potassium, thorium and uranium are

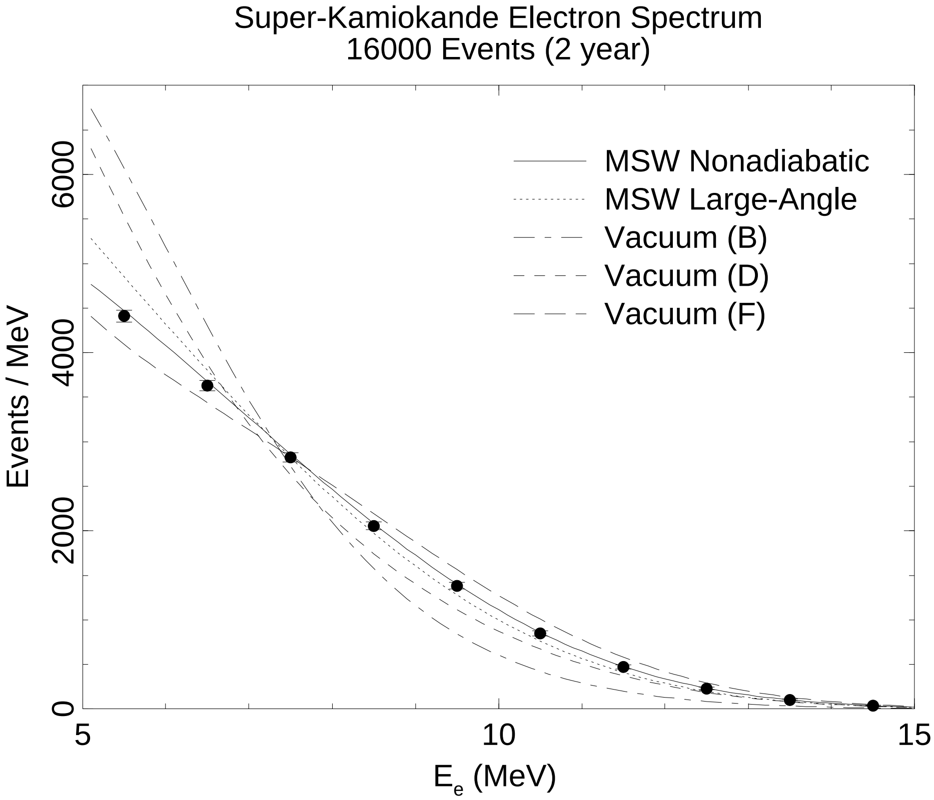

Figure 1.6: Spectral distortion at the SuperKamiokande experiment for various oscillation scenarios(from [39]). The error bars correspond to the statistical uncertainties for a total of 16000 events. The oscillation parameters used in the MSW scenarios are using the combined fit values in Figure 1.5. Δm^2 used in scenarios B, D, F are 1.1×10^{-10}, 7.8×10^{-11}, and 5.0×10^{-11} eV^2, whilst 0.88, 0.75 and 0.93 are used for $\sin^2 2\theta$. It should be noted that the electron-type neutrino survival probability $P(\nu_e \rightarrow \nu_e|E_\nu)$ is almost constant for E_ν >5 MeV in the large-angle MSW scenario. Hence, the spectral shape for this scenario is indistinguishable to that of the no-oscillation scenario.

10^{-14} g/g, 10^{-16} g/g and 10^{-16} g/g respectively. Also the constraint on the ^{14}C/^{12}C ratio is 10^{-18} g/g. Preliminary results from a scaled down prototype—the Counting Test Facility (CTF)—demonstrated that most of these purity requirements have been achieved. The anticipated count rate of the full scale Borexino detector is ~18000 ^{7}Be ν_e per year for the Bahcall-Pinsonneault Standard Solar Model.

Another proposed experiment at the Gran Sasso Laboratory is a 5000-tonne liquid argon time projection chamber — the ICARUS II detector [42]. Neutrinos can be detected by two different channels:

$$\nu_x + e^- \rightarrow \nu_x + e^- \tag{1.29}$$

$$\nu_e +^{40}\mathrm{Ar} \rightarrow {}^{40}\mathrm{K}^* + e^-. \tag{1.30}$$

The first of these channels is sensitive to all neutrinos, whilst the second reaction is sensitive to ν_e only. This latter channel will allow a measurement of the ^{8}B neutrino energy spectrum. A 3-tonne prototype of this experiment has been in operation at the European Laboratory for Particle Physics (CERN). The construction of a 600-tonne detector module at the Gran Sasso Laboratory has been recently approved and funded.

Another radiochemical neutrino detector is proposed for the Homestake mine [43]. This detector uses the reaction $^{127}\mathrm{I}(\nu_e, e)^{127}\mathrm{Xe}$ to detect solar neutrinos. With a threshold of 664 keV, this detector will primarily detect the ^{7}Be and ^{8}B neutrinos. The final detector is expected to contain 1000 tonnes of a NaI solution as target.

Two experiments have been proposed recently to measure the energy spectrum of the low energy pp neutrinos in real time. Both of these proposed detectors — HERON [44] and HELLAZ [45] — use helium as the target. The HERON detector plans to measure the low energy pp neutrino spectrum by observing the ballistic phonon propagation subsequent to neutrino interaction in a superfluid helium target. On the other hand, the HELLAZ detector is a time projection chamber which uses pressurised helium gas. The technical difficulties involved in these two experiments are very high and it may be some years before their realisation.

Chapter 2

The Sudbury Neutrino Observatory

Too low they build, who build beneath the stars.

EDWARD YOUNG
Night Thoughts, Night viii (1741)

One of the greatest pains to human nature is the pain of a new idea.

WALTER BAGEHOT
Physics and Politics, Ch. 5 (1872)

In the 1960s, there were several direct counting solar neutrino detectors under construction. One of them was a 2000-litre D_2O detector built by Jenkins *et al.* at Case Western Reserve [46, 47]. Like most of the other detectors, this D_2O detector was abandoned after the chlorine experiment had shown that the ^{8}B neutrino flux was low. Another problem associated with this experiment was its high background rate—the detector was located only 610 m deep in a salt mine. At that time, only the ν_e charged-current interaction with the deuteron was considered:

$$\nu_e + d \ \rightarrow \ p + p + e^- . \tag{2.1}$$

In 1979, Pasierb *et al.* discovered the weak neutral-current interaction of $\bar{\nu_e}$ disintegration of deuterons in a measurement using fission $\bar{\nu_e}$ from the 2000-MW fission reactor at Savannah River [48]. In this measurement, the neutral-current reaction

$$\bar{\nu_e} + d \ \rightarrow \ n + p + \bar{\nu_e} \tag{2.2}$$

and the charged-current reaction

$$\bar{\nu_e} + d \ \rightarrow \ n + n + e^+ \tag{2.3}$$

were observed concurrently.

In the early 1980s, H.H. Chen from the University of California at Irvine realised that by observing both the charged-current reaction in Eqn.(2.1) and the neutral-current ν disintegration of the deuteron

$$\nu_x + d \;\rightarrow\; n + p + \nu_x, \qquad x = e, \mu, \tau \tag{2.4}$$

one can "determine the total solar neutrino flux *even if neutrinos oscillate* [49]." He proposed using 1000 to 1500 tonnes of D_2O as the target to observe ^8B neutrinos. In this chapter, we shall discuss the characteristics of one such D_2O detector—the Sudbury Neutrino Observatory (SNO). We shall also discuss further the question of how SNO can look for physics beyond the standard electroweak model.

2.1 Physical Description of the Sudbury Neutrino Observatory Detector

The Sudbury Neutrino Observatory is a real time neutrino detector in its final phase of construction in the Creighton mine, owned by the International Nickel Company (INCO), near Sudbury, Ontario, Canada. A cavity housing the detector is shaped like a barrel with a height of approximately of 30 m and a diameter of about 21 m at its widest point. The cavity is located at a depth of 2070 m underground, with an overhead shielding equivalent to 6000 m of water. At this depth, the high energy cosmic muon flux is $\sim$350 m^{-2} yr^{-1}. In Figure 2.1, the cross sectional view of the cavity and the detector is shown.

The heart of the detector is 1000 tonnes of D_2O contained in a 12-m diameter spherical vessel. This water is on loan from Atomic Energy of Canada Limited (AECL), and has a deuterium isotopic purity of 99.92%. Such a high purity is essential to SNO's operation, as a high hydrogen content in the D_2O would significantly reduce the neutral-current detection efficiency. This is because of hydrogen's higher neutron absorption cross section.

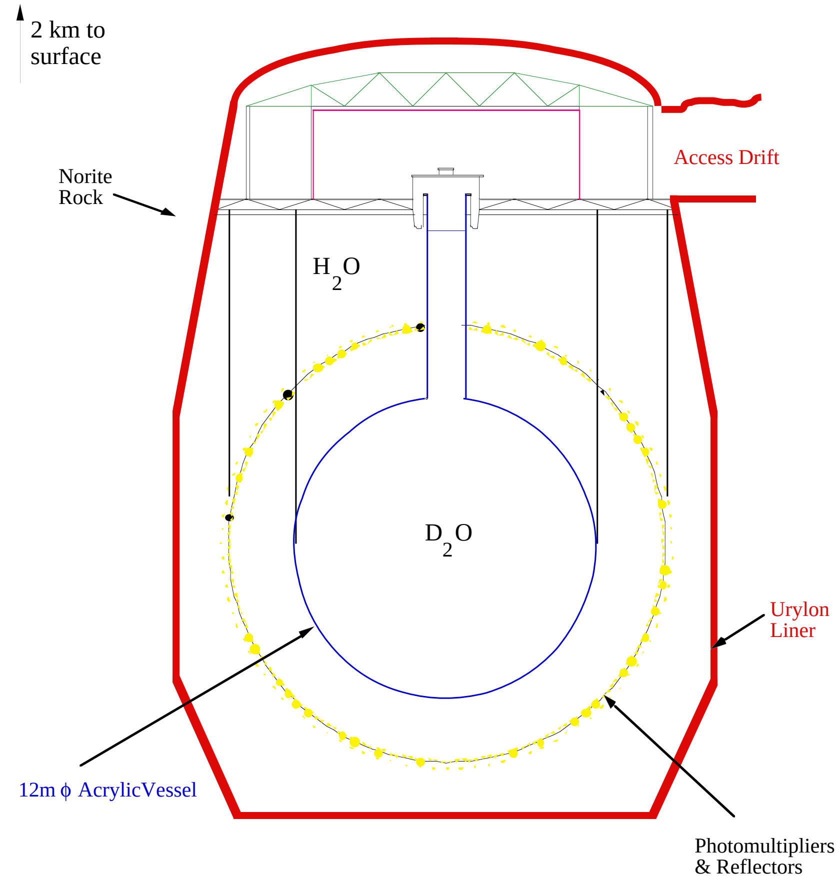

Figure 2.1: The Sudbury Neutrino Observatory detector.

The acrylic vessel is constructed out of 122 ultraviolet transmitting acrylic panels. These panels are 5.5 cm thick, except for ten of the twenty panels in the equatorial band which are 11.4 cm thick. There is a U-shaped rope groove on these ten equatorial panels to accommodate a vectran support rope used to suspend the acrylic sphere. Outside the acrylic vessel, 7000 tonnes of ultra-pure water will be used to shield radioactive background originating in the cavity wall.

The SNO detector has 9456 20-cm Hamamatsu R1408 photomultiplier tubes (PMTs) to detect the Čerenkov light emitted by relativistic charged particles. Low background Schott 8246 glass is used in these PMTs. These PMTs are mounted on 751 "honeycomb" panels that are in turn arranged on a spherical stainless steel support structure. These inward facing PMTs provide a photocathode coverage of 31%. A non-imaging light concentrator is mounted on each PMT to increase the photocathode coverage to about 56%. These concentrators also shield the PMTs from seeing the background signals originating at their neighbours. Another 91 PMTs are mounted facing outward to act as cosmic veto counters. Magnetic coils were built into the cavity wall to cancel out the vertical component of the Earth's magnetic field. The maximum residual field at the PMT array is less than 19μT.

The SNO electronics system is designed to provide sub-nanosecond time and charge measurement of the PMT analogue pulses in the range of 1 to 1000 photoelectrons. The system is capable of handling a background rate in excess of 1 kHz for solar neutrino runs. In fact, there is enough on-board memory in all of the front end cards to buffer a total of about one million events during a supernova burst. Two separate oscillators are used to keep track of the absolute and the relative times. A commercial Global Positioning System (GPS) provides a 10 MHz clock to correlate SNO data with other astrophysical detectors. There is also a 50 MHz quartz oscillator to provide high precision timing for physical events in the detector.

As of March 1998, the construction of the acrylic vessel and the mounting of all the PMTs are complete. And the detector is expected to be fully filled with D_2O by summer 1998.

2.2 Neutrino Physics at SNO

The SNO detector is capable of detecting neutrinos and antineutrinos in a variety of ways. In this section, we shall first discuss the various neutrino detection mechanisms at SNO. We shall then discuss how the neutrino results from SNO can change our understanding of this particle.

2.2.1 Neutrino Detection Mechanisms

In contrast to all the previous solar neutrino experiments, the SNO detector has more than one neutrino detection channel. In addition, the SNO detector is also capable of detecting antineutrinos originating from other astrophysical sources. In the following, we shall discuss these neutrino reactions individually.

Charged Current (CC): $\nu_e + d \rightarrow p + p + e^-$

This reaction produces a relativistic recoil electron which the SNO detector can detect by observing its Čerenkov radiation. Since the outgoing electron should carry most of the energy in the final state, one expects the electron energy E_e and the neutrino energy E_{ν_e} to be approximately related by

$$E_{\nu_e} \sim E_e - Q, \tag{2.5}$$

where Q=-1.442 MeV. However, one should not treat this approximation as a one-to-one direct correspondence between E_{ν_e} and E_e. This is because the reaction populates the two-proton states only in the continuum [50].

Threshold (MeV)	STD (SNU)	SMA (SNU)	LMA (SNU)	VAC (SNU)
4	6.9	2.3	1.6	1.4
5	6.0	2.0	1.3	1.3
6	4.8	1.7	1.1	1.2
7	3.5	1.3	0.8	1.0

Table 2.1: The charged-current event rate at SNO as a function of the energy threshold and the neutrino oscillation scenario. In the table, STD stands for standard solar model expectations. The small angle (SMA), large mixing angle (LMA) MSW scenarios and the pure vacuum oscillation (VAC) have (Δm^2,$\sin^2 2\theta$) values at (5.4×10^{-6} eV^2,7.9×10^{-3}), (1.7×10^{-5} eV^2,0.69) and (6.0×10^{-11} eV^2,0.96) respectively [50].

This charged-current reaction is a pure Gamow-Teller transition. To first order, the recoil electron has an angular distribution $P(\theta)$ given by [51]:

$$P(\theta) = 1 - \frac{1}{3}\left(\frac{v}{c}\right)\cos\theta \approx 1 - \frac{1}{3}\cos\theta \tag{2.6}$$

where v is the recoil velocity of the electron, θ is the direction relative to the incident neutrino. Because of this two-to-one backward to forward asymmetry, this reaction can be used to identify the source of incident neutrinos.

Since the CC event rate depends on the incident ν_e flux, its rate varies depending on the neutrino oscillation parameters if neutrino oscillation does occur. In Table 2.1, we list the expected CC event rates for different oscillation scenarios and detector energy threshold. Furthermore, the energy dependence in neutrino oscillation can distort the observed CC shape in the SNO detector. A distorted CC energy spectrum provides indisputable evidence for neutrino oscillation. In Figure 2.2, we show the CC energy spectra for different oscillation scenarios.

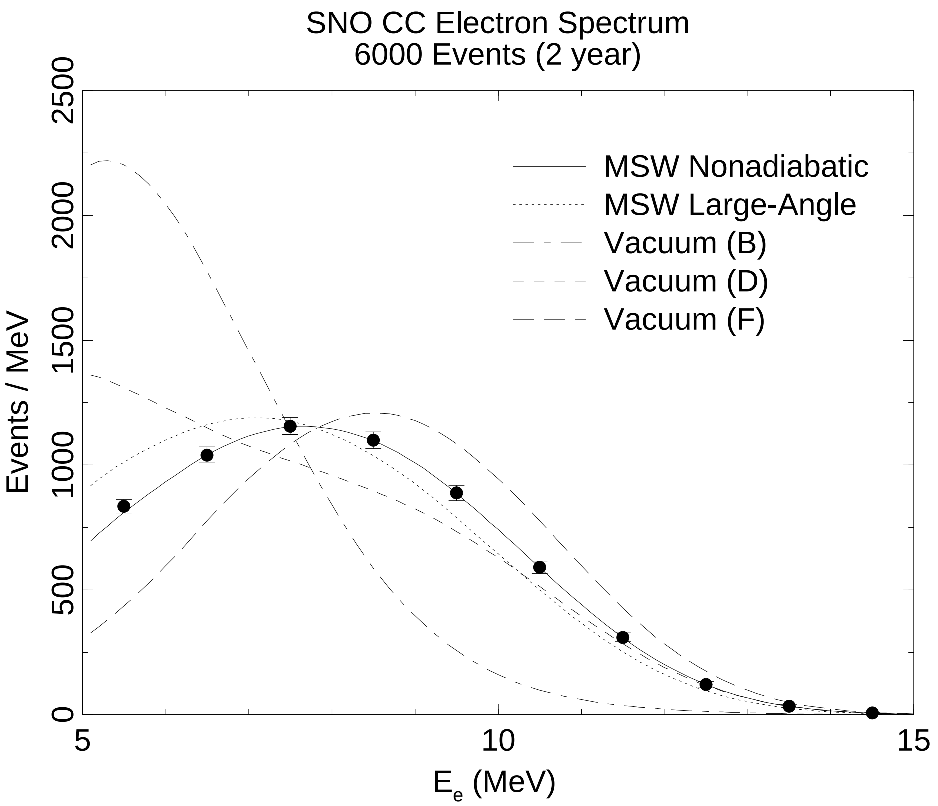

Figure 2.2: Charged-current energy spectral distortion at SNO for various oscillation scenarios(from [39]). The error bars correspond to the statistical uncertainties for a total of 6000 events. The oscillation parameters used in the MSW scenarios are from the combined fit values in Figure 1.5. Values of Δm^2 used in scenarios B, D, F are 1.1×10^{-10}, 7.8×10^{-11}, and 5.0×10^{-11} eV^2, whilst 0.88, 0.75 and 0.93 are used for $\sin^2 2\theta$. It should be noted that the electron-type neutrino survival probability $P(\nu_e \to \nu_e|E_\nu)$ is almost constant for $E_\nu > 5$ MeV in the large-angle MSW scenario. Hence, the spectral shape for this scenario is indistinguishable to that of the no-oscillation scenario.

Neutral Current (NC): $\nu_x + d \rightarrow n + p + \nu_x$

This reaction, which has a kinematic threshold of 2.225 MeV, can be used to determine the *total* neutrino flux. The cross section for this reaction is independent of the flavour of the incident neutrino. SNO therefore has the capability to reveal the presence of neutrino oscillations independent of solar properties. The signature of this reaction is the detection of the free neutron from deuteron disintegration. If the rate of this reaction exceeds that of the charged-current reaction after a proper normalisation of the respective cross sections, then neutrinos must be oscillating. In the Bahcall-Pinsonneault Standard Model calculation, the predicted ^{8}B ν_e neutral-current interaction rate at SNO is [50]

$$\langle \phi\sigma \rangle \; = \; 3.2^{+0.6}_{-0.5}\,\mathrm{SNU} \tag{2.7}$$

where the quoted 1σ uncertainty combines the solar model, the ^{8}B neutrino energy spectrum and the neutral-current interaction cross section uncertainties in quadrature.

The SNO collaboration currently has various schemes to detect free neutrons from this neutral-current channel. When a thermal neutron is captured by a deuteron, a 6.25 MeV gamma ray is emitted. The SNO detector can observe the free neutron by detecting this gamma ray. About 37% of the free neutrons are captured by the deuteron in this pure D_2O scenario [52]. However, a substantial fraction of the 6.25 MeV gamma-ray photopeak is below the ~5 MeV analysis threshold. To enhance the neutron capture and detection efficiency, the SNO collaboration has a plan to add $MgCl_2$ to the D_2O at a concentration of ~0.2 to 0.3%. The free neutrons are captured through $^{35}\mathrm{Cl}(n,\gamma)^{36}\mathrm{Cl}$, and a cascade of gamma rays with a total energy of 8.6 MeV is emitted. In this neutron detection scheme, the neutron capture efficiency is increased to 89%. But only about half of the gamma-ray cascades produce a signal that is above ~5 MeV.

Because of the similarity in the photomultiplier tube array's response to electrons and to gamma rays, one cannot distinguish the CC and the NC events on an event-by-event basis with high efficiency. The SNO collaboration has a plan to install discrete ^{3}He proportional counters in the D_2O volume to capture the free neutrons through the ^{3}He(n,p)^{3}H reaction. In this scheme, the NC and the CC events are recorded separately and can be distinguished event by event. This Neutral Current Detector (NCD) array consists of 96 strings of ^{3}He proportional counters deployed on a square lattice of 1 metre spacing. The body of the counters is made up of chemical vapour deposited (CVD) nickel, which has an ultra-low radioactivity. Each of these strings is a concatenation of one or more individual ^{3}He counters. The neutron detection efficiency is about 45% for the whole array [53].

Elastic Scattering (ES): $\nu_x + e^- \rightarrow \nu_x + e^-$

In the standard electroweak theory, neutrinos of all flavours scatter from electrons by the exchange of the neutral Z° boson. Only ν_e can scatter from electrons by an additional channel through the exchange of the charged W^+ boson. As a result, the scattering cross section of ν_e is six to seven times larger than that for ν_μ or ν_τ. This elastic scattering cross section is therefore sensitive primarily to ν_e. The cross section for this reaction is also much lower than the CC reaction above, but is compensated somewhat by the fact that there are five times more electrons than deuterons in D_2O. The event rate for this ES reaction is about an order of magnitude lower than the CC channel.

However, by combining a measurement of this reaction with the independent measurement of ν_e flux from the CC channel, the total neutrino flux can be determined. Even though the event rate for this ES channel is significantly smaller than the CC channel, the angular distribution of the recoil electrons is sharply forward peaked. For a 5-MeV recoil electron, there is a 90% chance for its outgoing path to be within a cone of a half-angle of 14.6° [40]. This sharp angular response will allow the ES events to be separated from the CC events on a statistical level.

Antineutrino Reactions

Whilst the Sun is not expected to be a source of antineutrinos, astrophysical sources, for example supernovæ, emit $\bar{\nu_e}$. The SNO detector can detect $\bar{\nu_e}$ interaction in its D_2O volume by the reaction

$$\bar{\nu_e} + d \ \rightarrow \ n + n + e^+. \tag{2.8}$$

The signature of this reaction is the prompt Čerenkov light from the positron followed by two delayed neutron capture signals. The kinematics of this reaction are analogous to the CC reaction, except that this reaction has a higher kinematic threshold at 4.03 MeV.

The $\bar{\nu_e}$ from astrophysical sources may also interact in the light water through the reaction

$$\bar{\nu_e} + p \ \rightarrow \ n + e^+. \tag{2.9}$$

The signature of this reaction is the Čerenkov light from the positron, whose angular distribution is almost isotropic with respect to the incident $\bar{\nu_e}$. The neutron would get captured by the hydrogen in the light water, followed by the emission of a 2.2 MeV gamma ray. This gamma ray is lower than the normal analysis threshold of $\sim$5 MeV. But if the event rate is high enough, as in the case of a supernova explosion in a galaxy nearby, a time correlation analysis between the prompt positron signal and the delayed neutron signal may be performed.

2.2.2 Background

A very low background event rate is crucial for the successful operation of the SNO detector due to the rare occurrence of a solar neutrino event. In Figure 2.3, we show the different components of the neutrino and the background signals for the pure D_2O

running scenario. Most of the background signals are low energy events which make up the steep sloped "background wall." In this section, we shall discuss the various types of background events at SNO.

With an overhead shielding of 6000 m.w.e., the only surviving cosmic-ray components that may generate any detectable signals are neutrinos and high energy muons. It is estimated that only $\sim$100 muons pass through the D_2O volume in the SNO detector each day, out of which only $\sim$30 are stopped. The muon induced ^{16}O spallation products—^{8}B, ^{12}B and ^{12}N—are long lived ($\tau_{1/2}$ $\sim$10 to 800 ms), high energy (13 to 16 MeV β end points) β emitters. But these events can be identified rather easily by the initial high energy muon signal followed by the delayed β-decay signal.

The most troublesome type of background is the decay signals produced directly or indirectly by natural radionuclei—^{232}Th, ^{238}U—and their daughters, and ^{40}K. The low-energy background wall in the energy spectrum shown in Figure 2.3 is dominated by the decays of two daughters in the ^{232}Th and the ^{238}U chains: ^{208}Tl and ^{214}Bi. The decay schemes of these two nuclei are shown in Figures 2.4 and 2.5 respectively. These β-γ radionuclei can also generate gamma rays of energy greater than the deuteron binding energy. Hence, these gamma rays are capable of breaking up the deuterons in a similar manner as the neutrinos in NC reaction. One neutron is produced per $\sim$470 2.615-MeV gamma rays from ^{208}Tl decay. For ^{214}Bi decay, one neutron is generated per $\sim$750 2.445-MeV gamma rays [54]. Therefore, the SNO collaboration has placed a very stringent limit on the radioactive purity of all construction materials in order to minimise this photodisintegration background. In Table 2.2, we list the concentration levels of ^{232}Th and ^{238}U in the D_2O, H_2O and the acrylic vessel that would generate one neutron per day in the SNO detector.

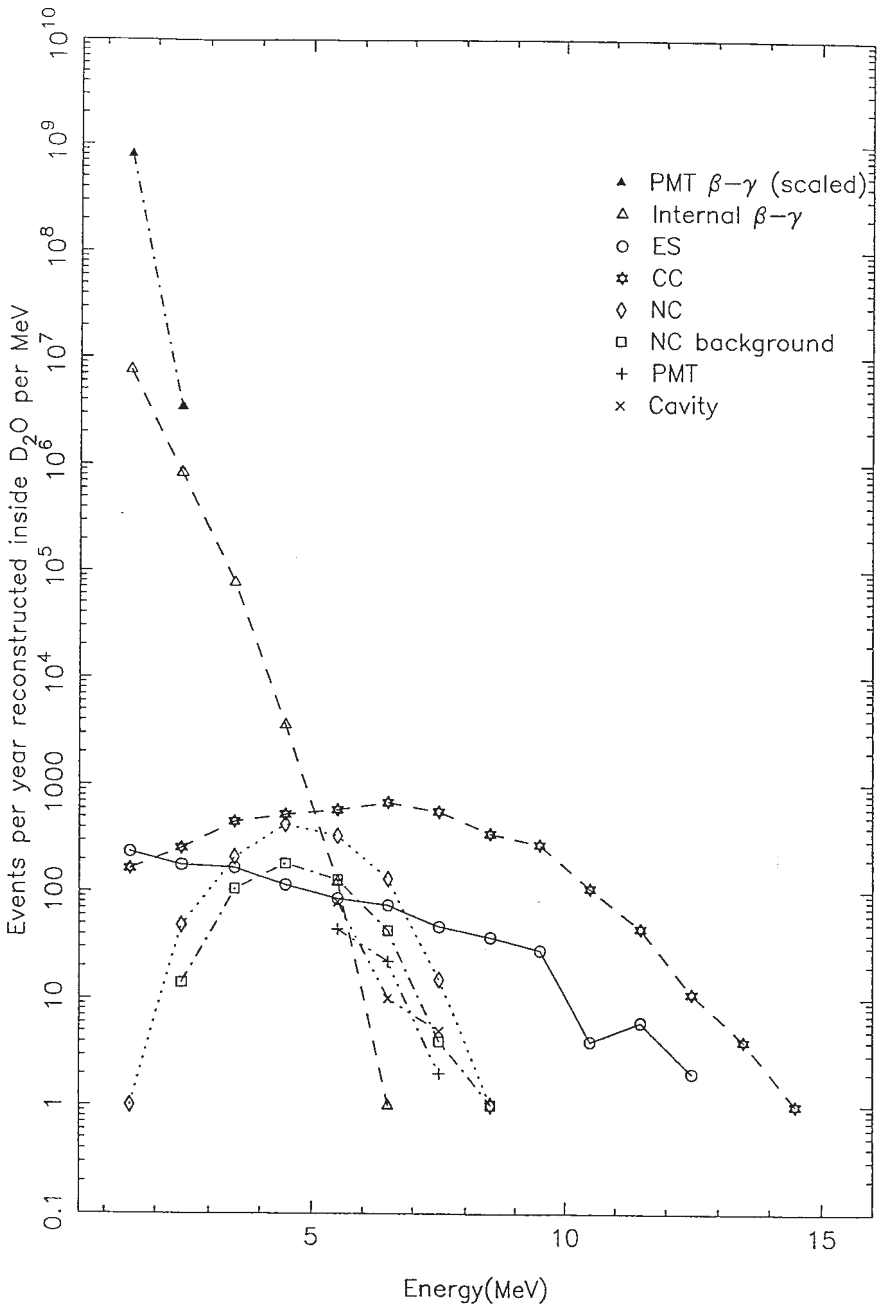

Figure 2.3: Expected signals at the Sudbury Neutrino Observatory detector from 1 year of pure D_2O running. Anticipated signals are shown individually in this plot.

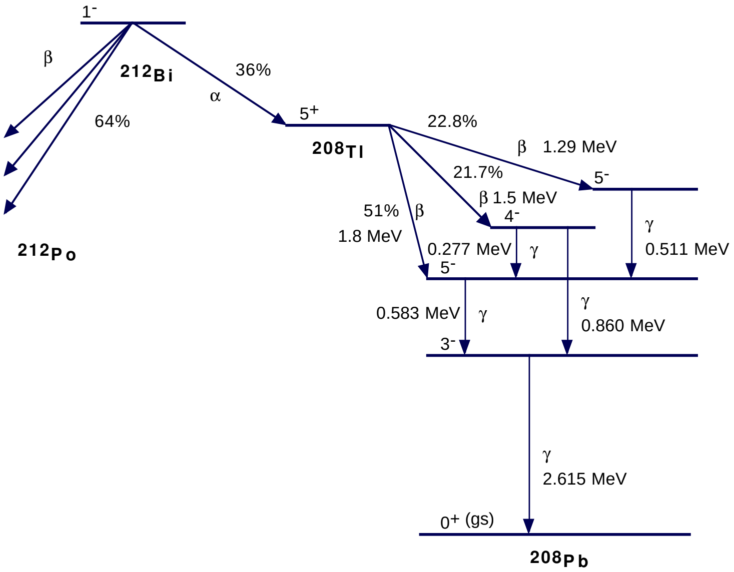

Figure 2.4: Simplified decay schemes for ^{212}Bi. The 2.615 MeV gamma ray from ^{208}Tl decay can generate a background neutron by photodisintegrating the deuteron.

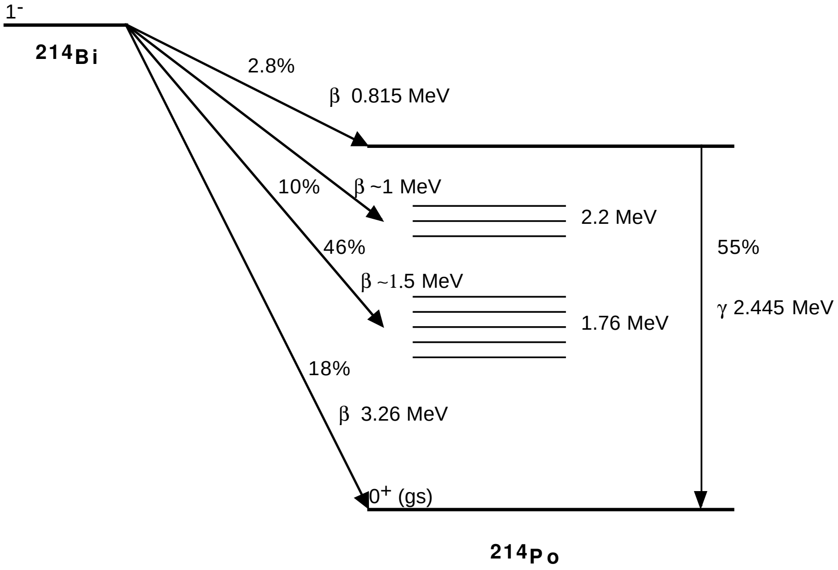

Figure 2.5: Simplified decay schemes for ^{212}Bi. The 2.445 MeV gamma ray can generate a background neutron by photodisintegrating the deuteron.

	^{232}Th (pg/g)	^{238}U (pg/g)
D_2O	0.0037	0.045
H_2O	0.13	1.0
Acrylic	1.9	3.6

Table 2.2: Tolerable radioactive purity level of the D_2O, H_2O and the acrylic vessel at SNO. These numbers represent the radioactive purity level that would generate a photodisintegration neutron background of one per day [54].

2.3 Calibration of the SNO Detector

The calibration of the SNO detector will be achieved by the insertion of optical light, neutron, β and γ sources into the heavy water and the outer light water regions in order to determine the optical, neutron and energy responses of the detector. The calibration sources cover a wide range of output and will be placed at a sufficient variety of positions in the detector. The design criteria [55] call for an energy calibration uncertainty to be less than 1% , and the statistical accuracy of neutral-current efficiency determination to be better than 2%.

Maneuvering of sources inside the D_2O volume will be provided by the source manipulator system. This system is shown in Figure 2.6. The manipulator source carriage is connected to the central rope of the system. Side ropes run through the pulleys on the carriage to the rope anchors located on the acrylic vessel at 10° above the equator. By controlling the tension and the length of the ropes, sources can be deployed to two different planes in the D_2O volume.

In the following, we shall describe the calibration sources being developed by the SNO collaboration.

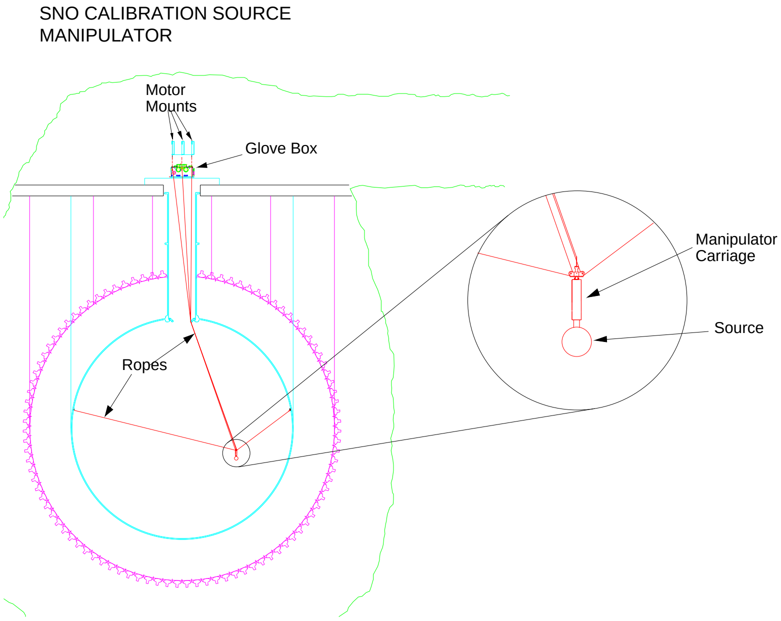

Figure 2.6: The SNO calibration source manipulator system

2.3.1 Optical Light Sources

Optical light sources are used to determine the optical light attenuation and scattering in the heavy water, the light water and the acrylic vessel. They will also be used to determine the timing and the quantum efficiencies of the photomultiplier tubes.

Optical properties of the detector and the characteristics of the photomultiplier tubes will be established by means of a “laser ball.” A N_2 laser is used to pump separate dye lasers to provide four separate wavelengths in the range of 337 nm and 386 nm. The laser light is transported to a diffuser ball through an optic fibre. This is the default optical calibration source at SNO.

The short wavelengths are where the D_2O and the acrylic attenuations are largest. The frequency response of the photomultiplier tubes must also be determined *in situ*. The SNO collaboration plans to use a fast N_2 pulser lamp and light filters to produce light with wavelengths less than 337 nm.

To achieve accurate photomultiplier tube timing calibration, the SNO collaboration has developed a sonoluminescence source. The laser ball and the laser lamp are not ideal for this purpose because of the wavelength dependence of light dispersion in the optic fibre and filters. Optical light pulses of width $<$100 ps are emitted when sound waves compress the air bubbles in water — sonoluminescence. The frequency spectrum of such a source is similar to that of a blackbody ranging from several thousand to tens of thousands of Kelvin.

2.3.2 Neutron Sources

Because an excessive neutral-current to charged-current signal ratio in SNO would indicate physics beyond the standard electroweak model, a thorough understanding of the neutron efficiencies is therefore of utmost importance. The default neutron source to be used for neutron calibration at SNO is a ^{252}Cf fission source. A ^{17}N β-n source is also under development.

The ^{252}Cf triggerable fission source will be housed in an acrylic capsule where a small plastic scintillator disc is also located. The fission source produces on average 4 neutrons and 20 γ-rays per fission. The trigger will be provided by the scintillation light emitted from the scintillator disc.

The ^{17}N source β-n decay branches have a total branching ratio of about 95%. Whilst the average neutron energy is about 2 MeV for the ^{252}Cf source, the ^{17}N source has somewhat lower neutron energies, dominated by the 0.38 MeV and the 1.17 MeV branches. One feature of this source is that it is able to use the same gas transport system as another proposed $\beta - \gamma$ source ^{16}N.

2.3.3 β and γ Sources

Relativistic electrons and γ-rays will be used for energy calibration, for understanding Čerenkov light production in D_2O and H_2O, and for understanding deuteron photodisintegration background in D_2O. An accurate determination of the energy calibration constants is important because the SNO CC energy spectrum is susceptible to distortion due to the energy dependence of neutrino oscillations. Therefore, a thorough understanding of the background in SNO is crucial to the determination of the CC to NC ratio. The SNO collaboration is developing several β and γ sources with energies ranging from less than 2 MeV to about 20 MeV.

In the ^{228}Th plated wire proportional counter source, the trigger signal will be provided by the β emitted by ^{208}Tl, which is a daughter in the natural Th chain. Subsequent to the β decay is a prompt γ of energy up to 2.6 MeV. This source is particularly useful in understanding the deuteron photodisintegration background, as most of the background in SNO will come from the $\beta - \gamma$ decays in the natural ^{232}Th and ^{238}U chains.

Another calibration source, namely the ^{24}Na source, is being developed to help the SNO collaboration to understand the $\beta - \gamma$ signal from the natural chains. The ^{24}Na simultaneously emits two γ rays with energies of 1.37 and 2.74 MeV. Therefore it can serve both as an energy calibration and as a fair simulation of the $\beta - \gamma$ background with the Compton electron from the 1.37 MeV γ mimicking the β.

The default energy calibration source at SNO is the ^{16}N source. There are two principal ^{16}N decay modes; it produces a β with an endpoint of 4.27 MeV and a γ of 6.13 MeV 60% of the time, and it produces a 10.4 MeV endpoint β with a 29% branching ratio. The ^{16}N nucleus will be produced through the reaction ^{16}O(n,p)^{16}N, and will be transported by an aerosol through a capillary tube into a decay chamber, which has already been lowered into the heavy water volume of the SNO detector. The decay chamber has a sufficiently thick wall to stop the 10.4-MeV endpoint β's. There is a scintillator coupled to a small photomultiplier tube inside the chamber. This will allow the 6.13-MeV γ-ray signal seen by the SNO photomultiplier tube array to be tagged by the 4.27-MeV endpoint β.

The two nuclei ^{8}Li and ^{8}B are mirror nuclei and have similar beta endpoint energies: ^{8}Li has a β^{-} endpoint of 13 MeV, whilst ^{8}B has a β^{+} endpoint of 14 MeV. This makes ^{8}Li an ideal electron source to mimic the ^{8}B solar neutrino spectrum, which is what SNO was built to detect. The ^{8}Li will be produced via the reaction ^{11}B(n,α)^{8}Li and the ^{8}Li nuclei will be transported by an aerosol to a decay chamber. The decay chamber will be a wire chamber so that the ^{8}Li decays are tagged by the 2α decay of its daughter ^{8}Be.

Finally, the SNO collaboration needs calibration sources that are capable of generating γ-rays with energies beyond the endpoint of the solar neutrino energy spectrum. This capability allows a systematic check on the SNO detector's linearity in the energy response. In the arsenal of calibration sources, there are two high energy gamma-ray sources proposed: the ^{7}Li(p,γ)^{8}Be and the ^{3}H(p,γ)^{4}He (pT) sources. Both of these sources have a similar conceptual design — an ion source to generate an ion beam, which is subsequently accelerated towards a fixed solid target. The ^{7}Li(p,γ)^{8}Be reaction generates gamma rays at 14.3 MeV (83%) and 17.3 MeV (17%), whilst the pT source generates a monoenergetic line at 19.8 MeV.

Although similar in design, these two sources have their own attributes. Because of a higher Coulomb barrier in the p+^{7}Li system, this ^{7}Li(p,γ)^{8}Be source will have to accelerate the protons to a much higher energy in order to provide the same gamma-ray yield as the pT source. Chasteler and Weller [56] have proposed a similar ^{7}Li(p,γ)^{8}Be source using a compact proton source based on the Zetatron neutron generator design [57]. They estimated that such a device would produce $\sim$430 17.3-MeV gamma rays sr^{-1} min^{-1} and $\sim$2070 14.3-MeV gamma-rays sr^{-1} min^{-1} if using a 100 μA pure atomic beam at 80 keV.

Efforts have been devoted to constructing such a calibration device for SNO at Queen's University in Kingston, Canada [58, 59]. However, there has not been any concrete evidence for the observation of the gamma rays due to various technical difficulties with the operation of the ion source.

We designed and constructed a 19.8-MeV gamma-ray source using the radiative capture reaction $^3\mathrm{H}(p,\gamma)^4\mathrm{He}$. This is the first self-contained and portable high energy γ-ray source ($E_\gamma >$10 MeV) ever built. In the rest of this thesis, we shall devote our discussion to the design, construction, and the operation of this pT source. We shall further discuss ways to calibrate the SNO detector using a monoenergetic gamma-ray source.

Chapter 3

The Design of a ^{3}H(p,γ)^{4}He High Energy Gamma-Ray Source

> *He had been eight years upon a project for extracting sunbeams out of cucumbers, which were to be put in phials hermetically sealed, and let out to warm the air in raw inclement summers.*
>
> Jonathan Swift
> Gulliver's Travels, Part iii. Chap. V (1726)

As we have seen in the last chapter, the SNO collaboration has an extensive list of calibration sources for understanding the SNO detector response. The energy range these sources cover extends to well beyond the endpoint of the solar neutrino spectrum.

A high energy calibration point is very important to understanding the detector's energy response. As the energy increases, the probability that a photomultiplier tube would get hit by more than one Čerenkov photon increases. Therefore, a calibration point beyond the solar neutrino energy endpoint will provide vital information on this multiple hit effect at energies beyond the solar neutrino endpoint.

We have successfully constructed a 19.8-MeV gamma-ray energy source using the $^3\mathrm{H}(p,\gamma)^4\mathrm{He}$ (pT) reaction. In this chapter, we shall first outline the design criteria for a high energy gamma-ray calibration source at SNO. We shall then describe the design of the pT source. The results of a yield calculation on the source's output are also presented. We shall conclude this chapter by summarising the operational characteristics of the ion source used in this pT source. The research and development work on a non-radioactive prototype using the ^{2}H(p,γ)^{3}He reaction is summarised in the next chapter. Results from testing the actual pT source can be found in Chapter 5.

3.1 Design Criteria

One way to calibrate the high energy response ($10< E <20$ MeV) of a water Čerenkov detector like SNO is to use monoenergetic electrons originating from different locations in the detector. However, this requires the acquisition of a high energy electron accelerator, and the construction of the associated beam line for transporting the electron beam into various parts of the active D_2O volume. This is an expensive and technically challenging task. The SuperKamiokande collaboration has adopted this energy calibration approach.

Another approach to provide a high energy calibration is to use high energy gamma rays generated from radiative capture reactions in low mass nuclei. This is the approach we have adopted at SNO. The devices which provide these high energy gamma-rays must be compact enough to be maneuvered to different regions in the D_2O volume using the SNO calibration source manipulator system. This allows the sources to be deployed to various parts of the detector where a high energy electron beam cannot reach. The largest insertion port for calibration devices at SNO can accommodate devices up to about 30 cm in diameter and 75 cm in length. This physical constraint limits the actual size of such calibration devices. For instance, a previous proposal [60] of using the ^{3}He(n,γ)^{4}He reaction to provide a 21-MeV calibration line was abandoned because the neutron shielding required to reduce neutron leakage into the D_2O volume would exceed this physical constraint.

Because the SNO detector is essentially a 100% efficient, 4π detector to gamma rays, one does not need to design a high energy source with a high gamma-ray production rate. The calibration time in SNO is a few hours for such a source. A statistical accuracy of $\sim$1% can be achieved with a gamma-ray yield of 0.2 s^{-1} in about twelve hours.

The high energy gamma-ray source is required have a low neutron production rate. This will minimise the signal interference of the gamma rays resulting from thermal neutron capture by ^{35}Cl in D_2O in the "salt" running scenario and the dead time in the data acquisition system. A neutron production of less than 10^4 s^{-1} is needed for the design goal of >0.2 γ s^{-1}. We shall evaluate the neutron and gamma-ray productions by the *pT* source in Chapter 5. The reader is referred to Figure 5.15 for the expected energy calibration spectrum of the *pT* source in SNO.

The *pT* source will be deployed to calibrate the SNO detector whenever there is a change to the detector configuration (e.g. after the installation of the Neutral Current Detector array), or when a high energy calibration is called for (e.g. after a supernova explosion). Therefore, the source must last for several 12-hour calibration runs. An operational lifetime of >60 hours for the *pT* source will be more than enough to calibrate the SNO detector during its anticipated life span.

Electromagnetic interference between this high energy calibration source and the photomultiplier tube array must be minimal. For instance, the accelerator sources like the *pT* source have to be run in direct current (d.c.) mode, instead of pulsed mode, to eliminate possible electromagnetic pickup by the photomultiplier tube array.

3.2 Attributes of a ^{3}H(p,γ)^{4}He Source

The ^{3}H(p,γ)^{4}He reaction has a Q-value of 19.82 MeV. Since ^{4}He does not have a bound excited state, the gamma ray emitted in this reaction is monoenergetic. Building a compact gamma-ray calibration source using this reaction is an attractive proposal for several reasons.

First of all, the projectile and the target have unit charge. Therefore, the effect of Coulomb suppression on the cross section for this reaction is less than reactions with other combinations of incoming charged projectiles and targets. Hence, the beam energy and power will be minimised. This will allow the beam to be run in a d.c. mode without incorporating a complicated cooling system for the target.

As the Q-value of ^{3}H(p,n)^{3}He is -0.763 MeV, or a reaction threshold of 1.02 MeV in the laboratory frame, the pT source is essentially "neutron-free" if the proton energy is below this threshold. However, isotopic "impurities" and the co-mingling of the beam and the target will give rise to undesirable neutrons through the ^{2}H(t,n)^{4}He, ^{3}H(d,n)^{4}He, and ^{3}H(t,nn)^{4}He reactions. The Q-value of the first two reactions is 17.59 MeV, and that of the last reaction is 11.3 MeV. In principle, one can eliminate this neutron production problem by mass analysing the beam. However, this option is not possible in the pT source given the physical size constraint.

A monoenergetic calibration source like the pT source has its advantage in a water Čerenkov detector like SNO. Radcliffe [61] demonstrated by Monte Carlo calculations that the SNO detector does not have enough energy resolution to resolve the two lines from a ^{7}Li(p,γ)^{8}Be source. Therefore, one would need to have a good knowledge of the gamma-ray line shapes and gamma-ray attenuation by the source hardware in this system in order to calibrate the detector to a high degree of accuracy.

3.3 Yield Calculation

In this section, we shall calculate the yield for reactions that are relevant to the pD and the pT sources. The pD source is a non-radioactive prototype of the pT source using the radiative capture reaction ^{2}H(p,γ)^{3}He to generate 5.5-MeV gamma rays. Details about the pD source can be found in the next chapter. In subsequent chapters, we shall refer to the results from the yield calculations below in order to understand the sources' performance.

3.3.1 Low Energy Charged Particle Cross Section

For low energy charged-particle capture reactions between two particles of charges Z_0 and Z_1 and a reduced mass μ, the reaction cross section $\sigma(E)$ at a centre-of-mass energy E can be parameterised by an energy dependent function $S(E)$ [62]:

$$\sigma(E) \;=\; \frac{S(E)}{E}\exp\left(-\sqrt{\frac{E_G}{E}}\right), \tag{3.1}$$

where the Gamow energy E_G, which is a measure of the Coulomb barrier, is given by (in the units of $\hbar = c = 1$) [62]

$$E_G \;=\; (2\pi\alpha Z_0 Z_1)^2\left(\frac{\mu}{2}\right). \tag{3.2}$$

For non-resonant reactions, the energy dependent function $S(E)$, also known as the S-factor, is expected to be a slowly varying function at low energy. One can expand this function in a Maclaurin series:

$$S(E) \;\simeq\; S(0)\left(1+\frac{S'(0)}{S(0)}E+\frac{1}{2}\frac{S''(0)}{S(0)}E^2\right). \tag{3.3}$$

The parameters $S(0)$, $S'(0)$ and $S''(0)$ can be extracted from laboratory measurements of the cross section for the reactions concerned.

3.3.2 A Survey of the Astrophysical S-Factors

We did a literature search on the cross sections, and hence the S-factors, for reactions that are relevant to the pD and the pT sources. In this section, we shall summarise the findings.

The ^{2}H(p,γ)^{3}He and the Neutron Generating Reactions

The S-factors recommended in Fowler, Caughlan and Zimmerman (FCZ) [62] for the ^{2}H(t,n)^{4}He, ^{3}H(d,n)^{4}He, and ^{3}H(t,nn)^{4}He neutron-producing reactions are in agreement with a wide range of theoretical calculations and experiments [63]. In our yield calculations in Section 3.3.3, we shall use those parameters recommended in FCZ.

For the ^{2}H(p,γ)^{3}He reaction, the S-factor measured by Griffiths *et al.* [64] is in disagreement with a recent measurement by Schmid *et al.* [65]; the S-factor extracted by Schmid *et al.* is 52% lower than that of Griffiths *et al.* We shall use both cross sections in our yield calculations in Section 3.3.3.

The ^{3}H$(p,\gamma)^4$He Reaction

For the ^{3}H$(p,\gamma)^4$He reaction, the S-factor recommended in FCZ is in disagreement with two independent measurements at low energy. The S-factor recommended in FCZ is based on a measurement by Perry and Bame [66]. When we calculated the S-factor using the parameters recommended in FCZ, we found a large discrepancy between the calculated and the measured values. A recent measurement of the cross section by Hahn *et al.* [67] is in good agreement with Perry and Bame. In Figure 3.1, we show a comparison of the measured S-factors in Perry and Bame and Hahn *et al.* to the calculated values using parameters recommended in FCZ.

In Table 3.1, we have listed the possible transitions along with the corresponding gamma-ray angular distributions in the ^{3}H$(p,\gamma)^4$He reaction. The 19.8-MeV gamma rays emitted from this reaction have been shown experimentally to have a predominant $\sin^2\theta$ distribution from a proton energy of a few hundred keV to over 10 MeV [66, 68, 69, 70, 71, 72, 73, 74]. This angular distribution arises from E1 (electric dipole) capture of p-wave protons. Data at proton energies $1< E_p <6$ MeV also show that the relative strength of E2 capture of singlet d-wave protons increases with energy [66].

The predominant $\sin^2\theta$ distribution can be described as a direct capture process [75, 76]. For an electric dipole capture process involving a projectile of mass M_1, charge Z_1, spin s_1 and lab energy E_1 captured by a target of mass M_2, charge Z_2 and total angular

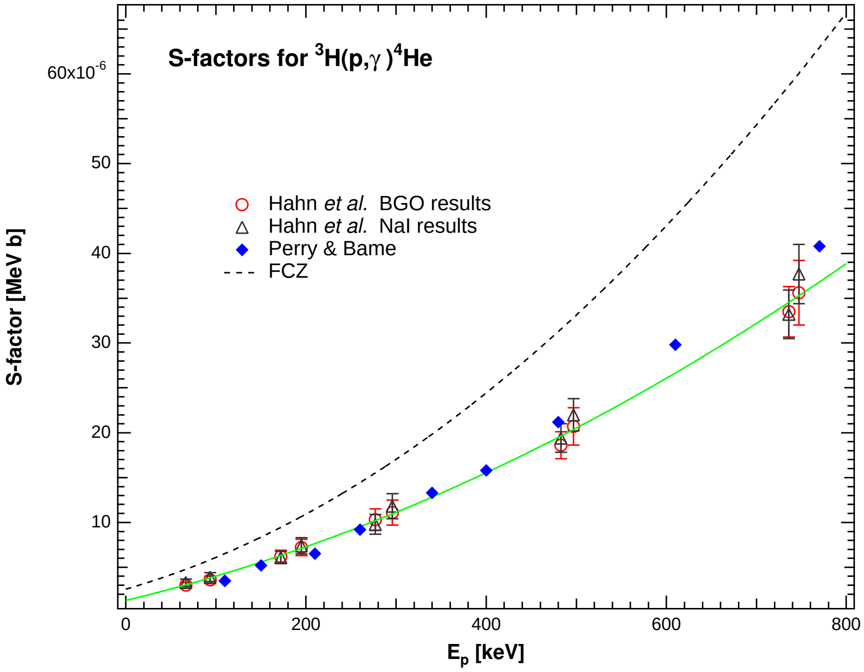

Figure 3.1: Comparing the S-factor in the ^{3}H$(p,\gamma)^4$He reaction as a function of proton energy. Measured S-factors by Perry and Bame [66] and Hahn *et al.* [67] are shown as data points in this plot. Hahn *et al.* used a BGO detector and a NaI detector in their measurements, and the results for these two detectors are shown separately here. The calculated S-factor using parameters recommended in Fowler, Caughlan and Zimmerman (FCZ) [62] is shown as the dashed curve. The solid curve is a χ^2 fitted curve to the combined data in Hahn *et al.*

Entrance channel			Transition		Angular distribution
S	L	J			
0	0	0	$^1\mathrm{S}_\mathrm{o}\rightarrow{}^1\mathrm{S}_\mathrm{o}$		γ-ray forbidden
0	1	1	$^1\mathrm{P}_1\rightarrow{}^1\mathrm{S}_\mathrm{o}$	E1	$\sin^2\theta$
0	2	2	$^1\mathrm{D}_2\rightarrow{}^1\mathrm{S}_\mathrm{o}$	E2	$\sin^2\theta\cos^2\theta$
1	0	1	$^3\mathrm{S}_1\rightarrow{}^1\mathrm{S}_\mathrm{o}$	M1	isotropic
1	1	0	$^3\mathrm{P}_\mathrm{o}\rightarrow{}^1\mathrm{S}_\mathrm{o}$		γ-ray forbidden
1	1	1	$^3\mathrm{P}_1\rightarrow{}^1\mathrm{S}_\mathrm{o}$	E1	$1+\cos^2\theta$
1	2	1	$^3\mathrm{D}_1\rightarrow{}^1\mathrm{S}_\mathrm{o}$	M1	$5\text{-}3\cos^2\theta$
1	2	2	$^3\mathrm{D}_2\rightarrow{}^1\mathrm{S}_\mathrm{o}$	E2	$1\text{-}3\cos^2\theta+4\cos^4\theta$

Table 3.1: Multipole transition and angular distribution of the ^{3}H$(p,\gamma)^4$He reaction. Transitions of order higher than electric quadrupole have been omitted. From [66].

momentum J_2, the cross section is (in the units of $\hbar = c = 1$) [76]:

$$\sigma_1 = \frac{16\pi}{9} E_\gamma^3 \left(\frac{M_1}{2E_1}\right)^{\frac{1}{2}} \frac{1}{(2J_2+1)(2s_1+1)} \sum_{m\mu_1\mu_2\mu_f} |Q_{1m}|^2 , \tag{3.4}$$

where E_γ and m are the energy and the polarisation of the emitted gamma ray, and μ_1, μ_2 and μ_f are the angular momentum projections of the projectile, target and final state nuclei respectively. The transition element for polarisation m, Q_{1m}, is given by [76]

$$Q_{1m} = \frac{eM_1M_2}{M_1+M_2}\left(\frac{Z_1}{M_1}-\frac{Z_2}{M_2}\right)\int rY^*_{1m}(\theta,\varphi)\Phi^*_f(r,\theta,\varphi)\Phi_i(r,\theta,\varphi)\,d^3r \tag{3.5}$$

where r, θ, φ are the relative coordinates of the projectile and the target nuclei, and $\Phi_i(r,\theta,\varphi)$ and $\Phi_f(r,\theta,\varphi)$ are the initial and final state wave functions.

We attempted to understand theoretically the behaviour of the cross section for E1 capture of p-wave protons in ^{3}H$(p,\gamma)^4$He at low proton energies. Christy and Duck [76] derived analytically the electric dipole moment matrix element between an undistorted initial Coulomb wave function and a final bound state function of the residual nucleus in the long-wavelength limit. In this approximation, they found that for many reactions of low binding energy E_B the integrand rises to a maxiumum value at a radius r_m which is many times the nuclear radius r_n:

$$r_n \sim 1.4\,(A_1^{\frac{1}{3}} + A_2^{\frac{1}{3}})\,\mathrm{fm}, \tag{3.6}$$

where A_1 and A_2 are the atomic weights of the projectile and the target nucleus. The irregular Coulomb function, which interacts strongly with the nucleus, is negligible at r_m. Hence, the capture matrix element is determined by regions external to r_n.

A closed form of the S-factor was found for cases that satisfy the conditions α >1 and η >1, where

$$\alpha = Z_1 Z_2 e^2 \sqrt{\frac{\mu}{2E_B}} \quad \text{and} \tag{3.7}$$

$$\eta = Z_1 Z_2 e^2 \sqrt{\frac{M_1}{2E_1}} \tag{3.8}$$

with E_B being the Q-value of the reaction, and μ the reduced mass. For reactions that satisfy these conditions, the derived S-factor is

$$\begin{aligned} S &= 8\pi^2 e^2 E_B \left(\frac{3E_B}{E_\gamma}\right)^{\frac{1}{3}} \left(\frac{Z_1}{M_1} - \frac{Z_2}{M_2}\right)^2 \langle l_1, l_2\rangle\, \theta^2\, \frac{(2\alpha)^{\frac{7}{6}}}{x_n^{\frac{3}{2}}} \\ &\times \exp\left[\frac{2\,(l_2^2 - l_1^2)}{12^{\frac{1}{3}}\alpha^{\frac{2}{3}}} \left(\frac{E_\gamma}{E_B}\right)^{\frac{1}{3}} - 2 + 4\sqrt{2\alpha x_n} - \frac{2l_2^2}{\sqrt{2\alpha x_n}} + \frac{\frac{2}{3}x_n^2}{\sqrt{2\alpha x_n}}\right], \end{aligned} \tag{3.9}$$

where l_1 and l_2 are the orbital angular momenta of the initial and the final states, $\langle l_1, l_2\rangle$ represents the larger value of l_1 and l_2, θ^2 is the reduced width, and $x_n = r_n\sqrt{2\mu E_B}$.

We expressed the energy dependence of S in Eqn.(3.9) as

$$S \propto \frac{1}{\left(1 + \frac{E}{E_B}\right)^{\frac{1}{3}}} \exp\left[-\beta\left(1 + \frac{E}{E_B}\right)^{\frac{1}{3}}\right] \tag{3.10}$$

where E is the centre-of-mass energy of the projectile and β is a positive constant for all $p \to s$ wave transitions. Upon a close examination of this expression, we found that it is a monotonically decreasing function for gamma rays of any energy. While this energy dependence is typical of many direct capture reactions it is opposite to the experimental data shown in Figure 3.1, indicative of significant nuclear interior contributions and the inapplicability of the long-wavelength approximation.

For the $^3\mathrm{H}(p,\gamma)^4\mathrm{He}$ reaction, α=0.031 and $\eta < 1$ for proton energies E_p >25 keV. These values do not satisfy the conditions for S in Eqn.(3.9) to apply in this reaction, we argue that a simple long-wavelength approximation calculation is not adequate in this reaction. The radius r_m at which the radial integrals in this long-wavelength approximation peaks, in the case of α <1 and η >1, is [76]

$$r_m = \frac{x_m}{\sqrt{2\mu E_B}}, \tag{3.11}$$

where x_m is defined as

$$\sqrt{x_m} = \sqrt{\frac{1}{2}\alpha} + \sqrt{\frac{5}{4} - \frac{1}{2}\alpha}. \tag{3.12}$$

We found that for the $^3\mathrm{H}(p,\gamma)^4\mathrm{He}$ reaction at E_p <25 keV, r_m=1.8 fm; whereas the nuclear radius r_n (Eqn.(3.6)) is found to be 2.8 fm. This is a consequence of the exceptionally high binding energy and is a clear indication that nuclear interior effects must be taken into account in calculating the cross section for this reaction. We could not find any detailed calculation of the $^3\mathrm{H}(p,\gamma)^4\mathrm{He}$ reaction cross section at low energies in the literature.

In order to estimate the cross section of the $^3\mathrm{H}(p,\gamma)^4\mathrm{He}$ reaction for proton energies E_p <30 keV, we resorted to performing a χ^2 minimisation of $S(E)$ to the empirical form in Eqn.(3.3) using the lowest energy data ($0.1 \leq E_p \leq 0.75$ MeV) from Hahn *et al.* [67]. In the cross section measurement by Hahn *et al.*, gamma rays from the $^3\mathrm{H}(p,\gamma)^4\mathrm{He}$ reaction were measured simultaneously by a BGO detector and a NaI detector. We combined the BGO and the NaI data sets from their study in this fitting. The fitted curve is shown in Figure 3.1, and we have summarised the fitting results in Table 3.2. We want to emphasise that this type of empirical fitting without any guidance from a theoretical

	$S(0)$ (MeV b)	$S'(0)/S(0)$ (MeV^{-1})	$\frac{1}{2}S''(0)/S(0)$ (MeV^{-2})
FCZ recommended values [62]	2.56×10^{-6}	15.1	44.6
Our fitted values	$(1.30\pm0.40)\times10^{-6}$	25±12	38.8±7.3
Correlation	1.00	-0.99	-0.65
Matrix	-0.99	1.00	0.53
	-0.65	0.53	1.00
χ^2_ν		0.22	

Table 3.2: χ^2 minimisation results in fitting the S-factors from Hahn *et al.* Values recommended by Fowler, Caughlan and Zimmerman (FCZ) [62] are also shown for comparison.

model cannot be relied upon because there may be significant effects at the low energy regime where no experimental data exists.

We compared the S-factors calculated from the parameters in FCZ ($S_{FCZ}(E)$) and from our empirical fitting to the data in Hahn *et al.* ($S_{fit}(E)$) at centre-of-mass energies below 100 keV in Figure 3.2. Also shown in the figure is the ratio S_{FCZ}/S_{fit}. It is clear from the figure that if one uses the parameters recommended in FCZ, the calculated S-factor is too high by almost a factor of 2 in this energy range.

In Table 3.3, we summarise the parameters to be used in the next section to calculate the yields for reactions that are relevant to the pT source and the pD prototype.

3.3.3 Gamma-Ray and Neutron Production Rate Calculation

The main concern of the pT source is the degree to which tritium gets mixed into the hydrogen discharge gas. The higher the tritium content in the gas, the higher the neutron flux that results. Neutrons are generated primarily through three reactions: ^{2}H(t,n)^{4}He, ^{3}H(d,n)^{4}He, and ^{3}H(t,nn)^{4}He. The minimum amount of deuterium in the target is limited by the isotopic purity of the tritium gas used in the target fabrication process. On the

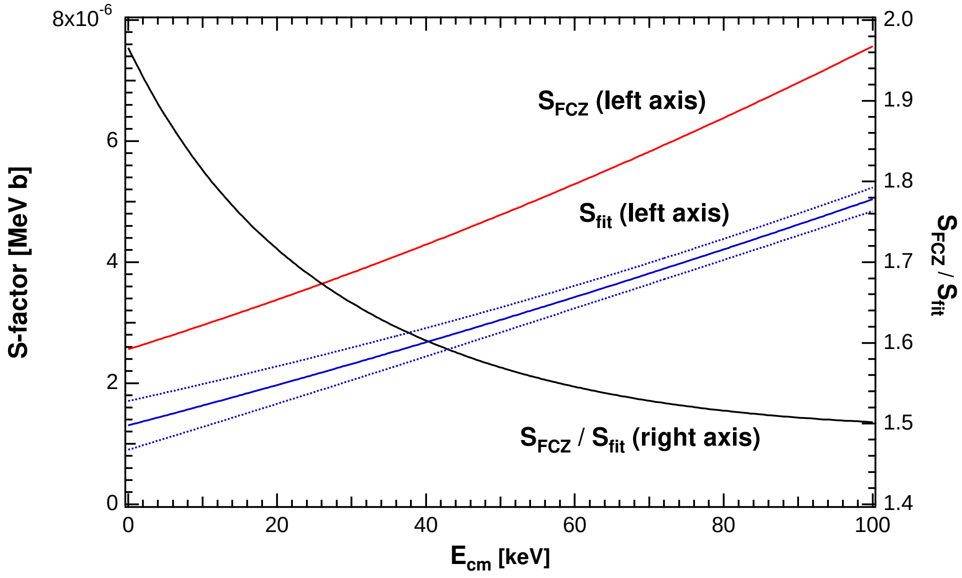

Figure 3.2: Extrapolated S-factors at centre-of-mass energy E <100 keV. The S_{FCZ} curve was calculated using parameters recommended by Fowler, Caughlan and Zimmerman [62], whilst the S_{fit} curve was calculated using the fitted parameters in Table 3.2. The "band" around the S_{fit} curve is the 1σ uncertainty calculated using the covariance matrix in Table 3.2. The ratio S_{FCZ}/S_{fit} is also shown to demonstrate that the extrapolated cross section differed by over 50% for E <100 keV.

Source	Reaction	$\sqrt{E_G}$ ($\mathrm{MeV}^{-\frac{1}{2}}$)	$S(0)$ (MeV-barn)	$S'(0)/S(0)$ MeV^{-1}	$\frac{1}{2}S''(0)/S(0)$ MeV^{-2}	Ref.
pD	^{2}H(p,γ)^{3}He	8.108×10^{-1}	2.50×10^{-7}	—	—	[64]
		8.108×10^{-1}	1.21×10^{-7}	—	—	[65]
	^{2}H(d,n)^{3}He	9.928×10^{-1}	5.30×10^{-2}	4.95	—	[62]
pT	^{3}H$(p,\gamma)^4$He	8.598×10^{-1}	1.30×10^{-6}	2.5×10^{1}	3.88×10^{1}	[67]
	^{3}H(d,n)^{4}He	1.087	1.10×10^{1}	1.38×10^{1}	6.23×10^{2}	[62]
	^{3}H(t,nn)^{4}He	1.215	1.60×10^{-1}	—	—	[62]
	^{3}H$(t,\gamma)^6$He	1.215	—	—	—	—

Table 3.3: S-factors for reactions that are relevant to the pD and the pT sources. Two sets of S-factors are listed for the ^{2}H(p,γ)^{3}He reaction here as they differ by over 50%. The S-factors for the reaction ^{3}H$(t,\gamma)^6$He, whose Q-value is 12.3 MeV, is not known. The S-factors listed for the ^{3}H$(p,\gamma)^4$He reaction are extracted from data in Hahn *et al.* [67] (see text).

other hand, isotopic purity of the H_2 discharge gas determines the amount of deuterons in the beam. Tritons and deuterons can also appear in the discharge gas due to co-mingling of the target and the beam.

For an "infinitely" thick target like the scandium tritide film we proposed for the pT source, the gamma-ray or the neutron yield can be expressed as

$$Y(E_L) \;=\; g\phi_{ion}n_{target}\int_0^{E_L}\frac{\sigma(E)}{\left(-\frac{dE}{dx}\right)}\;dE \tag{3.13}$$

where E_L and ϕ_{ion} are the energy and the flux of incident ions, n_{target} is the number density of the target nuclei, $\sigma(E)$ is the reaction cross section, and g is the multiplicity. This multiplicity factor is unity for all the reactions that are relevant to the pT source, except for the ^{3}H(t,nn)^{4}He reaction, which has a multiplicity of 2 because of the two neutrons in the final state.

We used the program SRIM [77] to generate the stopping power ($-dE/dx$) for protons in the proposed scandium tritide target. Those for the deuterons and for the tritons were then evaluated using the scaling law which states that for a particle of mass M_2, charge Z_2 and kinetic energy T_2, its stopping power $-dE_2/dx$ can be approximated by [78]:

$$-\frac{dE_2}{dx}(T_2) \;=\; -\frac{Z_2^2}{Z_1^2}\frac{dE_1}{dx}\left(T_2\frac{M_1}{M_2}\right) \tag{3.14}$$

where M_1 and Z_1 are the mass and the charge of another particle whose stopping power is known. In Figure 3.3, we show the stopping power for very low energy protons in a scandium di-tritide film.

The gamma-ray and neutron yields for the reactions that are relevant to the pD prototype and the pT sources were then calculated using the parameters listed in Table 3.3. In these calculations, we assumed that the incident ions are stopped in the target material. This assumption is valid given the low energy ($\leq$30 keV) of the incident ions in these sources. We have also assumed a non-relativistic system. In Figure 3.4, the normalised

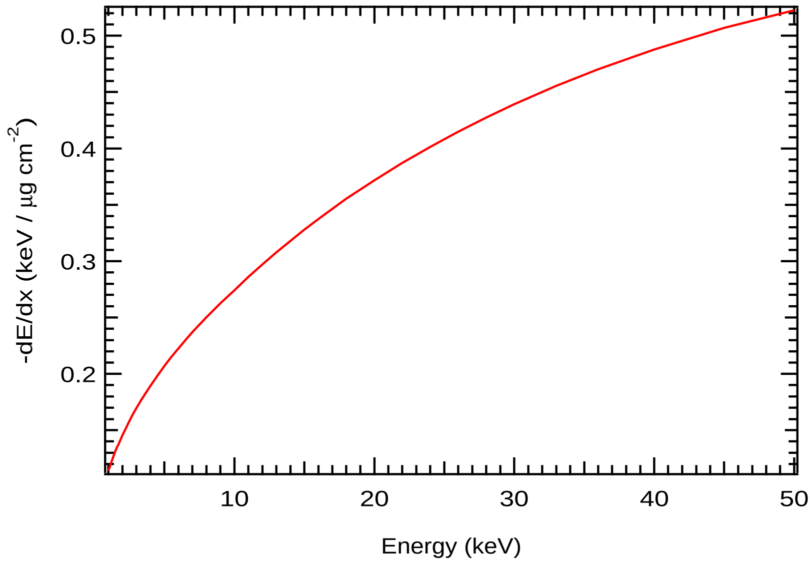

Figure 3.3: Stopping power for protons in scandium di-tritide. The stopping power was calculated with the computer program SRIM [77].

yield $y(E_L)$:

$$y(E_L) \;=\; \frac{Y(E_L)}{I\lambda_i} \tag{3.15}$$

where I is the current of the incident ions in μA, is plotted against the ion energy E_L. The ion beam was assumed to be a pure atomic beam. The parameter λ_i is the ratio between the number of deuterons or tritons (N_i, $i = d, t$) in the target to that of the scandium (N_{Sc}):

$$\lambda_i \;=\; \frac{N_i}{N_{Sc}}. \tag{3.16}$$

We have also summarised the yield $y(E_L)$ in Table 3.4.

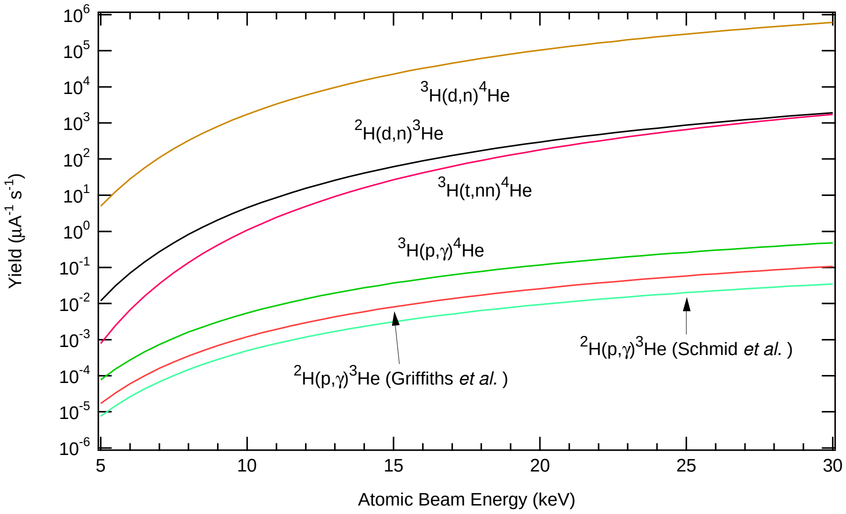

Figure 3.4: Calculated normalised yield $y(E_L)$ for reactions that are relevant to the pD prototype and the pT source. The bottom axis is the energy of a pure atomic beam (p, d, or t). The yield curves for the ^{2}H(p,γ)^{3}He reaction were calculated using S-factors from Griffiths *et al.* [64] and Schmid *et al.* [65]. These yields were calculated for $\lambda_i = 1$.

E_L (keV)	Yield $y(E_L)$ (μA^{-1} s^{-1})					
	^{2}H(p,γ)^{3}He		^{2}H(d,n)^{3}He	^{3}H(p,γ)^{4}He	^{3}H(d,n)^{4}He	^{3}H(t,nn)^{4}He
	Ref. [64]	Ref. [65]				
5	1.55×10^{-5}	7.49×10^{-6}	1.20×10^{-2}	7.77×10^{-5}	4.93	7.73×10^{-4}
7.5	2.13×10^{-4}	1.03×10^{-4}	4.86×10^{-1}	1.10×10^{-3}	1.94×10^{2}	7.17×10^{-2}
10	1.01×10^{-3}	4.89×10^{-4}	4.44	5.42×10^{-3}	1.73×10^{3}	1.07
12.5	2.94×10^{-3}	1.42×10^{-3}	2.01×10^{1}	1.62×10^{-2}	7.62×10^{3}	6.76
15	6.44×10^{-3}	3.11×10^{-3}	6.16×10^{2}	3.66×10^{-2}	2.27×10^{4}	2.64×10^{1}
17.5	1.18×10^{-2}	5.72×10^{-3}	1.47×10^{2}	6.93×10^{-2}	5.27×10^{4}	7.61×10^{1}
20	1.94×10^{-2}	9.35×10^{-3}	2.97×10^{2}	1.17×10^{-1}	1.04×10^{5}	1.79×10^{2}
22.5	2.92×10^{-2}	1.41×10^{-2}	5.31×10^{2}	1.80×10^{-1}	1.81×10^{5}	3.62×10^{2}
25	4.12×10^{-2}	1.99×10^{-2}	8.69×10^{2}	2.61×10^{-1}	2.89×10^{5}	6.59×10^{2}
27.5	5.55×10^{-2}	2.68×10^{-2}	1.33×10^{3}	3.61×10^{-1}	4.30×10^{5}	1.10×10^{3}
30	7.22×10^{-2}	3.49×10^{-2}	1.92×10^{3}	4.80×10^{-1}	6.07×10^{5}	1.73×10^{3}

Table 3.4: Calculated yield y for reactions that are relevant to the pD and the pT sources. These yields were calculated for $\lambda_i = 1$ per μA of atomic beam at an energy of E_L. Beam-target mixing effect was not included in this calculation. An infinitely thick target was assumed, with the stopping power calculated by SRIM [77].

Yield in the Beam-Target Complete Mixing Scenario

To calculate the yield of the real pD and pT sources, we need to consider the hydrogen isotope exchange between the target and the beam. Protons entering the target must exchange with the hydrogen isotopes in the target because the targets we fabricated were initially saturated with deuterium or tritium. Because of the target heating by the beam, diffusion of hydrogen isotopes within the target is enhanced. Therefore, the hydrogen isotope exchange is not confined to the beam spot on the target.

We assumed a complete hydrogen isotope mixing between the target and the discharge gas. In this complete mixing scenario, the deuteron or triton-to-scandium atomic ratio in the target is reduced because some of the deuterons or tritons are replaced by the protons in the beam. Similarly, the proportion of protons in the beam is reduced due to deuterons or tritons getting into the discharge gas through this isotope exchange. The deuteron or triton-to-scandium atomic ratio Λ_i in the target in this mixed scenario is

$$\Lambda_i = L_i \frac{N_i}{N_i + N_H} \qquad i = d, t \tag{3.17}$$

where L_i is the atomic ratio in the target prior to any mixing and N_H is the number of protons initially present in the source.

Because the beam is not mass-analysed in the pD and the pT sources, atomic and molecular ions both contribute to the total yield. Let us consider the case of gamma-ray yield in the pT source. If the fraction of the mass-1 component in the beam is f_1, the currents of the mass-1 component I_p, the H_2^+ component $I_{H_2^+}$ and the HT^+ component I_{HT^+} are

$$I_p = I_{beam} f_1 \frac{N_H}{N_t + N_H} \tag{3.18}$$

$$I_{H_2^+} = I_{beam}(1 - f_1)\left(\frac{N_H}{N_t + N_H}\right)^2 \tag{3.19}$$

$$I_{HT^+} \;=\; 2I_{beam}(1-f_1)\frac{N_H N_t}{(N_t+N_H)^2} \tag{3.20}$$

where I_{beam} is the total beam current in μA. In the expressions above, we have assumed that the tri-atomic ion component does not contribute to the total current in the beam. Therefore, the gamma-ray yield for a beam energy of E_L from each of these ion components is

$$Y_p \;=\; y(E_L)\Lambda_t I_p \tag{3.21}$$

$$Y_{H_2^+} \;=\; 2y(E_L/2)\Lambda_t I_{H_2^+} \tag{3.22}$$

$$Y_{HT^+} \;=\; y(E_L/4)\Lambda_t I_{HT^+}. \tag{3.23}$$

Therefore, the total yield Y_{total} is

$$Y_{total} \;=\; Y_p + Y_{H_2^+} + Y_{HT^+} \tag{3.24}$$

The yields in other reactions in this complete mixing scenario can be calculated similarly. We shall use these results when we evaluate the performance of the pD and the pT sources later.

We shall now give a lower bound estimate on the gamma-ray yield of the pT source at its maximum operating beam energy of 30 keV. As we shall see later in this chapter, a total beam current I_{beam} of 80 μA is easily attainable. To obtain a lower bound estimate of the yield, we shall assume this to be purely di-atomic, i.e. f_1=0. For an un-mixed scandium target with a triton-to-scandium ratio of 2 and a N_t/N_H ratio of 2.9 (see Table 5.3), Λ_t and $I_{H_2^+}$ are 1.49 and 5.26 μA respectively. Therefore, the total yield in this pure di-atomic beam scenario is 0.58 γ s^{-1}. This yield meets the design criterion of > 0.2 s^{-1}.

3.4 The Ion Source

Because of the physical constraints imposed by the calibration system hardware at SNO, there is no room for any secondary electron suppression system installed in the final *pT* source to allow an accurate on-line measurement of its beam current. A mass analyser is not used to analyse the beam for the same reason. Therefore, we have performed several experiments to understand the beam characteristics of the *pD* and the *pT* sources. In this section, we shall describe these experiments in detail.

3.4.1 Source Design

With keeping the system as clean as possible in mind, we built the *pD* and the *pT* sources with ultra-high vacuum (UHV) hardware. A photograph of the *pT* source is shown in Figure 3.5, and the mechanical drawings can be found in Appendix A. The sources can essentially be divided into three sections: the gas discharge line, the ion acceleration line and the target chamber. In the following, we discuss briefly the design of these three sections.

We use a SAES St-172 getter (model LHI/4-7/200) as the hydrogen discharge gas reservoir for the ion source. This eliminates the need for attaching complicated vacuum hardware and an external gas bottle to the source. The getter has 360 mg of a zirconium-vanadium-iron alloy gettering material. The getter is mounted to the BNC connector next to E1 in Figure 3.5. The alloy must be activated by heating to ~800°C for 5 to 10 minutes. Once activated, even when cold, it will adsorb chemically active gases. Gases like N_2 and CO_2 are absorbed permanently. Hydrogen is absorbed reversibly and can be driven off again by heating the getter. In Section 4.2, we shall describe in detail how to load the getter with hydrogen.

The gas discharge line is a cold Penning ion source. A cold Penning source allows the

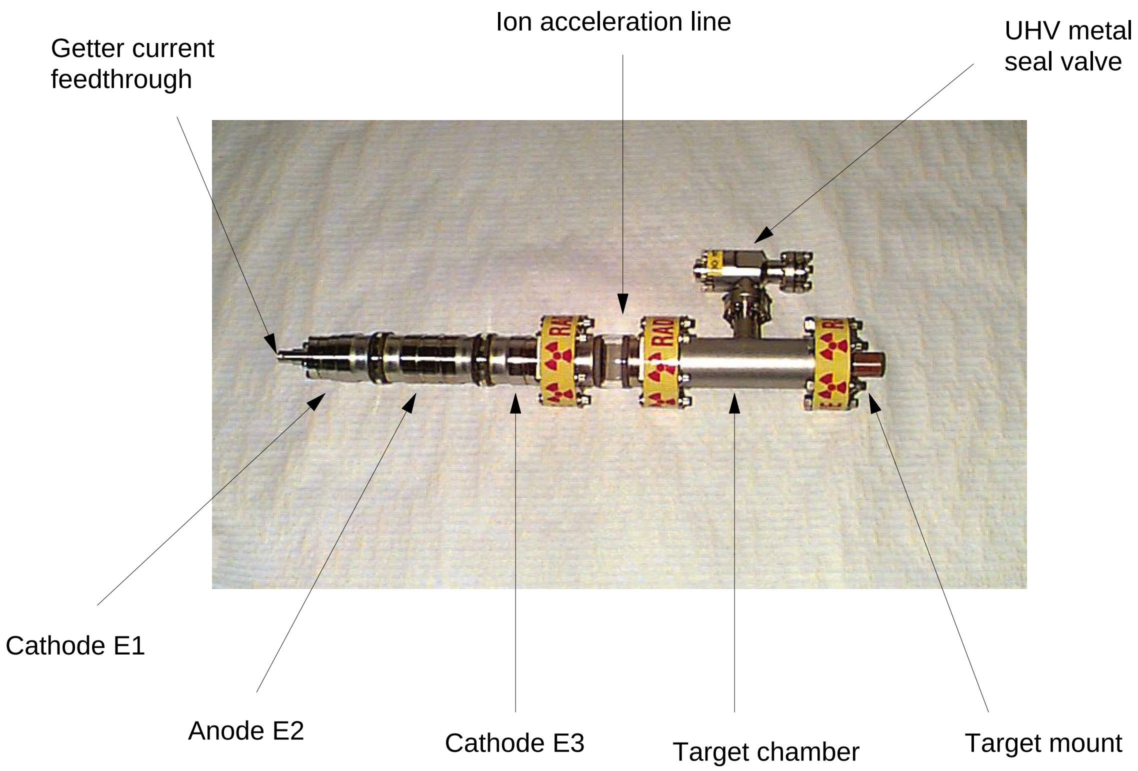

Figure 3.5: A photograph of the *pT* source. The cylindrical permanent magnet, which is used to provide the axial magnetic field for a Penning discharge, is not shown here in order to expose the electrode arrangement. The total length of the *pT* source is 50 cm.

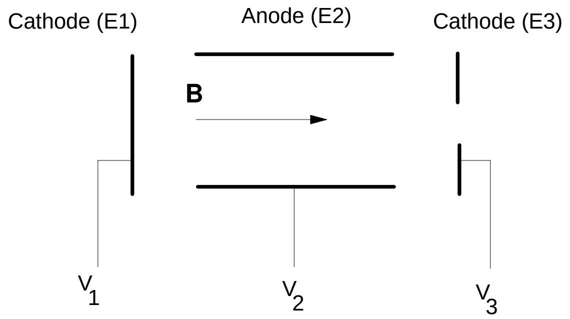

Figure 3.6: Schematics of a cold Penning source. The axial magnetic field is employed to increase the electron path lengths. To trap the electrons in this discharge region, the anode voltage V_2 must be kept at a higher potential than the cathode voltages V_1 and V_3.

ion source to run in d.c. mode, with a very modest power consumption. In Figure 3.6, the general schematic of a cold Penning source is shown. An axial magnetic field is used to increase the path length of the electrons in the discharge region. This increases the probability of an electron triggering another ionisation before being absorbed by the electrode walls. The anode (E2) is raised to a higher potential than the two cathodes E1 and E3, trapping electrons in the discharge region.

The outer housing of the gas discharge line consists of two glass-to-stainless-steel adapters[1]. Each of these adapters is 7.62 cm in length with a piece of 1.27-cm long Pyrex glass to isolate the two ends. The electrodes E1, E2 and E3 are welded to these adapters. The usage of these glass-to-stainless-steel adapters provides convenient high voltage isolation between the anode and the cathodes. The placement of the various electrodes in the gas discharge line was designed using the simulation program MacSimion [79]. In the design, efforts were made to minimise ion loss to the electrode walls; hence, a higher beam current can be attained for a given discharge current. Efforts were also expended

---

[1] Manufactured by Larson Electronic Glass, Redwood City, CA, USA, to our specifications

to deliver a "broad" beam image at the target. This reduces the areal power density on the target, and improves the longevity of the target. Under the normal running scenario, the cathodes (E1 and E3) are kept at ground, whilst the anode (E2) is maintained at +2 kV d.c.

The axial magnetic field required in the discharge is provided by a cylindrical magnet composed of seven 13.34 cm (outer diameter) by 5.88 cm (inner diameter) by 1.91 cm (thick) ceramic (barium ferrite feroxdur) rings. The maximum magnetic field inside the central bore of the magnet is about 0.06 T. We had experimented with a solenoid to provide the magnetic field, but we found that it would require external cooling in order to maintain the same field strength as the permanent magnet. Therefore, we abandoned this idea because of the physical constraints imposed on calibration sources at SNO.

The ion acceleration line is a double-ended glass adapter[2], with one end attached to the gas discharge line and the other connected to the target chamber which is biased at a negative high voltage. In this scheme, the construction of complicated accelerating and focusing electrodes is avoided, and the length of this prototype source can also be kept to a minimum. When the ions exit this acceleration line and enter the target chamber, they have acquired an energy equivalent to the target bias voltage, in addition to their ejection energy from the ion source.

At the end of the ion acceleration line in the pT source is the target mount flange. The target is secured to a copper heat sink, as shown protruding from the flange in Figure 3.5, by a stainless steel screw-on cap. This mounting mechanism is designed to allow efficient target mounting in the tritium glovebox in which this operation is to be performed. After 98.8 hours of "beam-on" time of the pT source, a thin conductive layer originating from target sputtering was formed on the interior of the double-ended glass adapter in the ion acceleration line. This layer caused a high voltage break-down

---

[2] Manufactured by MDC Vacuum Products Corp., Hayward, CA, USA. (part number DEG-150).

across the insulator. In March 1998, a new pT source was constructed with a target anti-sputtering aperture installed. The reader is referred to Appendix A (Figure A.13) for the design of this aperture.

The total length of the pT source is only 50 cm. For deployment in SNO, it will be housed inside a 25.4-cm diameter by 60 cm stainless steel cylindrical deployment capsule. The dimensions of this capsule are well within the physical limits imposed by the SNO calibration-source-deployment hardware.

3.4.2 Calorimetric Measurement of the Ion Beam Current

To determine how much beam current would strike the target in the pT source, it is necessary to measure this current *in situ.* This is because we need to determine the ion scattering effect in a realistic setting. We have chosen to measure the ion beam current generated by the proton source using two different methods. In this section, we shall describe a calorimetric measurement to determine the ion beam power. In the next section, we shall describe another measurement using a Faraday cup with a secondary electron suppression scheme. This latter setup also allows us to determine the beam profile.

When an ion beam of power W hits a target of mass M and heat capacity c, the rate of change in the target temperature T is given by

$$\frac{dT(t)}{dt} = \left[\frac{W}{Mc} - \mu(T(t) - T_\circ)\right] \tag{3.25}$$

where $T_\circ$ is the ambient temperature and μ is a constant relating to the thermal conductivity of the surroundings. If the beam is turned off after the target has reached thermal equilibrium, its cooling is given by

$$\frac{dT(t)}{dt} = -\mu(T(t) - T_\circ). \tag{3.26}$$

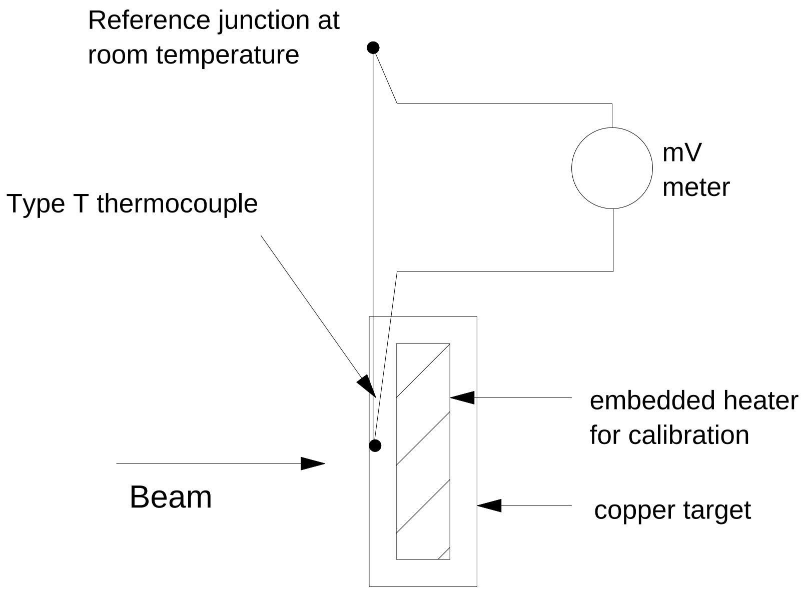

Figure 3.7: Target for a calorimetric measurement of the beam current. The heater embedded in the target is for beam power calibration.

Therefore, the temperature of the target can be described by

$$T(t) = \begin{cases} T_\circ + \frac{W}{\mu M c}\left[1 - \exp\left(-\mu t\right)\right] & t < t_c \\ T_\circ + \left(T_c - T_\circ\right)\exp\left[-\mu\left(t - t_c\right)\right] & t \geq t_c \end{cases} \tag{3.27}$$

where t_c is the time when the beam is turned off, and $T_c = T(t_c)$.

In Figure 3.7 the setup for this beam calorimetry measurement is shown. Copper was chosen as the target material because of its high thermal conductivity. A resistive heater was placed inside the rectangular target for calibrating the target dependent factor Mc in Eqn.(3.25). A Cu-Ni type-T thermocouple was used to monitor the temperature variation of the target. The junction voltage of this thermocouple was measured by a millivolt meter. The target-heater assembly was positioned at the location where the final source's target would be.

In the measurement, the factor Mc was first extracted by heating the target with a known power output by the embedded heater. By fitting the measured temperature of the target to Eqn. (3.27), we found that $Mc = (16.93 \pm 0.38)$ J K^{-1} for our target.

The temperature variation due to beam bombardment was then measured. To determine the gas pressure dependence of the beam current striking the target, the temperature profile was measured at several H_2 partial pressures: $(0.84\pm0.07)\times10^{-3}$ mbar, $(1.25\pm0.07)\times10^{-3}$ mbar, $(1.87\pm0.07)\times10^{-3}$ mbar, and $(2.49\pm0.07)\times10^{-3}$ mbar. In Figure 3.8, plots of target temperature as a function of time for an 18 keV beam bombardment are shown. In these plots, the parameters μ and W/Mc in Eqn.(3.27) were fitted. The resulting fits are shown as solid lines in the plots. In Figure 3.9, we show the beam current extracted from these runs.

Although this calorimetric measurement of the beam current can eliminate the secondary electron emission problem, it is a time consuming process. The time required for the target under beam bombardment to reach a stable temperature depends critically on the ambient gas pressure. In the next section, we shall describe an alternate method using a Faraday cup assembly to measure the beam current in a more time-efficient manner. We shall also compare the calorimetric measurement results with those obtained by this cup measurement.

3.4.3 Profile Measurement of the Ion Beam

Ion beam currents are usually measured by a Faraday cup. In this type of measurement, the measured current may be uncertain because of secondary electron emission induced by ions striking the conducting surface of the cup. In Figure 3.10, the setup used to measure the profile of the ion beam generated by the proton source is shown. In this setup, a copper Faraday cup, with a 3.18-mm diameter by 12.7-mm depth central bore, was positioned behind a rectangular copper shield. The shield had a 0.64-mm wide slit, which was aligned with the central bore of the Faraday cup. This Faraday cup-slotted

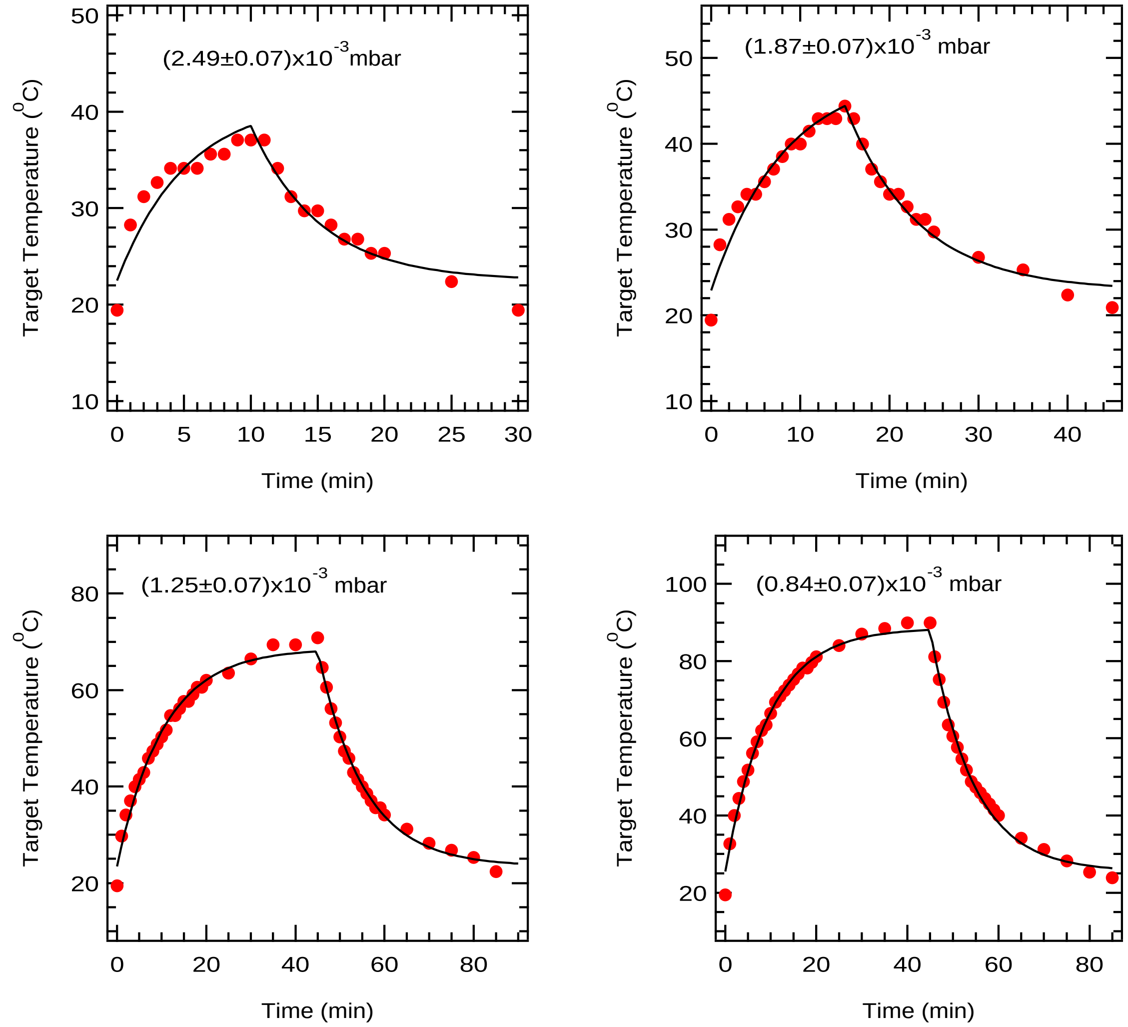

Figure 3.8: Target temperature in the calorimetric measurement of beam current at 18 kV. The temperature of the target was monitored at various H_2 partial pressures shown above. Solid lines show the fit to Eqn. (3.27).

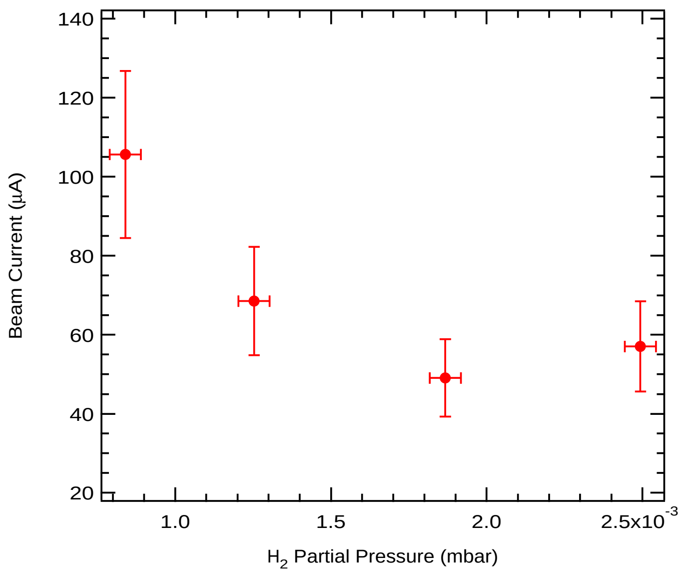

Figure 3.9: Calorimetric measurement of beam current at 18 kV.

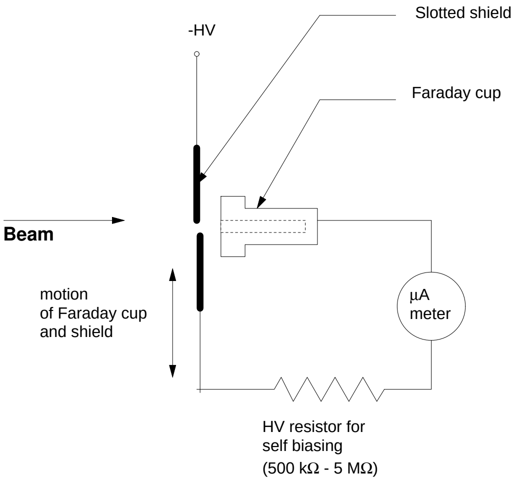

Figure 3.10: Setup for measuring the beam profile. We use the beam current itself to bias the Faraday cup to a higher potential than the slotted shield. Secondary electrons which emerge from the beam bombardment on the copper Faraday cup will get reflected back by the lower potential near the shield.

shield assembly was mounted on a linear motion feedthrough traversing the beam axis to scan the ion beam profile. In order to suppress the secondary electron emission effect, the Faraday cup was electrically connected to the shield through a high voltage resistor. This allowed the beam that struck the Faraday cup to bias itself to a higher potential than the shield. Secondary electrons that emerged from the beam bombardment on the copper Faraday cup would then get reflected back by the lower potential near the shield. The large depth-to-diameter ratio of the cup's central bore also reduced the secondary electron current that would emerge from the cup by cutting down the solid angle of emergence. The total beam current could then be found by integrating the measured beam profile. This method has the advantage of allowing both the beam profile and the total beam current to be determined *in situ* simultaneously. Moreover, this method is much more time-efficient than the calorimetric measurement described in the last section.

We measured the beam profile at various H_2 gas pressures and beam voltages. The measured profile for each run was then fitted to a Lorentzian distribution:

$$I(x) \; = \; I_\circ + \frac{A}{(x-\mu)^2+\omega^2} \tag{3.28}$$

where $I_\circ$ is the baseline, A is the amplitude, μ is the peak position, and ω is the half width at half maximum. In Figures 3.11, the beam width dependence on H_2 partial pressure at fixed beam energies is shown. We found the beam extraction efficiency to be very low when the target voltage was below 5 kV. At a fixed gas pressure, the beam was sharply focussed at a target voltage of 10 kV and its width gradually increased at increasing voltages.

With the beam profile determined, we then integrated each profile to determine the total beam current. In Figure 3.12, the extracted beam current is shown as a function of the beam acceleration voltage. The general trend is clearly shown in this plot. As the acceleration voltage increases, the total beam current increases as well. This is expected

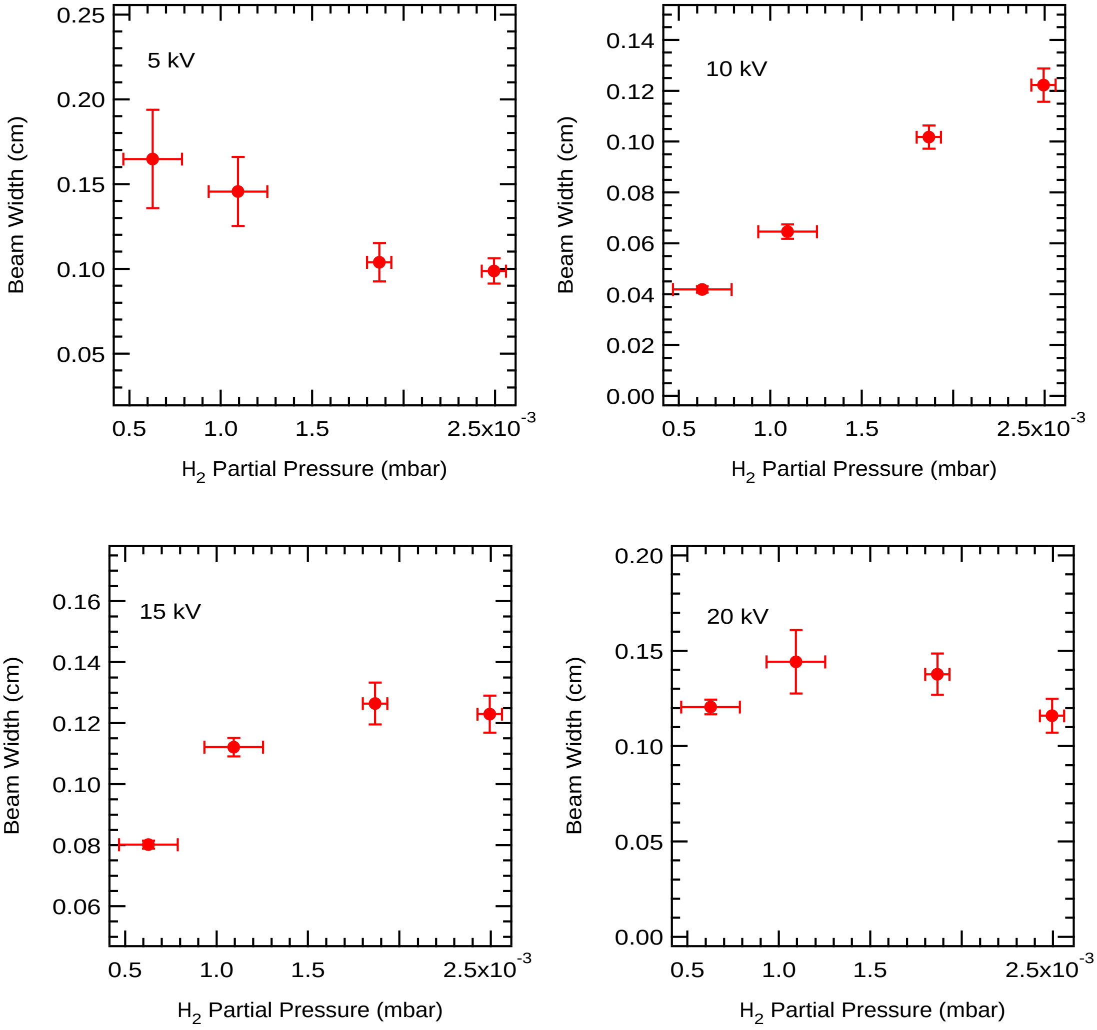

Figure 3.11: Ion beam width dependence on H_2 partial pressure. The four panels show the measured beam profile at the indicated beam voltages.

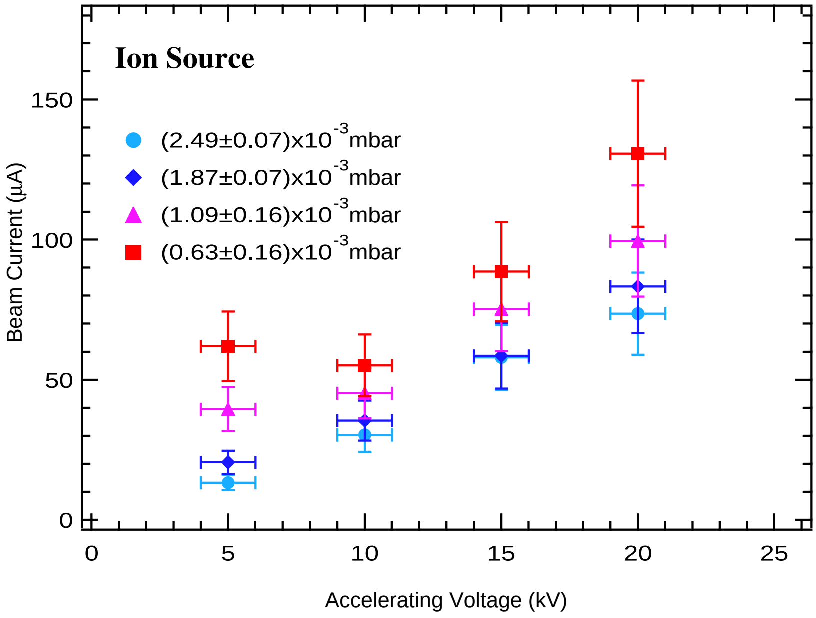

Figure 3.12: Total beam current dependence on the accelerating voltage

since the higher the acceleration voltage, the higher the ion extraction efficiency from the gas discharge region.

In Figure 3.13, the total beam current is plotted against the H_2 partial pressure at fixed acceleration voltages. In this case, it is clear that as the pressure decreases, the total beam current increases. This is due to a reduction of beam scattering by the residual gas as the pressure decreases. A comparison of the calorimetric measurement to this set of Faraday-cup measurements is also made in Figure 3.13. It is clear that the agreement between the results from these two different types of measurement is good.

3.4.4 Mass Composition Measurement of the Ion Beam

Because of the physical constraints imposed on the pT source by the SNO calibration hardware, a mass analyser cannot be installed in the pT source to analyse the beam

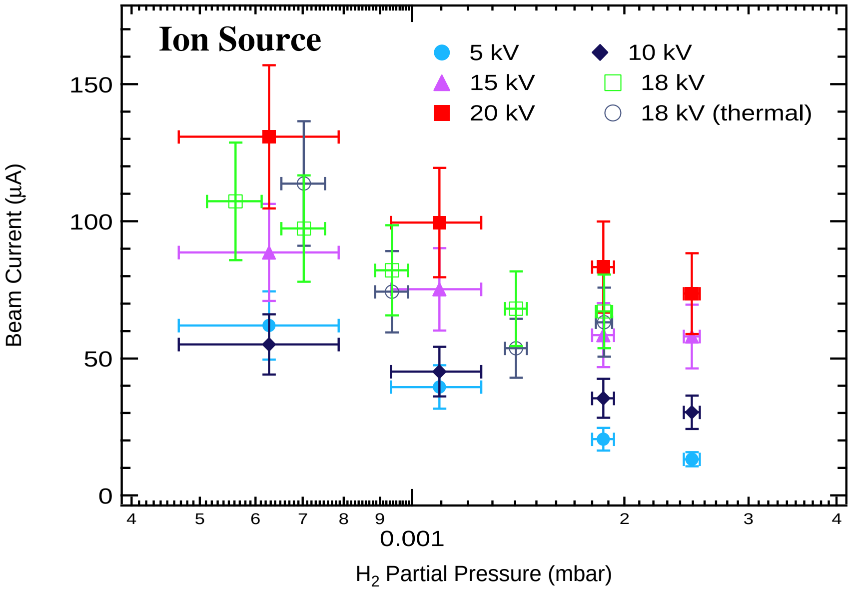

Figure 3.13: Total beam current dependence on H_2 partial pressure

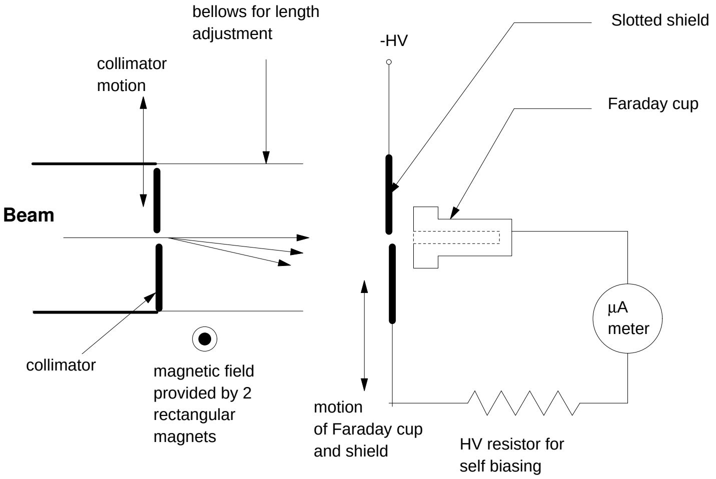

Figure 3.14: Setup for measuring the mass composition of the ion beam. Two bar magnets provide a maximum magnetic field of ~0.025 T to separate the different mass components. The mass spectrum is scanned by the same secondary electron suppression system shown in Figure 3.10.

generated by the ion source. In this section, we present the results of an *in situ* measurement of the mass composition in the beam in the H_2 partial pressure range of (0.3-0.6)$\times 10^{-3}$ mbar.

The schematic of the setup we used is shown in Figure 3.14. At the location where the final target would be, a 0.8-mm wide slit served as the beam collimator. The target chamber in Figure 3.5 was extended by a bellows whose length could be adjusted conveniently. Two rectangular magnets were placed on either side of the bellows to provide a transverse magnetic field for mass separation. The maximum magnetic field provided by these two magnets on the axis of the beam was about 0.025 T. The Faraday cup assembly which we used in making the beam profile measurement was connected to the other end of this bellows. By scanning the mass-analysed beam profile, we determined the mass composition of the beam.

In this experiment, the beam energy was varied from 5 keV to 15 keV. The H_2 gas pressure was kept between 0.3×10^{-3} mbar and 0.6×10^{-3} mbar. The measured profiles were found to have only two peaks. We fit the current profile $I(x)$ to a double Lorentzian distribution

$$I(x) \;=\; I_\circ + \sum_{i=1}^{2} \frac{A_i}{(x-\mu_i)^2 + \omega_i^2}. \tag{3.29}$$

One such fit for a 15-keV beam is shown in Figure 3.15. In this figure, only two broad peaks are visible. These are the mass-1 and the mass-2 peaks. The reader is reminded that since the ion source is a self-contained unit, the gas pressure is uniform throughout the source. As a result, scattering of the ion beam by the discharge gas in the source limited the resolution of the mass spectrometer.

The mass composition of the beam was found to remain constant within the pressure and acceleration voltage ranges over which the measurement was performed. The fractional composition of protons in the beam was determined to be (0.63±0.09) in this

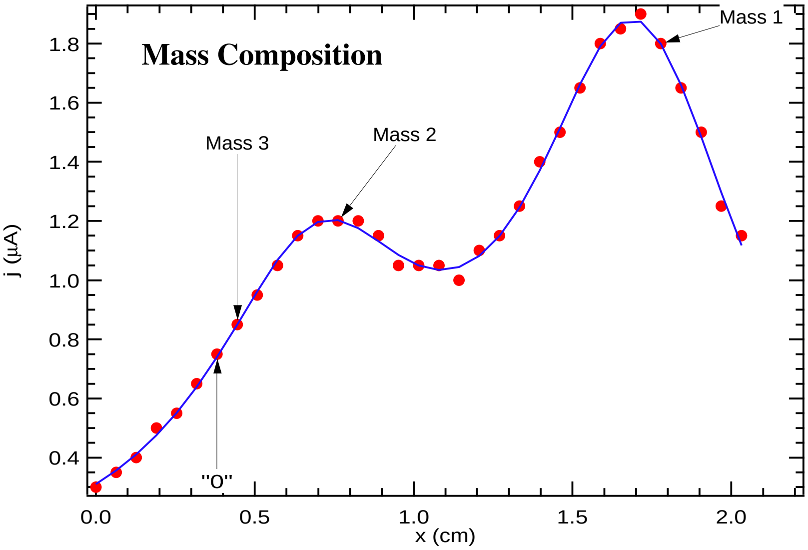

.

Figure 3.15: Mass profile of the ion beam. The profile was fitted to a double Lorentzian distribution. The location of the beam profile centroid in the absence of the magnetic field is labelled as “0” above. Also the location of the mass-3 peak is indicated above as “Mass 3”. Unfortunately, scattering effects limited the resolution of the mass spectrometer, and the mass-3 peak could not be resolved.

pressure range. Because of the scattering effect at higher gas pressure, we were not able to measure the mass composition for pressures above 0.6×10^{-3} mbar.

As we shall see later, the H_2 partial pressure in the *pD* and the *pT* sources under normal operating condition is about five times higher than that in the measurement above in order to maintain long-term beam stability and to reduce the beam power on the target.

Because the hydrogen isotopes in the target and the discharge gas are exchanged during the sources' operation, the mass composition in the beam cannot be measured in the same manner described above. This is because the analyser does not have high enough resolution to distinguish ions with very similar masses (for example, H_2^+ and the deuteron). Therefore, it is impossible to determine the dynamics of hydrogen isotope exchange between the beam and the target in our setup.

Chapter 4

The ^{2}H(p,γ)^{3}He 5.5-MeV Prototype Source

The lyf so short, the craft so longe to lerne,
Th'assay so hard, so sharp the conquerynge

GEOFFREY CHAUCER
The Assembly of Fowles (c.1380)

The main technical difficulty associated with constructing a pT source for SNO calibration is the target fabrication process. Because tritium is radioactive, fabricating a solid tritiated target requires that much attention be given to environmental and personnel safety. This means that target fabrication can be a very costly and time consuming process. With this problem in mind, we set out an experimental program to construct a realistic prototype — a non-radioactive ^{2}H(p,γ)^{3}He (pD) source — before attempting the more hazardous pT source. The pD reaction generates a monoenergetic 5.5-MeV gamma ray.

In this chapter, we shall summarise the work on the research and development of a ^{2}H(p,γ)^{3}He (pD) source. We constructed two different pD prototypes to fine tune the construction process for the final pT source. This was also done to verify that the construction process was repeatable. The development of the scandium deuteride target fabrication process will be discussed in length in this chapter. Discussion on the actual construction and testing of the pT source will be deferred until the next chapter.

4.1 Fabrication of a Solid Deuterated Target

As we have seen in Section 3.3 the reaction cross section for the ^{3}H(p,γ)^{4}He reaction is very low at the proposed beam energy of $\leq$30 keV. Therefore, it is necessary to have a tritiated target with a high triton areal density in order to enhance the gamma-ray yield. Most commercial tritiated targets for use in neutron generators have a deuterium content of a few percent [80]. This is undesirable in our pT source because of very high neutron production rate in the ^{2}H(t,n)^{4}He reaction once the beam and the target have mixed.

It is well known that hydrogen and its isotopes are reversibly sorbed in certain refractory metals. The most common metal hydride films use titanium as the "sorbent" [81, 82, 83, 84, 85]. Singleton and Yannopoulos [86] measured the loss rate of tritium in titanium tritide, yttrium tritide and scandium tritide films at an elevated temperature under several different ambient environments. It was demonstrated that both yttrium and scandium films have a lower tritium loss rate than titanium films under the testing conditions. Although this study was performed using moderately loaded tritiated films (Y:^{3}H and Sc:^{3}H ratios were $\sim$1:1), we believe that this general observation of scandium tritide films having very good thermal stability holds even for heavily loaded films. This property is essential for a target system which does not have an external cooling mechanism like the calibration source we are developing.

McGuire and Kempter [87] provided some information on the crystalline structure of scandium hydride. In their study, it was found that the maximum atomic ratio of scandium (in metal form) to hydrogen to be about 1 to 2. They speculated that a ratio of 1:3 might form at high hydrogen ambient pressure. The scandium hydride lattice was found to be face-centre cubic. Since we wanted to construct a ^{2}H(p,γ)^{3}He (pD) prototype before attempting the more hazardous pT source, we set out to make a scandium deuteride target with a scandium-to-deuteron atomic ratio of 1:2 for our deuterium prototype. In

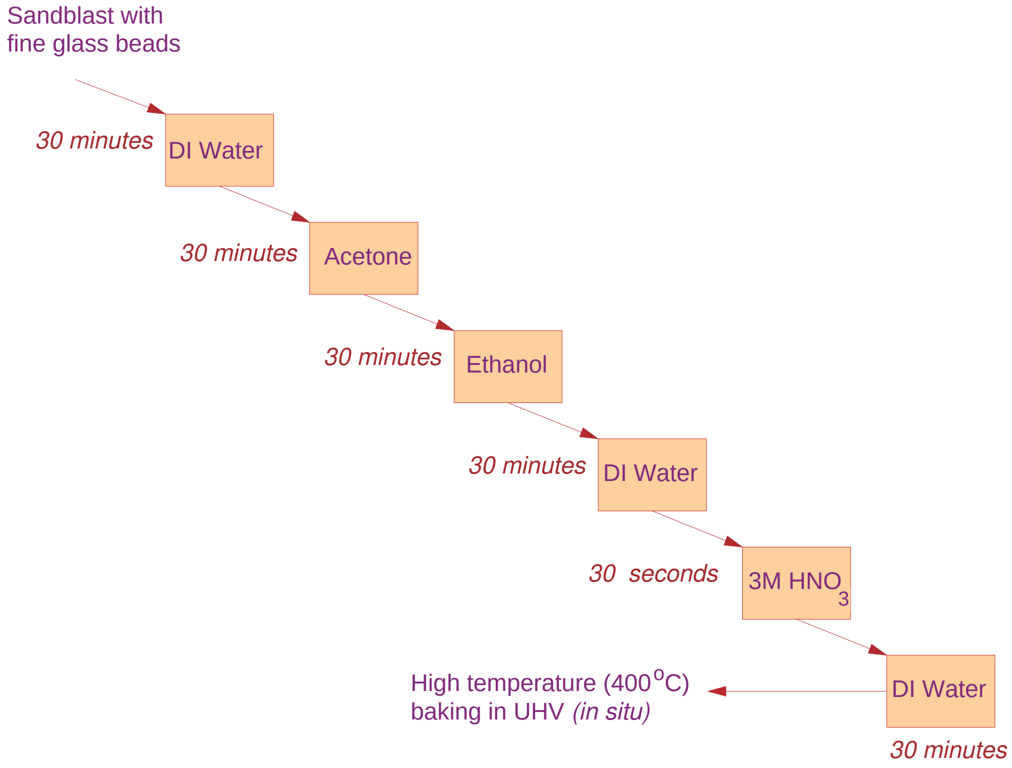

Figure 4.1: Preparation of the molybdenum target substrate. The molybdenum substrate is treated chemically and vacuum baked extensively prior to scandium film evaporation to ensure good film-to-substrate adhesion strength. All the solvent cleansing, except for the 30-second HNO_3 acid etch, were done in an ultrasonic bath.

the following, we summarise the technical details in achieving this goal.

4.1.1 Substrate Preparation

We have chosen molybdenum as the substrate for the scandium film because of strong adhesion between the two materials [88]. To ensure high adhesion strength of the scandium film to the molybdenum substrate, it was prepared by going through a series of mechanical and chemical treatments prior to film deposition. Figure 4.1 shows the procedure of the substrate preparation process.

A substrate disc of diameter 2.86 cm was first cut out from a 1-mm thick sheet of 99.95% pure molybdenum using the electro-discharge machining (EDM) technique. This was to minimise the usage of machining oil on the substrate. The substrate was then sandblasted by fine glass beads in order to increase its effective surface area. We found this process to be important in enhancing the film adhesion strength. The scandium film would peel off much more easily from a non-roughened substrate surface.

The substrate was then treated chemically in a multi-stage process. It was first cleansed in acetone in an ultra-sonic bath for half an hour. The substrate was subsequently ultra-sonically cleansed in ethanol, then deionised water, for half an hour in each solvent. This sequence of chemical cleansing ensured that hydrocarbons that might have deposited on the substrate during the EDM process to be removed. We further treated the substrate surface by etching it in a 3 M nitric acid (HNO_3) bath for 30 seconds. The whole chemical cleansing process was completed by a 30-minute deionised water wash in an ultra-sonic bath.

Once the substrate had gone through this series of preparation processes, it was mounted to a copper holder in which a 110-W coil heater was embedded. This assembly was subsequently placed inside the ultra-high vacuum (UHV) evaporation system which we shall describe in the following section. This heater block was outfitted with thermocouples for monitoring its temperature. The substrate was baked at 400°C in the vacuum system for about four days, then at 250°C for about a week to reduce outgassing from its surface.

4.1.2 Scandium Deuteride Target Fabrication

The vacuum schematics of the UHV evaporation system is shown in Figure 4.2. Pumping of the system was provided primarily by a high capacity (1150 litre s^{-1}) oil-lubricated turbomolecular pump. Further pumping and hydrocarbon trapping was provided by a

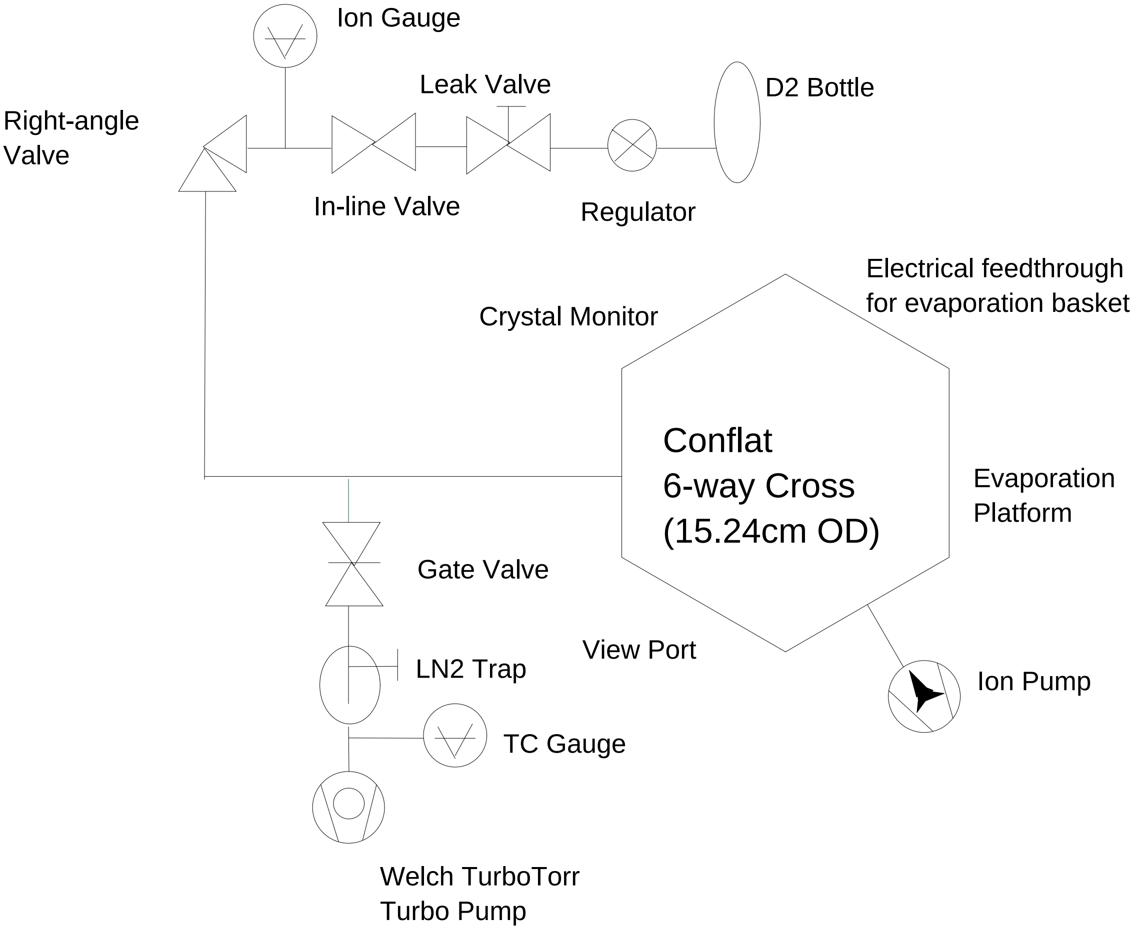

Figure 4.2: Vacuum system layout for the scandium deuteride target evaporation system. The six-way cross is the evaporation chamber. A 20 litre s^{-1} ion pump was connected to this chamber to provide direct pumping.

large volume liquid nitrogen (LN_2) cryogenic trap. A 20 litre s^{-1} ion pump was connected to the evaporation chamber, which was a standard Conflat six-way cross with an outer flange diameter of 15.24 cm. The ion pump served two purposes: to provide direct pumping to the evaporation chamber and to measure the pressure in the chamber through the ion current of the pump. Additional pumping by this ion pump was particularly useful during the scandium film evaporation process to ensure the freshly evaporated film would not be saturated by the residual gas in the system.

To ensure cleanliness of the system, all the major vacuum components used were constructed out of stainless steel or copper to reduce the outgassing effect. Metal seals were used in all vacuum component interfaces. The evaporation chamber and other vacuum components were baked at 200°C for more than ten days to reduce the outgassing rate. This baking process took place concurrently with the molybdenum substrate bake to ensure that gases driven out of the vacuum hardware would not condense on the substrate. After this extensive pumping, we were able to achieve a base pressure of less than 1×10^{-9} mbar after all the components had returned to room temperature.

The evaporation setup is shown in Figure 4.3. The arrangement of the evaporation hardware inside the evaporation chamber was made to be compatible with a similar evaporation setup at the Ontario Hydro Technologies tritium research laboratory (see Figure 5.2) [89]. This was to ensure that this prototype test would simulate a real tritium run as closely as possible.

Two high current feedthroughs were connected to the evaporation chamber. A 5-coil conical tungsten evaporation basket[1] was mounted between these feedthroughs. A lump of 99.99% pure, sublimed dendritic scandium was placed inside this basket, and positioned directly above the molybdenum substrate in the heater block. The separation between the bottom of the tungsten basket and the molybdenum substrate was (14±2) mm. A

---

[1] R.D. Mathis Company, Part Number B12B-3x.025W

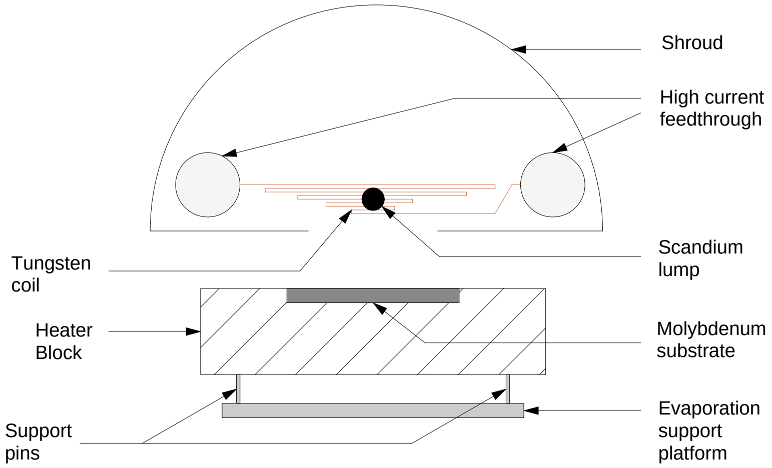

Figure 4.3: End-view of the evaporation basket and substrate configuration. The scandium lump was evaporated by heating up the tungsten basket. The heater block rested on the evaporation support platform through the support pins. Support pins were used to reduce heat transfer between the heater block and the support platform.

stainless steel shroud was positioned around the feedthrough-basket assembly to prevent deposition on the viewport in the evaporation chamber and to reflect radiation back to the coil to enhance heating efficiency.

A crystal deposition monitor was mounted to the port directly opposite the high current feedthroughs in the evaporation chamber. The monitor was used for monitoring the thickness of the deposited scandium film, and the amount of deuterium sorbed by the film.

The evaporation process began with gradually increasing the current fed to the tungsten basket. This current was increased at a rate of approximately 1 A $\min^{-1}$ until the scandium lump began to evaporate. A gradual increase in the heating current was to prevent "flash" evaporation of the scandium lump, which would reduce the adhesion strength of the evaporated film. A drop in the evaporation chamber pressure, and an increase in the crystal monitor reading were clear indications that the scandium lump had started to evaporate. The tungsten basket current was maintained at this level (~35 to 40 A) until the whole scandium lump was evaporated. Despite the intense heat of the tungsten basket, the chamber pressure did not exceed 8×10^{-7} mbar in the evaporation runs.

After the scandium film evaporation process, the substrate was raised to 400 °C by turning on the heater embedded in the heater block. This was primarily for increasing the pumping speed and capacity of the film. The evaporation chamber was then isolated from the external pumps, and shots of deuterium were admitted to the chamber until the film had reached its capacity. Each dose contained ~18 mbar cm^3 of deuterium. The substrate heater was subsequently turned off to allow the substrate to return to room temperature.

Before the scandium deuteride target was removed from the evaporation chamber for mounting into the ion source, it was tested for thermal stability. This was performed by looking for gas release from the target after the temperature of the substrate was raised to ≤150 °C. We did not observe any change in the ambient pressure of the evaporation chamber in which this test was performed. This was a good indication that the substrate was thermally stable at 150 °C.

We loaded (45±1) mg (Target I) and (18±1) mg (Target II) of scandium in the two evaporation runs. The thickness of the two scandium films was (1.83±0.53) mg cm^{-2} and (0.73±0.22) mg cm^{-2} respectively. By monitoring the change in the crystal monitor reading during the deuteration process, we found the Sc:^{2}H atomic ratio to be 1:2.4±0.2 for Target I and 1:1.9±0.3 for Target II.

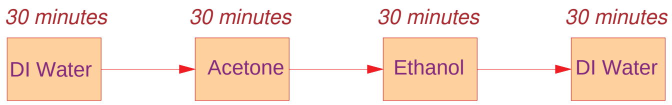

Figure 4.4: Chemical cleansing procedure for the ion source. All the steps shown above were performed in an ultrasonic bath.

4.2 Final Assembly of a Sealed *pD* Prototype

The ion source must be cleansed before it could accept the deuterated target. This is because the getter has a small capacity. If the outgassing rate of the ion source is too high, the getter would lose most of its capacity on pumping the residual gas in the source, rather than serving its purpose as the hydrogen discharge gas reservoir.

The ion source was first cleansed chemically. The chemical cleansing procedure is shown in Figure 4.4. After this chemical cleansing, the source was baked in an ultra-high vacuum system the schematic of which is shown in Figure 4.5. The ion source was baked at about 150°C for about a week. Although the source interior would be briefly exposed to the atmosphere during the target mounting process, this baking improved the overall cleanliness of the ion source prior to the mounting. After this bakeout process, the ion source was high-voltage conditioned (i.e. all the electrodes were gradually raised to their operating voltages) for a day. We found this conditioning step to be important as the ion source would not hold a stable beam with energy greater than $\sim$10 keV if this step were not taken.

Once the target was fabricated, it was removed from the target evaporation system, and mounted inside the ion source. The ion source was then pumped down in the same source bakeout vacuum system shown in Figure 4.5. After the system had reached its base pressure, H_2 from the external gas bottle was let into the system through the leak valve, and an ion beam was allowed to strike and to bombard the target for 5 minutes. During

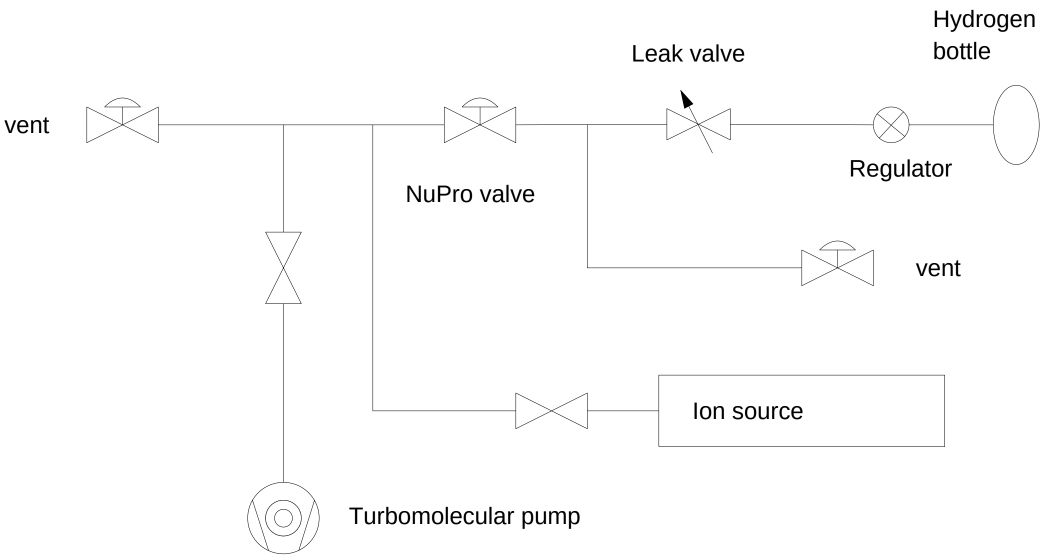

Figure 4.5: Vacuum system for getter loading. After the getter was activated, hydrogen was injected into the system through the leak valve.

this time, the beam energy was gradually increased from 0 to 25 keV. This procedure was necessary to cleanse the Penning electrodes by electro-discharge. Contamination on the target, which might have deposited on the target surface during the target mounting process, would also be removed by this brief beam bombardment. It was found that if this step was not carried out, the getter in the source would not be able to handle the residual gas load in the source once sealed.

After the completion of this last electro-cleaning process, we began loading H_2 discharge gas to the getter. For the SAES St-172 getter, hydrogen is pumped in a reversible manner, and this process can be described by a van't Hoff relationship [90]

$$\log P = 4.325 + \log Q^2 - \frac{5730}{T} \tag{4.1}$$

where P is the equilibrium pressure (in mbar), Q is the hydrogen concentration in the getter (in cm^3 mbar/mg), and T is the temperature (in Kelvin).

Property	$pD-I$	$pD-II$
Isotopic purity of H_2	2×10^{-4} ^{2}H	$<2\times10^{-5}$ ^{2}H
Scandium film thickness (mg cm^{-2})	(1.83±0.53)	(0.73±0.22)
Sc:^{2}H atomic ratio	1:2.4±0.2	1:1.9±0.3

Table 4.1: Construction properties of the two *pD* prototype sources

The St-172 getter had to be activated before hydrogen reversible pumping can take place. To activate the getter, it was heated for 10 minutes at 800°C by passing a 4.5 A current through it. Once activated, the getter current was lowered to about 1.6 A in order to maintain a temperature of 200°C. The getter was then loaded with hydrogen by allowing an ambient H_2 pressure of 3.3×10^{-4} mbar into the ion source through the leak valve in Figure 4.5. After 30 minutes, 200 cm^3 mbar of H_2 would have been absorbed by the 360 mg of active material in the getter. One can increase the H_2 concentration in the getter by leaving it in the H_2 environment for a longer period of time. The getter loading procedure was completed by turning off the getter current, and by pumping out the residual H_2 gas in the ion source. After the base pressure was reached, the source was isolated and detached from the rest of the vacuum system by closing the metal-seal valve on the source.

We used H_2 gas of different isotopic purity in the two *pD* prototypes we constructed. In the first prototype, we used research grade H_2, which has a deuteron content at its natural abundance level of 2×10^{-4}. For the second prototype, we used isotopically purified H_2 at a HD level of $< 2 \times 10^{-5}$. The level of co-mingling between the beam and the target could then be determined by observing the neutron production rate in these two *pD* prototypes. Table 4.1 is a summary of the construction properties of the two *pD* sources.

4.3 Detector Systems for Testing the ^{2}H(p,γ)^{3}He Prototype

We tested the two pD prototypes with two different detector systems. For the first prototype $pD{-}I$, we used a 12.7-cm diameter by 15.2-cm long sodium iodide (NaI) crystal as the gamma-ray detector, and a 12.7-cm diameter by 5.1-cm long liquid scintillator as the neutron detector. For the second prototype $pD - II$, we used the same detector system initially. We subsequently used two 55% high-purity germanium (HPGe) crystals in the detector system. As we shall see later in this chapter, this change was made because in the testing of the $pD - I$ source, we found that the neutrons generated by the prototype induced a significant background in the NaI energy spectrum. HPGe crystals have the advantage of very high resolution, and a much lower sensitivity to neutrons. The main disadvantage of using HPGe in this search was its low efficiency to 5.5-MeV gamma rays.

In this section, we shall describe these systems in detail. And in Section 4.4, we shall summarise the results of this testing.

4.3.1 The NaI Gamma-Ray Detector System

The top view of the apparatus configuration for testing $pD - I$ is shown in Figure 4.6. A discussion of the liquid scintillator neutron detector in the setup is deferred until the next section. We shall concentrate on the sodium iodide (NaI) gamma-ray spectrometer here.

In our setup we used a 12.7-cm diameter by 15.2-cm long Bicron 5H6/5-X model NaI detector as the gamma-ray detector. The photomultiplier tube (PMT) coupled to this crystal was encapsulated in a μ-metal shell at the factory. We placed an extra layer of μ-metal around the PMT in order to reduce the magnetic effect from the discharge magnet of the pD source. We placed a 2.54-cm thick annular plastic scintillator around

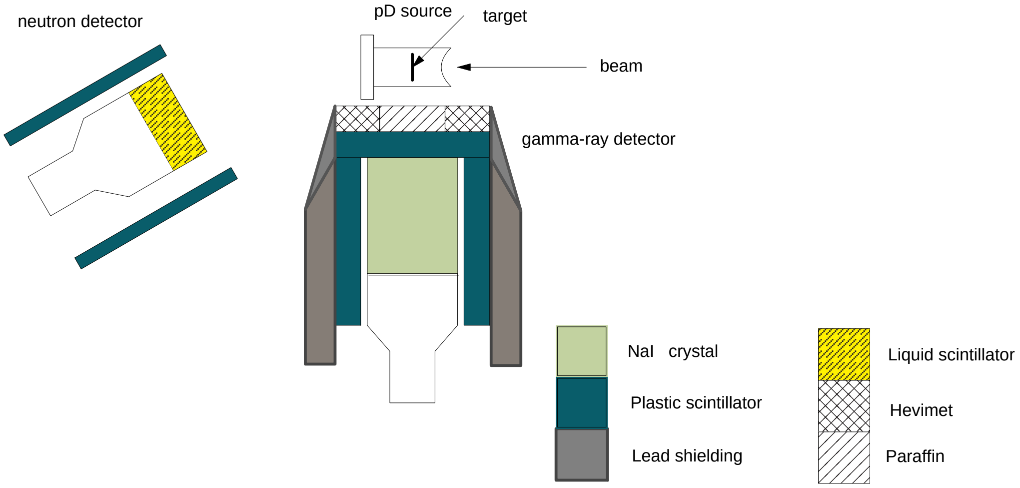

Figure 4.6: Experimental setup for the NaI and the liquid scintillator detector system. Hevimet is the trade name of a tungsten alloy.

the crystal and a flat plastic scintillator of the same thickness in front of the crystal to serve as a cosmic veto counter. Hamamatsu R329 5.1-cm diameter PMTs were optically coupled to the annular shield and the front veto scintillator. On four sides of the crystal, there was lead shielding of thickness ranging from ~5 to 15 cm. In front of the crystal was a collimator constructed out of 6.35-cm thick Hevimet which is a tungsten alloy[2]. The central bore of the collimator was filled with paraffin to cut down the neutron flux going into the NaI crystal.

The centre of the $pD-I$ target was 13±1 cm away from the front face of the NaI. The source was oriented with the proton beam direction perpendicular to the symmetry axis of the NaI crystal. This was because the 5.5-MeV gamma rays emitted in the ^{2}H(p,γ)^{3}He reaction has a predominant $\sin^2\theta$ distribution [65, 68]. This source-detector orientation enhanced the number of gamma rays incident on the detector .

---

[2] Hevimet is the trade name of a tungsten alloy. This alloy has a density of 18 g cm^{-3}, and was manufactured by Kulite Tungsten, East Rutherford, New Jersey, USA.

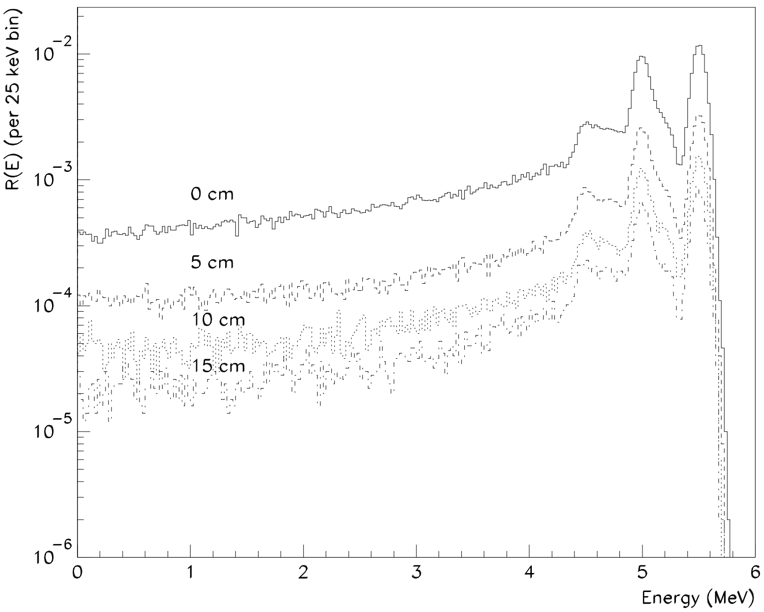

Figure 4.7: GEANT calculated response function for a 5.5-MeV point source situated at various distances from a 12.7-cm diameter by 15.3-cm long NaI crystal. The point source is on the symmetry axis of the crystal.

In order to understand the detection efficiency of the NaI spectrometer, we used the computer package GEANT [92] to simulate its response. GEANT is a detector simulation package commonly used in the high energy physics community. Since this package was designed with high energy physics experiments in mind, we first had to determine its reliability in the energy regime we are interested in. This investigation is summarised in Appendix B. It is demonstrated there that GEANT can calculate the gamma-ray detection efficiency and response functions reliably for a wide range of detector configurations.

We calculated the response functions for a 5.5-MeV isotropic gamma-ray point source situated 0, 5, 10, and 15 cm on the symmetry axis of a 12.7-cm diameter by 15.3-cm long NaI crystal. The calculated response functions are shown in Figure 4.7.

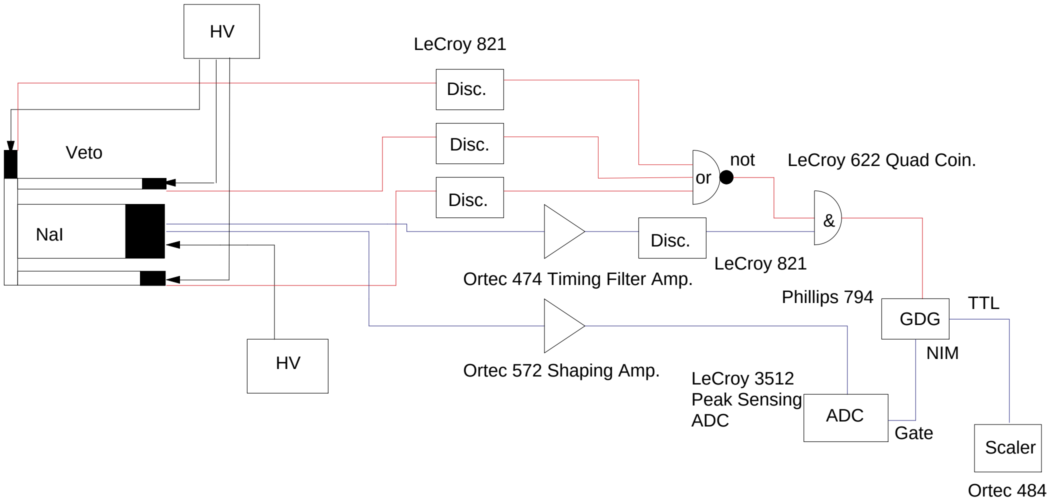

Figure 4.8: Electronics schematic for the NaI gamma-ray detector system

Electronics

The electronics scheme for the NaI gamma-ray spectrometer is shown in Figure 4.8. The anode output of each of the PMTs coupled to the veto scintillators was fed to a LeCroy 821 discriminator. The logic signals from these discriminators were 100-ns fast NIM pulses, and were logically summed. The anode output of the photomultiplier tube coupled to the NaI crystal was first fed to an Ortec 474 timing filter amplifier, then to a LeCroy 821 discriminator. This discriminator output was subsequently allowed to form a coincidence with the complementary output of the veto logic pulse. If the event did not trigger both the veto shield and the NaI crystal, a 5-μs gate was generated by a Phillips 794 gate-and-delay generator (GDG) for the LeCroy 3512 peak sensing amplitude-to-digital converter (ADC). The same anode pulse in the NaI chain was shaped by an Ortec 572 spectroscopy amplifier, and timed to arrive at the ADC within the gate. The ADC output was sent to the data acquisition computer through a CAMAC bus. The events were recorded on an event-by-event basis.

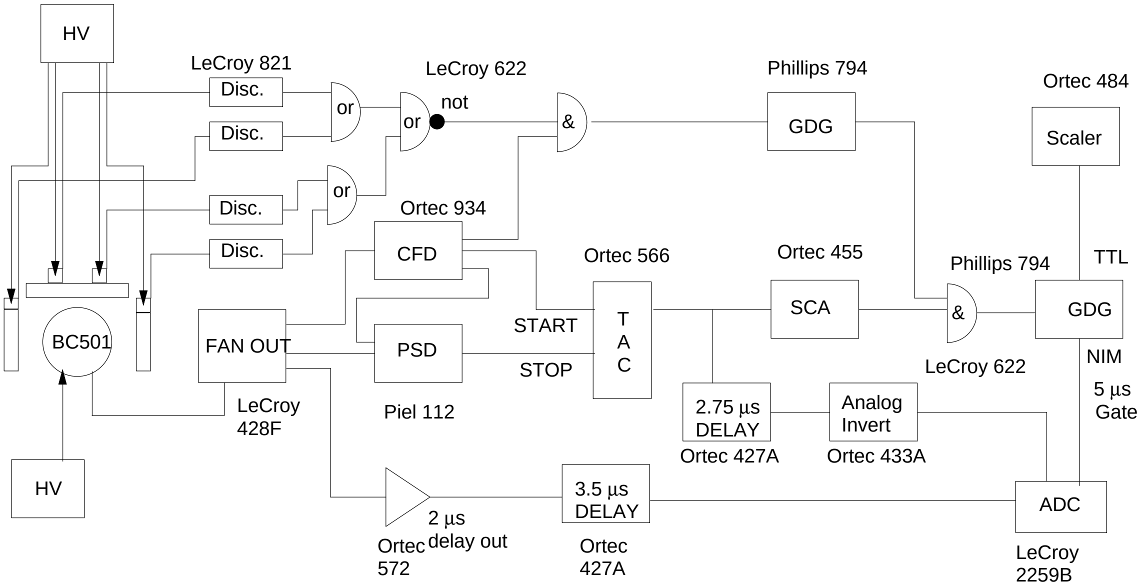

Figure 4.9: Electronic schematic for the liquid scintillator neutron detection system.

4.3.2 The Liquid Scintillator Neutron Detector System

One common method of fast neutron detection is to employ neutron-proton elastic scattering in organic scintillators. The relative light yield of the fast and slow components of some organic scintillators depends on the nature of ionisation. Since gamma-ray induced electrons generate a larger fraction of their scintillation light in the prompt component than recoil protons, it is possible to perform pulse shape discrimination to separate neutrons from gamma rays [91].

In Figure 4.9, the electronics scheme we used in our neutron detection system is shown. The neutron detector was a 12.7-cm diameter by 5.1-cm thick Bicron BC 501 liquid scintillator, which was optically coupled to a Hammamatsu R1250 PMT. An active cosmic veto system employing three panels of 1.27-cm thick plastic scintillator was placed around the neutron detector. The separation between the front face of the liquid scintillator and the pD source was (38±2) cm.

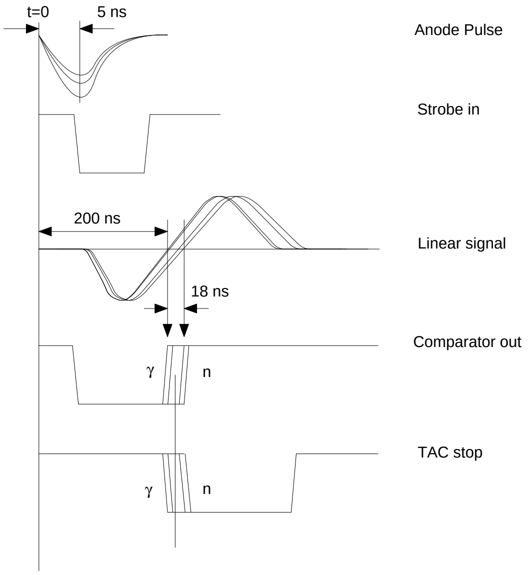

Figure 4.10: Pulse shape discrimination scheme for neutron and gamma-ray events. From [93].

In order to discriminate gamma-rays from neutrons, we used a Piel 112 pulse shape discriminator (PSD) which measured the decay time of the scintillator pulse [93]. We show how this PSD measures the decay time of the scintillator pulse in Figure 4.10. The PSD requires the anode output from the PMT and a timing pulse ('Strobe in' in Figure 4.10) as inputs. This timing pulse was generated by a constant fraction discriminator (CFD) triggered on the anode pulse. The anode pulse is then processed by a shaping amplifier in the PSD to produce a bi-polar pulse. This pulse is subsequently input to a zero-crossing circuitry to produce a logic pulse ('Comparator out') whose time delay depends on the proportion of the decay components in the light output. This pulse was used as the stop signal to a time-to-amplitude converter (TAC), which had already been started on the CFD logic pulse. This TAC output was then fed to a peak sensing ADC after being delayed for 2.75 μs.

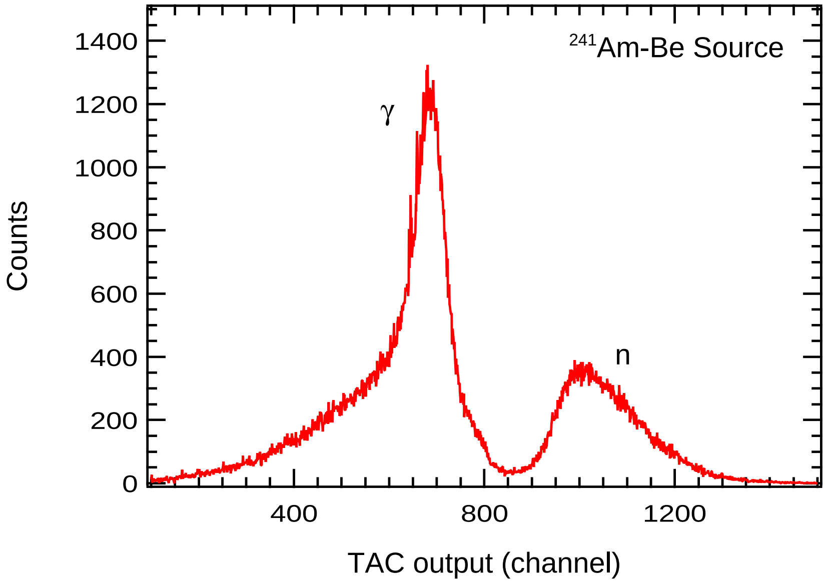

Figure 4.11: Timing distribution of liquid scintillator pulses generated by neutrons and gamma rays in a ^{9}Be(α,n)^{12}C* source. Neutrons are cleanly separated from the gamma-rays using the pulse shape discrimination scheme outlined in the text.

The anode signal of each of the PMTs optically coupled to the veto plastic scintillators was fed to a LeCroy 821 discriminator. The outputs from the discriminators were logically summed. A gate was generated by a Phillips 794 GDG if the complementary output of this sum and the CFD output from the liquid scintillator branch were in coincidence. So a gate was generated only if signals from the plastic scintillator were in anticoincidence with the veto. The Ortec 566 TAC output from the neutron-gamma ray discrimination chain was also fed to an Ortec 455 single channel analyser (SCA) to form a logic signal. If this SCA output and the GDG output from the veto-liquid scintillator anticoincident logic were in coincidence, a 5-μs wide master gate to the LeCroy 2259B ADC was formed by another Phillips 794 GDG. Meanwhile a shaped liquid scintillator output would arrive at the ADC after the master gate was formed. Therefore, the ADC recorded both the cross-over time and the pulse height information of the liquid scintillator anode output. In Figure 4.11, we demonstrate the neutron-gamma separation ability from the TAC's timing output.

4.3.3 The HPGe Gamma-Ray Detector System

The top view of the high-purity germanium (HPGe) gamma-ray spectrometer setup is shown in Figure 4.12. This setup was modified from an above-ground double beta decay experimental apparatus [94]. The heart of this spectrometer was two medium size (55%[3]) HPGe detectors placed on the sides of the $pD-II$ source target chamber. The detectors were each surrounded by a 2.54-cm thick annular plastic scintillator serving as cosmic veto shield. Surrounding the veto shields were 10.2-cm thick of oxygen-free-high-conductivity (OFHC) copper on four sides, then 10.2-cm thick of lead all around this assembly. These

---

[3] This is how commercial manufacturers specify the "size" of germanium detectors. This percentage is the photopeak efficiency of the germanium detector relative to that of a standard 7.62 cm by 7.62 cm cylindrical NaI crystal. This value is normally specified for the 1.333-MeV gamma-ray peak from a ^{60}Co source located 25 cm away from the front face of the germanium detector.

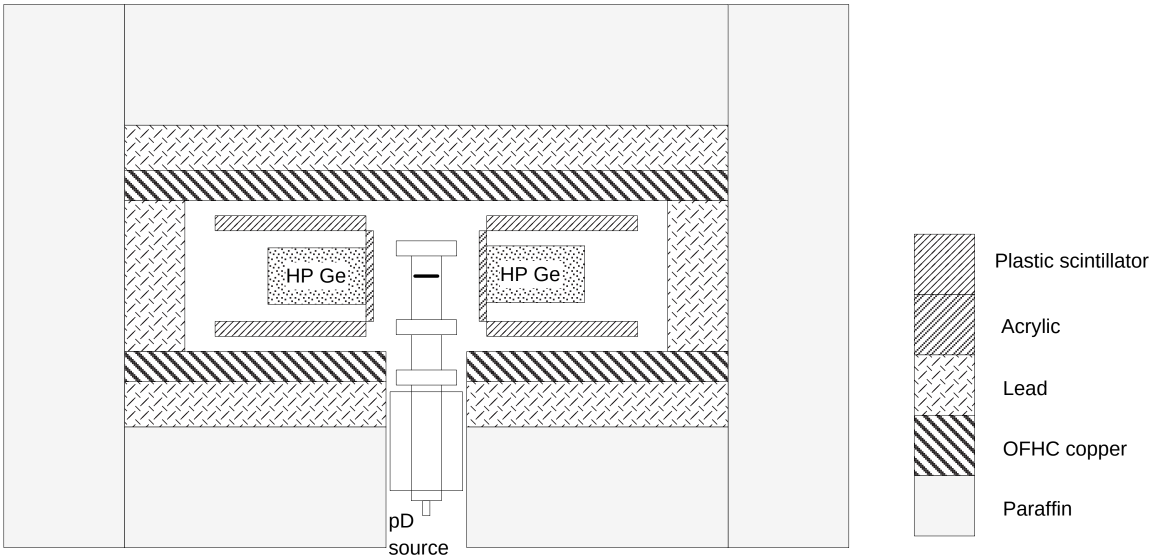

Figure 4.12: Top view of the experimental setup for the germanium detector system

copper and lead layers served as shielding for background gamma rays. This shielding was completed with 30 cm of paraffin serving as neutron shield on five sides (no shielding in the bottom) of the setup. In this experiment, the centre of the $pD - II$ target was located 7 cm equidistant from the front faces of the two HPGe detectors.

The electronics scheme for the HPGe detector system is shown in Figure 4.13. The cosmic veto logic in this system was identical to the NaI system, and the reader is referred to page 97 for a discussion of the electronics scheme.

Prior to making the measurement, we simulated the response of the HPGe system using GEANT. In Table 4.2 we have summarised the GEANT calculated efficiency integrated over the solid angle subtended by the detector ($\varepsilon\Delta\Omega/4\pi$) for isotropic 5.5-MeV gamma rays emitted from the centre of the detector system.

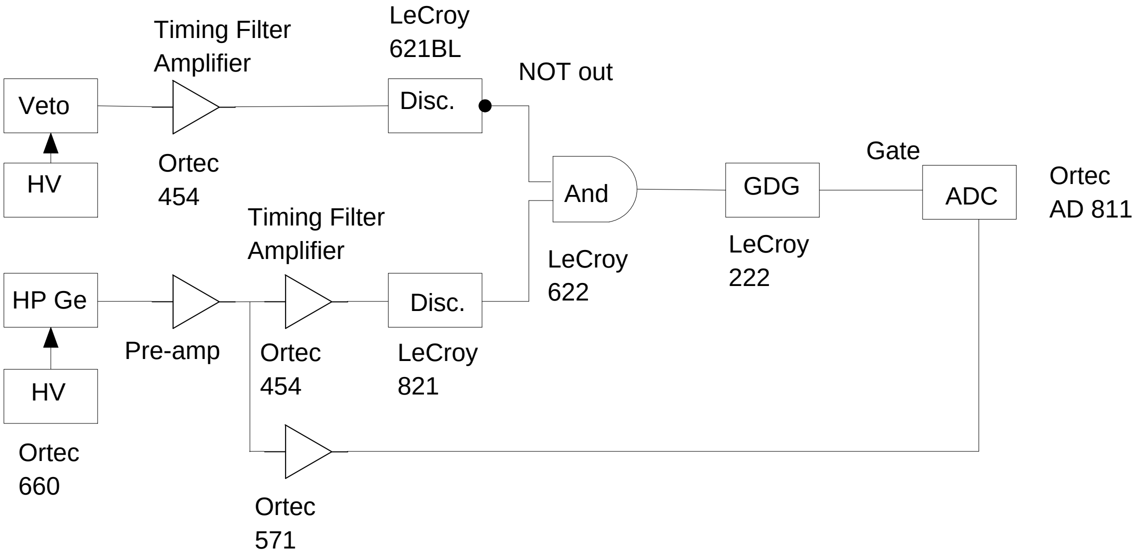

Figure 4.13: Electronics scheme for the germanium detector system. This diagram shows the electronics scheme for each of the two HPGe detectors in this test.

	Energy Range (MeV)	$\varepsilon\Delta\Omega/4\pi$
Full energy peak	5.50±0.02	$(2.54\pm0.04)\times10^{-3}$
Single escape peak	4.99±0.02	$(1.94\pm0.03)\times10^{-3}$
Double escape peak	4.48±0.02	$(0.96\pm0.02)\times10^{-3}$

Table 4.2: GEANT-calculated efficiency for 5.5-MeV gamma ray detection in the HPGe detector system. The efficiencies shown here are the full energy peak, single and double escape peak efficiency for isotropic gamma rays in each of the two HPGe detectors. The energy range from which the efficiencies were extracted is also shown above.

4.4 Testing the ^{2}H(p,γ)^{3}He Prototype

We tested the $pD - I$ source with the NaI and the liquid scintillator systems for over 200 hours of "beam-on" time. For the $pD - II$ source, it was tested with the same system for 33 hours before switching to the HPGe system for another 98 hours.

The primary goal of this prototype source testing was to convince ourselves that the construction procedures outlined previously in this chapter were sound. In the following, we shall summarise how the testing was done and our findings.

During the testing of the pD sources with the NaI system, energy calibration was done every hour to two hours in order to monitor the gain of the detector. Calibration of the HPGe system was done once every few hours because the gain of the system was found to be very stable. Energy calibration of these two detector systems was done in the same manner. We used the ^{137}Cs(0.662 MeV), ^{12}C*(4.4 MeV), and ^{16}O*(6.13 MeV) lines to calibrate these systems.

We ran the $pD - I$ source at a beam energy of 22 keV for the first 41 hours. Then the beam energy was increased to an average of 27 keV for the remainder of its testing. For the $pD - II$ source, it was run at 27 keV for the first 8 hours before it was lowered to the energy range of 17 to 22 keV for the rest of the testing. In these runs, the total beam current was maintained at about (70±30) μA. Because the pD sources did not have the capability of measuring the beam current and mass composition on-line, the total beam current above was estimated from the temperature of the getter, which was calculated using Eqn.(4.1) and the loaded H_2 gas volume of 200 cm^3. The discharge gas pressure in the pD source was $(3\pm1)\times10^{-3}$ mbar.

We estimated the minimum gamma-ray yield from $pD - I$ and $pD - II$ based on the formalism we developed in Section 3.3.3. The reader is reminded that a complete mixing of hydrogen isotopes between the target and the discharge gas was assumed in this

Parameter	$pD-I$	$pD-II$
^{2}H/Sc atomic ratio prior to mixing (L_d)	2.4±0.2	1.9±0.3
Amount of $^2H_2$ in target prior to mixing (N_d)	$(1.2\pm0.1)\times10^{-4}$ mol	$(3.8\pm0.3)\times10^{-5}$ mol
Amount of H_2 in discharge gas prior to mixing (N_H)	$(2.0\pm0.5)\times10^{-5}$ mol	$(2.0\pm0.5)\times10^{-5}$ mol

Table 4.3: Physical parameters of the *pD* sources that were used in estimating the gamma-ray yield. The total gamma-ray yield in Eqn.(3.24) was calculated using the parameters listed above.

formalism. The gamma-ray production rates were estimated using the *pD* cross section measurement by Schmid *et al.* [65]. In calculating this total yield in Eqn.(3.24), we have used the physical parameters from the actual *pD* sources listed in Table 4.3.

In Figure 4.14, we show the estimated total yield for the two sources as a function of the mass-1 fraction f_1 in the beam. The curves shown in this figure should be treated as rough estimates of the yields because target degradation was not taken into account in the calculation. Also, we have made the assumption of complete beam-target mixing in this calculation. Because the dynamics of this mixing and target degradation are uncertain, the margin of error in this estimation can be large.

To analyse the radiation output of the sources, run spectra were summed according to the detector system used, and the beam energy of the run. Over 28 days of "beam-off" background energy spectra were taken for the NaI system. In Figure 4.15, the background energy spectrum is shown. It should be noted that in the region of interest (4 to 6 MeV), the background was very smooth. The peak at 6.8 MeV was the neutron capture peak by ^{127}I in the NaI.

In Figure 4.16, the room background subtracted "beam-on" energy spectrum in the NaI detector is shown. This was taken at a beam energy of 27 keV. Although there are

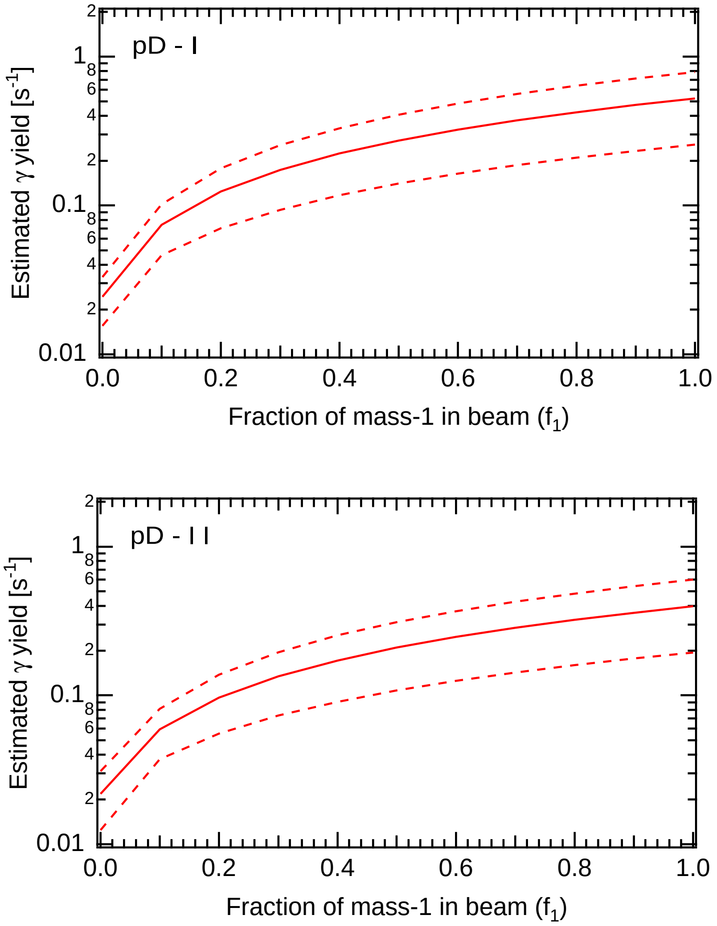

Figure 4.14: Estimated gamma-ray yield from the pD prototypes. The yields are plotted against the mass-1 fraction f_1 in the beam. Hydrogen isotopes in the beam and the target was assumed to be completely mixed. The yields shown here should be treated as rough estimates because target degradation was not taken into account in the calculation. The dotted lines are the calculated uncertainties based on the uncertainties in the physical parameters in Table 4.3 and the cross section in Schmid *et al.* [65].

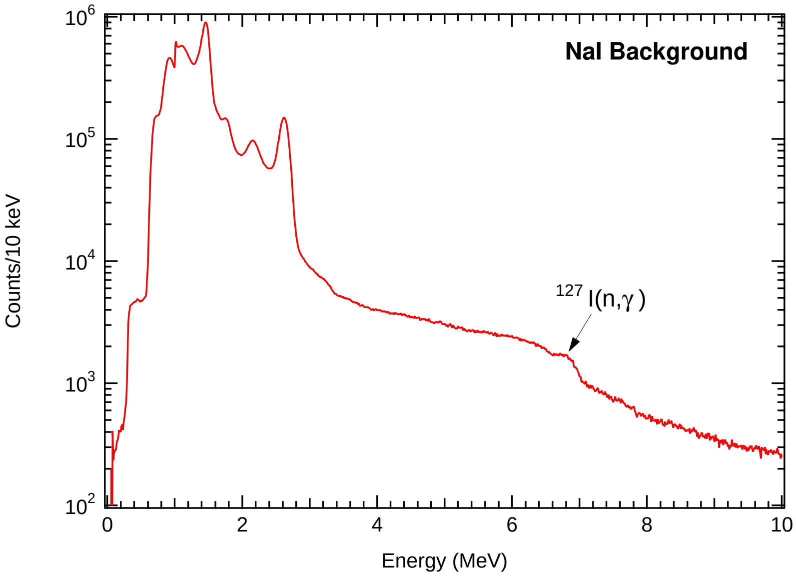

Figure 4.15: Background energy spectrum in the NaI detector. The indicated peak at 6.8 MeV is the neutron capture peak by ^{127}I in the NaI.

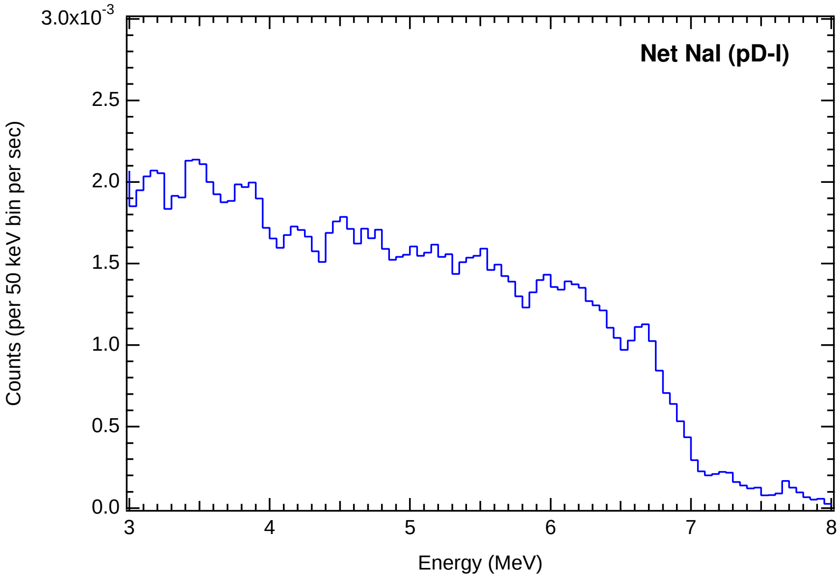

Figure 4.16: Background-subtracted “beam-on” energy spectrum in the NaI detector. This was taken at a beam energy of 27 keV. Although there are structures at the expected full photopeak and first escape peak energies, signal-to-noise ratio is obviously very poor.

structures at the expected full photopeak and first escape peak energies in the figure, signal-to-noise ratio is obviously very poor. And the question of whether or not any 5.5-MeV gamma ray was seen could not be settled. The enormous background in this figure came from neutron capture by the detector shielding material and the NaI crystal itself. This was confirmed by a 25% concurrent increase over the background in the neutron counting rate by the liquid scintillator. Furthermore, when we put more lead shielding around the NaI spectrometer, we saw an increase in the neutron induced background in the region of interest. This extra shielding enhanced neutron thermalisation and the subsequent capture. The neutron background during "beam-on" runs came primarily from neutrons generated from the ^{2}H(d,n)^{3}He reaction in the source.

The two pD prototypes were almost identical in all aspects. The only difference between them was the usage of isotopically purified H_2 discharge gas in the $pD-II$ source (Table 4.1). This was to allow a comparison of beam-target exchange of hydrogen isotopes in the two different sources. When we compared the $pD-II$ energy spectra taken with the NaI spectrometer to those of $pD-I$ we found a similar signal-to-noise ratio in the region of interest. This was a clear indication that the neutron background came from beam-target exchange of hydrogen isotopes in the source, not the isotopic purity of the H_2 discharge gas.

We also analysed energy spectra taken at a beam energy of 22 keV. The neutron to gamma-ray yield ratio decreases as the beam energy decreases (see Table 3.4). Although the neutron induced background was reduced, the gamma-ray signal was too small to provide any definitive statement on the detection of the 5.5-MeV gamma rays.

Hence, we used the HPGe system to monitor the gamma-ray output by the $pD-II$ source. HPGe crystals have very high energy resolution, and very low response to neutrons, although their efficiency in detecting 5.5-MeV gamma rays is very low. Before we used the HPGe system to test the $pD-II$ source, we placed a ^{9}Be(α,n)^{12}C fast neutron source at the centre of the detector system. The resulting neutron induced spectra in the two HPGe detectors did not show any peak feature in our region of interest.

In Figure 4.17, plots showing the total sum spectrum from the two HPGe crystals for a beam energy of 22 keV are shown. In these plots, the region surrounding the full energy, single and double escape peaks are shown, along with the room background spectrum in the same regions. For an accumulated run time of 98 hours in the HPGe system, a total of ~220 counts was estimated in the photopeaks in the two detectors. This estimate was based on the results in Figure 4.14 with a mass-1 fraction f_1 =0.63 (page 80).

In these spectra, there are hints of our long sought signal at the appropriate energy, especially near the full energy and the single escape peaks. We tried to improve the signal-to-noise ratio in the peak regions by superimposing the full energy and the single escape peaks. This superimposed peak is about 3σ above the background. This is shown in Figure 4.18. There is a total of 205 counts above the background in the figure. This number appears to agree with our estimate above. If we fit this superimposed spectrum within ±250 keV of the superimposed peak to a linear background, we found the χ^2 of the fit to be 123.3 for 79 degrees of freedom. When we fitted this spectrum with a combination of the background and the GEANT generated line shape, χ^2 of the fit was found to be 118.8 for 78 degrees of freedom. We tried to test the significance of this drop in χ^2 by shifting the GEANT calculated gamma-ray line in energy, and refitted the data with a combination of the background and this energy-shifted line. In Figure 4.19, a plot of χ^2 as a function of this energy shift δE is shown. Although χ^2 has a minimum at δE=0, this evidence is not strong enough to draw any conclusion on the long sought 5.5-MeV gamma-ray peak.

After extensive testing of the *pD* sources, we have the following observations and conclusions:

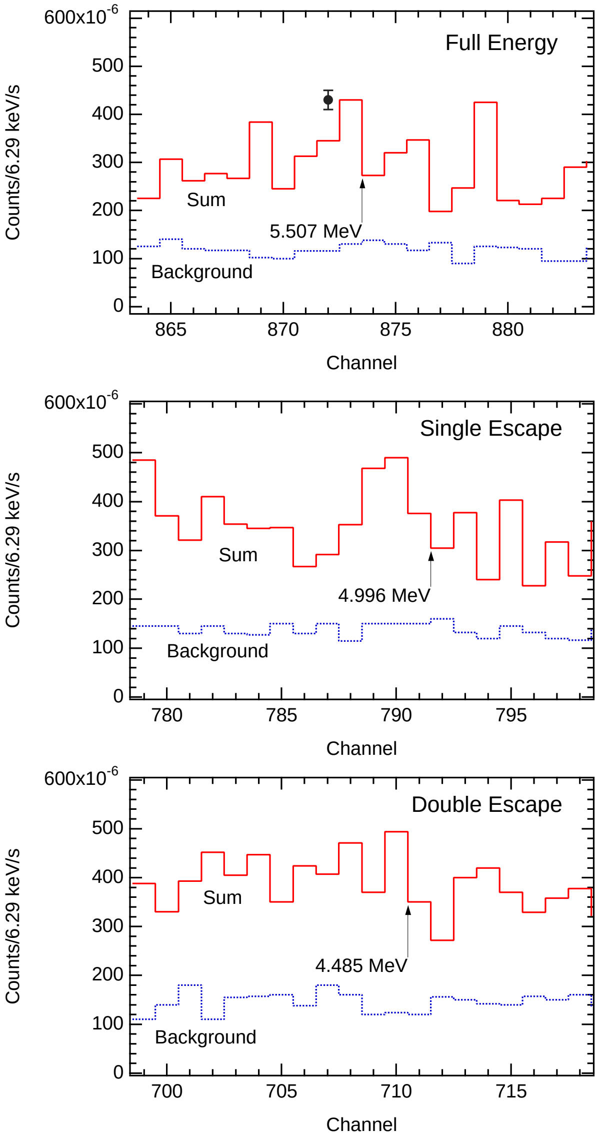

Figure 4.17: Energy spectrum from the HPGe detector system. In these plots, the region surrounding the full energy, single escape and double escape peaks are shown as solid histograms. Room background spectra are shown as dashed histograms. The magnitude of the uncertainty is shown as the error bar in the top panel. In these plots, the bin width is 6.29 keV.

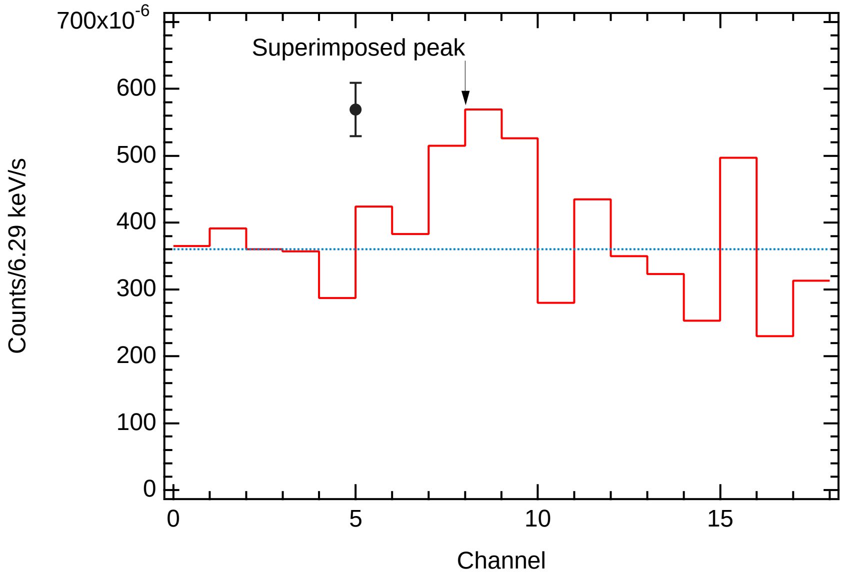

Figure 4.18: Superimposed energy spectrum of full energy and single escape peaks in HPGe data. The magnitude of the uncertainty is shown as the error bar, and the dashed line is our estimate of the background level. The total energy range shown here is about 120 keV.

- There are weak evidences for the observation of the 5.5-MeV gamma rays.

- Using isotopically purified H_2 gas did not help reducing the neutron induced background. This was an indication of beam-target hydrogen isotope exchange.

- Although our estimated signal of 220 counts agrees fairly well with the observed "signal" of 205 counts, we should point out that our estimate was based on the assumption that the hydrogen isotope mixing is complete between the beam and the target. Because there is no room for diagnostic of this mixing in the sealed source, the margin of error in our estimates can be large. Target degradation was also left out in the calculation. The dynamics of this effect is also impossible to determine experimentally in our sealed sources. Moreover, if we use the S-factors measured by Griffiths *et al.* [64], our estimated count rate would be increased by a

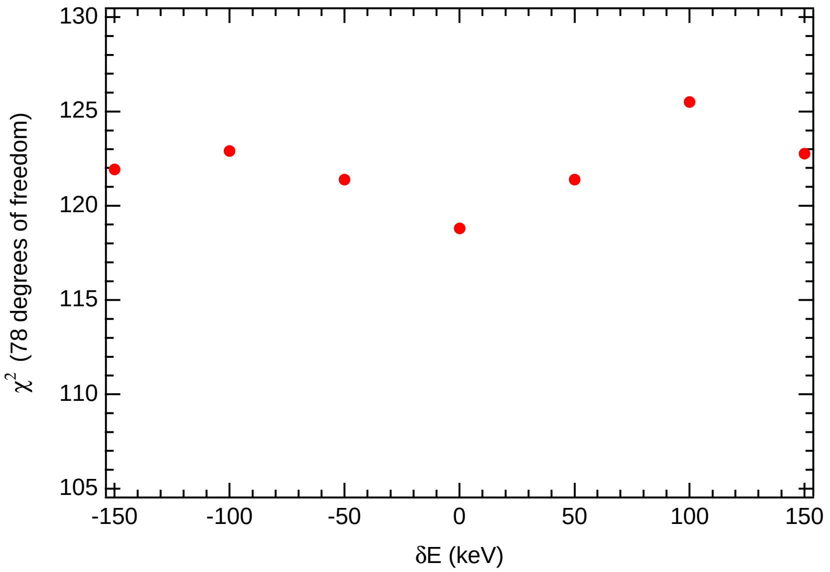

Figure 4.19: χ^2 as a function of the energy shift (δE) in the Monte Carlo generated HPGe spectrum. The superposition of the full energy and the single escape peaks within an energy range of ±250 keV was fitted to a combination of a linear background and the Monte Carlo generated line shape. The centroid of this line was shifted by an amount δE. χ^2 has a minimum at δE=0, but the significance is small.

factor of ~2.

The observation of neutrons generated by the pD sources convinced us that the sources were functional. We decided to proceed to the construction of the pT source. Testing of the pT source would be easier than the pD measurement primarily because of better signal-to-noise ratio in the region of interest. The pT reaction generates gamma rays at 19.8 MeV. At this energy, the most significant background is of cosmic origin. Also, the gamma-ray yield for the pT reaction is also about an order of magnitude higher than the pD reaction in the beam energy range we consider. In the next chapter, we shall describe the constructing and testing of the pT source.

Chapter 5

The ^{3}H(p,γ)^{4}He 19.8-MeV Gamma-Ray Source

> *What is now proved was once only imagin'd.*
>
> William Blake
> The Marriage of Heaven and Hell (1790-93)

In the last chapter, we described in detail the development of a pD 5.5-MeV gamma-ray source. This work was done to familiarise ourselves with the construction procedure of a sealed source. In this chapter, we shall describe the construction and the performance of the radioactive pT source.

5.1 Construction of the pT Source

5.1.1 Target Evaporation Apparatus and Preparation

Fabrication of the scandium tritide target, and the subsequent assembly of the pT source were performed at the tritium laboratory at Ontario Hydro Technologies (OHT) in Toronto, Ontario, Canada. Similar to the deuterated target we described in the last chapter, this target was evaporated onto a molybdenum substrate. We used the same preparation procedure as the deuterated target to prepare this substrate. The reader is referred to Section 4.1.1 for a comprehensive description of the substrate preparation procedure.

The experimental apparatus is shown in Figure 5.1. This experimental apparatus is housed inside a tritium-compatible glovebox that is continuously purged with dry nitrogen. The moisture level in the glovebox is typically 30 to 50 ppm by volume. The nitrogen purge gas is routed through a Zr_2Fe tritium trap in order to reduce its tritium content before venting to the environment [95]. The exhaust of the vacuum system is also routed through a Zr_2Fe trap before venting.

Similar to the vacuum system we used in our deuterium prototype, components of this tritium system were constructed entirely out of ultra-high vacuum (UHV) hardware. A schematic of the vacuum system is shown in Figure 5.2. To ensure that a high vacuum could be achieved in this tritium run, we used oil-free vacuum pumps in this system. The evaporation chamber is a UHV six-way cross with an outer flange diameter of 15.24 cm.

The arrangement of the evaporation assembly in this tritium system is similar to the deuterium setup in Figure 4.3. One major difference between these two setups is that the high current feedthroughs and the evaporation basket in the tritium setup were mounted on a flange that connects to a stainless steel bellows. The stainless steel shroud surrounding the evaporation basket is also mounted onto this flange. This flange is in turn mounted to a linear translation stage. This configuration allows the deposition assembly to be removed and isolated from the evaporation chamber after the film evaporation, thereby reducing tritium consumption during the tritiation process. In the deposition assembly, the tungsten evaporation basket is positioned directly above the centre of a 3.81-cm-diameter orifice on the shroud. In the target fabrication experiment, we loaded (26±1) mg of 99.99% pure, sublimed dendritic scandium in the tungsten evaporation basket.

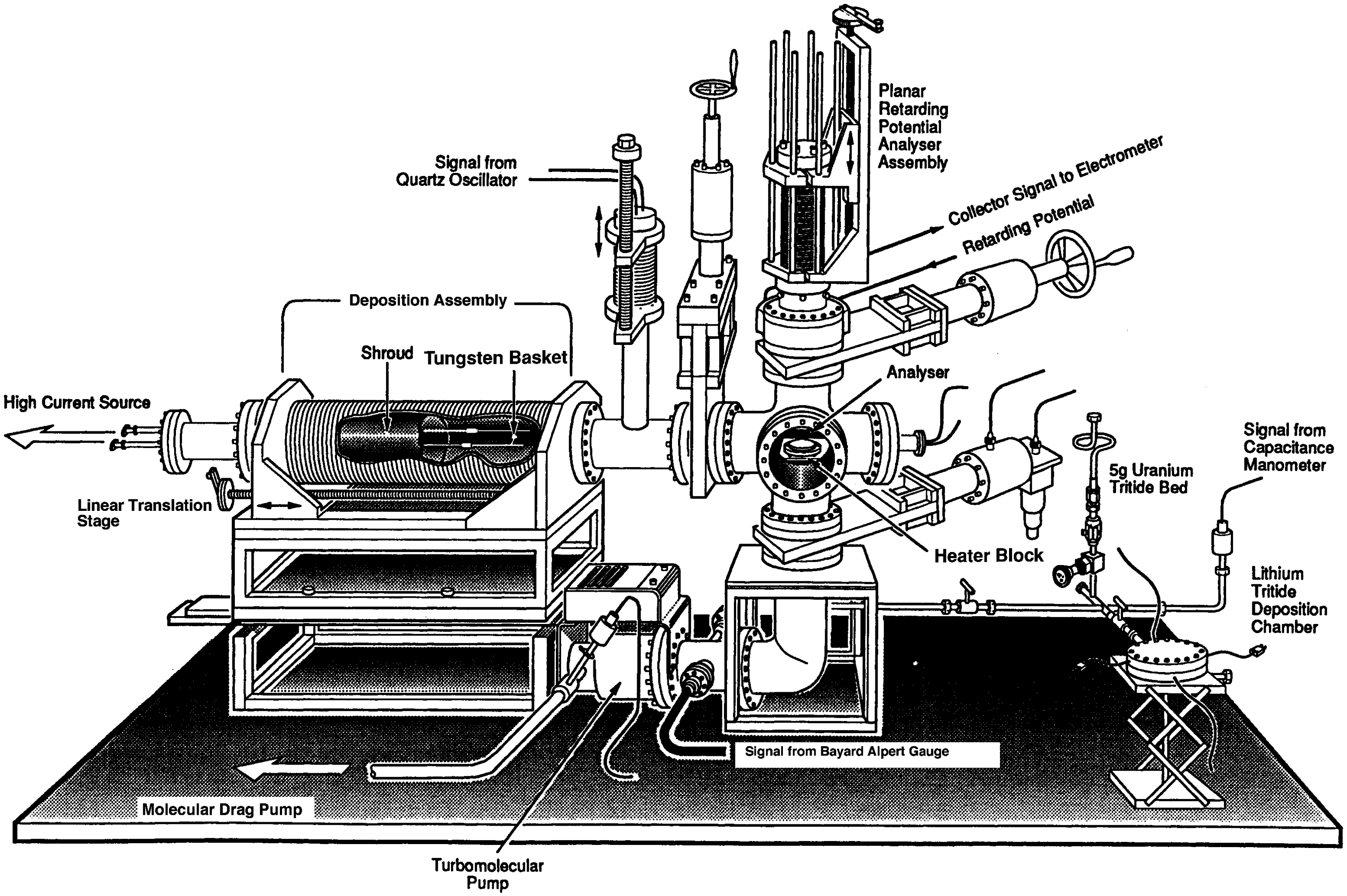

Figure 5.1: Schematic of the scandium tritide target evaporation system. All the components shown in this picture are enclosed in a dry nitrogen environment inside a glovebox (from [89]).

Isotope	Composition
^{1}H	(0.79±0.04)%
^{2}H	(0.12±0.01)%
^{3}H	(99.09±0.05)%

Table 5.1: Isotopic composition of the tritium gas used in the target (from [98]).

A quartz oscillator is installed at the end of a bellows as shown in the setup in Figure 5.1. When the deposition assembly is inserted into the evaporation chamber, the oscillator can be lowered to the back side of the assembly through an aperture in the main shroud. This oscillator can then be used to monitor the deposition rate of scandium. The distance between the scandium source (in the tungsten evaporation basket) and the oscillator was 27 cm. In the evaporation chamber, there is a high pressure vacuum gauge with a sensitivity range of 1×10^{-7} to 1 mbar. During the experiment, the analog output of this gauge was fed to a digital voltmeter, which in turn was connected to a data acquisition computer through a GPIB bus interface. This gauge was used to monitor tritium sorption by the evaporated film.

As shown in Figure 5.2, there are two main gas lines connected to the evaporation chamber in the vacuum system of the setup. One of these branches is connected to a 5-g depleted uranium bed. This uranium bed is used to store tritium which can be readily desorbed by raising it to sufficiently high temperature [96, 97]. In Table 5.1, the isotopic purity of the tritium gas in this bed we used is shown.

Prior to film evaporation, the whole apparatus was baked for over a week at ~150-200 °C, whilst the molybdenum substrate, which was mounted to the heater block, was kept at 400 °C. This baking was to reduce the outgassing rate of the evaporation system. The tungsten evaporation coil was also baked by running a 10 A current through it. At this current, the basket was not glowing, and would not be hot enough to evaporate the

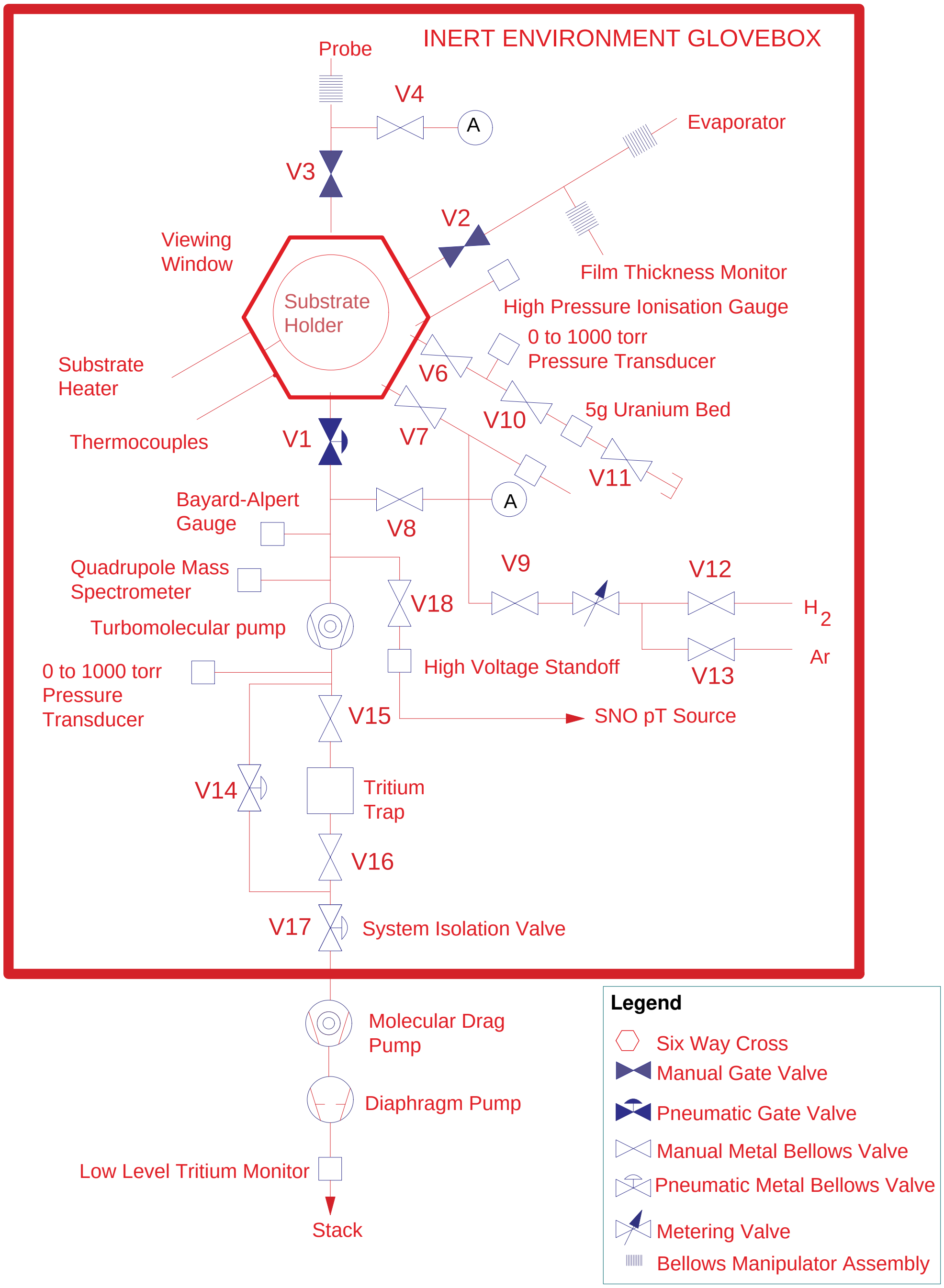

Figure 5.2: Schematic of the scandium tritide target evaporation vacuum system. Most of the setup is enclosed in a dry nitrogen environment inside a glovebox (from [95]).

scandium lump. The base pressure of the system was $\sim 6\times10^{-7}$ mbar during the bakeout. After the baking, the evaporation system reached a base pressure of 5.8×10^{-8} mbar.

5.1.2 Scandium Tritide Target Fabrication

After the evaporation system had reached its base pressure following an extensive bakeout, the deposition assembly (i.e. the high current feedthrough-evaporation basket assembly) was delivered into the evaporation chamber by winding in the linear translation stage to which the deposition assembly flange was connected. The tungsten evaporation basket was positioned directly above the centre of the molybdenum substrate.

The current fed to the tungsten basket was raised at a rate of about 1 A min^{-1} during the first thirty minutes of the experiment. This rate was then decreased to 0.2 A min^{-1} as the outgassing rate in the vacuum chamber was higher than the deuterium system in Figure 4.2. This was because the turbomolecular pump in this tritium system has a lower pumping capacity than the one we used in the deuterium system. In the deuterium system, there was also an ion pump connected to the evaporation chamber to provide further pumping. By slowing down the rate at which the tungsten basket was heated up, and hence most of the evaporation hardware, the vacuum pumps were given more time to remove the residual gas in the system.

It was found that the quartz oscillator had stopped working during the deposition process. We therefore kept raising the basket current to 46 A, at which point the coil temperature was ~1900 °C. This was to ensure that all the scandium, whose melting point is 1539 °C, was evaporated.

Because the evaporation feedthrough in this setup was identical to the deuterium system we used, we could use the known geometry in the deuterium system to calculate the amount of scandium deposited in this run. The separation between the scandium source and the heater block was (14±2) mm. Therefore, the scandium film thickness was

(1.1±0.3) mg cm^{-2}.

Immediately after the scandium deposition, we removed the deposition assembly from the evaporation chamber by winding out the linear translation stage. The gate valve (V2 in Figure 5.2) separating the deposition assembly and the evaporation chamber was then closed. Before we let tritium into the evaporation chamber, it was isolated by closing the remaining gate valves (V1 and V3 in Figure 5.2) connected to it. We subsequently raised the molybdenum substrate temperature to 400 °C. This was to enhance tritium sorption by the scandium film later on.

The uranium tritide bed was first heated to 135 °C to drive out the ^{3}He from tritium decay in the bed. At this temperature, tritium is still "locked" inside the bed. The released ^{3}He was first pumped out of the system before the uranium bed temperature was raised to 220-240 °C at which temperature the tritium is desorbed. In order to measure the amount of tritium sorbed by the scandium film, the tritium gas released from the uranium bed was first trapped in the small volume between valves V6 and V10 (see Figure 5.2) before releasing to the isolated evaporation chamber. This trap has a volume of (31.9±2.2) cm^3. With the tritium pressure measured by the pressure transducer connected to this volume, the amount of tritium used could then be determined. Although the pressure inside the evaporation chamber was higher than that in the deuterium system during the evaporation process, we could still maintain a high tritium loading in the scandium film by injecting an order of magnitude higher in tritium gas volume in each of the doses compared to the deuterium run. In Table 5.2, we have listed the pressure inside this trap for the tritium doses we injected into the evaporation chamber. A total of (8.19±0.57) Ci of tritium was injected into the chamber.

In Figure 5.3 the pressure inside the evaporation chamber is plotted against the time after each tritium dose was injected. It is clear from the figure that the sorbing capacity of the scandium film decreased as the tritium concentration in the film increased.

Run Number	Trap Pressure (mbar)
1	7.6
2	8.0
3	7.1
4	6.9
5	8.8
6	7.2
7	7.9
8	7.7
9	7.5
10	7.9
11	7.6
12	8.8
13	15.7

Table 5.2: Tritium dosage injected into the evaporation chamber for each tritium sorption run. The trap pressure shown here is the pressure measured by the pressure transducer between V6 and V10 (with these valves closed) in Figure 5.2. This trap has a volume of (31.9±2.2) cm^{3}.

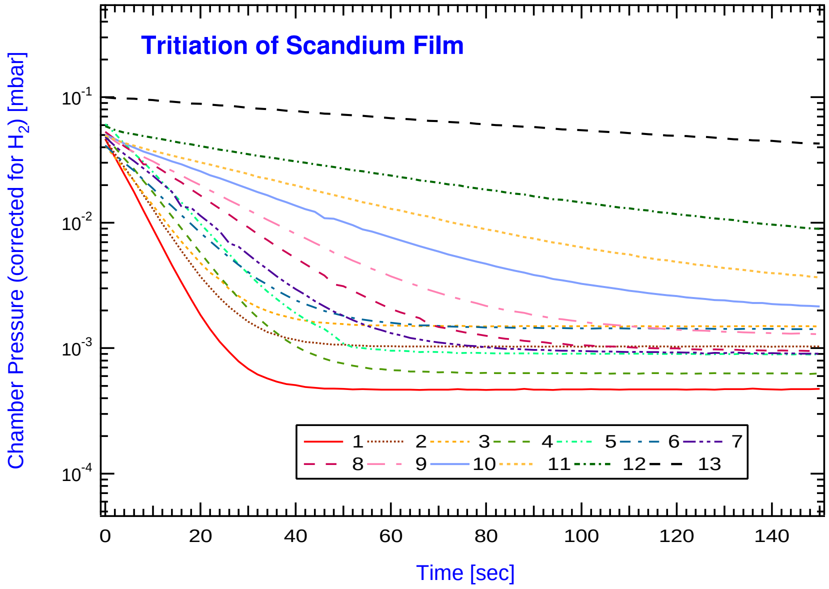

Figure 5.3: Tritium pumping by the scandium film. The pumping curve for each of the runs in Table 5.2 is shown here.

To calculate the Sc:^{3}H atomic ratio in the target, we need to know the amount of scandium present in the evaporation chamber and the amount of tritium which was absorbed by this film. Scandium deposited on the heater block spanned a circular "shadow" of radius (2.1±0.1) cm. The size of this shadow was defined by the position of the source relative to the orifice in the shroud of the evaporation feedthrough. This shadow is not to be confused with the 1.02-cm-radius scandium tritide target, which was situated at the centre of this shadow. Therefore, the mass of scandium in this shadow (M_{shadow}) was

$$M_{shadow} = M_{Sc}\frac{\Delta\Omega_{shadow}}{4\pi} = (5.7 \pm 0.6)\ \mathrm{mg}, \tag{5.1}$$

where M_{Sc} is the mass of the original scandium source, and $\frac{\Delta\Omega_{shadow}}{4\pi}$ is the fractional solid angle subtended by the shadow. This amounts to $(1.3\pm0.1)\times10^{-4}$ mol of scandium in the shadow.

The amount of tritium absorbed by the scandium shadow can be extracted by comparing the initial and the final pressure recorded by the high pressure vacuum gauge connected to the evaporation chamber. We found that 89.9% of the tritium that was injected into the chamber was absorbed by the scandium film. This corresponds to (7.38±0.51) Ci or $(1.29\pm0.09)\times10^{-4}$ mol of tritium. Therefore the Sc:^{3}H atomic ratio is

$$\frac{^3\mathrm{H}}{\mathrm{Sc}} = \frac{2\,(1.29 \pm 0.09)}{1.3 \pm 0.1} = 2.0 \pm 0.2. \tag{5.2}$$

Finally, we need to determine the activity of the scandium tritide target for radioactive licensing purposes. The activity of the target was

$$(7.38 \pm 0.51) \times \frac{\Delta\Omega_{target}}{\Delta\Omega_{shadow}} = (3.3 \pm 0.8)\ \mathrm{Ci}, \tag{5.3}$$

where $\Delta\Omega_{target}$ is the solid angle subtended by the target.

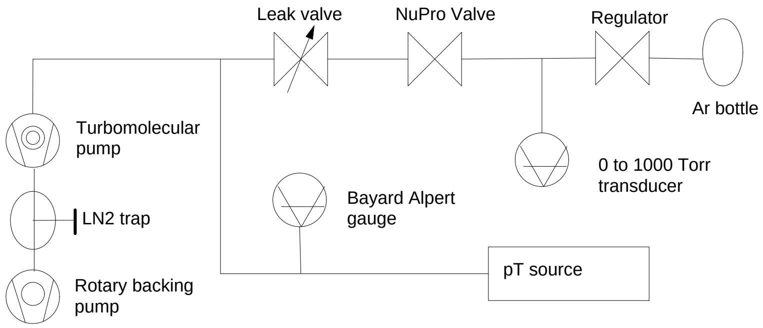

Figure 5.4: Schematic of the vacuum system that was used to pump down the pT source. The ion source was baked in this system prior to target mounting. This vacuum system was purged with argon for approximately 5 to 10 minutes daily during this bakeout period of approximately two weeks.

5.1.3 Assembly of the pT Source

Similar to the pD source, the ion source must be cleansed before the tritiated target could be mounted (see page 91). We followed the same chemical cleansing procedure outlined in Figure 4.4. Subsequent to this chemical cleansing procedure, the ion source was mounted to a tritium-free bakeout system whose schematic is shown in Figure 5.4. The ion source was baked at 150 °C for about two weeks. The bakeout vacuum system was flushed with argon for approximately 5 to 10 minutes daily during this bakeout period. We found that this flushing procedure did improve the overall cleanliness of the vacuum system.

After the target fabrication, the ion source was removed from the bakeout system and wrapped in layers of Parafilm™ which is a flexible, thermoplastic material. It was used to minimise tritiated particles depositing on the outer surface of the ion source once it was taken into the glovebox where the target evaporation system was set up. The tritiated target was removed from the evaporation system and mounted to the pT source. The ion source was then connected to the vacuum system as indicated in Figure 5.2. Once the pT source was pumped down, we followed the same electro-discharge cleansing and hydrogen gas loading procedure as outlined in Section 4.2 before sealing it. After the *pT* source was sealed, it was removed from the glovebox. This was then followed by decontamination of the source's outer surface before shipping to Queen's University for quality assurance testing.

5.2 Quality Assurance Test of the *pT* Source

After the *pT* source was assembled at the Ontario Hydro Technologies (OHT) tritium laboratory, it was transported to Queen's University in Kingston, Ontario, Canada for quality assurance testing. Queen's University is sufficiently close to the OHT tritium laboratory (about 300 km), and has facilities for this testing.

At Queen's University, we used a 12.7-cm diameter by 7.6-cm long bismuth germanate ($Bi_4Ge_3O_{12}$, or BGO) crystal as the gamma-ray detector [99]. We also employed the same liquid scintillator we used in the *pD* prototype testing as the neutron detector in this test. In this section, we shall describe this detector system in more detail. We shall summarise the results of the 19.8-MeV gamma-ray search in this quality assurance run.

5.2.1 Overview of the Detector System

Bismuth Germanate (BGO) Detector

Recently bismuth germanate ($Bi_4Ge_3O_{12}$, or BGO) crystals are gradually finding their places in high energy gamma-ray spectrometers because of BGO's shorter gamma-ray range compared to NaI. The range for 20-MeV gamma rays in NaI and BGO is 6.1 cm and 2.8 cm respectively [100, 101]. This means that one can use a much smaller BGO crystal to achieve the same intrinsic detection efficiency as a NaI crystal.

Background in the *pT* gamma-ray energy spectrum around 20 MeV will mostly be cosmic-ray induced. Since the cosmic muon rate is proportional to the surface area of the detector, the average cosmic muon count rate in a BGO detector would be about four times lower than that of a NaI detector with the same intrinsic gamma-ray detection efficiency. And since the density of BGO (ρ_{BGO}=7.13 g cm^{-3}) is about twice that of NaI's (ρ_{NaI}=3.67 g cm^{-3}), traversing muons will deposit about the same amount of energy in a BGO crystal as in a NaI crystal that is twice the size in all linear dimensions. As a result, the rate of energy deposited per event (i.e. number of counts per MeV per unit time) in a BGO detector will be about four times lower than that in a NaI detector of the same intrinsic detection efficiency.

BGO is also less sensitive to neutrons than is NaI. Drake *et al.* [102] determined that the neutron sensitivity of BGO, expressed as the probability for thermal neutron capture per unit volume, is less than a quarter of that for NaI.

One disadvantage of BGO is that its light output is only 12-14% of NaI's [103]. This results in poorer energy resolution in BGO compared to NaI detectors. For the ^{137}Cs(0.662 MeV) line, NaI has a 7% full-width-at-half-maximum (FWHM) energy resolution, and that for BGO is typically 15% [103]. This difference in energy resolution should become smaller at higher energies as more light would be generated. If we assume that the resolution function varies with energy, E, as $\sim 1/\sqrt{E}$, the FWHM resolution at 20 MeV would be about 1.3% and 2.7% for NaI and BGO respectively.

Experimental Arrangement

The orientation of the pT source with respect to the gamma-ray and the neutron detectors in this quality assurance run is shown in Figure 5.5. A description of the liquid scintillator neutron detector can be found in Section 4.3.2. In the gamma-ray spectrometer, the 12.7-cm diameter by 7.6-cm long BGO crystal was surrounded by five panels of 1.3-cm thick plastic scintillators serving as an active cosmic veto. The BGO crystal was manufactured by Harshaw/Filtrol, and it was coupled to a 12.7-cm diameter SRC 125B01

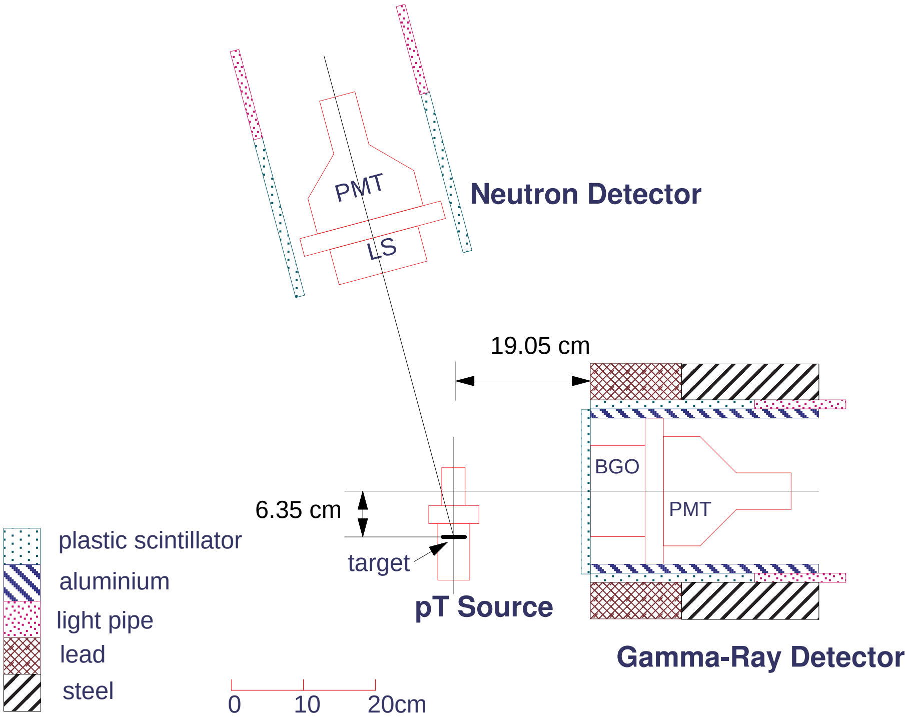

Figure 5.5: Top view of the detector setup for the quality assurance testing of the pT source. The separation between the liquid scintillator (LS) and the target of the pT source is 35.56 cm.

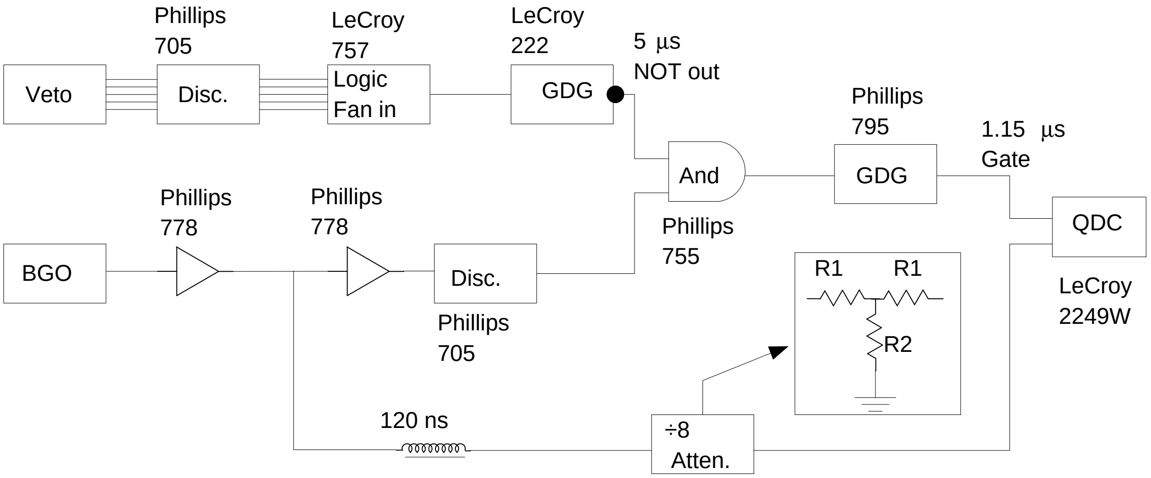

Figure 5.6: Electronics scheme for the BGO gamma-ray detector at Queen's University. The schematic of the attenuator is also shown here. The resistors had values R1= 39Ω and R2= 13Ω to provide an attenuation factor of ∼8 for a 50Ω load.

photomultiplier tube (PMT) manufactured by A.D.I.T. Co. This PMT was surrounded by μ-metal for magnetic shielding. Because of the close proximity of the pT source's discharge magnet to the PMT, 5-cm thick slabs of steel were placed around it in order to reduce the magnetic effect on its gain. Even with this shielding, we found that the pulse height resolution was degraded to about 15% from ∼12.5% for the ^{137}Cs(0.662 MeV) line [99]. Lead of about 5 cm thick was stacked on the top and to the sides of the BGO crystal to shield the crystal against cosmic ray induced bremsstrahlung and neutron capture gamma rays.

Electronics

The electronics schemes for the BGO detector gamma-ray detector system and the liquid scintillator neutron detector system are displayed in Figures 5.6 and 5.7.

For the gamma-ray spectrometer, the anode output of each of the PMTs coupled to

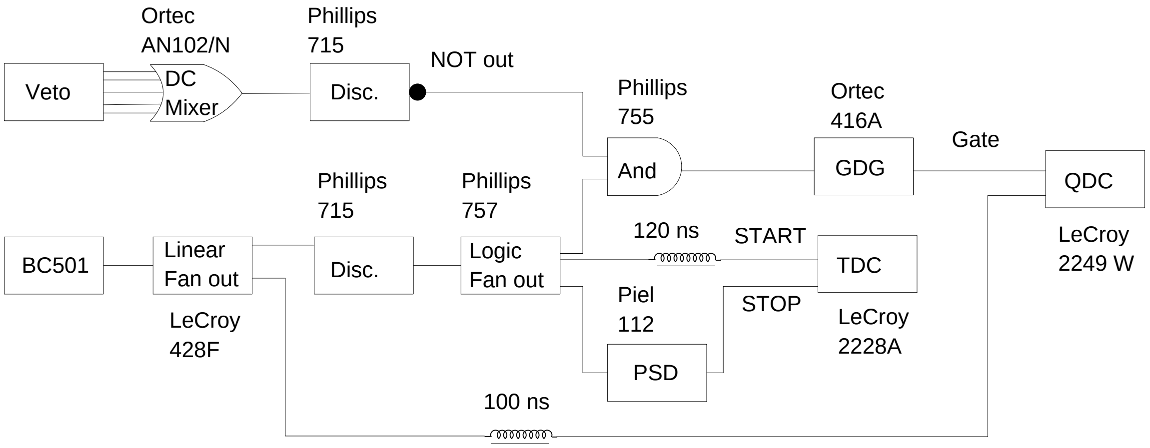

Figure 5.7: Electronics scheme for the neutron detector at Queen's University.

the veto scintillators was sent to a Phillips 705 discriminator. The discriminator outputs were then logically summed by a LeCroy 757 logic fan-in module. This summed logic signal was in turn used to trigger a LeCroy 222 gate-and-delay generator (GDG) to generate a 5 μs inverted gate. The anode output of the BGO detector was first sent to a Phillips 778 fast amplifier. This amplifier output was branched into two, in which one of them was delayed by 120 ns and attenuated before feeding to a LeCroy 2249W charge-to-digital converter (QDC). This signal attenuation was necessary in order to avoid saturating the QDC (-512 pC full scale). The attenuator shown in Figure 5.6 was suitable for fast PMT signals [78]. The other amplified BGO output was amplified again by a Phillips 778 fast amplifier. The output of this second amplifier was sent to a Phillips 705 discriminator whose output was checked for anticoincidence with the GDG output from the veto branch. If the anticoincidence condition was satisfied, a 1.15-μs gate would be generated by a Phillips 795 GDG to trigger the QDC.

For the neutron detector, the electronics scheme was similar to the one used in the pD prototype (Section 4.3.2), except for a couple of minor simplifications in the scheme. First of all, all of the photomultiplier tube anode outputs were summed by an Ortec AN102/N DC mixer before feeding into a Phillips 715 discriminator. Another change was that a gate to the QDC was generated whenever there was an anticoincidence between the liquid scintillator discriminator output and the veto discriminator output. Finally the liquid scintillator output was fed to the QDC without any amplification. These simplifications reduced the overall dead time of the system.

5.2.2 Monte Carlo Simulation of the BGO Spectrometer Response

The response function for the BGO spectrometer was calculated using GEANT [92]. A discussion on the reliability of this widely-used simulation tool can be found in Appendix B. In this simulation, the exact geometry of the spectrometer and the target mount of the pT source were modelled. Moreover, the relative orientation between the pT source and the spectrometer was modelled to be the same as in the actual quality assurance run. The energy resolution of the detector was taken to be 15% at ^{137}Cs(0.662 MeV) line, and was assumed to vary as $1/\sqrt{E}$. Since the angular distribution of the gamma rays in the ^{3}H$(p,\gamma)^4$He reaction is expected to be predominantly a dipole distribution ($W(\theta) \sim \sin^2\theta$, see Section 6.1), we generated 19.8-MeV gamma rays with this angular distribution in the simulation.

In Figure 5.8, the calculated response function is shown. This response function includes a cut on events that triggered the veto counter. The trigger threshold of the veto counter was 0.6 MeV in this run and this amounted to 9.5% of the events that deposited more than 15 MeV of energy in the crystal. In this calculation, it was found that a 19.8-MeV gamma ray generated by the pT source with a dipole distribution has a probability of $(8.39\pm0.07)\times10^{-3}$ of depositing more than 15 MeV of energy in the BGO crystal without triggering the veto counter. In Figure 5.9, a histogram of the gamma-ray

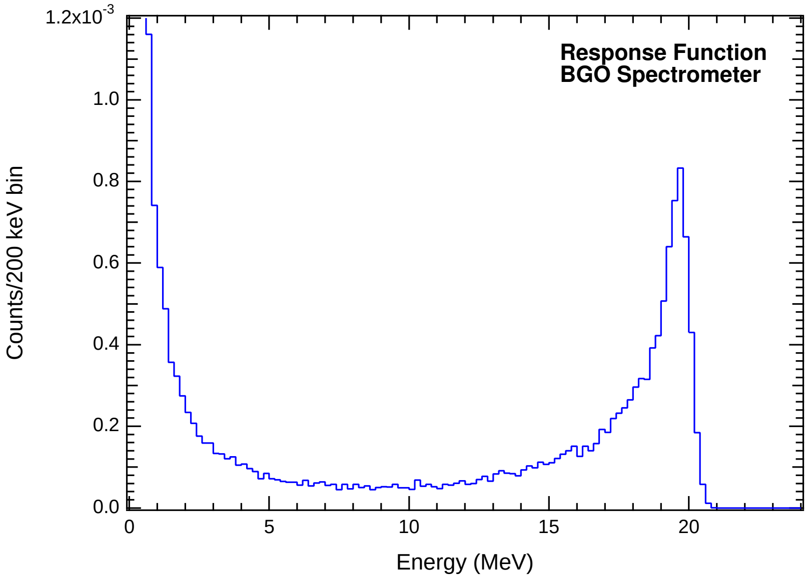

Figure 5.8: The Monte Carlo simulated response function for the BGO spectrometer in the quality assurance run. The pT source's orientation with respect to the BGO spectrometer is shown in Figure 5.5. All the active and passive shieldings to the spectrometer were modelled in the simulation. The target mount of the pT source was also modelled in this calculation in order to correct for gamma-ray attenuation through the mount. The gamma-ray angular distribution was assumed to be $\sin^2\theta$ in this calculation.

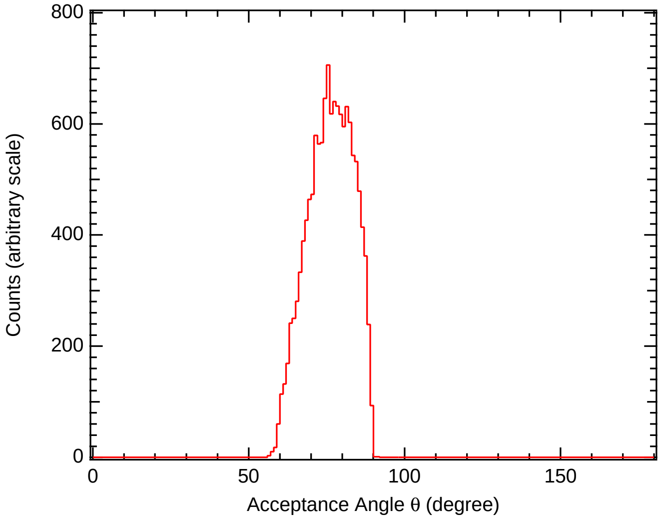

Figure 5.9: Monte Carlo simulation of the emission angle for events depositing more than 15 MeV of energy in the BGO crystal.

emission angle for these events is shown. The sharp cutoff at $\theta = 90^\circ$, although gamma-ray emission is greatest at this angle, is due to the pT source's spatial orientation with respect to the BGO crystal in this run.

5.2.3 Gamma-Ray Search in the Quality Assurance Test

In this section, we shall present the results of the search for the 19.8-MeV gamma-ray in the quality assurance test. Because we expected the gamma-ray production rate by the pT source to be low, we measured the background energy spectrum in the BGO detector to make sure that the background rate was sufficiently low for this quality assurance test. The background energy spectrum over the region of interest in the BGO detector is shown in Figure 5.10. Also shown in the figure is an exponential fit of the form

$$y_B(E) \;=\; y_\circ + \exp\left(-\mu E\right) \qquad (5.4)$$

to the background spectrum in the energy range of 15 to 30 MeV. At 20 MeV, the background rate was approximately 12 counts/MeV/hr, and was acceptable.

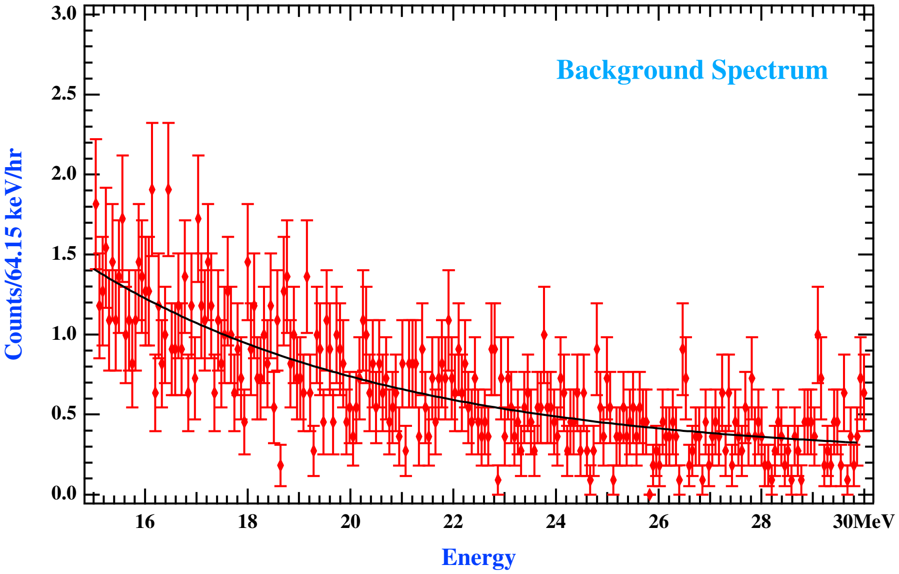

Figure 5.10: The background energy spectrum over the region of interest. The spectrum shown here represents 11 hours of counting. The solid curve shows an exponential fit to the background energy spectrum.

Parameter	Value
^{3}H/Sc atomic ratio prior to mixing (L_t)	2.0±0.2
Amount of $^3H_2$ in target prior to mixing (N_t)	$(5.8\pm0.4)\times10^{-5}$ mol
Amount of H_2 in discharge gas prior to mixing (N_H)	$(2.0\pm0.5)\times10^{-5}$ mol

Table 5.3: Physical parameters of the pT source that were used in estimating the gamma-ray yield. The total gamma-ray yield in Eqn.(3.24) was calculated using the parameters listed above.

We proceeded with measuring the gamma-ray and neutron production rates by the pT source. As in the case for the pD prototype testing, we estimated the beam current on target from the temperature of the getter (page 104). The beam current was estimated to be (50±20) μA at a beam energy of 27 keV. The H_2 partial pressure inside the source was adjusted during the run to maintain a constant current.

We estimated the total gamma-ray yield Y_{total} (Eqn.(3.24)) from the pT source based on the formalism we developed in Section 3.3.3. In Table 5.3, we have listed the physical parameters of the pT source that we used in this calculations. In Figure 5.11, we show the estimated total yield as a function of the mass-1 fraction f_1 in the beam.

Energy calibration of the BGO detector was provided by the ^{22}Na 0.511-MeV and 1.275-MeV lines, the $^1H(n,\gamma)^2H$ 2.22-MeV line, and the $^{12}C^*$(4.4 MeV) de-excitation line. The source was initially run at a beam energy of 22 keV. After about three hours of running, we raised the beam energy to 27 keV. After the first eight hours of running at 27 keV, we saw a small drift (~3.5%) in the gain of the BGO signal. We subsequently calibrated the gain of the BGO spectrometer with a $^{12}C^*$(4.4 MeV) de-excitation line and a $^1H(n,\gamma)^2H$ 2.2-MeV line every hour.

The sum data after 14.4 hours of running at E_p =27 keV, $y(E)$, was first fitted to the form

$$y(E) \; = \; N_B \, y_B(E) \tag{5.5}$$

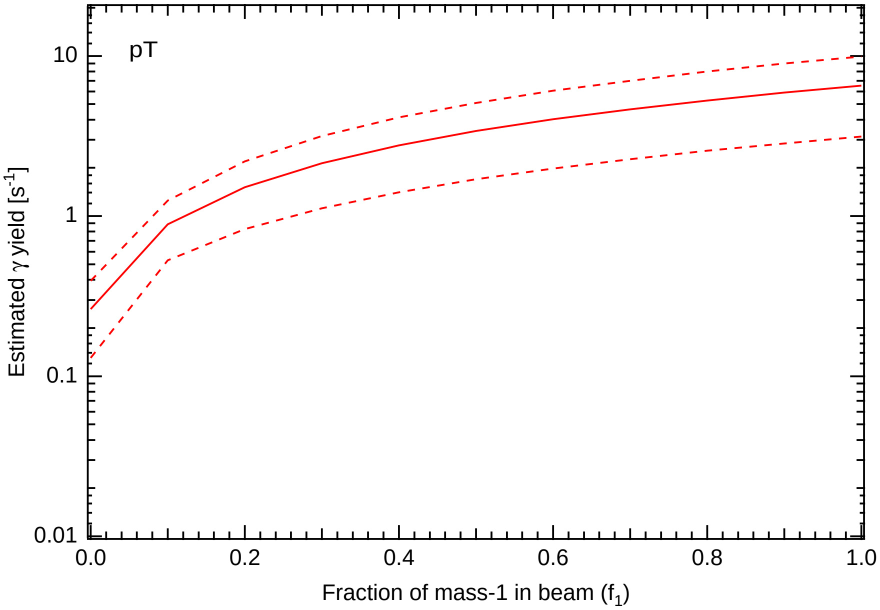

Figure 5.11: Estimated gamma-ray yield from the pT source. The yield is plotted against the mass-1 fraction f_1 in the beam. Hydrogen isotopes in the beam and the target was assumed to be completely mixed. The yield shown here should be treated as the upper limit because target degradation was not taken into account in the calculation. The dotted lines are the calculated uncertainties based on the uncertainties in the physical parameters in Table 5.3 and the cross section (Section 3.3.2).

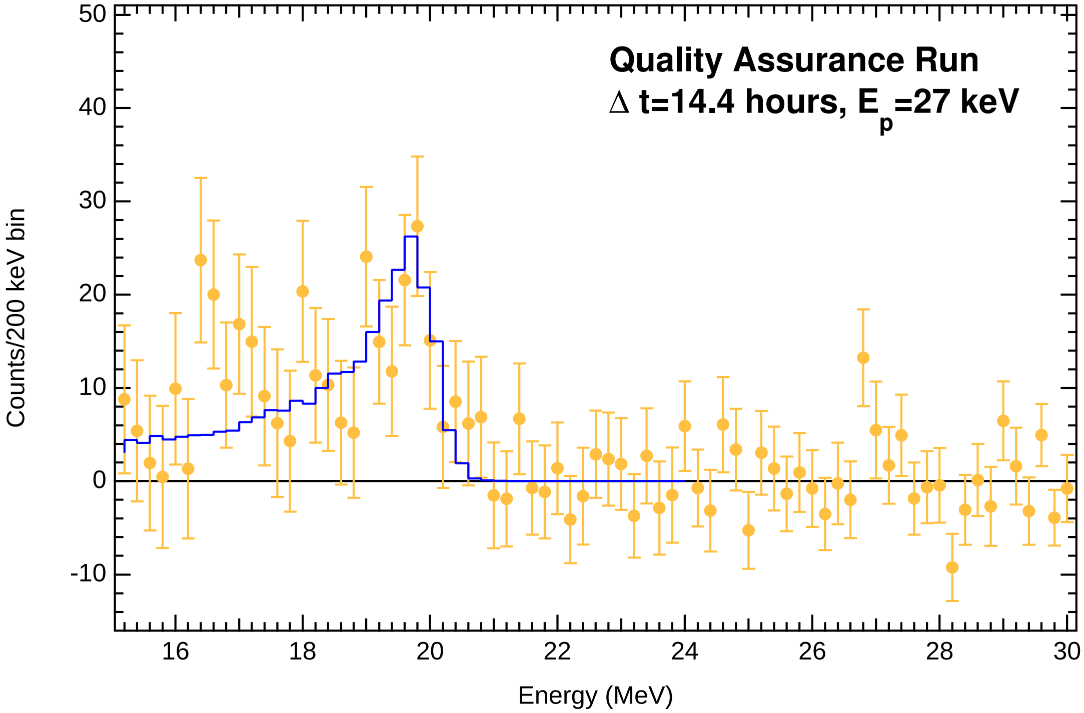

Figure 5.12: Background-subtracted BGO energy spectrum in the quality assurance run. The data points constitute the background-subtracted energy spectrum. The histogram shown is a fit using a response function for the BGO spectrometer generated by GEANT.

in the energy range of 22 to 30 MeV using the program MINUIT [104]. In this expression, N_B is the fitted amplitude of the background and $y_B(E)$ is the background function in Eqn.(5.4). In Figure 5.12, the background-subtracted BGO energy spectrum is shown. This background-subtracted spectrum was then fitted to the form

$$y(E) \;=\; N_\gamma \, y_\gamma(E) \tag{5.6}$$

in the energy range of 15 to 22 MeV, where $y_\gamma(E)$ is the Monte Carlo simulated response function in Figure 5.8, and N_γ is the fitted amplitude. Given the normalisation of the response function, this amplitude represents the total number of 19.8-MeV gamma rays emitted by the pT source assuming a pure $\sin^2\theta$ distribution. We did not extend the fit to an energy below 15 MeV because of a possible contribution from the tail of the 10.2-MeV gamma ray emitted from neutron capture on ^{73}Ge. Since the neutrons are captured in the BGO crystal, it is likely that all this energy would be absorbed in the detector. To ensure that the contribution from the tail of this radiative capture is negligible, we applied the 15-MeV low energy cut in this fit.

The fit of this data to the Monte Carlo simulated response function gives a fitted amplitude N_γ of $(3.15\pm0.37)\times10^4$ with a χ^2 per degree of freedom of 0.802. Because the data points are distributed according to a Poisson distribution, χ^2 minimisation consistently underestimates the area under a peak by an amount $\simeq \chi^2_{min}$ where χ^2_{min} is the minimised χ^2 (see Chapter 12 of [105]). We added χ^2_{min} to the total number of counts under the fitted curve in Figure 5.8 to get an adjusted amplitude N_γ of $(3.47\pm0.37)\times10^4$.

We now have to assess the systematic uncertainty in this quality assurance run. The three main sources of systematic uncertainty in the extracted N_γ above are the accuracy of the GEANT Monte Carlo simulation, energy resolution of the BGO detector, and the source-detector orientation.

The uncertainty in the Monte Carlo simulation of the response function is the uncertainty of the gamma-ray interaction probability in the target mount, the BGO crystal and other shielding material. As we shall see in the next chapter, we estimated this uncertainty to be ±5%.

We did not have a calibration source with an energy close to 19.8 MeV to calibrate the energy resolution and the response linearity of the BGO. In our Monte Carlo program, we have made an assumption of $1/\sqrt{E}$ variation in the detectors' energy resolution. We assumed an uncertainty of ±1% in the absolute full-width-at-half-maximum resolution of the BGO detector at 19.8 MeV, and generated Monte Carlo spectra with this resolution smearing. We then shifted the simulated spectra by ±1% in energy, and the background-subtracted spectrum was re-fitted to these shifted spectra. The uncertainty due to this variation in energy resolution and calibration was found to be ±6%.

We estimated the uncertainties associated with the source-detector distance and angular orientation to be 1 cm and 2° respectively. These uncertainties contribute a 10% uncertainty to the fitted N_γ.

Adding all these uncertainties in quadrature, we get

$$N_\gamma \; = \; (3.47 \pm 0.57) \times 10^4. \tag{5.7}$$

This gives a gamma-ray yield by the pT source of (0.67 ± 0.11) s^{-1} at a proton energy $E_p \leq 27$ keV. This measured rate exceeds the design criterion of 0.2 s^{-1}.

If we assume a mass-1 fraction f_1 of 0.63 (page 80), the estimated gamma-ray yield from Figure 5.11 is ~ 4 s^{-1}. Our measured rate is lower than the estimated rate by a factor of ~ 6. When we compare our results to the yield estimates in Figure 5.11, our results appear to suggest that f_1 is ~ 0.08. This is a sharp drop from 0.63 which we measured in Section 3.4.4. During this quality assurance run, the gas pressure inside the pT source was 3×10^{-3} mbar, which is a factor of 5 higher than that in the mass composition measurement in Section 3.4.4.

Before jumping into the conclusion of a sharp drop in f_1 as the reason for this lower-than-estimated yield, we should assess all the factors which might have contributed. We might have overestimated the yield in our calculation, or we might have underestimated the gamma-ray output by the source in our experiment.

The gamma-ray yield of the pT source Y_{total} was extracted from the experimental data as

$$Y_{total} = \frac{N_{BGO}}{\int_{\Omega_{BGO}} \varepsilon W(\theta) d\Omega} \tag{5.8}$$

where N_{BGO} is the number of detected gamma rays by the BGO detector, ε is the detection efficiency, $W(\theta)$ is the gamma-ray angular distribution, and Ω_{BGO} is the solid angle subtended by the BGO detector. In the data analysis, we have assumed $W(\theta) = \sin^2\theta$. As we shall see in the next chapter, our measurement of the angular distribution is consistent with a picture of a dipole $\sin^2\theta$-type distribution, but it does not rule out a significant isotropic component. We ran a Monte Carlo simulation to calculate how much the yield would change if we assume an isotropic distribution. This was found to be a <20% effect. We have also demonstrated in the next chapter that the simulated detector efficiency in the analysis can contribute only a 5% uncertainty. Therefore, these uncertainties are not significant contributors to the lower-than-estimated yield.

We now address the reliability of our estimation of the total yield. In Eqn.(3.13), we see that the calculated yield depends on the beam flux ϕ_{ion}, the target density n_{target}, the stopping power $-dE/dx$ and the cross section $\sigma(E)$.

We used the total beam current in the run in the yield calculation. A low mass-1 fraction f_1 would lower the calculated yield. But it is inconceivable for f_1 to drop by almost an order of magnitude when the H_2 gas pressure was raised from 0.6×10^{-3} mbar to 3×10^{-3} mbar, given that it is constant over the pressure range of $(0.3\text{-}0.6)\times10^{-3}$ mbar.

Unfortunately, the mass composition of the beam cannot be determined *in situ* simultaneously once the source was sealed. Therefore, it can be a significant contributor to the lower-than-estimated yield. Moreover, we did not take target degradation into account in our yield calculation. This effect will reduce the gamma-ray yield of the pT source.

The stopping power we calculated using SRIM [77] is accurate to within ~2% [106]. As we pointed out in Section 3.3.2, the cross section of the $^{3}\mathrm{H}(p,\gamma)^{4}\mathrm{He}$ reaction is unknown in the energy regime where the pT source operates. In our calculation, we extrapolated the cross section from the energy range of ~100 to 800 keV, where experimental data exist, down to the pT source operating beam energy of 30 keV. This extrapolation was performed by an empirical fitting without any theoretical guidance, and might have led to an overestimation of the calculated yield.

In summary, the uncertainties in the beam composition during the experimental run, target degradation and the cross section of the $^{3}\mathrm{H}(p,\gamma)^{4}\mathrm{He}$ reaction can attribute to an overestimation of the calculated yield. However, the observed gamma-ray yield of the pT source is sufficient for calibrating the SNO detector. All the effects mentioned above will not hamper the source's usefulness in SNO. In March 1998, we have constructed a second pT source. This new source will be used exclusively for calibrating the SNO detector. The first pT-calibration run in SNO will take place around the end of 1998. We plan to vary the operating conditions of this new pT source during calibration runs at SNO. This will allow us to understand the beam characteristics better. Such tests were not performed with the original pT source because it died during a gamma-ray angular measurement which we shall describe in the next chapter.

5.3 Neutron and Gamma-Ray Production by the pT Source

In this section, we shall evaluate the neutron production rate by the pT source. All the experimental results presented here are based on the data taken during the lifetime of the pT source. The pT source was operated in the quality assurance test as described in the last section. It was also used in a measurement to determine the gamma-ray angular distribution in the pT reaction. A complete description of this measurement can be found in the next chapter. The total operational lifetime of the pT source was 98.8 hours.

In all the experimental runs in which the pT source was turned on, we monitored its neutron production rate by a Bicron BC 501 liquid scintillator. Details of this neutron detector system can be found in Section 4.3.2. This monitoring was done to ensure that the neutron production rate is low enough to allow an accurate energy calibration of the SNO detector.

As we mentioned in Section 3.3.3, most of the neutrons are generated through the ^{3}H+^{3}H interaction. Although the discharge gas we loaded into the hydrogen reservoir in the pT source was initially free of any tritium, tritium would get into the discharge gas through beam-target exchange after a period of beam bombardment. Moreover, deuterium present in the discharge gas (at a 1.5×10^{-4} level) and in the target (at a 1.2×10^{-3} level) would also enhance neutron production by the source through the ^{3}H(d,n)^{4}He reaction. In the following we shall present the results of this neutron production measurement.

The fast neutron detection efficiency of the liquid scintillator was calibrated using an ^{241}Am-^{9}Be source which generates neutrons through ^{9}Be(α,n)^{12}C. The source we used has a calibrated neutron strength of $(7.1\pm0.7)\times10^3$ n s^{-1}. This source was placed on the axis of the detector with a separation of 20.6 cm. This is the same distance between the tritiated target and the neutron detector in the gamma-ray angular distribution runs. Gamma rays and neutrons generated by the source could be cleanly separated by the pulse shape discrimination technique described in Section 4.3.2 (see Figure 4.11). The net neutron count rate was extracted after the correction of a (7.1±0.1)% dead time and the subtraction of a background rate of 0.7 s^{-1}. The detection efficiency was found to be

$$\varepsilon\frac{\Delta\Omega}{4\pi} = (3.6 \pm 0.4) \times 10^{-3}. \tag{5.9}$$

Neutrons generated by the pT source would inevitably be scattered or absorbed by its construction material. Hence the detected neutron rate (R_{det}) would be less than actual pT-source generated rate (R_{gen}) by a reduction factor η_n defined as

$$\eta_n = \frac{R_{det}}{R_{gen}}. \tag{5.10}$$

To measure this reduction coefficient, the ^{241}Am-^{9}Be source was placed on the target mount inside an untritiated model source, which has the same mechanical construction as the pT source. This model source was then placed in the same orientation to the liquid scintillator as in the gamma-ray angular distribution runs. After correcting for the dead time, and comparing the neutron detection rate to that in the calibration runs without the presence of this model source, the reduction factor was found to be

$$\eta_n = 0.62 \pm 0.06. \tag{5.11}$$

With the detection efficiency and the "shadowing" coefficient determined, we extracted the neutron production rate by the pT source. The detected neutron rate in these pT-source runs was first corrected for the dead time of the detector system. Then the background neutron rate was subtracted. This net rate was subsequently corrected for the source shadowing using Eqn.(5.10).

Because there was a variation in beam intensity on target amongst different runs, the neutron production rate was normalised to the leakage current back to the target bias supply in order to provide a fair comparison. This current was a combination of the actual

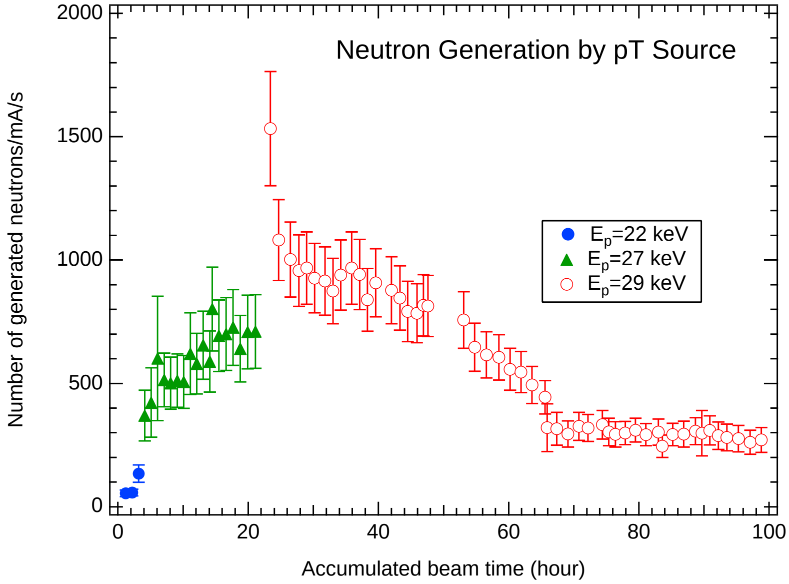

Figure 5.13: Neutron production by the pT source. The abscissa is the total beam-on-target time after the pT source has been sealed. Neutron production rate is normalised against the leakage current to the high voltage supply of the target.

ion current on target and the contribution from secondary electron emission. The reader is reminded that the pT source does not have any internal secondary electron suppression scheme because of physical constraints imposed by the SNO calibration hardware. But this leakage current would provide a fair normalisation for this time variation comparison. In Figure 5.13 we have plotted this normalised neutron production rate as a function of accumulated beam-on-target time from the time when the pT source was sealed.

Astute readers will realise that we have made two assumptions in extracting this neutron generation rate by the pT source:

1. the neutrons generated by the pT source have the same energy spectrum as fast neutron spectrum from the ^{241}Am-^{9}Be calibration source;

2. the angular distribution of neutrons generated by the pT source is isotropic as in

the ^{241}Am-^{9}Be case.

We should address the energy spectrum question first. Neutrons are produced predominantly by the ^{3}H+^{3}H interaction in the pT source. The reactions which are energetically possible in this system are:

$$^3\mathrm{H}(t,nn)^4\mathrm{He} \tag{5.12}$$

$$^3\mathrm{H}(t,n_1)^5\mathrm{He}^*(n)^4\mathrm{He} \tag{5.13}$$

$$^3\mathrm{H}(t,n_0)^5\mathrm{He}(n)^4\mathrm{He}. \tag{5.14}$$

In a measurement at a triton energy E_t=500 keV, the branching ratio for these reactions was found to be 70%:20%:10% (in the same order as they appear above) [107]. The neutron energy spectrum for each of these reactions is somewhat different. Without any final state effect, the direct three-body breakup reaction in (5.12) would yield neutrons at an average energy of $\sim \frac{1}{2} \cdot \frac{5}{6}Q$. With a Q-value of 11.3 MeV, the neutron energy spectrum from (5.12) would be a broad peak centered at about 4.7 MeV. This shape is indeed very similar to the neutron spectrum from ^{9}Be(α,n) sources [108].

Reaction (5.13) is a sequential decay proceeding through a broad ^{5}He excited state at about 2 MeV, whilst reaction (5.14) proceeds through the ground state. The ground state transition yields a ∼8-MeV monoenergetic neutron n_0, and the excited state transition yields a neutron with a broad energy distribution at a lower energy. Because of the small branching ratio for the excited state transition and the broad energy distribution of this n_1 and the subsequent decay neutron, the excited state transition would not contribute much to the uncertainty in our extracted neutron generation rate by the pT source. The secondary neutron from the ground state transition has an energy of 0.9 MeV. At this energy, the efficiency for the liquid scintillator is almost null. Therefore, the uncertainty introduced by this secondary neutron, along with the one in the excited state transition, is at most 15% if one assumes none of these secondary neutrons were detected. For the prompt neutron n_0 from the ground state transition, we estimated its contribution, along with that by a similar 14 MeV monoenergetic neutron from ^{3}H(d,n)^{4}He, to the uncertainty in the extracted pT-source neutron rate to be about 9% at E_p=29 keV.

We should now address the question of neutron isotropy. Although the neutron detector was placed in different orientations to the pT source in the quality assurance runs and in the gamma-ray angular distribution measurement, continuous beam-target exchange rendered it impossible to extract the neutron angular distribution without the presence of a second neutron detector for normalisation purposes. Wong *et al.* [107] measured the angular distribution for the ^{3}H+^{3}H system at E_t=500 keV. They found that the ground state transition neutron group is isotropic to within an accuracy of ±10%. They also found that in the neutron energy range of 2 to 7.5 MeV, the continuum neutron group is also isotropic to within an accuracy of ±20% in the laboratory angle range of 4 to 100°. For the ^{3}H(d,n)^{4}He reaction, the angular distribution is isotropic at and below the resonance [109]. Given these facts, we have made the assumption that the neutrons emitted by the pT source are isotropic.

In order to look at the time variation of the neutron production rate by the pT source more closely, we renormalised the neutron production rate for all the runs in Figure 5.13 to the same atomic beam energy at 29 keV. In other words, the rate in all of the E_p=22 keV and 27 keV runs were scaled up by a factor corresponding to the difference in cross section at that atomic beam energy to that at 29 keV. The resulting plot is shown in Figure 5.14.

In Figure 5.14, it is clear how the neutron production rate in the pT source varied over time. We can see that the neutron production rate was gradually increasing initially. This is a clear indication of beam-target exchange, as tritium in the target gets into the discharge gas stream. The neutron production rate then began to decrease. This can

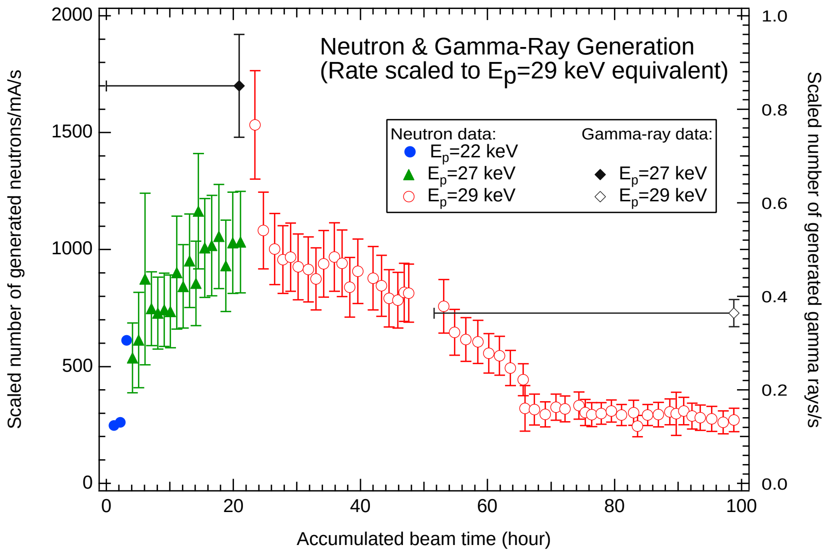

Figure 5.14: Scaled neutron and gamma-ray production by the pT source at E_p=29 keV. This plot is similar to Figure 5.13, except that the production rates for the E_p=22 keV and 27 keV runs have been scaled to the E_p=29 keV level. The scaling was done by assuming a pure atomic beam of protons or tritons since the contribution to the signals from molecular ions are much smaller. The "error bars" on the accumulated beam time for the gamma-ray results represent the time intervals in which the mean production rates were calculated.

be explained by the fact that the rate of hydrogen isotope exchange was reaching an equilibrium, and sputtering of the target became the dominant process. The target sputtering effect had caused the build-up of a thin film on the high voltage insulator in the acceleration section of the source. Under the normal operating condition, one end of this insulator is grounded whilst the other end is biased at ∼-30 kV. With a thin conductive film build-up, a leakage current flowed across the insulator and caused a high voltage breakdown. This build-up limited the lifetime of the pT source to 98.8 hours.

During the lifetime of the pT source, the beam was operated mostly at 29 keV and at ∼85 μA. The pD prototypes were operated at a much lower beam power (∼17 to 27 keV, 50 μA), and they had a much longer lifetime. The $pD - I$ and $pD - II$ sources were still operational after 200 hours and 130 hours of beam bombardment (page 104). In order to increase the operational lifetime of the pT source, we re-designed the interior construction of the target chamber the source. In this new design, an aperture is placed between the target and the high voltage insulator to prevent the sputtered target material from depositing on the high voltage insulator. In March 1998, a new pT source was constructed with this new design incorporated. The reader is referred to Appendix A for the detailed mechanical drawing of this new design.

Another evidence for this explanation of beam-target mixing and target sputtering is the decrease of the gamma-ray production rate in the pT source. As we have noted before (page 137), the average gamma-ray production rate at E_p =27 keV during the quality assurance run in the first 20.9 hours of the source's lifetime was found to be (0.67±0.11) s^{-1}. On the other hand, the rate at E_p =29 keV during the gamma-ray angular distribution measurement in the last 47.2 hours of the source's lifetime was (0.364±0.029) s^{-1} (page 178). We did not evaluate the gamma-ray production rate in between these two times because of a noise problem in the electronics system, and the gamma-ray yield could not be extracted reliably. In Figure 5.14, the gamma-ray production rate was renormalised to that for a 29-keV atomic beam. It is clear that the gamma-ray yield decreased over time.

We should now give an estimate on the neutron production rate of the *pT* source during calibration in the SNO detector. Using the highest data point in Figure 5.14, we estimated the maximum neutron generation rate to be less than $(2.50\pm0.4)\times10^3$ n s^{-1}. The uncertainty here does not include the monoenergetic neutron and the secondary neutron contributions we discussed above. However, the estimated rate quoted above should be seen as the upper limit of neutron production as it was estimated using the highest data point in the data. In Figure 5.15, the results of a Monte Carlo simulation of the SNO detector response to neutrons and gamma rays generated by the *pT* source are shown. This simulation was performed using the program SNOMAN. For a description of this program, the reader is referred to Section 7.1. In this simulation, fast neutrons generated by the *pT* source were assumed to be monoenergetic at 4.7 MeV. Full *pT* source and deployment capsule geometries were employed in this simulation, but neutron absorbers inside the source's stainless steel deployment housing were not. This is equivalent to assuming the worst possible neutron leakage into the heavy water. A neutron production rate of 2,500 s^{-1} and a gamma-ray production rate of 0.6 s^{-1} were assumed. The spectra in the figure represent about 3 hours of run time in the SNO detector. From these figures, it is clear that the neutron production rate of the *pT* source is low enough that the gamma-ray signal that a $\sim$1% statistical accuracy in calibrating the SNO detector can be achieved in just a few hours.

5.4 Post-Mortem Examination of the *pT* Source

To complete our examination of the *pT* source's performance, we opened the *pT* source after it died. This examination was performed at the tritium laboratory at Ontario Hydro

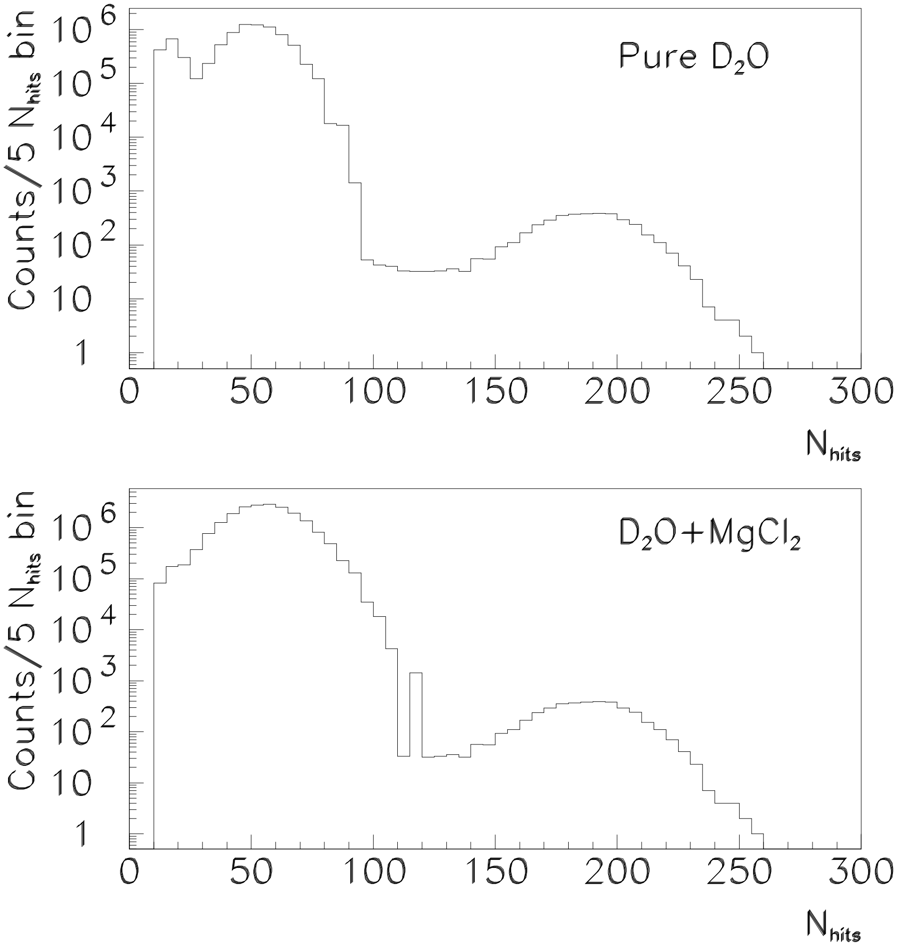

Figure 5.15: The SNO photomultiplier tube array response to neutrons and gamma rays that are generated by the pT source. In the pure D_2O running scenario, a monoenergetic 6.25-MeV gamma ray is emitted following the neutron capture by the deuteron. This is the peak centering at N_{hits} ~50 in the top panel. The other peak in the pure D_2O spectrum comes from the 2.2-MeV gamma ray emitted following the neutron capture by hydrogen in the D_2O. In the salt running scenario, neutron capture by ^{35}Cl generates a cascade of gamma rays with a total energy of 8.6 MeV. This is the reason for the broader neutron capture peak in the bottom panel. In these figures, a neutron production rate of 2,500 s^{-1} and a gamma-ray production rate of 0.6 s^{-1} were assumed. The sharp "peak" in the bottom panel arises from scaling of the Monte Carlo spectrum to correspond to the neutron production rate above. The spectra represent about 3 hours of run time in the SNO detector.

Technologies (OHT) in Toronto. Because some of the 3.3 Ci of immobilised tritium in the scandium tritide target was mobilised by the isotope exchange during the operation of the source, extra precautions were necessary. An experiment which we performed to determine the mobilisation of tritium is described below.

The *pT* source was placed inside a tritium compatible fumehood at OHT. A Scintrex 209E tritium-in-air monitor was connected to the metal seal valve of the *pT* source. This monitor has an internal pump with a pumping speed of 5 litre min^{-1}. The metal seal valve was slowly opened until the Scintrex monitor read ~10,000 μCi m^{-3}. This condition was maintained for about ten minutes before the valve was closed. During this time, about 0.5 mCi of tritium was released from the source. In order to determine accurately the total amount of tritium released from the source, the setup was modified to that shown in Figure 5.16. In this new setup, a water bubbler was used to trap the released tritium. Water is very effective in trapping mobilised tritium by forming HTO molecules. After three days of pumping in this configuration, the Scintrex reading equilibriated at ~840 μCi m^{-3}. This reading represents the tritium content in the water vapour in the bubbler. Water sample was extracted from the bubbler, and mixed with a liquid scintillator cocktail for counting in a scintillation counter. We found that the total tritium content in the water bubbler to be 2.9 mCi. That is, a total of 3.4 mCi of tritium was released from the *pT* source. This number should be viewed as the upper limit of mobilised tritium inside the *pT* source. This is because tritium in the scandium tritide target and the getter for storing the H_2 discharge gas was continuously picked up by the water vapour in the gas flow for several days.

We removed the scandium tritide target and the getter from the *pT* source after this experiment. We placed the Scintrex monitor next to the target and the getter. In the target case, the monitor did not register a reading above the background of 20 μCi m^{-3}, whereas a reading of 40 μCi m^{-3} was seen in the getter case. This represents a tritium

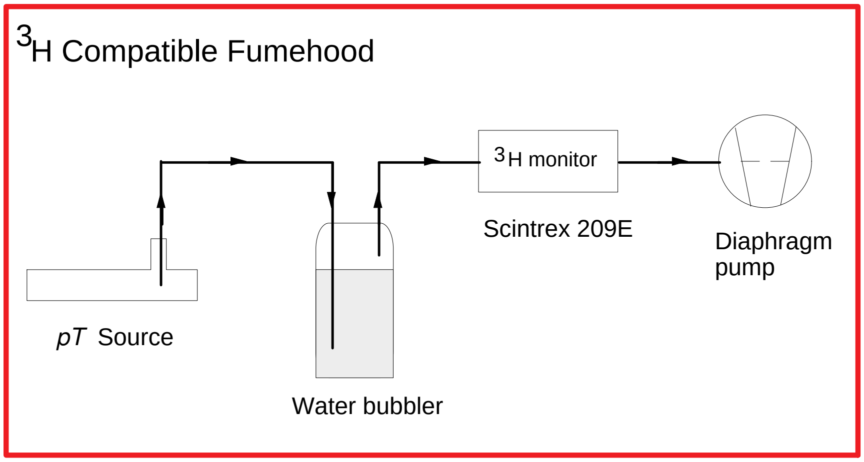

Figure 5.16: Water bubbler setup for determining the tritium release by the scandium tritide target. The amount of tritium released by the *pT* source was established by measuring the activity of the water in the bubbler.

outgassing rate of 0.1 μCi min^{-1} in the getter. Given its lower tritium outgassing rate in atmosphere, the scandium tritide target we fabricated was indeed much more “air-stable” than the getter.

Upon close inspection , we found two beam spots on the scandium tritide target. The beam spot at the centre of the target was fainter than the other one which was 0.7 cm away. We attribute this second beam spot to slight misalignment of the discharge magnet during the several runs in the source’s lifetime.

Chapter 6

Gamma-ray Angular Distribution in ^{3}H(p,γ)^{4}He at E$_p$ $\leq$29 keV

God keep me from the divinity of Yes and No... the Yea Nay Creeping Jesus, from supposing Up and Down to be the same thing as all experimentalists must suppose.

William Blake
Letter (1827)

Since the discovery of the ^{3}H$(p,\gamma)^4$He reaction by Argo *et al.* [69], various aspects of this reaction have been studied. Recently, much attention has been given to the ^{3}H$(p,\gamma)^4$He, ^{3}He(n,γ)^{4}He, ^{4}He(γ,p)^{3}H, and ^{4}He(γ,n)^{3}He reactions because a comparison of their measured total cross sections suggested possible charge-symmetry breaking in nuclear forces [110]. For the ^{3}H$(p,\gamma)^4$He reaction cross section, there is good agreement amongst different measurements for proton energies ranging from 0.1 MeV to 18 MeV [66, 67, 70, 71, 111], except for a recent measurement by Feldman *et al.* [112].

There have been several measurements of the gamma-ray angular distribution in the ^{3}H$(p,\gamma)^4$He reaction [66, 68, 69, 71, 72, 73, 74]. All of these measurements showed a predominant dipole $\sin^2\theta$ distribution. Amongst the low proton energy (E_p $\leq$1 MeV) measurements [66, 68, 72, 73, 74], however, there is a discrepancy in the measured strength of the different multipoles.

The pT source we have developed is in a unique position to contribute to our knowledge of the gamma-ray angular distribution at low energy. First of all, it has a low operating beam energy. The tritium target is sealed in an ion source, thereby eliminating the need to take extra precaution to reduce possible tritium contamination in an accelerator facility.

In this chapter, we shall summarise the present experimental status. Then we shall describe an experiment we carried out to measure the gamma-ray distribution using the pT source at an unprecedented low proton energy of 29 keV. The results of this experiment are also presented. Because of the small cross section at this beam energy, low detection efficiency and the finite lifetime of the pT source (98.8 hours), we were not able to achieve the same statistical significance in our results as other experiments that were carried out at beam energies at least an order of magnitude higher. In the future, we plan to use the pT calibration data from SNO to provide a better understanding of the angular distribution at this beam energy. The first pT calibration run in SNO will take place around the end of 1998.

6.1 Gamma-Ray Angular Distribution in ^{3}H$(p,\gamma)^4$He at Low Energy

In the following we shall summarise the present experimental status of the gamma-ray angular distribution measurements in the ^{3}H$(p,\gamma)^4$He reaction for proton energies less than 1 MeV.

Warren and Griffiths [68, 72] made the first measurement below 1 MeV. They measured the differential cross section of the ^{3}H$(p,\gamma)^4$He reaction at E_p =0.8 MeV. In this measurement, the gamma-ray angular distribution was determined to be $(\sin^2\theta + (0.13 \pm 0.03))$.

Perry and Bame [66] assumed the angular distribution $W(\theta)$ of the analytical form

$$W(\theta) \; = \; (\sin\theta + a \, \sin\theta \, \cos\theta)^2, \tag{6.1}$$

and measured the asymmetry coefficient a as a function of proton energy from 600 keV to 5.7 MeV. This asymmetry coefficient a was extracted from analytical fits of the measured angular distribution to Eqn.(6.1), and from the 60° to 120° yield ratio. They found that a increases from about 0.01 at 0.6 MeV to about 0.12 at 5.7 MeV. The authors, however, noted a possible isotropic component. They estimated that if the angular distribution were to assume the form

$$W(\theta) \; = \; b + (\sin\theta + a\,\sin\theta\,\cos\theta)^2, \tag{6.2}$$

the isotropic component b would increase linearly from 0±0.02 at zero proton energy to 0.02±0.02 at 6 MeV.

Del Bianco and Kajrys [74] measured the gamma-ray angular distribution in the proton energy range of 0.46 to 0.93 MeV. A general form of the angular distribution:

$$W(\theta) \; = \; A + B\,\sin^2\theta + C\,\cos\theta\,\sin^2\theta + D\,\sin^2\theta\,\cos^2\theta \tag{6.3}$$

was assumed in extracting the strength of different multipoles. The accuracy of their data was not sufficient to draw any definite conclusion for the D coefficient, and the authors resorted to fitting their data to the first three terms of the expression above. They found that the isotropic component A decreases smoothly from 0.016±0.002 at E_p=0.46 MeV to 0.0078±0.0006 at E_p=0.93 MeV, and the coefficient C is of the order of 0.08±0.03. This observed general behaviour of A is in disagreement with that by Perry and Bame [66]. Del Bianco and Kajrys also noted a disagreement between their extracted A/B ratio to the one from Warren and Griffiths [72]. However, they found good agreement between their extracted ratio and the ones by Meyerhof *et al.* [71] who had re-evaluated the data from Schrack *et al.* [73].

6.2 Overview of the Detector System

In our measurements, we used barium fluoride (BaF_2) crystals as our gamma-ray detectors. Pure BaF_2 crystals scintillate to alpha and beta particles, as well as to gamma rays. This high density (ρ=4.88 g cm^{-3}), non-hygroscopic material exhibits little absorption of its scintillation light, making it suitable for gamma-ray spectroscopy applications. One major attribute of BaF_2 is that it has two decay components. The fast component has a decay time of 0.8 ns, whilst the slow component's decay time is 620 ns. However, the light output for these components is only ~4% (fast) and 20% (slow) relative to NaI. Also, the wavelength of maximum emission is 225 nm (fast) and 310 nm (slow) respectively. Therefore, special ultra-violet enhanced photomultiplier tubes (PMT) must be used in order to use both components in critical timing or spectroscopic applications. The poor light output also means worse energy resolution compared to NaI. However, its higher density and atomic number compensate for this deficiency in gamma-ray spectroscopy applications.

This experiment was carried out in Cave 2 at the Nuclear Physics Laboratory (NPL) of the University of Washington. The top view of the detector system for measuring the gamma-ray angular distribution in ^{3}H$(p,\gamma)^4$He is shown in Figure 6.1. In this setup, we used three 14.5-cm diameter by 17.5 cm cylindrical BaF_2 crystals to detect the gamma rays. The three BaF_2 crystals were manufactured by two different manufacturers. Two of these crystals were manufactured by Optovac, and the other one by Engelhard/Harshaw. In the experiment, the two Optovac detectors were oriented at 45° and 135°, whilst the Engelhard detector was oriented at 90° to the beam direction. We shall denote them as D_{45}, D_{90}, and D_{135} where the subscripts signify the detectors' orientation to the beam.

Each of these crystals was optically coupled to a Hamamatsu R1251 PMT. Surrounding each BaF_2 was a 2.5-cm thick annular plastic scintillator, serving as an active cosmic veto. In front of each BaF_2 crystal was a 2.5-cm thick plastic scintillator to veto cosmic rays entering the crystals. All of these plastic vetoes were optically coupled to Hamamatsu R329 5.1-cm diameter PMTs. Each BaF_2-veto assembly was placed inside a custom-built lead shield with shielding ranging from 5 to 15 cm in thickness.

Because of the bulk of the lead shielding, the three BaF_2 detectors were not placed equidistant from the pT source. For D_{45} and D_{135}, the separation between their front

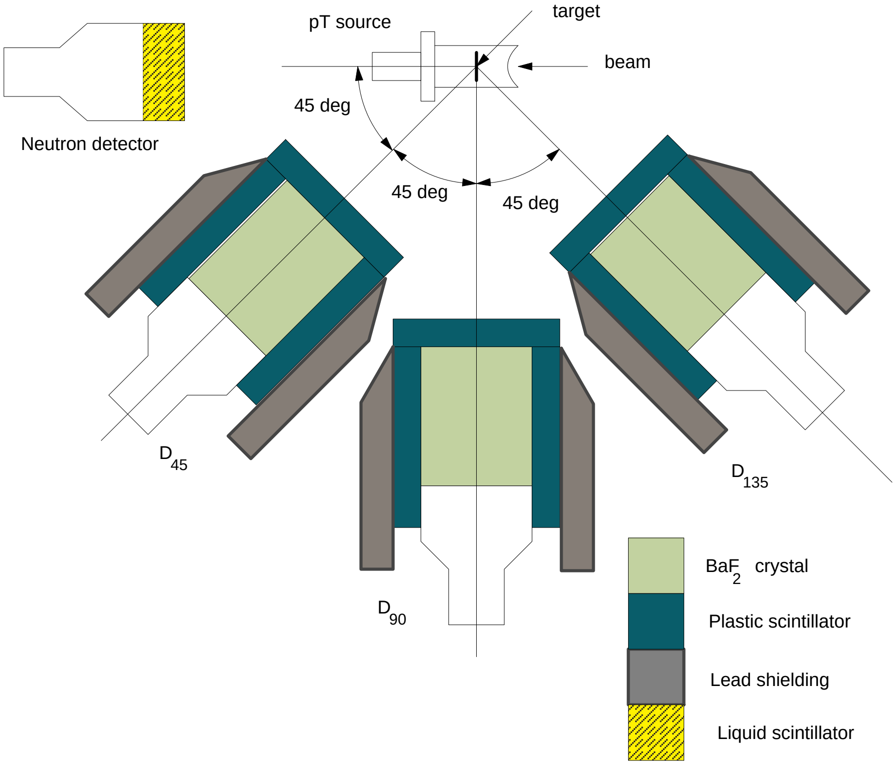

Figure 6.1: Schematic of the BaF_2 detector system. The three BaF_2 detectors were oriented at 45° (D_{45}), 90° (D_{90}), and 135° (D_{135}) to the beam direction, whilst the neutron detector was oriented at 2° to the beam direction. The separation between the centre of the target and the front face of the BaF_2 crystals was 35.6 cm for D_{90}, and 25.4 cm for D_{45} and D_{135}. The neutron detector was located at 20.6 cm from the centre of the target.

faces and the centre of the target was 25.4 cm. This distance was 35.6 cm for D_{90}. For a point source with predominant $\sin^2\theta$ angular distribution, this orientation yields approximately the same count rate in the three BaF_2 detectors.

We also monitored the time dependence of neutron output from the *pT* source through a liquid scintillator situated at 2° from the beam direction and 20.6 cm from the centre of the target. This neutron detector system was essentially the same one used in the *pD* measurement (Section 4.3.2). The only modification to the neutron detector system in this run was the removal of the cosmic veto.

The *pT* source was placed at the centre of this detector system. It was oriented such that its discharge magnet was located next to the lead shielding for D_{135}. We placed a 1.6-cm thick soft iron plate on the sides of the magnet to reduce its effect on the detectors. Even with the shielding, we saw a small reduction in the resolution of D_{135} given its close proximity to the magnet. However, we did not see any change in energy resolution in the other two detectors.

6.2.1 Electronics

Electronics setups for the BaF_2 detector system and the neutron detector are shown in Figures 6.2 and 6.3 respectively.

The electronics scheme for the three BaF_2 detectors was the same. Signals from the veto counters in each detector were summed by the resistor circuit shown in Figure 6.2. The analog sum was amplified by a Phillips 777 fast amplifier before feeding into a Phillips 711 discriminator set with a threshold corresponding to 0.5 MeV. Photomultiplier tube signals from the BaF_2 detector were first shaped and amplified by an Ortec 474 timing filter amplifier. This amplified output was fanned out to an Ortec 934 discriminator and an Ortec 572 spectroscopy amplifier. The shaped pulse was then fed to an Ortec 413A amplitude-to-digital converter (ADC). The BaF_2 discriminator output

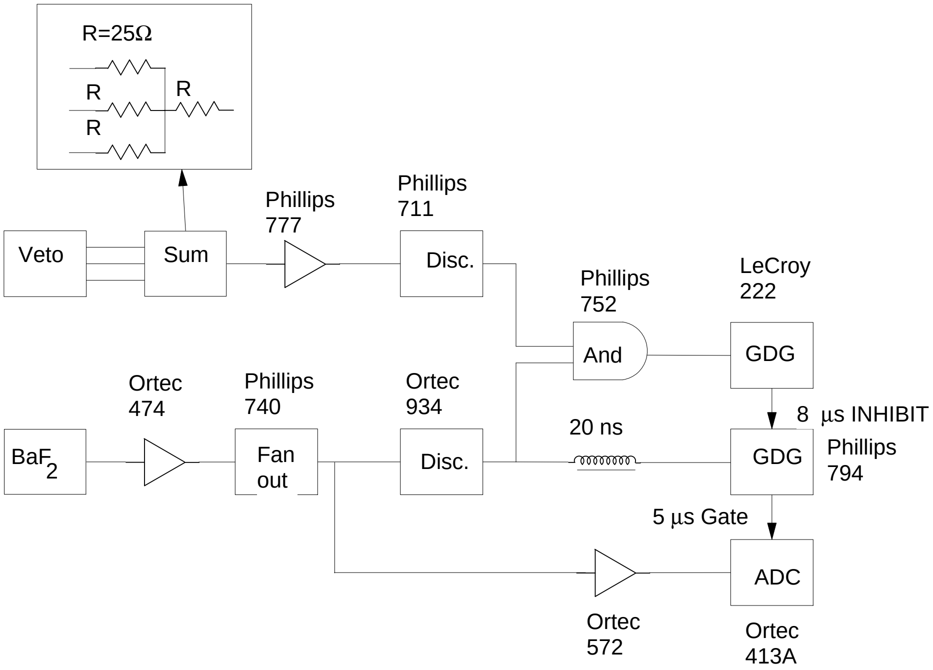

Figure 6.2: Electronics scheme for the BaF_2 detector system. This diagram shows the electronics scheme for each of the three BaF_2 detectors in the setup.

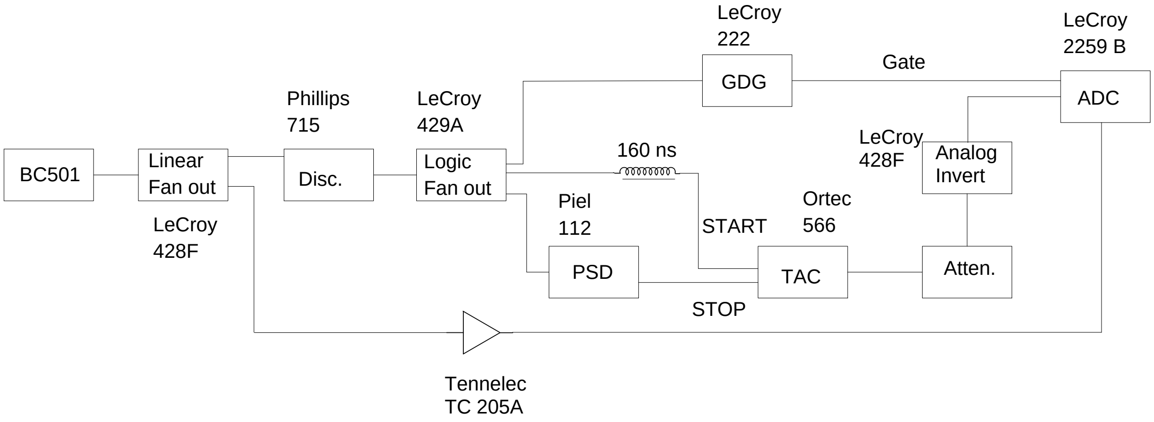

Figure 6.3: Electronics scheme for the neutron detector system in the $^3H(p,\gamma)^4He$ gamma-ray angular distribution measurement. The attenuator in the circuitry above is similar to the one shown in the insert in Figure 5.6. The resistors in this attenuator have values R1=33Ω and R2=20Ω to provide an attenuation factor of ~5 for a 50Ω load.

was used to trigger a Phillips 794 gate-and-delay generator (GDG) which provided a 5-μs gate for the ADC. However, if this discriminator output was in coincidence with the veto counter, an 8-μs inhibit pulse would be generated by a LeCroy 222 GDG, and would block the gate generation for the ADC.

We found this electronics scheme to be very efficient in vetoing cosmic ray events. In Figure 6.4, we compare the energy spectra in the three BaF_2 detectors in coincidence and in anti-coincidence with the veto counters. There was an order of magnitude difference in rate between these two modes at an energy of 20 MeV. At this energy, the background rate with the veto counter turned on was about 4 counts/MeV/hour. This was about a factor of three better than that in the quality assurance run described in the last chapter. This reduction in background rate was attributed to better passive shielding of the detector.

The electronics scheme for the neutron detector in this experiment was similar to the *pD* testing setup (Section 4.3.2) except that the veto counter was removed. Readers are referred to that section for a description of the operational characteristics of this system. We found that this removal of the veto counter did not change the background neutron rate in the detector significantly. A discussion of the neutron production by the *pT* source can be found in Section 5.3.

6.3 Monte Carlo Simulation of the Experiment

6.3.1 Simulation of BaF_2 Detector Response

We used GEANT [92] to simulate the response of the BaF_2 spectrometers. Active and passive shieldings for each of the spectrometers were put into the program. The efficiency over the solid angle subtended by each detector Ω_{det} was then calculated for an isotropic source located at the centre of the detector system. In Table 6.1, we have listed this

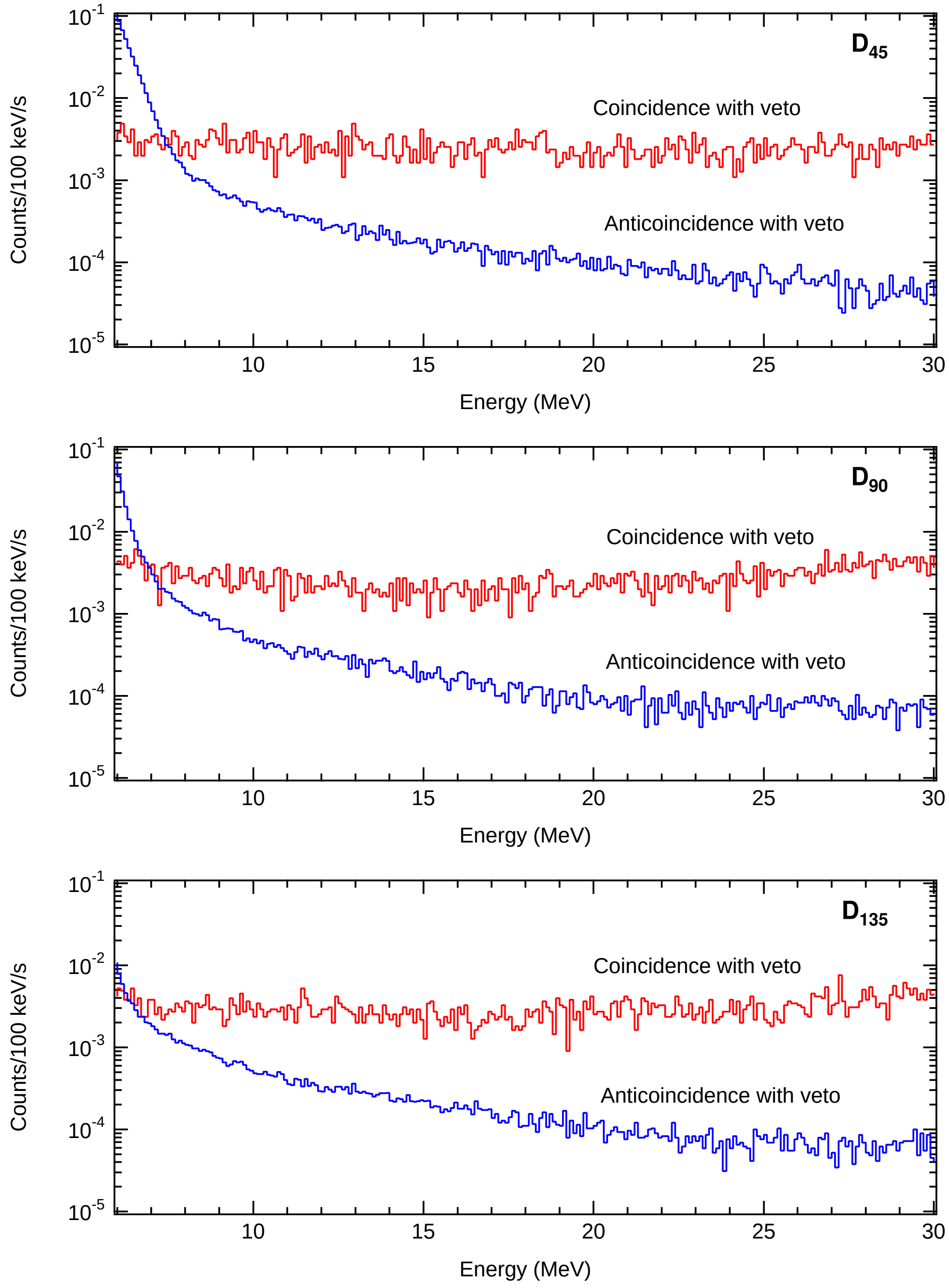

Figure 6.4: Background spectra compared to spectra in coincidence with the cosmic veto. The coincidence data was taken over about 90 minutes, whilst the background data was taken over about 100 hours.

Detector	$\frac{1}{4\pi}\int_{\Omega_{det}} \varepsilon \, d\Omega$	$\frac{1}{4\pi}\int_{\Omega_{det}} \varepsilon \, \eta_\gamma(\theta) \, d\Omega$
D_{45}	$(8.35\pm0.07)\times10^{-3}$	$(3.39\pm0.04)\times10^{-3}$
D_{90}	$(4.84\pm0.05)\times10^{-3}$	$(3.94\pm0.04)\times10^{-3}$
D_{135}	$(8.35\pm0.07)\times10^{-3}$	$(8.06\pm0.06)\times10^{-3}$

Table 6.1: GEANT-calculated efficiency for the three BaF_2 detectors. The first numerical column represents the proportion of 19.8-MeV gamma rays from a bare source that would deposit more than 15 MeV of energy in the detectors without triggering the veto counter. Absorption by the *pT* source target chamber is included in the second column.

efficiency for 19.8-MeV gamma rays depositing more than 15 MeV of energy in the three BaF_2 detectors without triggering the respective veto counter.

Gamma-ray attenuation by the target mount of the *pT* source must be understood in order to reliably extract the angular distribution in the *pT* reaction. In Figure 6.5, the target mount geometry programmed into GEANT is shown. Also shown in the figure is the GEANT calculated penetration coefficient $\eta_\gamma(\theta)$ for 19.8-MeV gamma rays. This is the proportion of gamma rays emerging from the target mount without any interaction. It is clear from the figure that the biggest attenuation comes in the forward beam direction. In fact, the penetration factor η_γ is only ~0.40 for D_{45}, whilst that for D_{135} is ~0.97.

To calculate the response function of the BaF_2 detectors in the presence of the *pT* source, the source was placed in the same orientation to the detectors as in the experiment. For each of the detectors, we simulated its response to isotropic and monoenergetic 19.8-MeV gamma rays originating from the centre of the target surface. In Table 6.1, the detection efficiency in this configuration is compared to the bare source case. This response function, normalised to the total number of gamma rays simulated, is shown for each of the detectors in Figure 6.6.

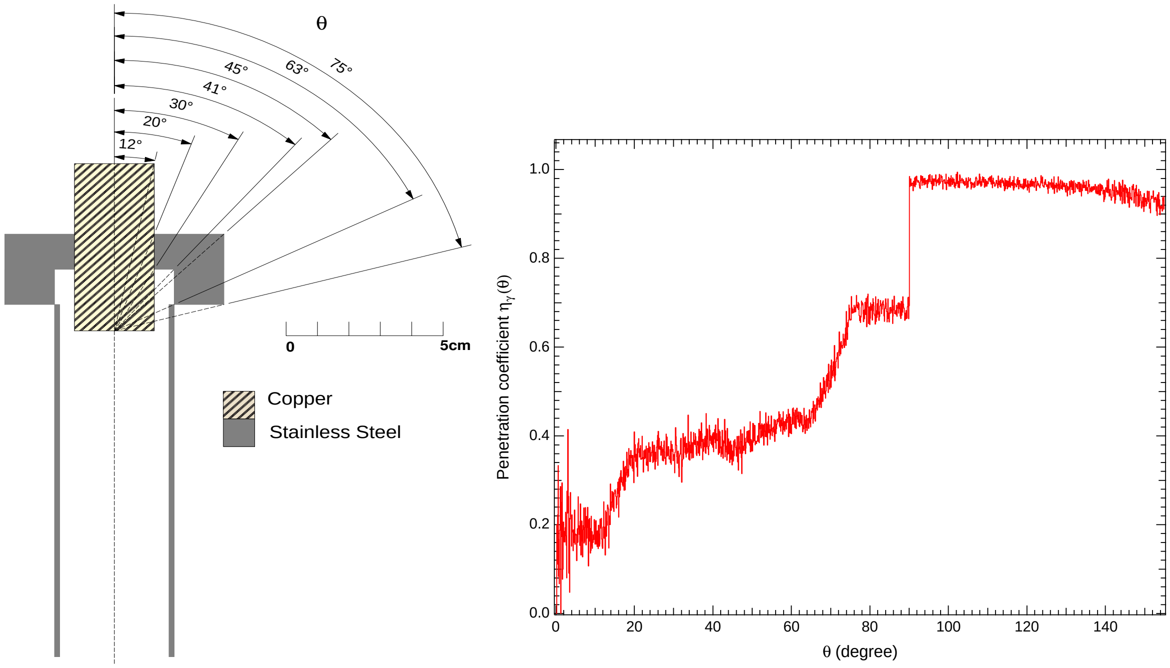

Figure 6.5: Attenuation of 19.8-MeV gamma rays by the target chamber. The left panel shows the geometry of the target mount used in calculating the attenuation as a function of angle θ. This attenuation function is shown in the right panel.

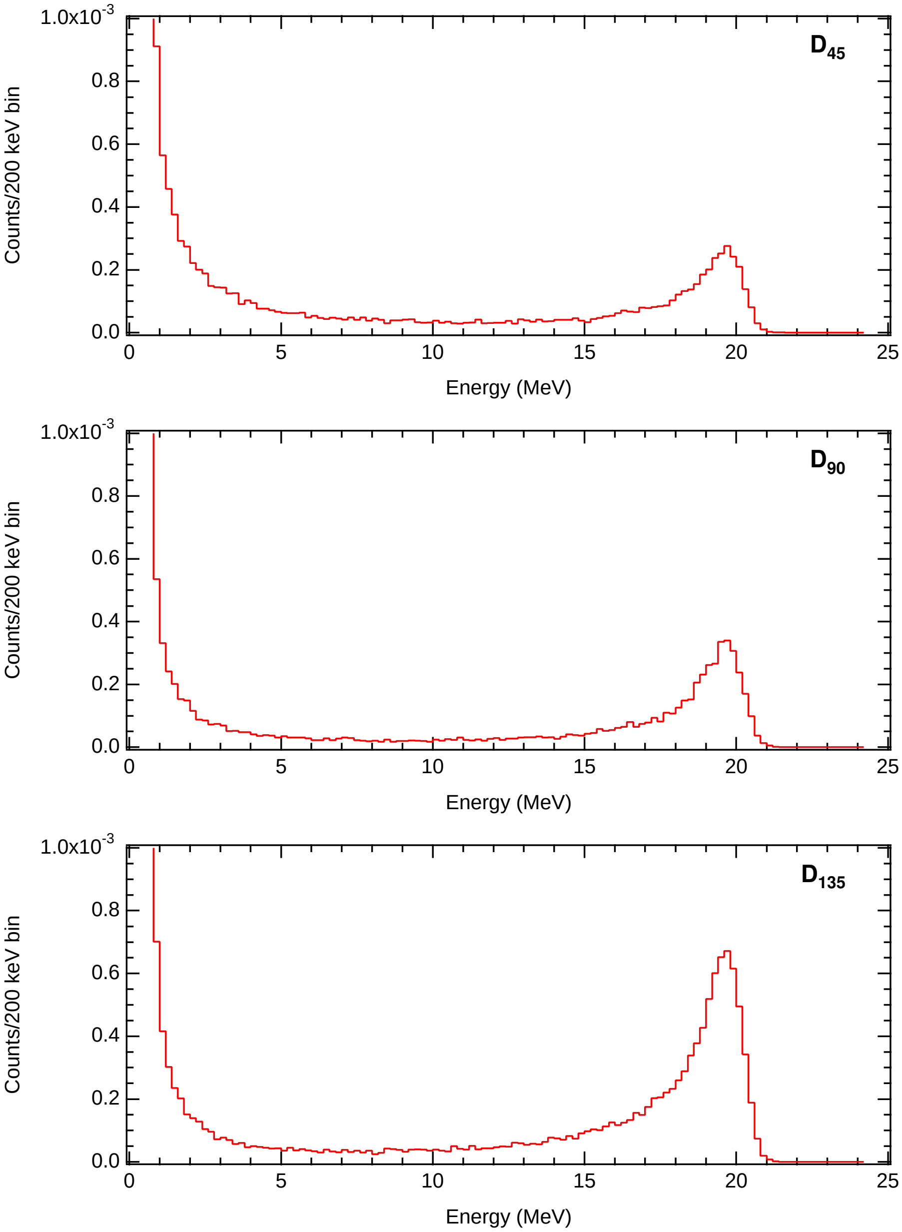

Figure 6.6: Simulated BaF_2 spectrometer response function to isotropic 19.8-MeV gamma rays. The differences in the relative heights amongst the three detectors are due to gamma-ray attenuation by the target chamber and the source-detector spatial separation.

6.3.2 Experimental Verification of the Monte Carlo Simulation

One has to verify experimentally that the detector efficiency and the gamma-ray absorption by the target chamber are calculated correctly by GEANT. In Appendix B, we have summarised an investigation on GEANT's reliability by comparing our GEANT calculations for a variety of detectors to published references. In the following, we shall summarise the experiments we have performed to concurrently understand the BaF_2 detectors' performance and the accuracy of our GEANT Monte Carlo code.

Without a readily available energy source with an energy close to 19.8 MeV, we measured the gamma-ray detection efficiency of a strength calibrated $^{13}C(\alpha,n)^{16}O^*$ source, which generates 6.13-MeV gamma-rays through $^{16}O^*$ de-excitation. We took energy spectra with this source placed at the centre of the detector system. At the time of this experiment, this source had a strength of $(4.07\pm0.33(3\sigma))\times10^3$ γ s^{-1}. Because of its high neutron output, we took other energy spectra with a 2.5-cm thick slab of lead placed between the source and the detectors to extract the neutron induced spectra. By comparing these two types of spectra, the gamma-ray line shape could then be extracted for each detector. In Figure 6.7, we show how the GEANT generated line shape compared to an experimentally determined spectrum. After correcting for the effects of lead absorption, neutron induced background and dead-time, the number of detected gamma rays and efficiency (ε_{exp}) were extracted. The average ratio between ε_{exp} and the GEANT calculated efficiency (ε_{MC}), $\varepsilon_{exp}/\varepsilon_{MC}$, was found to be (1.01 ± 0.04).

We measured the penetration function $\eta_\gamma(\theta)$ for the 6.13-MeV gamma-ray line in the three BaF_2 detectors. We placed this source inside an untritiated model *pT* source, whose mechanical construction was identical to the real *pT* source, at the location where the tritiated target would be mounted. The gamma-ray detection rate was then measured experimentally in a procedure similar to the efficiency measurement above. By

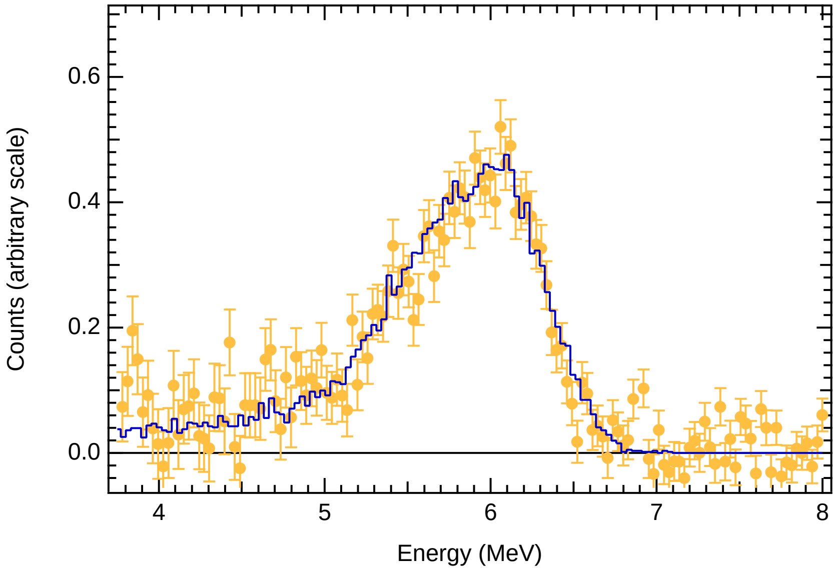

Figure 6.7: Comparing GEANT generated gamma-ray line shape to measurement. The data points correspond to the 6.13-MeV line from a calibrated ^{16}O* de-excitation source. The solid histogram is the GEANT generated line shape.

comparing this detection rate and the one without the presence of the model source, the average penetration factor over the solid angle subtended by the detectors $\langle \eta_\gamma(\theta) \rangle_{\Omega_{det}}$ was then extracted. In Figure 6.8, we compare the GEANT calculated $\langle \eta_\gamma(\theta) \rangle_{\Omega_{det}}$ for 6.13-MeV gamma rays to our measurement. The average percentage difference between our measured values and the simulated ones is $\sim \pm 3\%$.

In the pT data analysis, the most important parameter supplied by the Monte Carlo is $\frac{1}{4\pi}\int_{\Omega_{det}} \varepsilon\, \eta_\gamma(\theta)\, d\Omega$, which is the detection efficiency with the attenuation effect by the target mount included. The measurements above, however, sought to isolate ε and $\eta_\gamma(\theta)$ in order to test different parameters calculated by GEANT. To understand the combined uncertainty in $\frac{1}{4\pi}\int_{\Omega_{det}} \varepsilon\, \eta_\gamma(\theta)\, d\Omega$, we determined the gamma-ray strength of the α-^{13}C source (placed in the model source) by correcting the number of detected gamma-rays in each detector by the corresponding $\frac{1}{4\pi}\int_{\Omega_{det}} \varepsilon\, \eta_\gamma(\theta)\, d\Omega$ factor. We found that the extracted and the actual source strength differed by $\leq$5%. That is, the uncertainty associated with

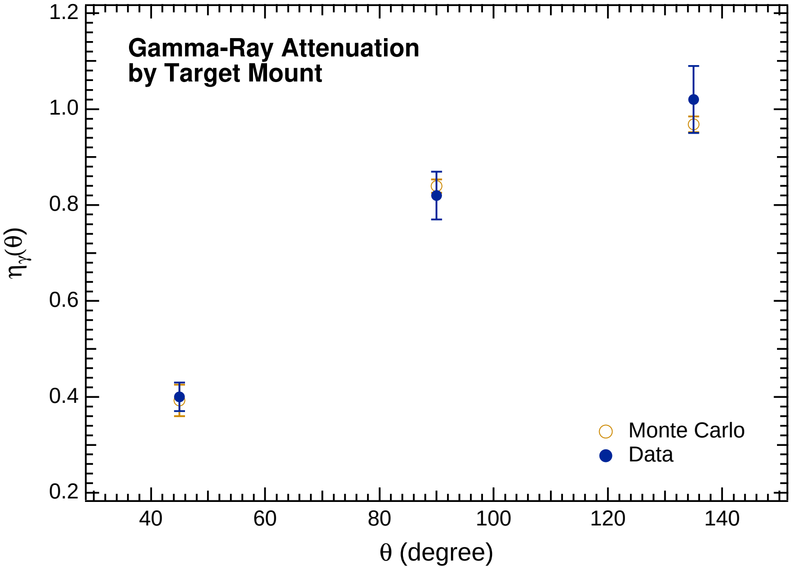

Figure 6.8: Measured target mount gamma-ray attenuation function $f(\theta)$. The measurement was made using a calibrated ^{16}O* 6.13-MeV de-excitation gamma-ray source.

$\frac{1}{4\pi}\int_{\Omega_{det}} \varepsilon\, \eta_\gamma(\theta)\, d\Omega$ is ±5%.

6.4 Data Collection and Analysis

6.4.1 Data Collection

Cosmic background spectra were first collected over a period of 100 hours. In Figure 6.9, we show the background energy spectrum for the three BaF$_2$ detectors. The background was fitted to an exponential in the same form as Eqn.(5.4).

Measurement of the gamma-ray angular distribution in the ^{3}H$(p,\gamma)^4$He reaction was made at a beam energy of 29 keV. We used the ^{137}Cs(0.662 MeV), ^{207}Bi(0.569 MeV), ^{207}Bi(1.063 MeV), ^{12}C*(4.44 MeV), and ^{16}O*(6.13 MeV) gamma-ray lines to calibrate the BaF$_2$ detectors once every 6 to 8 hours. To monitor the gain of the detectors during the measurement better , we used the 4.44-MeV and the 6.13-MeV lines to provide a partial calibration every hour. The data set in the following analysis represents 41.0 hours of

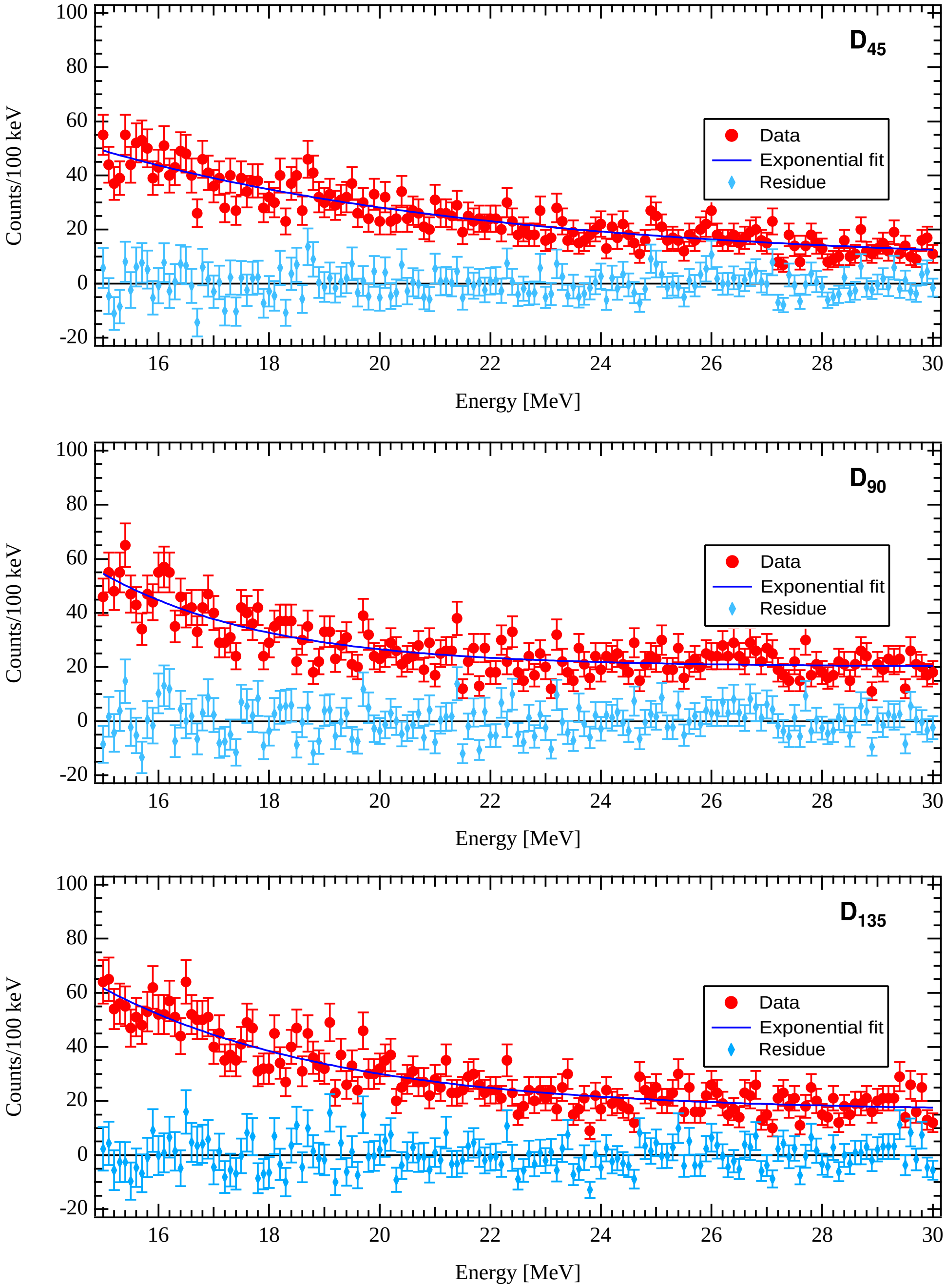

Figure 6.9: The background energy spectra in the region of interest. Data from 15 to 30 MeV were fitted to an exponential form.

beam-on data. We were not able to take more data because the pT source died after a total lifetime of 98.8 hours. This 41.0 hours of data was taken during the last 47.2 hours of the source's lifetime. The reader is referred to page 146 for a discussion of this lifetime problem.

As in the pD prototype testing, we estimated the beam current on target from the getter temperature (page 104). The total beam current during the run was estimated to be (85±30) μA, and the H_2 partial pressure was estimated to be $(3\pm1)\times10^{-3}$ mbar.

6.4.2 Extracting the Gamma-Ray Signal

The energy spectra from each individual beam-on run were first energy calibrated using the calibration data. The energy calibration lines were linear up to the 6.13-MeV calibration end-point. This line was then extrapolated to the region of interest. In Section 6.4.3 we shall give an estimate on the systematic uncertainty associated with this extrapolation.

All the energy-calibrated spectra were subsequently corrected for the system deadtime (~5%) and summed together. In Figure 6.10, the sum spectra for all three BaF_2 detectors are shown. The 15 to 30 MeV energy window of the sum spectra were then fitted to a functional form:

$$y(E;\theta) \;=\; N_{Bgd}(\theta)y_B(E;\theta) \,+\, N_\gamma(\theta)y_\gamma(E;\theta) \tag{6.4}$$

where $y_B(E;\theta)$ is the fitted background function in Figure 6.9, $y_\gamma(E;\theta)$ is the GEANT generated response function for the respective detector as shown in Figure 6.6, and $N_{Bgd}(\theta)$ and $N_\gamma(\theta)$ are the fitted amplitudes. In particular, the amplitude $N_\gamma(\theta)$ represents the total number of gamma rays generated by the pT source assuming that its angular distribution is isotropic. This fitting was done using the program MINUIT [104]. In Table 6.2, we have summarised the fitted values for $N_{Bgd}(\theta)$ and $N_\gamma(\theta)$, along with

D_{45}:		$N_{Bgd}(\theta)$	$N_\gamma(\theta)$
	Fitted values	0.957±0.018	$(3.5\pm1.0)\times10^4$
	Covariance	3.4×10^{-4}	-9.9×10^1
	Matrix	-9.9×10^1	1.0×10^8
	Correlation	-0.54	
	χ^2_ν	0.65	
D_{90}:		$N_{Bgd}(\theta)$	$N_\gamma(\theta)$
	Fitted values	0.824±0.017	$(6.86\pm0.76)\times10^4$
	Covariance	3.0×10^{-4}	-5.7×10^1
	Matrix	-5.7×10^1	5.8×10^7
	Correlation	-0.44	
	χ^2_ν	1.30	
D_{135}:		$N_{Bgd}(\theta)$	$N_\gamma(\theta)$
	Fitted values	0.886±0.025	$(3.40\pm0.44)\times10^4$
	Covariance	6.1×10^{-4}	-5.8×10^1
	Matrix	-5.8×10^1	2.0×10^7
	Correlation	-0.53	
	χ^2_ν	1.31	

Table 6.2: χ^2 minimisation results for signals seen in the three BaF_2 detectors. The fittings were performed using the program MINUIT [104]. The uncertainties in fitted $N_{Bgd}(\theta)$ and $N_\gamma(\theta)$ are 1σ uncertainties extracted from MINUIT χ^2 minimisation.

other statistical parameters extracted from the fits.

Given that the reduced χ^2 in the fits are ~1, the fits appeared to be believable. However, we have to verify that the "1σ" uncertainties given by MINUIT in Table 6.2 are good estimates to a 68.3% confidence level for the fitted parameters due to the smallness of the signal. To make this verification, we took the fitted spectrum from each detector, and simulated 10,000 spectra by generating a normal deviate on a bin-by-bin basis in the region of fitting. Each of these simulated spectra was then subjected to the same fitting procedure as the real data. In Figure 6.11, the scatter plots shown are the distributions of the fitted $N_{Bgd}(\theta)$ and $N_\gamma(\theta)$ amplitudes for these 10,000 simulated sets. Also shown as solid and dashed curves in the figure are the joint 68.3% and 95.4%

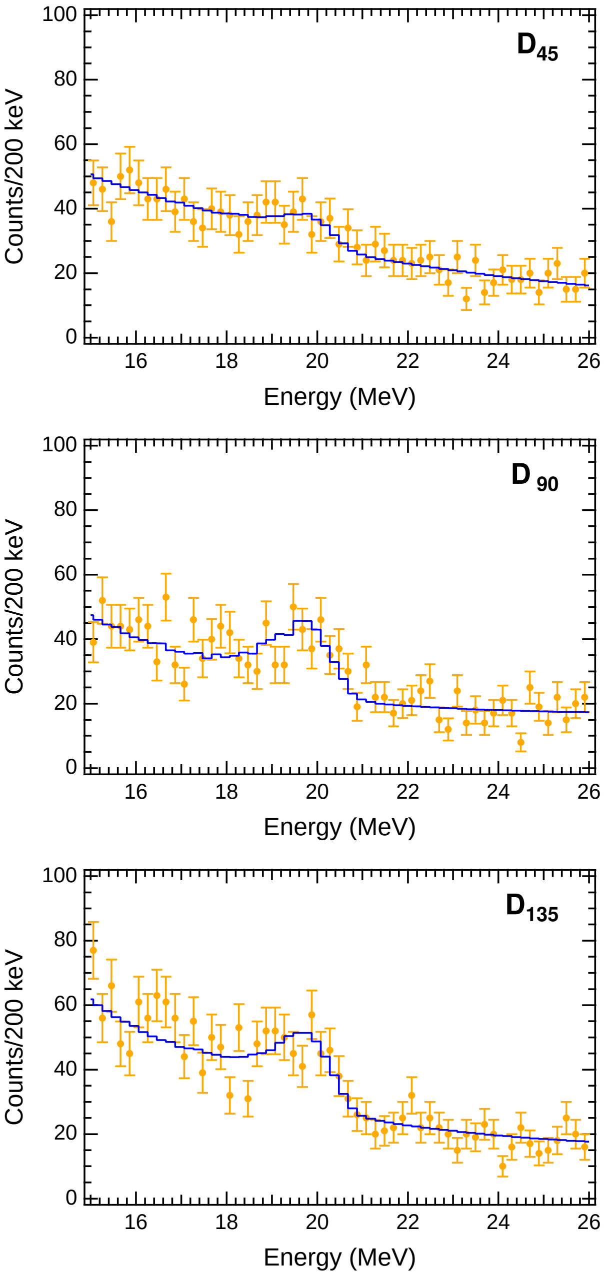

Figure 6.10: Fitting background and GEANT simulated response function to BaF_2 data. Data points constitute the total beam-on spectra, and the histograms are simultaneous fits of the background and the GEANT simulated response to the data. See text for more details.

	D_{45}	D_{90}	D_{135}
$N_\gamma(\theta)$	$(3.53\pm0.88)\times10^4$	$(6.85\pm0.69)\times10^4$	$(3.46\pm0.37)\times10^4$
χ^2_ν	0.62	1.54	0.81

Table 6.3: χ^2 minimisation results on separate fittings of the background and the photopeak. The results here agree very well with the background plus photopeak combined fitting results in Table 6.2.

confidence level ellipses calculated using the MINUIT-fitted statistics on the real data. The comparison in the figure convinced us that the 1σ statistical uncertainties quoted by MINUIT are reasonable estimates.

We also checked the consistency of the combined peak plus background fit in Eqn.(6.4) by "separating" the fit. For the data in each detector, we first fitted the spectrum outside the peak region in the energy range of 22 to 30 MeV to the background shape ($y(E;\theta) = N_{bgd}(\theta)y_B(E;\theta)$). The fitted background was then subtracted from the sum spectrum in the energy range of 15 to 30 MeV. The background-subtracted spectrum ($y_{sub}(E;\theta)$) was then fitted to the response function ($y_{sub}(E;\theta) = N_\gamma(\theta)y_\gamma(E;\theta)$) in the region of the peak (15 to 22 MeV). In Table 6.3, we summarise the fitted gamma-ray amplitudes ($N_\gamma(\theta)$) in this combined fitting. As shown in the table, the results from this separated fit agree very well with those in the combined fit in Table 6.2.

6.4.3 Systematic Uncertainties

In the last section, we investigated the statistical uncertainties associated with extracting $N_\gamma(\theta)$. We shall focus our attention on the systematic uncertainties in the following.

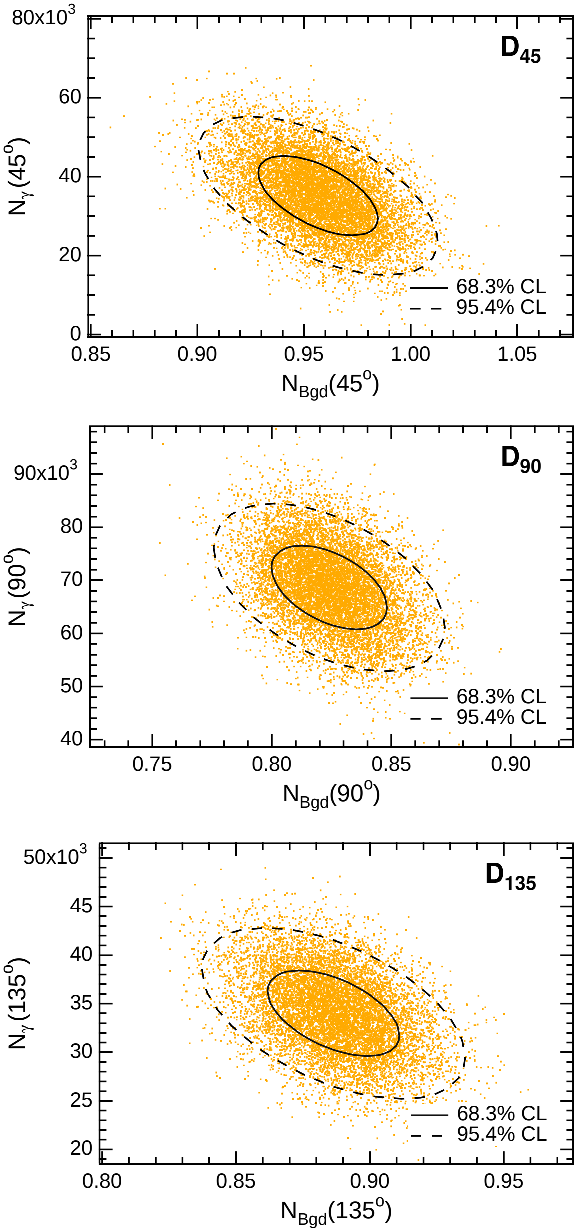

Figure 6.11: Comparing confidence intervals from χ^2 minimisation to fitted parameters in Monte Carlo simulated data sets.

Source-Detector Orientation

Because of the close proximity between the pT source and the detectors, a small uncertainty in their relative orientation can translate into a huge uncertainty in $N_\gamma(\theta)$. The BaF_2 detectors were mounted on a carefully machined table. We estimated the uncertainty associated with the source-detector distance and angular orientation to be <0.2 cm and $<2°$ respectively. We should point out that this estimation of the angular uncertainty includes the beam deflection by scattering effect. We ran Monte Carlo simulations to estimate the systematic uncertainty associated with these two correlated parameters. This uncertainty was found to be ±6%.

Energy Calibration and Resolution

The 6.13-MeV $^{16}O^*$ de-excitation line had the highest energy of all the calibration sources readily available to us. The calibration uncertainty at this energy was <1%. We chose a more conservative 2% uncertainty in the calibrated energy at 19.8 MeV, given the large extrapolation in energy.

The width of the Monte Carlo generated 19.8-MeV line would have an effect on the fitted amplitude $N_\gamma(\theta)$. Also, we have made an assumption of $1/\sqrt{E}$ variation in the detectors' energy resolution. We chose an uncertainty of 1% in *absolute* full-width-at-half-maximum (FWHM) resolution. This is equivalent to assuming a >20% uncertainty in the energy resolution at 19.8 MeV.

We ran Monte Carlo simulations to estimate the systematic effect in $N_\gamma(\theta)$ due to the two correlated uncertainties above. By shifting the data spectra by ±2% and smearing the Monte Carlo generated spectra by 1% in absolute FWHM resolution simultaneously, we refitted the spectra in the same manner outlined in Section 6.4.2. The combined uncertainty associated with $N_\gamma(\theta)$ was estimated to be ±7%.

	Item	Error
I	Source-detector orientation	±6%
II	Energy calibration & resolution	±7%
III	Finite geometry correction	±3%
IV	Monte Carlo efficiency & target mount absorption	±5%
	$\sqrt{\Sigma(\text{error})^2}$	±10.9%

Table 6.4: Summary of systematic uncertainties in the extracted BaF_2 signals. See text for a more detailed discussion.

Finite Geometry Correction

In extracting $N_\gamma(\theta)$, we used the simulated response function to isotropic gamma rays emitted from the pT source. A correction has to be made to this function because the emitted gamma rays do not have an isotropic distribution and the attenuation by the target mount depended on the real distribution. To estimate the magnitude of this effect, we simulated the response function for a pure $\sin^2\theta$ gamma-ray angular distribution. By comparing this response function and the one for isotropic gamma rays, we estimated the uncertainty in $N_\gamma(\theta)$ to be ±3%.

Monte Carlo Efficiency and Target Mount Absorption

Based on the measurements we made using the 6.13 MeV source , the target absorption coefficient as a function of angle relative to the detector was measured (see Section 6.3.2). The uncertainty associated with Monte Carlo calculation of $\frac{1}{4\pi}\int_{\Omega_{det}} \varepsilon\, \eta_\gamma(\theta)\, d\Omega$ was estimated to be ±5%.

If we add all the quoted systematic uncertainties above in quadrature, we would get a total systematic uncertainty of ±10.9% in the extracted $N_\gamma(\theta)$. In Table 6.4, we have summarised the systematic error budget as discussed above.

	D_{45}	D_{90}	D_{135}
$\langle\theta\rangle$	46.2±4.7	90.7±3.4	133.8±4.6
$R_\gamma(\theta)$	0.51±0.18	1.00±0.16	0.50±0.12

Table 6.5: Normalised gamma-ray output for all three BaF_2 detectors assuming an isotropic source.

6.4.4 Gamma-Ray Angular Distribution at $E_p \leq$29 keV

Because of gamma-ray attenuation by the target mount, the average acceptance angle at each BaF_2 detector is slightly different from its angular orientation relative to the pT source. In Table 6.5, we have summarised the average acceptance angle $\langle\theta\rangle$ for Monte Carlo events that deposit more than 15 MeV of energy in the detectors. In the same table, we have summarised the relative amplitudes, $R_\gamma(\theta)$, normalised to the signal at D_{90}. It should be noted that we did not add the systematic uncertainty in the normalisation of $N_\gamma(90°)$, because the systematic uncertainty would cancel out when $N_\gamma(90°)$ is normalised to itself. We should also point out that because the data points in the BaF_2 energy spectra are distributed with a Poisson distribution, the area under the fitted curves in Figure 6.10 would be underestimated by an amount of $\simeq \chi^2_{min}$, where χ^2_{min} is the χ^2 of the fit [105]. We found that this effect underestimates the signals in all three BaF_2 detectors at the same level of ~20%. So this effect would also cancel out in the normalisation.

We extracted the gamma-ray angular distribution for the $^3H(p,\gamma)^4He$ reaction using the first two terms in Eqn.(6.3). We used the program MINUIT [104] to fit $R_\gamma(\theta)$ to this function. The average acceptance angle $\langle\theta\rangle$ was used as the independent variable in the fit. We found that

$$\begin{aligned} A &= -0.04 \pm 0.23 \\ B &= 1.04 \pm 0.35. \end{aligned} \tag{6.5}$$

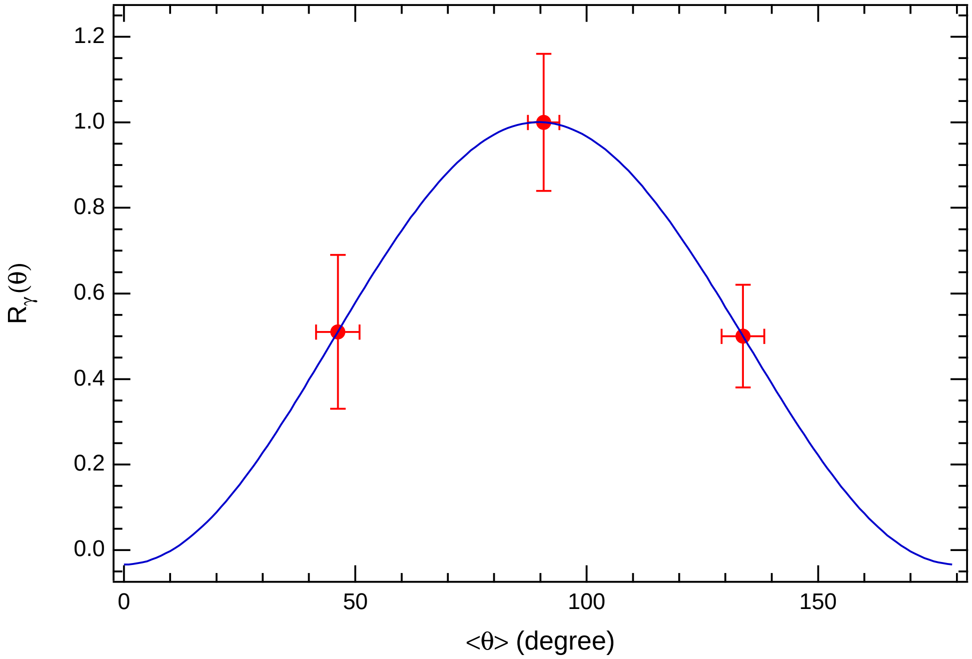

Figure 6.12: Gamma-ray angular distribution of the ^{3}H$(p,\gamma)^{4}$He reaction at $E_p \leq 29$ keV. The solid curve shown was a fit of the data to the function $W(\theta) = A + B\sin^2\theta$. The average acceptance angle $\langle\theta\rangle$ was used as the independent variable in the fit.

The covariance matrix from this fitting is shown in Table 6.6. In Figure 6.12, we have plotted our measured angular distribution along with the fit. We tried keeping the third term in the fit, but the accuracy of our data was not sufficient to draw any definite conclusion on the coefficient C.

We have shown the gamma-ray angular distribution for different partial wave captures in Table 3.1. When comparing to the angular distribution we measured in Figure 6.12, our results appear to be consistent with the picture of a predominant E1 capture of p-wave protons at $E_p \leq 29$ keV. This observation is consistent with other measurements made at much higher energies [68, 66, 72, 73, 74].

	A	B
A	0.061	-0.082
B	-0.082	0.13

Table 6.6: Covariance matrix for fitting the gamma-ray angular distribution in the *pT* reaction to the first two terms in Eqn.(6.3).

Using the fitted A and B coefficients in Eqn.(6.5) and their covariances in the covariance matrix in Table 6.6, the ratio A/B was found to be (-0.04±0.23) in this experiment.

The ratio A/B should be a positive quantity. Given the large uncertainty in this ratio, we used a Bayesian approach to estimate the upper limit on this ratio, assuming a Gaussian distribution in its uncertainty [100]. We found an upper limit of 0.35 in A/B at the 90% confidence level. In Figure 6.13, we compare this upper limit of A/B to previous measurements made at E_p <1 MeV. The s-wave contribution to the angular distribution is expected to increase as the beam energy decreases. Therefore, our results set an upper limit on A/B at higher beam energies.

The large uncertainty in this ratio is primarily due to the fact that a measurement at 0° or 180° was not performed. Such a measurement would improve the sensitivity to the isotropic coefficient A, as the $\sin^2\theta$ contribution is null at these angles. A signal above the background at these angles would allow us to determine the strength of the isotropic component to a better accuracy. Also, a target sputtering effect in the *pT* source (page 146) limited its lifetime to 98.8 hours, making further measurements at different angles impossible. In March 1998, we constructed a second *pT* source to be used exclusively for energy calibration at SNO. Energy calibration data from this source at SNO will provide a second measurement of this angular distribution. We estimated that a statistical limit of about 4×10^{-2} in A/B can be reached in 10 hours of running, assuming a gamma-ray production rate of $0.5\ \gamma\ s^{-1}$.

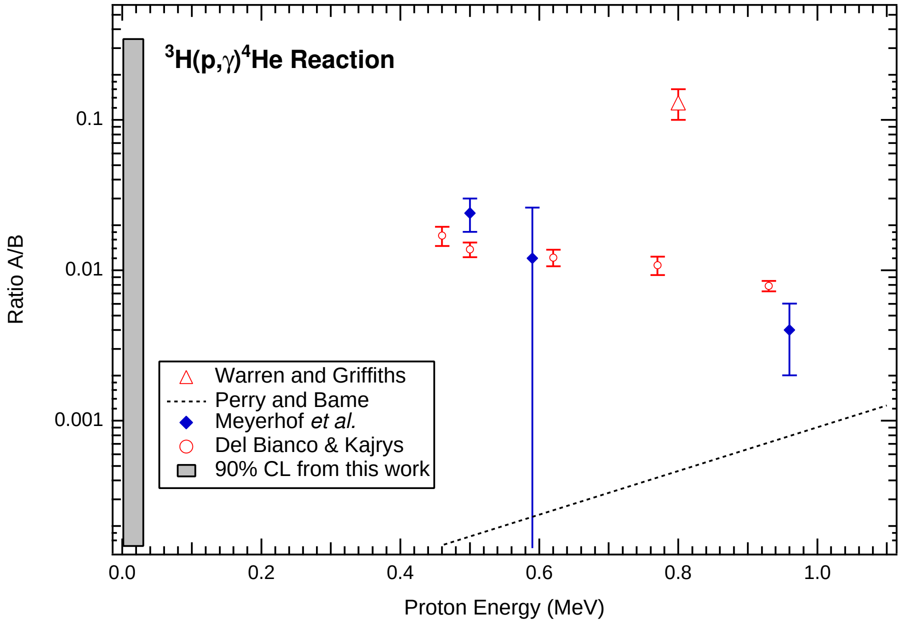

Figure 6.13: Comparing the 90% confidence limit of A/B from this work at $E_p \leq 29$ keV to previous works. Because the s-wave contribution is expected to be lower at higher energies, our result sets the upper limit for A/B. The accuracy in A/B can be improved significantly if measurements were made at $\theta = 0°$ or $180°$. The lifetime of the pT source (98.8 hours) limited the total run time of this experiment.

As a final note, the average gamma-ray yield in this angular distribution measurement at E_p =29 keV was (0.364±0.029) s^{-1}. This number has been corrected for the 20% count underestimation due to χ^2 fitting of Poisson distributed data (page 174). During the quality assurance run, the gamma-ray yield at E_p =27 keV was found to be (0.67±0.11) s^{-1} (page 137). The quality assurance run data was taken during the first 20.9 hours of the source's lifetime, whilst the angular distribution result represents the last 47.2 hours of its lifetime. This decrease in the gamma-ray yield is a clear indication of target degradation and hydrogen isotope exchange. The reader is referred to Section 5.3 for a discussion of these effects.

Chapter 7

Energy Response of the SNO Detector

Between the conception,
And the creation,
Between the emotion,
And the response,
Falls the Shadow.

T. S. Eliot
The Hollow Men, sct. 5

In this and the next chapter, we shall tackle several energy calibration issues that are important to reliable physics extraction from the SNO data. We shall also address how monoenergetic gamma-ray sources like the pT source can be used to understand the energy response of the SNO detector. In the following, we shall briefly outline our strategy for these two chapters.

This work on understanding various energy calibration issues was done through Monte Carlo simulations using the <u>SNO</u> <u>M</u>onte Carlo and <u>AN</u>alysis (SNOMAN) [113, 114] program. In Section 7.1, we give a brief description of SNOMAN and several issues that are related to this study.

In Section 7.2, we studied the energy response of the SNO detector to electrons and gamma rays in the pure D_2O and the Neutral Current Detector (NCD) array[1] installed running scenarios. Monoenergetic electron and gamma-ray events were generated for both running scenarios using SNOMAN. The energy dependence of the number of fired PMTs (N_{hits}) and the electronically calibrated charge (N_{pe}) in these events were studied without

---

[1] For a brief description of the NCD array, the reader is referred to page 37.

making any correction. The results of this "zeroth order" analysis are summarised in Section 7.2.1. In Section 7.2.2, we studied how the detector response depends on the vertex position and the Čerenkov cone direction of monoenergetic electron events. The results of an analogous study of these dependencies in gamma-ray events can be found in Section 7.2.4. It was determined that the energy response of the SNO detector has stronger positional and directional dependencies[2] in the NCD-installed scenario than the pure D_2O scenario.

In Section 7.2.3, a gain correction algorithm to correct for the positional and directional dependencies for electron events is outlined. This algorithm takes the energy signal (N_{hits} or N_{pe}), the vertex position and the Čerenkov cone direction from each event as inputs. To avoid a possible introduction of non-linear effects by an event fitter, the event position and Čerenkov cone direction generated by the Monte Carlo were used as inputs. We demonstrated that this algorithm can correct N_{pe} signals reliably. However, the non-linearity in N_{hits} caused the breakdown of this algorithm. In Section 7.3, we studied how well this gain correction algorithm can reconstruct the charged current energy spectrum in both the pure D_2O and the NCD-installed running scenarios.

Using the vertex position and the Čerenkov cone direction generated by SNOMAN as input to the gain correction algorithm is an idealised scenario. As we mentioned above, this was done to avoid non-linear effects being introduced by an event fitter. In a realistic setting, each event is first analysed by an event fitter in order to extract the event vertex position and the Čerenkov cone direction. In Section 7.4, we summarise the results of a survey on the performance of a simple fitter — the time fitter. The event fitting algorithm of the time fitter is introduced in Section 7.4.1. The event vertex and directional fitting performance of the time fitter are summarised in Sections 7.4.2

---

[2] In the following, we shall use the term "positional dependence" to refer to the dependence on the position of the event vertex, and the term "directional dependence" to refer to the direction of the Čerenkov cone.

and 7.4.3 respectively. In these two sections, we studied how well the time fitter can reconstruct electron and gamma-ray events in both the pure D_2O and the NCD-installed running scenarios. We found that the time fitter does not introduce any non-linearity to the fitted event. Moreover, the presence of the NCD array does not introduce any significant degradation in the time fitter's ability to reconstruct events when compared to the pure D_2O scenario.

With the reliability of the time fitter established, we studied how to calibrate the gain correction function in a realistic setting in Section 7.5. In Section 7.5.1, a discussion on how to use monoenergetic gamma-ray sources like the pT source to calibrate the gain correction function can be found. In this analysis, all the events were first analysed by the time fitter, and the results were input to the gain correction function. In Section 7.5.2, we discuss how well this gamma-ray calibrated gain correction function can reconstruct energy spectra.

As mentioned above, the gain correction scheme breaks down when the input signal (for example, N_{hits}) is non-linear. The non-linearity in N_{hits} arises from multiple photons firing a PMT. In Chapter 8, we discuss this multiple-hit effect in detail. We discuss the energy and positional dependencies of this multiple-hit effect in Section 8.1. Section 8.1.1 focuses on the energy dependence, and the positional dependence is discussed in Section 8.1.2. An algorithm to correct for this multiple-hit effect in electron events is introduced in Section 8.2. We demonstrated that this algorithm can linearise the N_{hits} signals. In Section 8.3, we demonstrated further that this multiple-hit correction algorithm can correct for gamma-ray events reliably without any modification. Therefore, it is not necessary to perform any particle identification before this correction algorithm is applied to the data. We combined both the gain correction and the multiple-hit correction algorithms in Section 8.4. In this section, a gain correction function using linearised N_{hits} signals was extracted. We then applied this function to monoenergetic electron and gamma-ray events. It is demonstrated that this "two-tier" correction scheme improves the energy resolution of the SNO detector significantly in the NCD-installed scenario. In Section 8.5, we conclude this survey of energy calibration issues in a discussion on the "N_{hits} resolution anomaly," in which the energy resolution extracted from the zeroth order analysis is better than the one extracted from the two-tier correction scheme in the pure D_2O running scenario. We show that this anomaly arises from incorrect photon counting statistics in N_{hits}.

7.1 The SNOMAN Monte Carlo Program

Since the SNO detector Monte Carlo analyses in Chapters 7 and 8 in this thesis were performed using the SNO Monte Carlo and ANalysis code (SNOMAN) [113, 114], a brief description of the Monte Carlo portion of the code is warranted.

The purposes of SNOMAN are to generate hit patterns for different classes of events by Monte Carlo simulation, and to provide all the necessary tools for analysing the real SNO data. The basic concept behind the design of SNOMAN is a central data structure set up by the ZEBRA memory manager [115]. Different software modules, or processors, communicate information through this structure. This modularity circumvents the lack of dynamic data structuring in FORTRAN which was chosen by the SNO collaboration as the native language for SNOMAN.

SNOMAN is capable of modelling the generation and the subsequent propagation of all relevant particles in different components of the SNO detector. At the heart of this particle transport simulation is the EGS4[3] code system [116] and the MCNP[4] neutron transport code. Both of these packages track particles through different geometries and media. Electrons and gamma rays are tracked by the former package, whilst the latter

---

[3] Electron-Gamma Shower

[4] Monte Carlo N-Particle

package deals primarily with neutrons. In SNOMAN, all the major detector components, including calibration sources, are coded into the SNOMAN geometry module.

In this Monte Carlo study, we used version 2.09 of SNOMAN. In this version of SNOMAN, the NCD array is modelled as 96 strings of nickel cylinders oriented vertically in the D_2O volume with a 1-metre lattice constant. Given that we are concerned only with signals external to the NCD array in this study, the geometry of the mechanical components internal to the counter body of each string can be ignored.

The counter body of the NCD is constructed out of chemical vapour deposited (CVD) nickel. Waltham [117] had measured the total reflectance of the CVD nickel-water interface in the visible regime using a spectrophotometer. This measurement was made on nickel samples before any chemical treatment. The total reflectance of the CVD nickel surface in water varies smoothly from about 1.5% at 300 nm to about 6% at 600 nm. We incorporated this data into SNOMAN by using a polynomial fit to generate the diffuse reflectance.

The total reflectance of the CVD nickel is noticeably higher after the chemical etching procedure. The purpose of this cleaning procedure is to remove surface contaminants. At the time of writing this thesis, the total reflectance of the etched nickel samples has not been measured. However, the overall effect of using the reflectance of unetched nickel would merely be a gain shift in the detector's energy response. Therefore, the general conclusions of this study are not very much affected by this systematic uncertainty.

7.2 The SNO Detector Response

Lay [118] has done some work in understanding the energy response of the SNO detector. In his study, he investigated the distribution of the number of fired photomultiplier tubes (N_{hits}) for monoenergetic electron and gamma-ray events as a function of energy.

A photomultiplier tube is "fired" if the calibrated charge in its electronic channel is equivalent to the level of $\frac{1}{4}$ photoelectron. In this section, we shall extend Lay's work. In particular, we shall look at both the N_{hits} and the electronically calibrated charge (N_{pe}) spectra in both the pure D_2O and the NCD-installed scenario in order to determine if there is any non-linear effect introduced by the NCD array. It is desirable to look at the energy dependence of both the N_{hits} and the N_{pe} distributions because one would expect multiple hits on a photomultiplier tube would render N_{hits} a non-linear quantity at high energy. However, one should not discount the fact that this multiple hit effect should also have a strong positional dependence on the event vertex. For instance, an event originating near the photomultiplier tube array would be more likely to have more multiple hits if the electron travels towards the array.

7.2.1 Energy Response to Electrons and γ Rays — A Zeroth Order Approximation

As a first step, we looked at the N_{hits} and N_{pe} distributions for monoenergetic, isotropic electrons and gamma rays generated evenly throughout the D_2O volume. The N_{pe} information was taken from the calibrated high gain, long time integrated channel electronic output from SNOMAN. In other words, N_{pe} is the electronically calibrated charge in units of photoelectrons. The N_{hits} and N_{pe} distributions at each energy were fitted to a Gaussian distribution to extract the means μ and the widths σ. In Table 7.1 and Table 7.2, we summarise the results for both pure D_2O and NCD-installed configurations. The 1σ statistical uncertainties on the fitted means and the widths are $<0.15\%$ and 1% respectively.

We want to emphasise that the numbers listed in Table 7.1 and Table 7.2 are only "zeroth order approximations." As we shall see in Section 7.2.2, the photomultiplier tube array response depends on both the position of the event vertex and the thrust vector

Monoenergetic Electrons								
E_e	Pure D_2O				D_2O + NCD			
(MeV)	$\mu_{N_{hits}}$	$\sigma_{N_{hits}}$	$\mu_{N_{pe}}$	$\sigma_{N_{pe}}$	$\mu_{N_{hits}}$	$\sigma_{N_{hits}}$	$\mu_{N_{pe}}$	$\sigma_{N_{pe}}$
2	19.3	4.0	25.2	6.0	17.7	3.1	22.7	5.9
3	30.0	6.3	39.8	9.7	25.8	6.1	34.2	8.8
4	41.1	7.7	54.9	12.0	35.3	7.6	47.1	11.6
5	52.2	8.8	70.2	13.6	44.6	9.1	59.9	13.8
6	63.3	9.9	85.6	15.5	54.0	10.2	72.8	15.7
7	74.0	10.9	100.8	17.2	62.9	11.6	85.6	17.9
8	84.6	12.0	115.7	18.9	72.0	13.0	98.2	20.1
9	94.8	12.5	130.4	20.2	80.9	13.7	111.4	21.8
10	105.4	13.4	145.8	21.8	89.6	14.8	124.2	24.0
11	115.7	14.0	161.1	23.2	98.0	15.7	136.8	25.6
12	125.3	14.8	174.7	24.6	106.8	16.5	149.5	27.9
13	135.7	15.4	190.4	25.6	115.1	17.1	161.7	29.5
14	145.5	15.9	205.2	27.0	122.9	18.1	173.8	31.9
15	155.1	16.7	219.6	28.7	131.1	18.6	186.5	32.8
16	164.8	17.2	234.2	29.8	139.3	18.9	198.8	34.2
17	174.3	17.5	249.1	30.7	147.3	20.3	211.7	36.8
18	183.8	18.3	263.6	32.8	155.5	20.6	224.6	38.5
19	192.8	18.7	278.4	33.5	162.5	21.4	235.7	40.7
20	202.1	19.0	292.9	34.3	170.8	21.4	248.5	41.8
25	247.2	21.6	366.4	40.1	209.0	24.0	311.4	50.5

Table 7.1: Mean μ and width σ of N_{hits} and N_{pe} distributions as a function of energy for monoenergetic electrons in SNO. Results for both pure D_2O and NCD-installed scenarios are shown. These numbers are valid for isotropic electrons generated evenly throughout the D_2O volume. Because of the directional and the positional dependence of the detector response, these numbers should only be treated as a "zeroth order approximation." These numbers also have a $\sim$2% systematic uncertainty because of the presence of the belly plates in the real detector, which was not modelled in this study. The quantum efficiency is about 10 photomultiplier tube hits per MeV in electron energy.

Monoenergetic Gamma rays								
E_γ (MeV)	Pure D_2O				D_2O + NCD			
	$\mu_{N_{hits}}$	$\sigma_{N_{hits}}$	$\mu_{N_{pe}}$	$\sigma_{N_{pe}}$	$\mu_{N_{hits}}$	$\sigma_{N_{hits}}$	$\mu_{N_{pe}}$	$\sigma_{N_{pe}}$
2	15.5	2.5	19.9	4.6	14.5	2.0	19.1	4.3
3	22.1	5.5	29.1	7.9	20.3	4.1	25.8	7.0
4	30.8	8.0	40.7	12.0	26.9	7.7	35.7	11.0
5	41.3	9.6	55.4	14.0	35.4	9.2	47.5	13.3
6	52.0	10.9	70.4	16.1	44.4	10.2	59.7	15.4
7	62.2	11.7	84.5	17.5	53.4	11.6	72.1	17.1
8	72.7	12.9	99.3	19.7	62.8	12.5	85.2	19.2
9	83.4	13.6	114.3	21.0	71.3	13.4	97.1	20.5
10	94.1	14.2	129.3	22.3	80.4	14.9	110.3	22.9
11	104.2	14.8	144.0	23.5	89.2	16.1	122.9	25.2
12	114.2	15.6	158.4	25.2	98.0	17.0	135.6	26.5
13	124.5	16.5	172.9	26.5	106.8	18.1	148.2	28.8
14	134.9	16.8	188.6	27.8	115.2	18.8	160.9	30.0
15	144.9	17.4	203.5	28.9	123.8	19.8	173.3	31.9
16	154.8	17.9	218.0	29.8	132.8	20.6	187.5	34.5
17	164.6	18.1	232.8	31.0	140.4	21.4	198.8	36.5
18	174.4	18.7	247.8	32.5	149.1	22.1	211.8	37.6
19	184.5	19.2	262.9	33.0	157.3	22.6	224.0	39.2
20	193.8	19.4	276.8	34.1	165.4	23.6	236.5	41.1
25	240.5	21.9	351.9	40.1	205.0	26.4	299.8	50.5

Table 7.2: Mean μ and width σ of N_{hits} and N_{pe} distributions as a function of energy for monoenergetic gamma rays in SNO. Results for both pure D_2O and NCD installed scenarios are shown. These numbers are valid for isotropic gamma rays generated evenly throughout the D_2O volume. Because of the directional and the positional dependence of the detector response, these numbers should only be treated as a "zeroth order approximation." These numbers also have a ~2% systematic uncertainty because of the presence of the belly plates in the real detector, which was not modelled in this study. The quantum efficiency is about 10 photomultiplier tube hits per MeV in electron energy. The fits in both N_{hits} and N_{pe} cases are worse than the corresponding ones in the monoenergetic electron set in Table 7.1. This is because of the different responses from the gamma ray conversion in the acrylic vessel for gamma rays generated near to the vessel (see Section 7.2.4).

of the electron. Hence, the results in Table 7.1 represent a gross average of the detector response which is an inadequate measure of the detector performance since the positional and directional dependencies have not been taken into account. As we shall demonstrate later, these dependencies can be corrected for. It should also be noted that the results have a $\sim$2% systematic uncertainty because of the presence of the thick belly plates in the real detector, which were not modelled in this study.

These results are displayed graphically in Figures 7.1 and 7.2. In these figures, the detector resolution is defined as the *full-width-at-half-maximum* resolution.

We want to point out several observations from this "zeroth approximation" analysis:

1. In the solar neutrino energy regime, N_{hits} varies roughly linearly with energy. A quadratic fit would provide a better fit. Lay [118] pointed out this same observation.

2. On the other hand, N_{pe} response is linear in the same energy regime. This strongly suggests that photomultiplier tubes are receiving multiple hits. We found that the N_{pe}/N_{hits} ratio increases substantially as the energy increases.

3. The detector resolution calculated using N_{pe} appears to be worse than that in the N_{hits} case in this "zeroth order approximation." This could be attributed to the fact that the calibrated charge, which has a rather broad distribution because of the poor charge resolution of the photomultiplier tubes, was used.

4. The detector resolution is degraded by $\sim$6 to $\sim$10% when the NCD array is present. However, as we shall demonstrate later, this "zeroth order" resolution is an inadequate estimation of the detector resolution function because of its strong positional and directional dependencies.

5. The amount of light loss due to the presence of the NCD array is $\sim$15%. This light

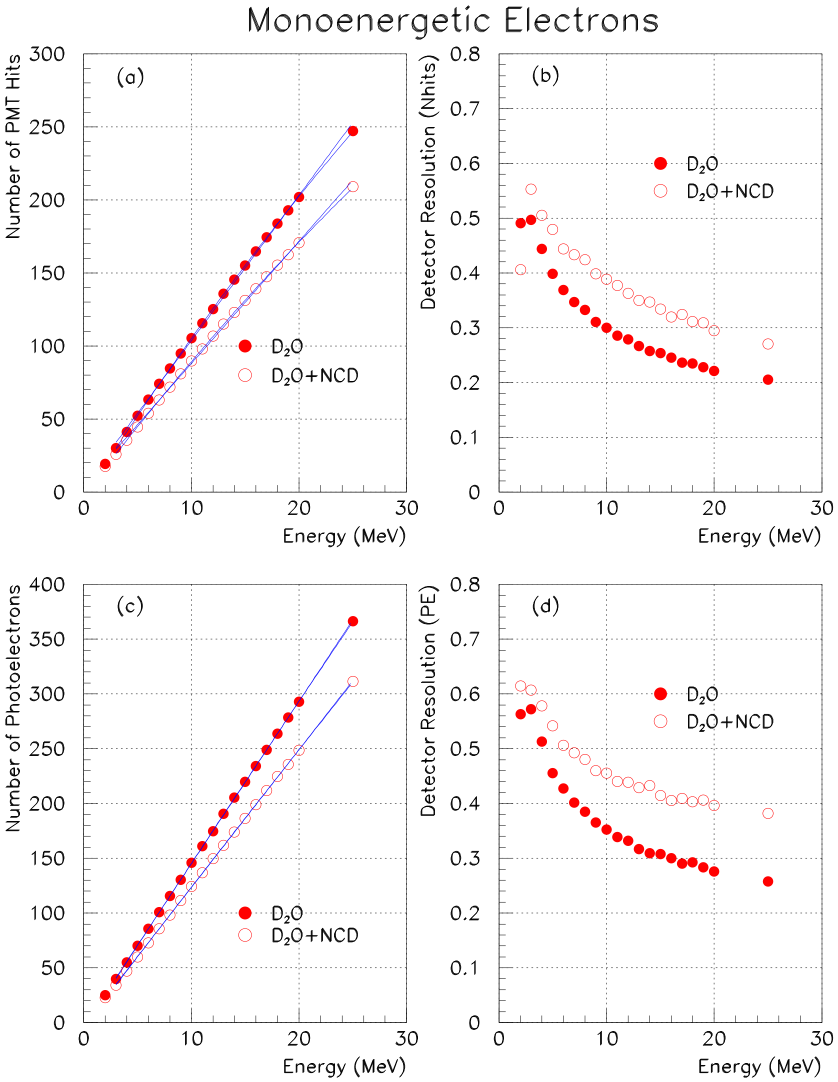

Figure 7.1: N_{hits} and N_{pe} energy calibration curve for monoenergetic electrons. The N_{hits} and N_{pe} distributions for each electron energy are fitted to a Gaussian distribution. (a) energy dependence on N_{hits} ; (b) detector resolution dependence on electron energy calculated based on N_{hits} distributions; (c) N_{pe} dependence on electron energy; (d) detector resolution dependence on electron energy calculated based on N_{pe} distributions. The degradation of the detector resolution calculated based on N_{pe} is a consequence of the convolution of the charge resolution of the photomultiplier tubes to the N_{hits} spectrum. The lines are linear and quadratic fits to the energy calibration curve, with the quadratic curve giving a slightly better fit. The “improvement” in energy resolution near 2 MeV is an artifact of the 10-hit hardware threshold.

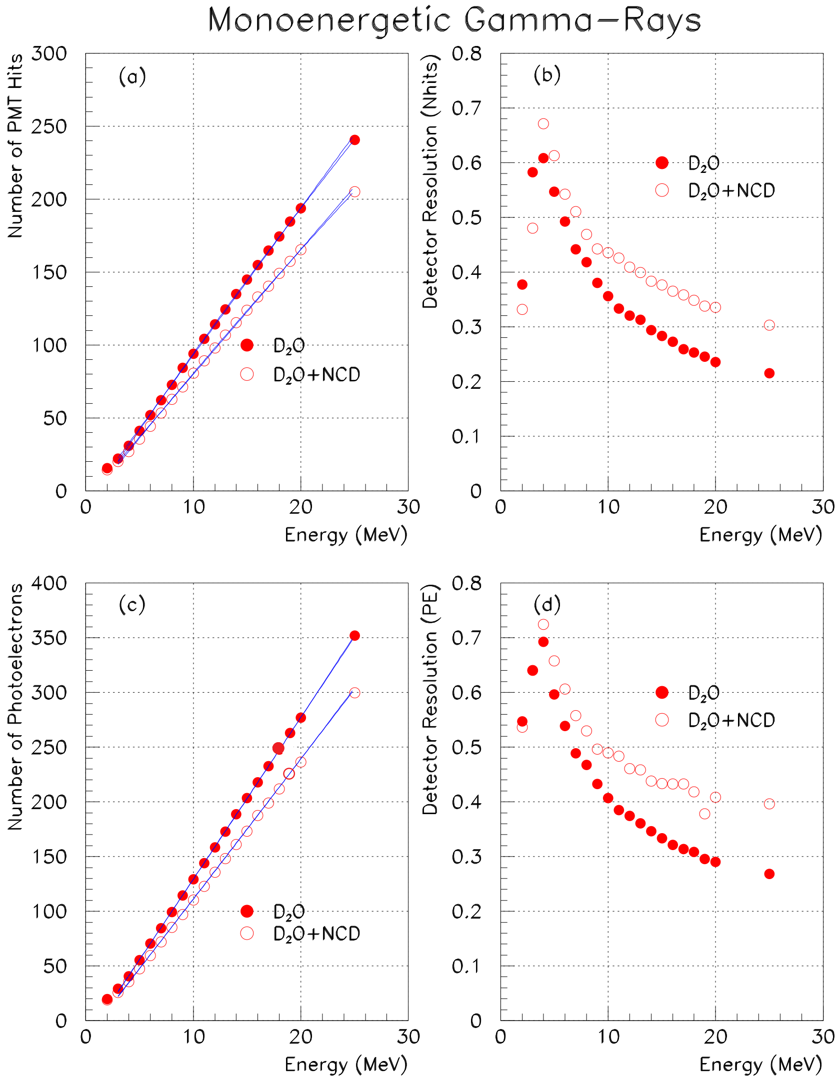

Figure 7.2: N_{hits} and N_{pe} energy calibration curves for monoenergetic gamma rays. The N_{hits} and N_{pe} distributions for each gamma-ray energy are fitted to a Gaussian distribution. (a) energy dependence of N_{hits} ; (b) detector resolution dependence on gamma-ray energy calculated based on N_{hits} distributions; (c) N_{pe} dependence on gamma-ray energy; (d) detector resolution dependence on gamma-ray energy calculated based on N_{pe} distributions. The degradation of the detector resolution calculated based on N_{pe} is a consequence of the convolution of the charge resolution of the photomultiplier tubes to the N_{hits} spectrum. The lines are linear and quadratic fits to the energy calibration curve, with the quadratic curve giving a slightly better fit. The “improvement” in energy resolution at $E \leq 3$ MeV is an artifact of the 10-hit hardware threshold.

loss ($L(E)$) is defined as

$$L(E) \;=\; 1 - \frac{N_{i,NCD}(E)}{N_{i,D2O}(E)} \qquad i = \text{hits, pe} \tag{7.1}$$

where $N_{i,NCD}(E)$ is the signal in the presence of the NCD, and $N_{i,D2O}(E)$ is the corresponding signal in the pure D_2O running scenario. The energy dependence of $L(E)$ is displayed in Figure 7.3.

6. Both N_{hits} and N_{pe} signals are smaller for gamma rays than for electrons. The resolution for gamma rays is also worse. This is attributed to multiple Compton scattering.

7. Both N_{hits} and N_{pe} spectral fits at high energies are worse in the gamma-ray cases because of the long tail at large N_{hits} or N_{pe}. As we shall demonstrate later (see page 205), this tail arises from gamma-ray conversion in the acrylic vessel.

However, these conclusions were reached based on a rather simple analysis. As we have pointed out earlier, these results should only be treated as "zeroth order approximations."

7.2.2 Energy Response to Electrons — Positional and Directional Dependence

One would expect the photomultiplier tube array response to have stronger positional and directional dependencies when the NCD array is in place. This response function should also depend on the direction of the Čerenkov cone as light absorption will be bigger for photons travelling a longer distance inside the D_2O volume. In Figure 7.5, we display how N_{hits} depends on the vertex position and the track direction for 10-MeV isotropic electrons generated evenly throughout the D_2O volume. The track direction is parameterised as $\cos(\delta)$ where δ is the opening angle between the position vector of the generated vertex and the generated direction of the outgoing track (see Figure 7.4).

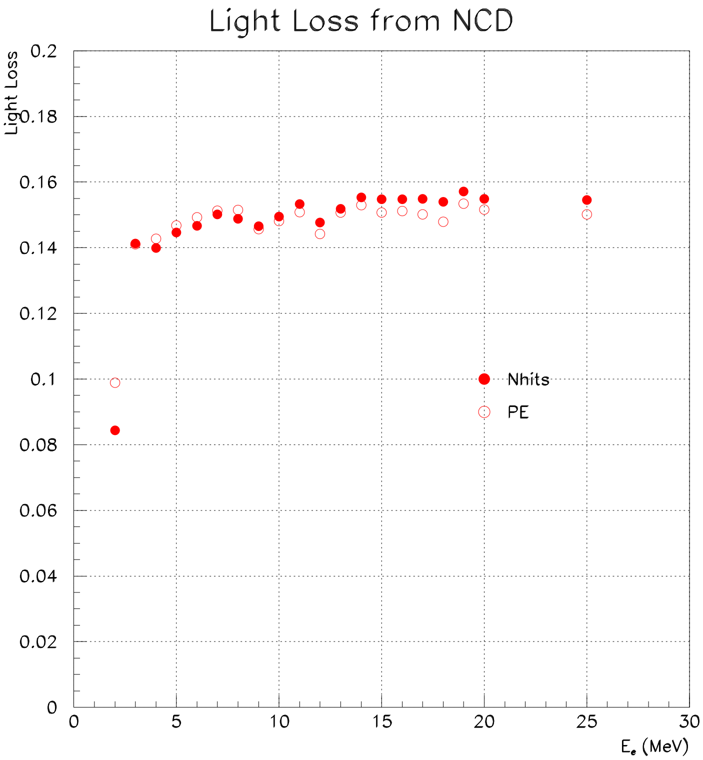

Figure 7.3: Fractional light loss as a function of electron energy in the NCD-installed scenario. This light loss is shown as N_{hits} and N_{pe} reduction in the presence of the NCD array. The drop in light loss at 2 MeV is an artifact in fitting a Gaussian to the N_{hits} and N_{pe} spectra when a significant part of the spectrum is below the hardware threshold of 10 fired photomultiplier tubes.

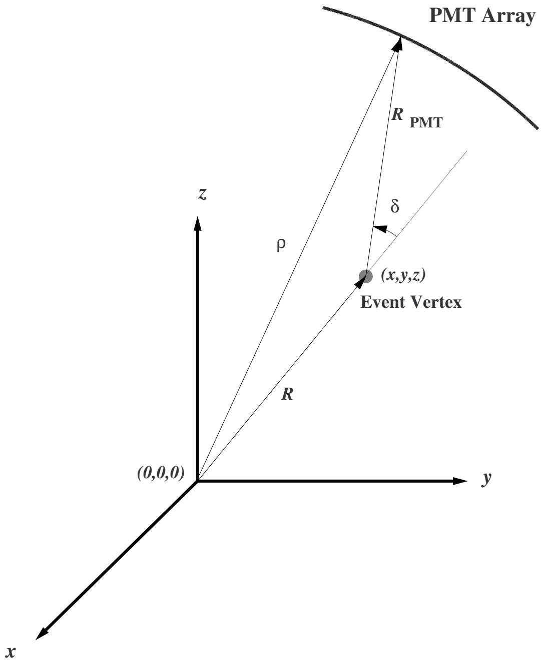

Figure 7.4: Definition of Definition of the various geometrical parameters. The parameter R_{PMT} is the distance between the event vertex and the projected point at the photomultiplier array along the electron direction.

That is, events with $\cos(\delta) \geq 0$ would be "outward" going, whilst those with $\cos(\delta) < 0$ would be "inward" going.

In Figure 7.5, it is evident that the "outward" going events, in which photons travel less distance than the "inward" going events, register more photomultiplier tube hits. In the case of the pure D_2O scenario, this can be explained by light attenuation of the D_2O and the acrylic vessel. The difference between the pure D_2O case and the NCD-installed case is primarily light absorption by the NCD array. The directional dependence is noticeably stronger in the presence of the NCD array as evident in the increased slope of the scatter plot compared to the pure D_2O case. The positional dependence of N_{hits} is also stronger in the presence of the NCD array as the N_{hits} versus the radial distance

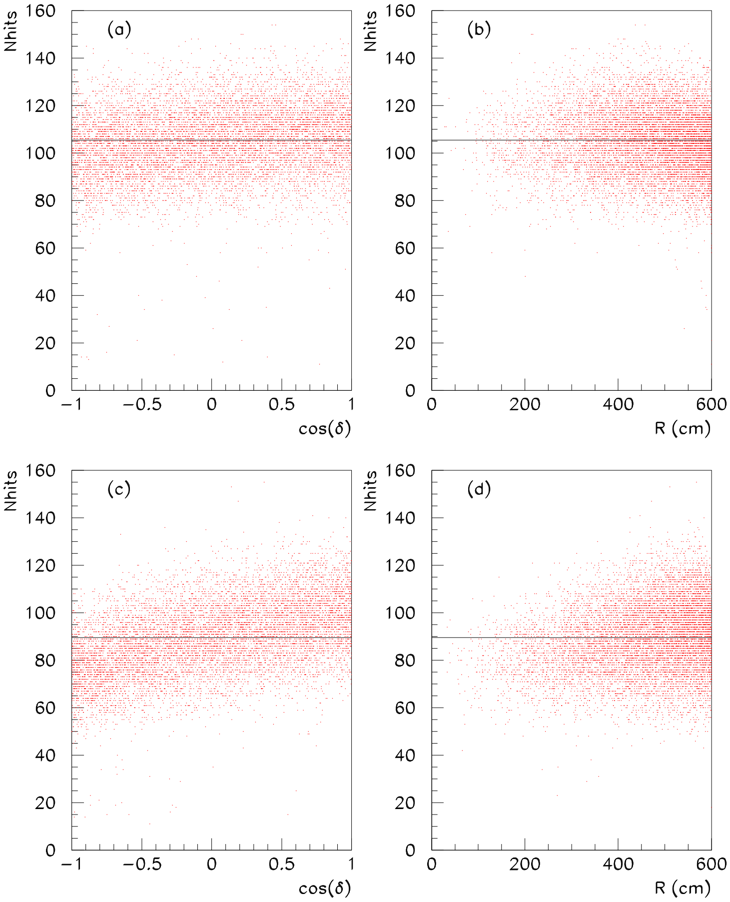

Figure 7.5: Scatter plots showing positional and directional dependence of N_{hits} distribution for 10000 10-MeV electron events generated isotropically and evenly throughout the D_2O volume. (a) N_{hits} dependence on the opening angle between the positional vector of the vertex and the direction of the electron track in pure D_2O scenario; (b) N_{hits} dependence on the radial distance of the vertex in pure D_2O scenario; (c) N_{hits} dependence on the opening angle between the positional vector of the vertex and the direction of the electron track in NCD-installed scenario; (d) N_{hits} dependence on the radial distance of the vertex in NCD installed scenario. The horizontal lines drawn are the mean N_{hits} calculated based on the "zeroth order approximation" approach in the last section.

of event vertex (R) scatter plots show a less symmetric profile in the NCD-installed case. Also shown as horizontal lines in Figure 7.5 are the mean N_{hits} for the two different detector operating conditions. The asymmetry of points about this line clearly indicates the shortcoming of the "zeroth order" fitting procedure.

As an attempt to account for both the directional and positional dependence, we constructed a parameter R_{PMT} defined as

$$R_{PMT} = -R\cos\delta + \sqrt{(R\cos\delta)^2 + \rho^2 - R^2} \tag{7.2}$$

where R is the radial distance of the vertex, δ is opening angle between the generated electron direction and the radial vector of the generated vertex, and ρ is the radial distance of the photomultiplier array (890 cm). In the expression above, the parameters R and δ are generated by the Monte Carlo. R_{PMT} is the distance between the event vertex and the projected point at the photomultiplier array along the electron direction. This parameter can be viewed as an estimation of the average distance each generated Čerenkov photon would travel. These definitions are shown in Figure 7.4.

The effect of light absorption by the NCD array was analysed by comparing the difference in N_{hits} or N_{pe} dependence on R_{PMT} in the pure D_2O case and the NCD-installed scenario. In Figure 7.6, the N_{hits} dependence on R_{PMT} for the same 10 MeV electron data set is shown for both of these scenarios. It is clear that as the Čerenkov photons travel more distance (i.e. large R_{PMT}), the reduction in N_{hits} is more significant in the NCD-installed scenario.

To compare the difference in R_{PMT} dependence between the pure D_2O and the NCD-installed scenarios, R_{PMT} was divided into 50-cm bins. The resulting N_{hits} spectrum in each of these bins was fitted to a Gaussian distribution. In Figure 7.7, the fitted means $\mu(R_{PMT})$ and resolutions for the same 10 MeV electron data set used in Figure 7.5 are plotted in the pure D_2O and NCD-installed scenarios.

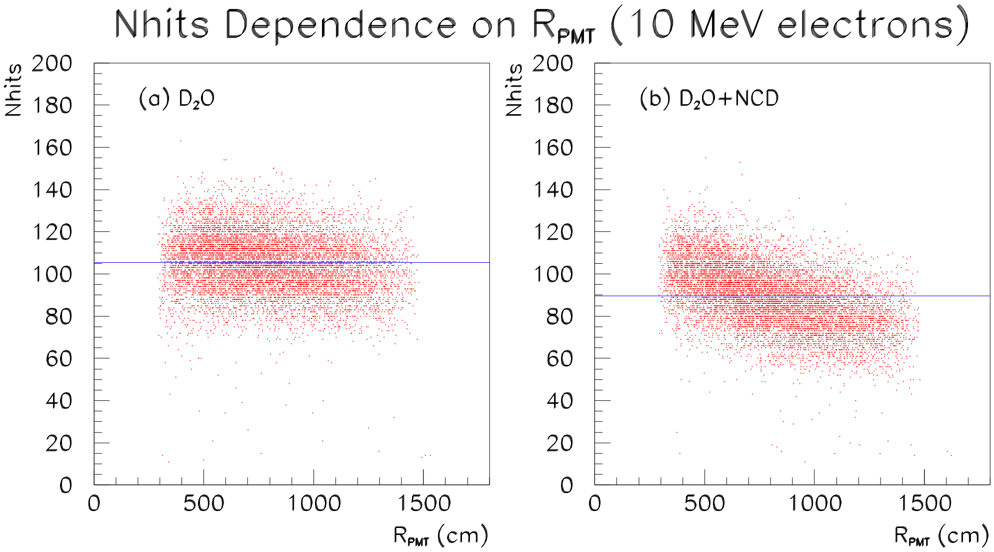

Figure 7.6: Scatter plots showing N_{hits} dependence on R_{PMT}. (a) pure D_2O ; (b) NCD-installed. The horizontal lines shown here are the means calculated using the "zeroth order approximation" approach in the previous section.

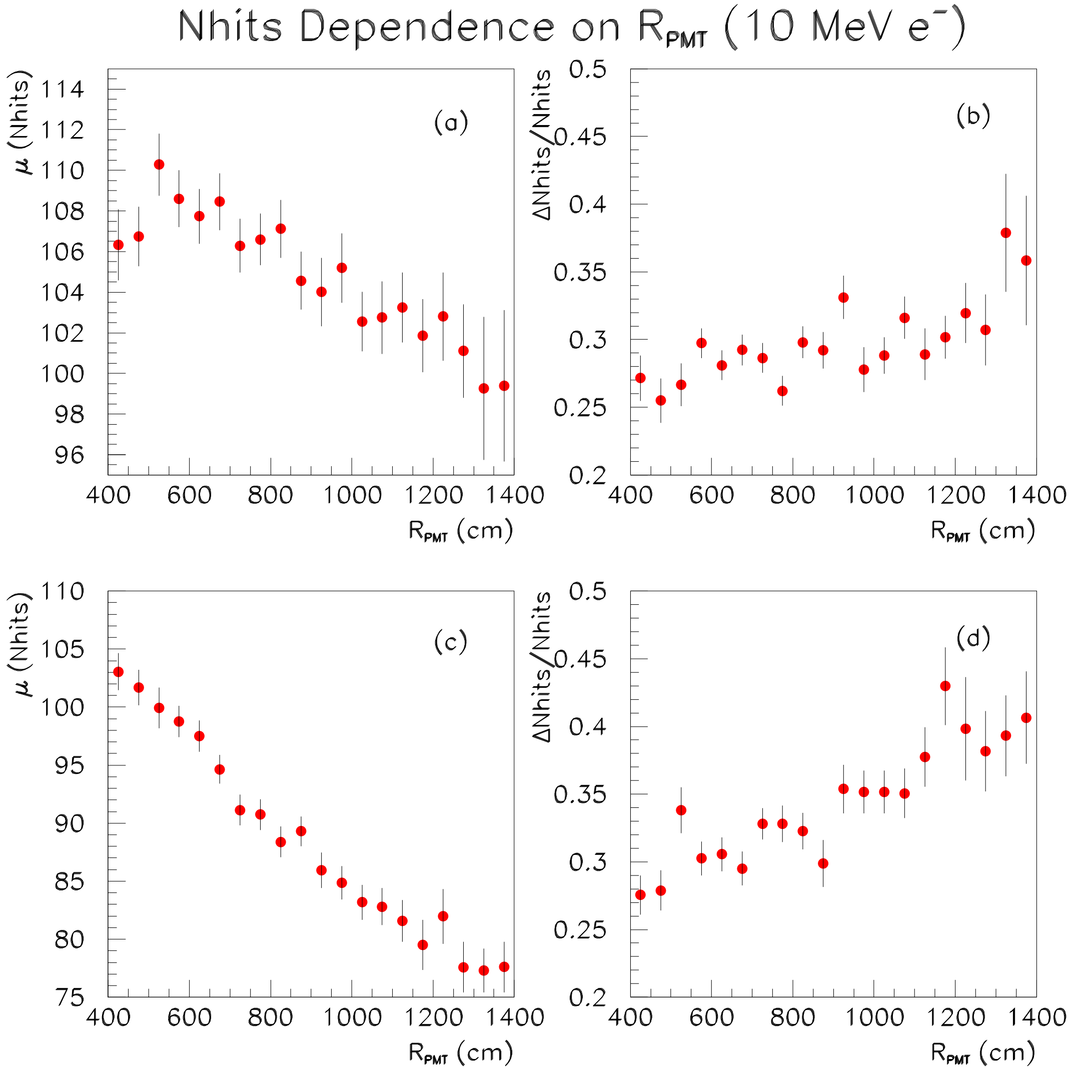

Figure 7.7: Plots showing the mean and the resolution as functions of R_{PMT} for 10-MeV electrons in pure D_2O and in the NCD array installed detector. (a),(b): N_{hits} centroid and resolution as functions of R_{PMT} in the pure D_2O scenario; (c), (d): N_{hits} centroid and resolution as functions of R_{PMT} in the NCD-installed scenario.

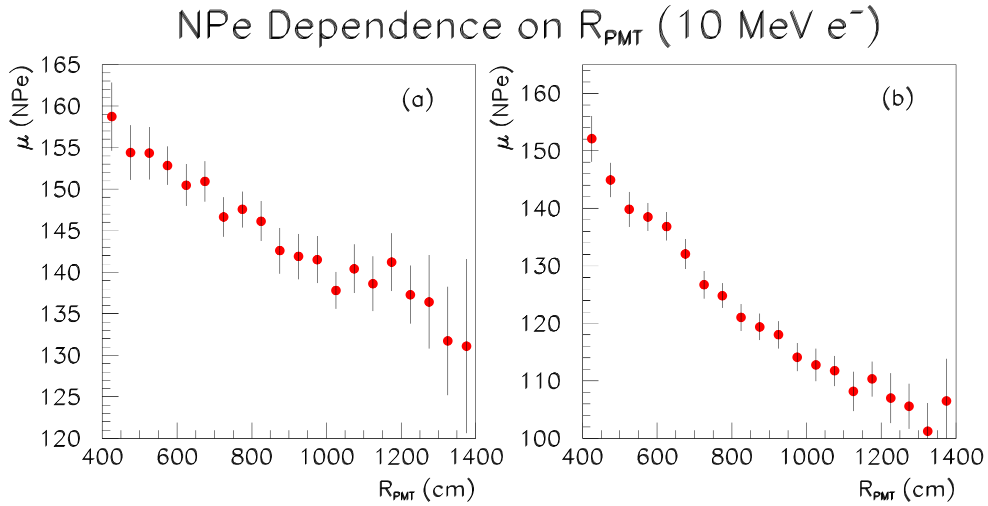

Figure 7.8: $\mu(R_{PMT})$ calculated based on N_{pe}. The "peak" structure at R_{PMT}~500cm is now gone.

In Figure 7.7, $\mu(R_{PMT})$ shows a maximum at R_{PMT}~500 cm. In fact, the "peak" gets more and more pronounced as the electron energy increases. Although this "peak" does not seem to exist in the NCD-installed case in the figure, it does appear at higher energies. Degradation of the signal at higher R_{PMT} can be understood as increased light attenuation in the D_2O with longer propagation path. The drop in $\mu(R_{PMT})$ at small R_{PMT} is a manifestation of photomultiplier tubes receiving multiple hits. To demonstrate this last point, similar plots of N_{pe} for the same 10 MeV electron data set is shown in Figure 7.8. Notice that the "peak" has disappeared in these latter plots.

The positional and directional dependence of the detector resolution is vividly shown in Figure 7.7. The difference between $\mu(R_{PMT})$ of pure D_2O and of NCD-installed cases demonstrates that light loss through absorption by the NCD surface is more significant than light attenuation in the heavy water. As a result, the detector resolution gets worse rather rapidly at higher R_{PMT} when the NCD is in place. In the following, we shall demonstrate a "gain correction" technique to more properly handle the "inward" and "outward" going events.

7.2.3 A Gain Correction Algorithm for Electron Events

The R_{PMT} dependence of $\mu(R_{PMT})$ in Figures 7.7 and 7.8 can be seen as a gain variation in the detector. One can therefore correct for the gain by comparing the signals in both operating scenarios to a "standard candle." The standard candles we used are monoenergetic electrons generated isotropically from the centre of the SNO detector. We defined the gain correction factor at each energy as

$$G^i_\alpha(R_{PMT}) = \frac{\mu^\circ_\alpha}{\mu^i(R_{PMT})}, \qquad i = \mathrm{D_2O},\ \mathrm{NCD};\ \alpha = N_{pe}, N_{hits} \tag{7.3}$$

where μ°_α is the extracted mean of N_{hits} or N_{pe} for the "candle," $\mu^{D_2O}(R_{PMT})$ and $\mu^{NCD}(R_{PMT})$ are the extracted means of N_{hits} or N_{pe} at a particular R_{PMT} for the pure D_2O and the NCD-installed scenarios. That is, they are the data points in the plots in Figures 7.7 and 7.8. In this analysis, we used 3, 5, 10 and 15-MeV monoenergetic electrons generated isotropically from the centre of the SNO detector as standard candles. The N_{hits} and N_{pe} spectra of the candle sets were fitted to a Gaussian distribution to extract μ°_α for that candle. In Table 7.3, we have listed the spectral information on the standard candle sets.

In principle, $G^i_\alpha(R_{PMT})$ should be an energy independent geometrical factor. However, as we have pointed out earlier, the effect of multiple hits causes a drop in N_{hits} at small R_{PMT}. This effect is, however, non-linear and energy dependent. In Figure 7.9, $G^i_{N_{hits}}(R_{PMT})$ is extracted using N_{hits} information and is plotted for several electron energy cases. It is clear that at small R_{PMT} the shape of this gain correction function is

E_e (MeV)	$\mu_{N_{hits}}$	$\sigma_{N_{hits}}$	$\mu_{N_{pe}}$	$\sigma_{N_{pe}}$
3	28.5	5.9	37.1	9.1
5	49.8	8.4	66.0	12.6
10	100.9	12.6	135.9	19.0
15	150.7	15.5	206.4	24.2

Table 7.3: Spectral information on the standard candle sets. The standard candles are monoenergetic electrons generated isotropically from the centre of the SNO detector. The resulting N_{hits} and N_{pe} spectra were fitted to Gaussian distributions to extract the means and the widths.

very much dependent on the energy of the calibration "candle."

To try eliminating the effect of multiple hits, we repeated the analysis by using the means in the N_{pe} spectra to calculate the gain correction factor. The corresponding $G^i_{N_{pe}}(R_{PMT})$ is shown in Figure 7.10. In this figure, the strong energy dependence of the multiple hit effect has disappeared at small R_{PMT}. The slight discrepancy at large R_{PMT} for the 3 MeV candle calibration is an artifact of the 10-hit hardware trigger, and poor energy resolution at low energy and large R_{PMT}.

With the knowledge of the gain correction function, one can correct for the "gain" in both the pure D_2O and NCD-installed running scenarios on an event by event basis. For an event with a signal N^i_α and a particular value of R_{PMT}, the gain-corrected signal N^{io}_α is

$$N^{io}_\alpha = G^i_\alpha(R_{PMT})N^i_\alpha \qquad i = \mathrm{D_2O,\ NCD}; \alpha = N_{pe}, N_{hits}. \tag{7.4}$$

The gain-corrected means of N^{io}_{hits} and N^{io}_{pe} for electron data sets are then used to form the energy calibration line $C^i_\alpha(E)$ for each of the candle sets. The resolution functions $R^i_\alpha(E)$ are also generated.

One can see how the multiple hit effect affects the energy calibration in this gain correction algorithm in Figures 7.11 and 7.12 in which $C^i_\alpha(E)$ and $R^i_\alpha(E)$ are displayed.

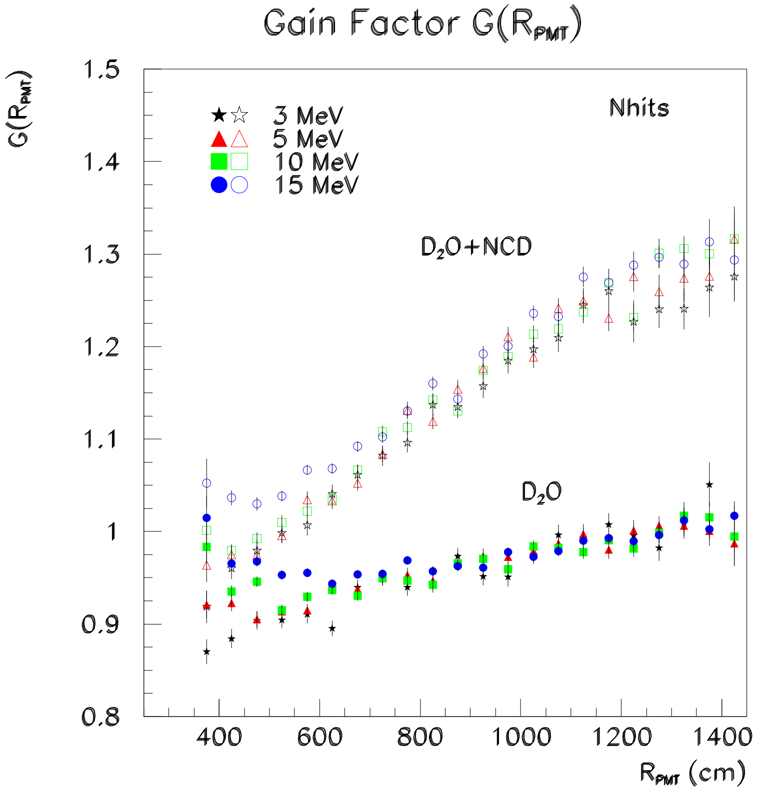

Figure 7.9: Energy dependence of $G_{N_{hits}}(R_{PMT})$ for 3, 5, 10 and 15-MeV candles. These plots demonstrate that $G(R_{PMT})$ is energy dependent when using only N_{hits} information. The discrepancies between the various “candle” calibration sets arise from the multiple hit effect especially at small R_{PMT}.

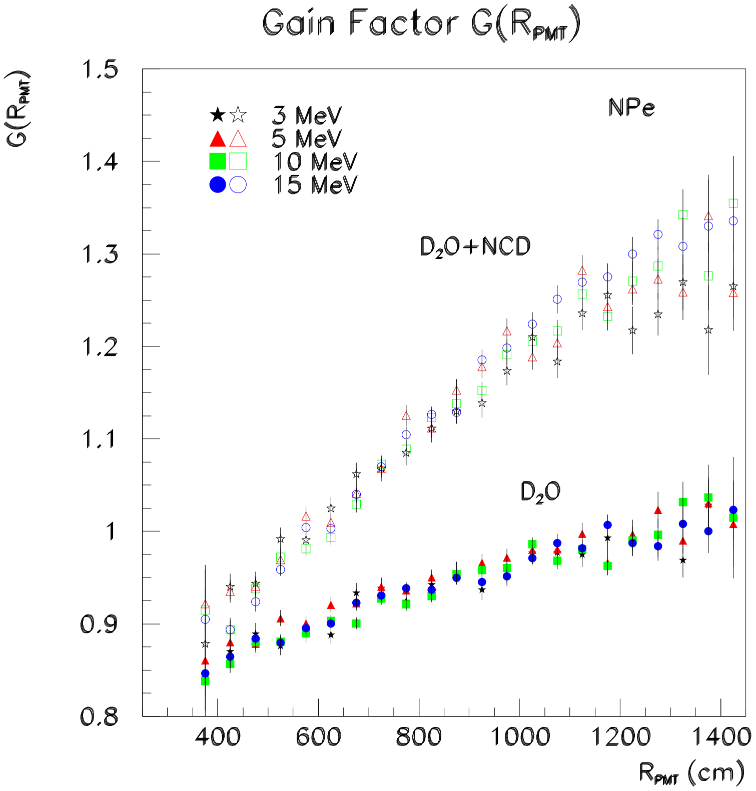

Figure 7.10: Energy dependence of $G_{N_{pe}}(R_{PMT})$ for 3, 5, 10 and 15-MeV candles . These plots demonstrate that the agreement in $G(R_{PMT})$ for small R_{PMT} is much better than the corresponding ones in Figure 7.9. The discrepancy at large R_{PMT} for the 3 MeV "candle" calibration is an artifact of the 10-hit hardware trigger, and poor energy resolution at low energy and large R_{PMT}.

In Figure 7.11, it is obvious that the slope of the energy calibration curve for the different candle sets is different using $G^i_{N_{hits}}(R_{PMT})$ extracted from N_{hits} information. For instance, the difference in the calibrated energy for 100 photomultiplier tube hits using the 3-MeV and the 15-MeV candle is 3% and 4% respectively in the pure D_2O and NCD-installed running scenarios. On the other hand, the calibrated energy from using the N_{pe} information is well within the statistical fluctuation of <1%.

This discrepancy indicates a shortcoming of the R_{PMT} gain correction scheme. Because of its simplicity, it does not take the detector asymmetry (e.g. neck of the acrylic vessel, NCD array) and other non-linear effects (e.g. multiple hits if dealing with N_{hits} spectrum) into account in a correct manner. From the goodness of agreement amongst different candle sets in the calibration curve extracted from N_{pe} information, it is clear that the detector asymmetry does not have much effect on this R_{PMT} gain correction technique. It is the non-linearity in the N_{hits} distribution which caused the breakdown of this technique. However, one can always use a multi-dimensional gain correction function to deal with this non-linearity correctly. Alternatively, one can use the N_{pe} information which is linear. In the next chapter, we shall demonstrate a technique to correct for the multiple-hit effect in the N_{hits} distribution.

It is also clear from this analysis that the SNO detector response has a strong dependence on *both* the event vertex position and the direction of the Čerenkov cone in both running scenarios. Therefore, one must include these two dependencies into the detector gain correction scheme.

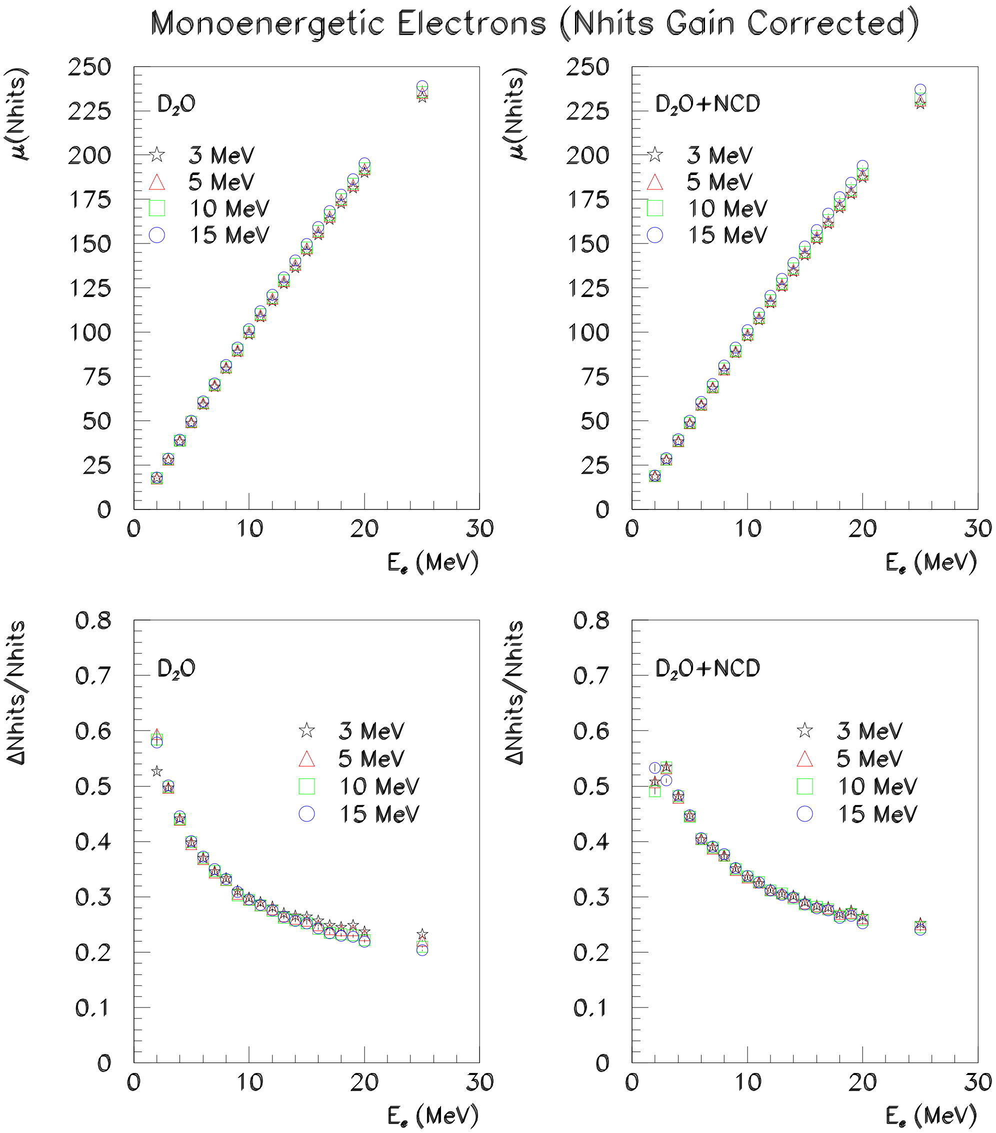

Figure 7.11: Calibration curves and energy resolution curves for different candle sets (N_{hits} gain corrected). The candle sets are 3, 5, 10 and 15-MeV monoenergetic electrons. The gain correction functions extracted from N_{hits} distributions are used in these plots. It is clear that there is a non-negligible discrepancy between different candle sets. The "improvement" in energy resolution at $E \leq 3$ MeV is an artifact of the 10-hit hardware threshold.

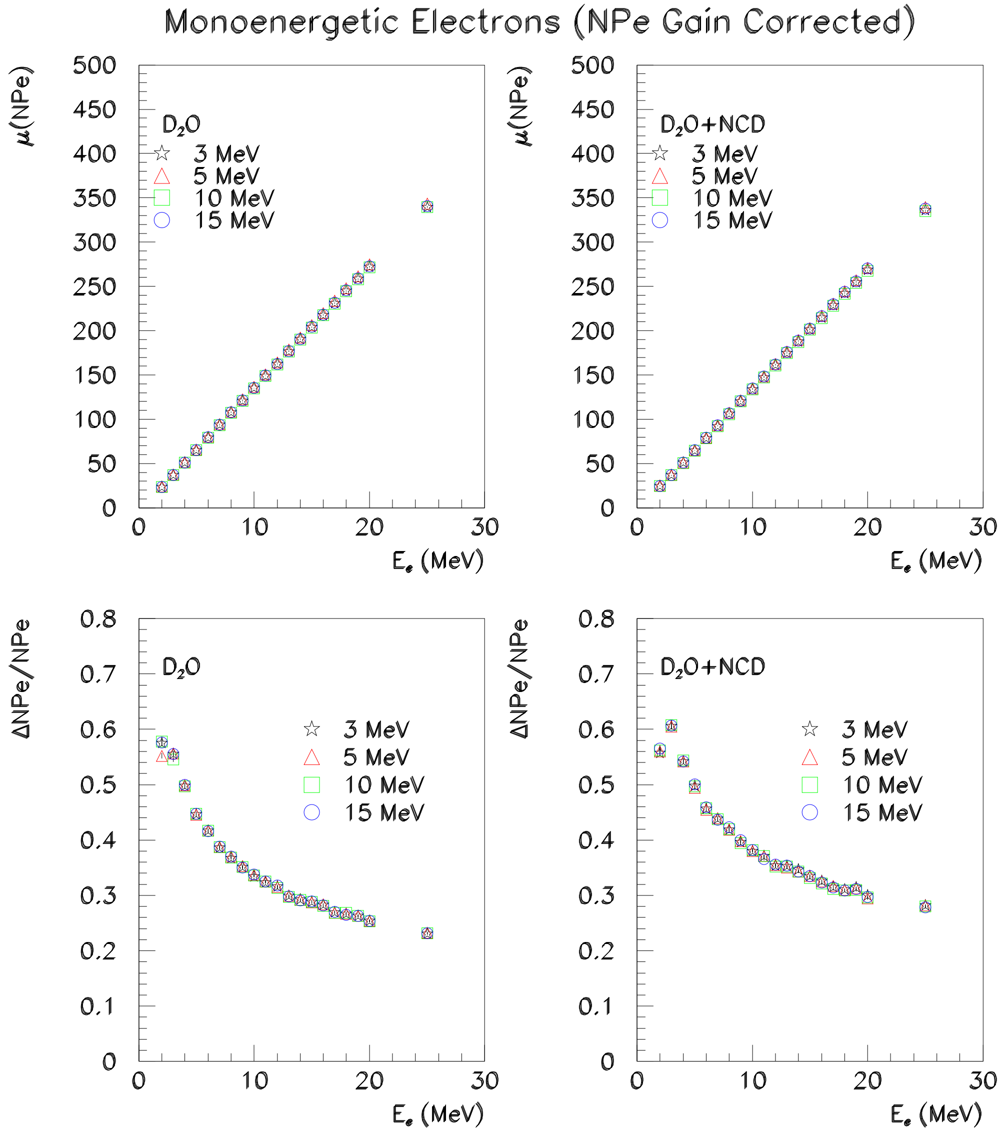

Figure 7.12: Calibration curves and energy resolution curves for different candle sets (N_{pe} gain corrected). The candle sets are 3, 5, 10 and 15-MeV monoenergetic electrons. The gain correction functions extracted from N_{pe} distributions are used in these plots. The agreement between different candle sets is much better than the corresponding cases in Figure 7.11. The “improvement” in energy resolution at $E \leq 3$ MeV is an artifact of the 10-hit hardware threshold.

7.2.4 Energy Response to Gamma Rays — Positional and Directional Dependence

In the pure D_2O and the added salt running scenarios, neutral-current events are identified by the detection of the γ rays emitted subsequent to the neutron capture on deuterium or chlorine nuclei. Photodisintegration background is also identified by the same channels. Therefore it is important to have a good understanding of the γ-ray response of the SNO detector.

To understand the γ-ray response, we used isotropic γ-ray events generated evenly throughout the D_2O volume. In Figure 7.13, the N_{pe}-R_{PMT} scatter plots are shown for 10 MeV γ rays in the pure D_2O and the NCD installed running scenarios. In these scatter plots, there is a long tail extending to large N_{pe} at small R_{PMT} which does not exist in the electron cases in Figure 7.6. If these raw γ-ray spectra are used to extract the R_{PMT} gain correction function as in Section 7.2.2, one would find that the correction function would drop off much more rapidly than the electron cases as R_{PMT} gets smaller. This indicates that the mean number of photoelectrons at small R_{PMT} in the γ-ray cases is much larger than that in the electron cases. This is also the origin of the slightly worse fit in the γ-ray N_{hits} and N_{pe} spectra in the "zeroth order approximation" we mentioned in page 190.

The origin of this tail in the scatter plots is the effect of Čerenkov light output enhancement in acrylic. The mean yield N of Čerenkov photons created in a track of length δx is [119]

$$N \;=\; \delta x \frac{\alpha}{c} \int_{\omega_1}^{\omega_2} \left(1 - \frac{1}{\beta^2 n^2}\right) d\omega \tag{7.5}$$

where ω_1 and ω_2 are the frequency cutoffs, n is the refractive index and β is the relativistic factor. There is a ~20% difference between the Čerenkov light yield in D_2O and in acrylic because of the difference in their refractive indices.

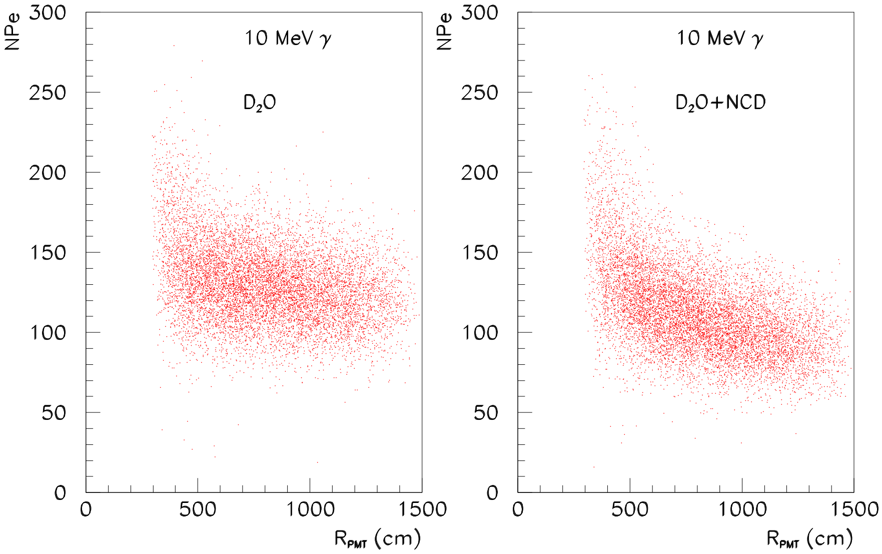

Figure 7.13: Dependence of N_{pe} on R_{PMT} for 10-MeV gamma rays in pure D_2O and NCD-installed running scenarios.

A gamma-ray event generated close to and directed towards the vessel has a higher probability of converting into electrons in the acrylic. These events are the ones with small R_{PMT}. To confirm this hypothesis, we put a spatial cut of $R \leq 500$ cm on the original γ-ray events. This cut would only keep γ rays generated at least two attenuation lengths from the acrylic vessel, thereby reducing the number of γ rays converted in the acrylic. We found that this spatial cut did remove the tail at small R_{PMT}, thus confirming our previous speculation.

What this analysis of the SNO detector's response to γ rays has shown is that one must be very careful in handling γ-ray events originating close to the acrylic vessel. To correctly extract the neutral-current energy spectrum in the added salt option or to extract the photodisintegration background signal, a careful γ-ray calibration near the acrylic vessel has to be done in order to determine the light output enhancement by the vessel.

7.3 Energy Spectrum of the Charged-Current Signal

As we have seen in Figure 2.2, SNO can provide indisputable evidence for neutrino oscillation by observing a distortion in the charged-current (CC) energy spectrum. Because the presence of the NCD array would inevitably deteriorate the energy resolution of the photomultiplier tube array, it is necessary to understand how this would affect SNO detector's ability to detect a spectral distortion in the charged-current signal. We shall devote our discussion in this section to the SNO detector's ability to detect this shape distortion.

Three sets of 1-year CC data at full standard solar model (SSM) rate for both pure D_2O and NCD-installed scenarios were generated. All the generated events were gain corrected in N_{pe} and energy calibrated as described in Section 7.2.3. A theoretical energy

Run	$\mathrm{Pr}_{\mathrm{D_2O}}$	$\mathrm{Pr}_{\mathrm{NCD}}$
1	0.723	0.999
2	0.942	0.835
3	0.989	0.942

Table 7.4: Kolmogorov-Smirnov probability for comparing the theoretical CC spectrum convoluted with the detector resolution and the gain-corrected, calibrated N_{pe} Monte Carlo spectrum. The Monte Carlo event sets consist of one-year of CC events at full standard solar model rate. These results indicate that the gain correction scheme can reproduce the CC spectrum in a self-consistent manner.

spectrum was also generated using the CC energy generator in SNOMAN. This latter spectrum was then convoluted with the gain corrected energy resolution in Figure 7.12. We chose to compare these spectra without introducing further complication such as fitter effects. Hence, we used the raw Monte Carlo event output instead of the event fitter fitted vertex and direction for the gain correction. We then compare the energy convoluted CC spectrum with the corresponding gain corrected Monte Carlo results by the Kolmogorov-Smirnov (K-S) test. In Section 7.5, we shall do a more realistic analysis with all the signals being analysed first by a simple event fitter.

In Table 7.4, we listed the K-S probabilities for the null hypothesis of the spectra being drawn from the same distributions for the three data sets in both run scenarios. It is clear from the table that the gain correction scheme does reproduce the CC spectrum in a self-consistent manner, whether or not the NCD array is in place. In Figure 7.14, we show how the three-year full SSM CC spectra compare.

In order to understand the sensitivity of this spectrum comparison to the energy calibration, we made an overall shift in the energy calibration function $C(E)$ and the energy resolution function $R(E)$ in Figure 7.12. In particular, we shifted these functions in one of two ways:

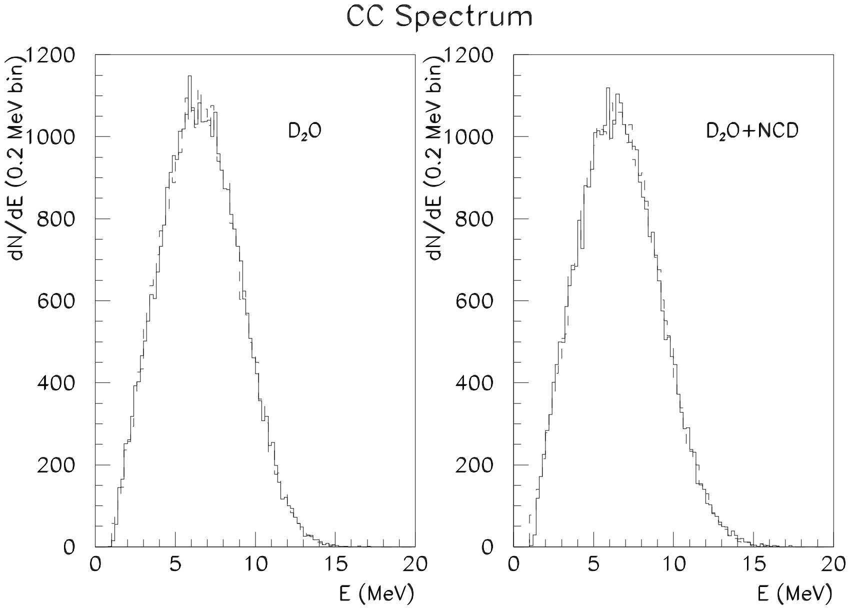

Figure 7.14: Three year data set of CC spectra. The dashed histograms in these two graphs are the energy resolution convoluted theoretical spectra. The gain corrected Monte Carlo spectra are shown as solid histograms.

$f_C(E)$	$f_R(E)$	$\mathrm{Pr}_{\mathrm{D_2O}}$	$\mathrm{Pr}_{\mathrm{NCD}}$
0.98	1.00	$< 10^{-5}$	$< 10^{-5}$
0.99	1.00	0.002	0.016
1.00	0.98	$< 10^{-5}$	$< 10^{-5}$
1.00	0.99	0.002	0.024
1.00	1.01	0.117	0.007
1.00	1.02	$< 10^{-5}$	$< 10^{-5}$
1.01	1.00	5×10^{-5}	0.004
1.02	1.00	$< 10^{-5}$	$< 10^{-5}$

Table 7.5: A test of the sensitivity of the CC energy spectrum to the energy calibration and the energy resolution functions. This comparison was performed using a 3-year CC data set at the full standard solar model rate.

1. $C(E) \rightarrow C(f_C E)$
2. $R(E) \rightarrow R(f_R E)$,

where f_C and f_R are the overall gain shift factors. In Table 7.5 we summarise our findings of this systematic analysis. In this analysis, we used 3-year-equivalent CC spectra.

From Table 7.5, it is clear that an introduction of an overall gain shift of as small as 1% would cause a non-negligible change to the shape of the observed CC energy spectrum. A similar statement can also be made for the energy resolution function. However, what this analysis has demonstrated is that the R_{PMT} gain correction technique is a self consistent technique which can reconstruct energy spectra to much better than 1%. This analysis has also shown that the CC energy can be reconstructed, without any significant distortion, when the NCD array is in place.

7.4 Event Vertex and Direction Fitting Performance

As shown in Figure 7.3, an average of 15% of the light is lost when the NCD array is installed. We have demonstrated that this loss has a strong positional and directional dependence as depicted in Figure 7.7. One concern is whether or not the event vertex and the electron direction can still be reconstructed reliably when the NCD array is in place. To answer this question, we compare the performance of the time fitter in SNOMAN in the pure D_2O and the NCD-installed scenarios. In this section, we shall first briefly introduce the time fitter, and we shall summarise our comparison of the time fitter performance under the two afore-mentioned running scenarios. We shall divide this investigation into two sub-categories: the vertex fitting performance in Section 7.4.2, and the directional fitting in Section 7.4.3.

7.4.1 The Time Fitter

The time fitter has the simplest possible fitting algorithm. The fitter takes the positions $\vec{r_i}$ and the recorded time t_i of each of the hit photomultiplier tubes within the trigger, and calculates its event transit time deviation Δt_i defined as

$$\Delta t_i \;=\; \frac{1}{\langle c \rangle}|\vec{r_i} - \vec{r}| - (t_i - t), \tag{7.6}$$

where $\langle c \rangle$ is the average speed of light in the D_2O. If this transit time deviation is normally distributed, the best fit ($\vec{r}$,t) is found when the χ^2 statistic

$$\chi^2 \;=\; \frac{1}{n-4}\sum_{i=1}^{n}\left[\frac{(\Delta t_i)^2}{\sigma_i^2}\right] \tag{7.7}$$

is minimised. In the default SNOMAN settings, photomultiplier tube hits that occur 8 ns earlier or 4 ns later than the fitted t are not used in the fit in order to reduce the effects of photomultiplier noise and scattered light.

7.4.2 Vertex Fitting Performance

Good vertex fitting resolution is critical to discriminating background events in the SNO detector. The time fitter, because of its simplicity, gives us a lower bound estimate on this resolution. We compared the time fitter's performance on monoenergetic electrons and γ rays generated isotropically and evenly in the D_2O volume in the two running scenarios. As an example, scatter plots displaying the dependence of the time fitter reconstructed radial distance R_{fit} on the Monte Carlo generated radial distance R for 10-MeV electrons in the two running scenarios are shown in Figure 7.15.

For each electron energy data set, we fitted each of the R_{fit}-R scatter plots to a linear relationship. We then compared the difference in linearity between the two running scenarios by taking the ratio of their respective slopes. These results are summarised in

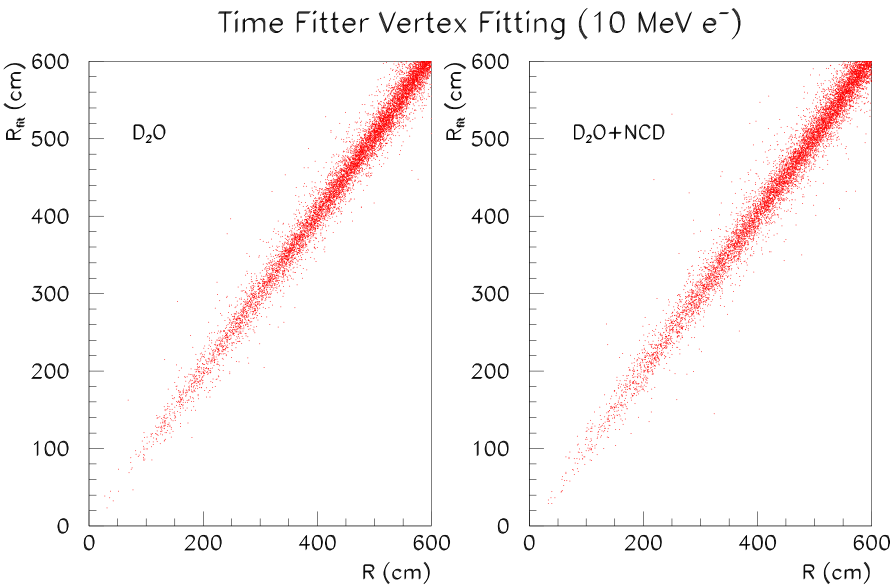

Figure 7.15: Scatter plots showing time fitter reconstructed radial distance in the two running scenarios for 10-MeV electrons. The time fitter does not introduce any non-linearity to the fitted radial distance of the vertex.

Figure 7.16. These plots indicate that the introduction of the NCD array does not affect the linearity of the time fitter's vertex fitting ability.

With the fact that the time fitter does not introduce any non-linear artifact in the vertex fitting established, the question of the accuracy of the vertex fit was investigated. To determine this accuracy, we looked at the distribution of R_{dev}, which is the distance between the fitted vertex $\vec{R}_{fitted}$ and the Monte Carlo generated vertex $\vec{R}_{MC}$:

$$R_{dev} = |\vec{R}_{MC} - \vec{R}_{fitted}|. \tag{7.8}$$

In Figures 7.17 and 7.18, the mean and the standard deviation of the R_{dev} distribution for electrons and γ rays are shown. In these figures, it is clear that R_{dev} is smaller for electrons than for gamma rays. The difference is essentially the attenuation length of the gamma rays, since the vertex of the γ-ray conversion, not the original gamma-ray vertex, was fitted by the fitter. It is also clear in these figures that the deviation levels off as energy increases for electrons whilst the deviation tends to increase at higher energies in

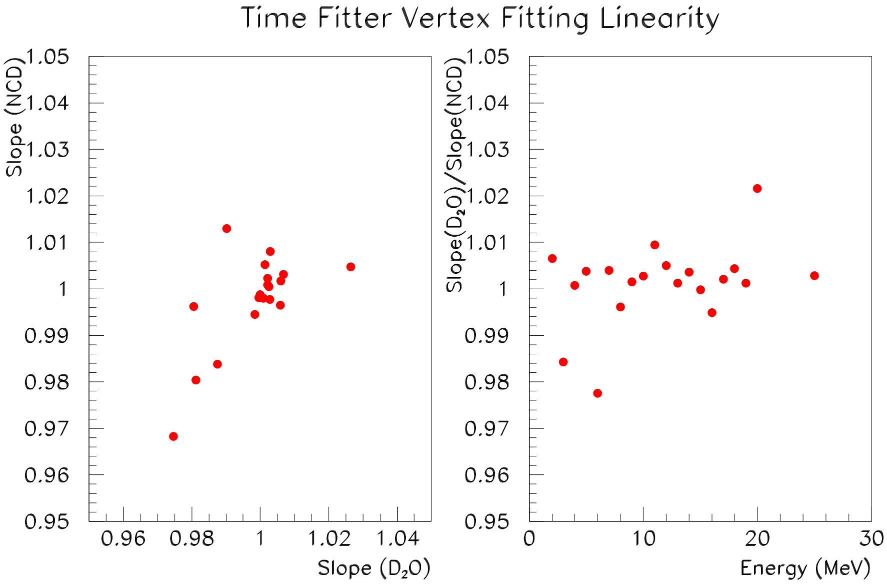

Figure 7.16: Linearity of the time fitter. *Left:* scatter plot showing the fitted slope for the R_{fit}-R relation at different electron energies; *Right:* plot showing the ratio between the fitted slopes in the D_2O and the NCD-installed scenario.

the γ-ray case. The drop of the mean R_{dev} as energy increases at low energy is attributed to the increased Čerenkov photon statistics for both electrons and γ rays. The increase of mean R_{dev} at high gamma-ray energies is due to the increase in gamma-ray attenuation length. At an energy of 2 MeV, the average R_{dev} gets worse by less than 20 cm for both electrons and γ rays in the NCD-installed scenario when compared to the pure D_2O scenario. This is essentially a statistical effect in event fitting because of light absorption by the NCD array.

7.4.3 Directional Fitting Performance

An accurate fitting of the Čerenkov cone direction is essential in separating the different classes of events in the SNO detector. For instance, it is desirable to be able to separate the charged-current and the elastic scattering events in SNO. Therefore, we investigated the directional fitting performance of the time fitter in the two running scenarios.

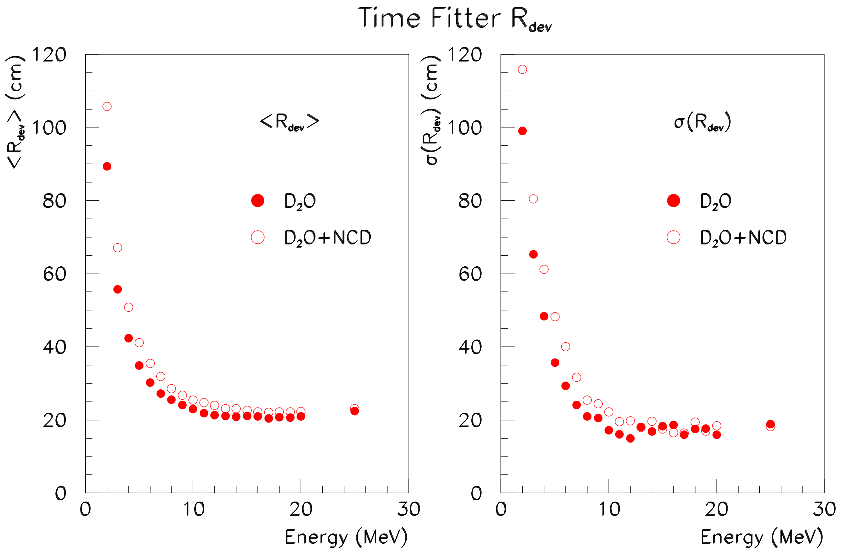

Figure 7.17: Deviation of the time fitter fitted radial distance for electrons. *Left:* The average radial distance deviation; *Right:* The standard deviation of the radial distance deviation.

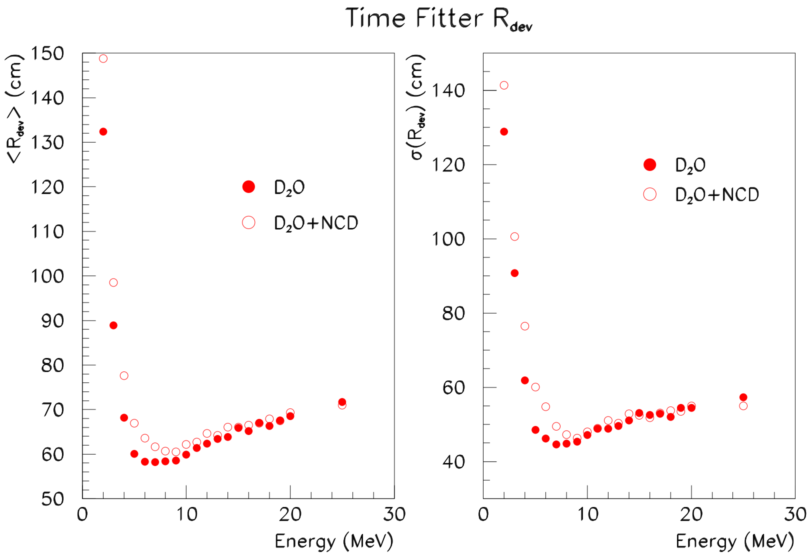

Figure 7.18: Deviation of the time fitter fitted radial distance for γ rays. *Left:* The average radial distance deviation; *Right:* The standard deviation of the radial distance deviation. The rise at high energies is attributed to the increased γ-ray attenuation length.

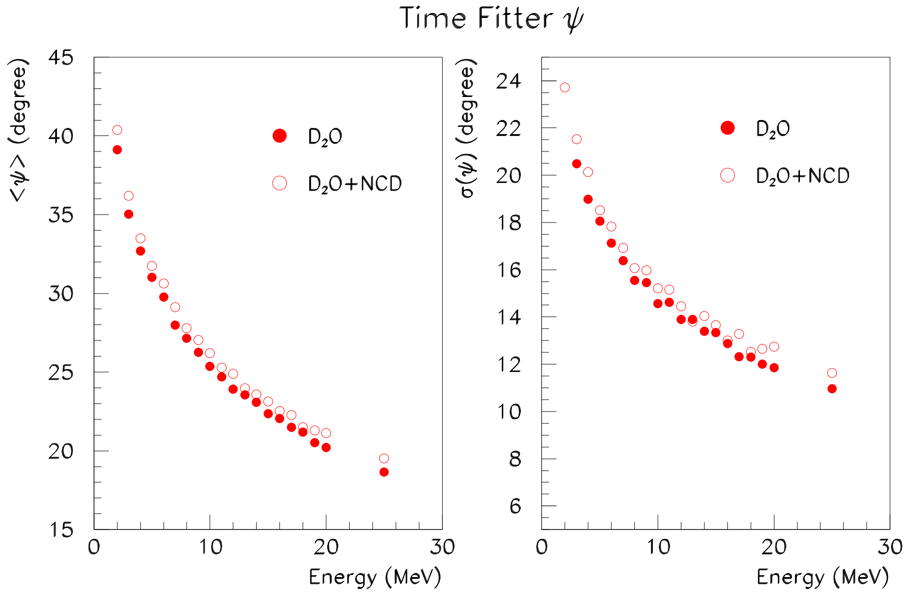

Figure 7.19: Opening angle ψ between the fitted direction and the Monte Carlo generated direction for electrons. *Left:* The mean of ψ distribution; *Right:* The standard deviation of the ψ distribution.

Similar to the vertex fitting analysis in the last section, we first tried to determine if the time fitter introduces any non-linear effect in the direction fitting in the electron cases. We came to the same conclusion as in the vertex fitting case that the time fitter does not introduce any non-linearity.

To determine the accuracy of the directional fitting, we looked at the angular deviation ψ defined as

$$\cos(\psi) = \frac{\vec{R}_{MC} \cdot \vec{R}_{fitted}}{|\vec{R}_{MC}||\vec{R}_{fitted}|}. \tag{7.9}$$

That is, ψ is the opening angle between the Monte Carlo generated direction and the time fitter fitted direction. We found that the fitted directional resolution is slightly worse in the NCD-installed case. The plots in Figures 7.19 and 7.20 demonstrate that the effects of the NCD array on the direction fitting performance are small, as the difference between $< \psi >$ in the pure D_2O case and that in the NCD-installed case is less than $2°$ for both the electrons and the γ rays in the energy range we investigated.

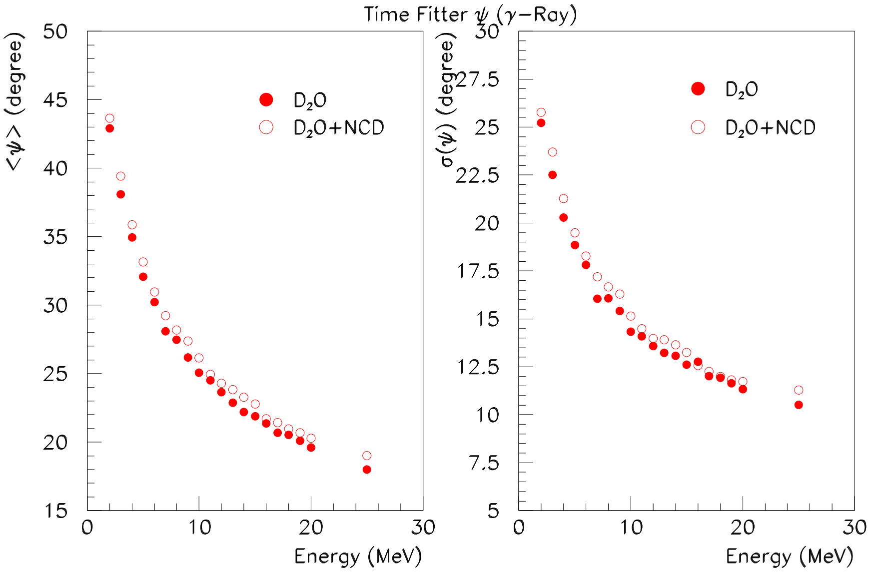

Figure 7.20: Opening angle ψ between the fitted direction and the Monte Carlo generated direction for γ rays. *Left:* The mean of ψ distribution; *Right:* The standard deviation of the ψ distribution.

In conclusion, we do not see any significant degradation in the time fitter's ability to reconstruct events in the NCD array running scenario when comparing to the pure D_2O scenario. The NCD array does not introduce any non-linear effect which would severely compromise the fitter performance. We should also emphasise that the event fitting performance summarised in this section should be considered as the worst case scenario due to the simplicity of the time fitter. More sophisticated event fitters are under development by the SNO collaboration.

7.5 Gain Correction Factor Calibration in the SNO Detector

So far we have considered using only the "hypothetical" monoenergetic electron sources to calibrate R_{PMT}. In the arsenal of the SNO calibration sources, two of the γ-ray sources might be suitable for this R_{PMT} calibration. These are the ^{16}N and the ^{3}H$(p,\gamma)^{4}$He sources. The ^{16}N emits a monoenergetic 6.13-MeV γ ray, whilst the ^{3}H$(p,\gamma)^{4}$He source generates a 19.8-MeV γ ray.

Throughout this study, we have been using the Monte Carlo generated vertex and direction for the gain correction algorithm. In reality, we do not have the luxury of knowing the origin of the events in the SNO detector. Therefore, we have to apply all the techniques we have been developing in the previous sections in a more realistic setting.

7.5.1 Extracting the Gain Correction Function Using γ Ray Events

We first looked at a similar plot to Figure 7.13 for the parameter R_{PMT}^{fit} defined as

$$R_{PMT}^{fit} = -R\cos\delta^{fit} + \sqrt{(R_{fit}\cos\delta^{fit})^2 + \rho^2 - R_{fit}^2} \tag{7.10}$$

where R_{fit} is the radial distance of the time fitter fitted vertex, δ^{fit} is the opening angle between the fitted position vector of the vertex and the fitted direction of the outgoing track. In essence, this relation is the same as Eqn.(7.2) with time fitter fitted parameters replacing the Monte Carlo generated parameters. An N_{pe}-R_{PMT}^{fit} scatter plot for 10-MeV γ rays generated evenly and isotropically in the D_2O volume is shown in Figure 7.21. In this plot, a spatial cut of $R_{fit}\leq 600$ cm is placed. That is, we kept only events that were reconstructed inside the D_2O volume.

A striking difference between Figures 7.13 and 7.21 is that the tail that exists in the small R_{PMT} region in the former figure no longer appears in the latter one. This can be explained by the fact that the time fitter systematically reconstructs the event vertex closer to the photomultiplier tube array than the actual vertex. Therefore, outward-going events generated near the acrylic vessel are more likely to get reconstructed outside the active D_2O volume. Combining this fact and the γ-ray attenuation length, one can see that most of the γ-ray events that would have been converted into electrons in the acrylic vessel are reconstructed outside the active D_2O volume by the time fitter. With

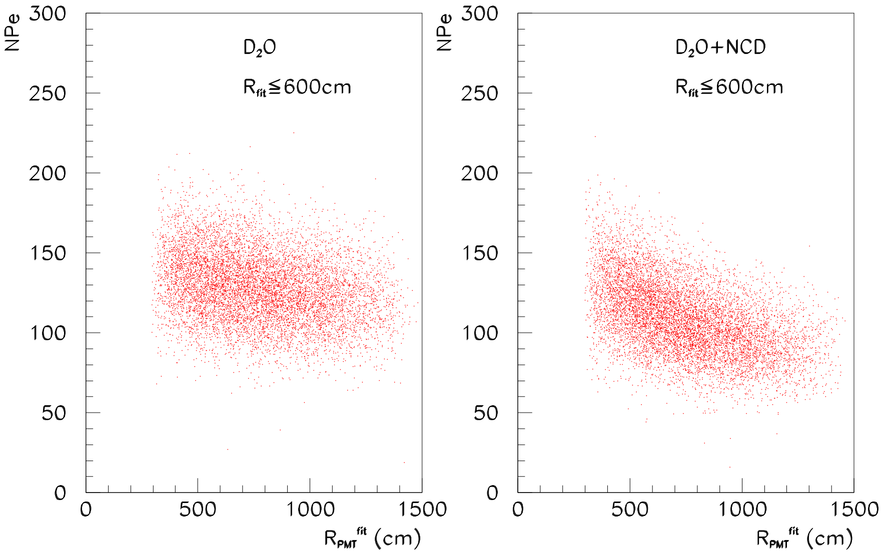

Figure 7.21: Dependence of N_{pe} on R^{fit}_{PMT} for 10-MeV gamma rays in pure D_2O and NCD-installed running scenarios. A spatial cut of $R_{fit}\leq600$ cm is placed on the data.

this spatial cut at $R_{fit}\leq600$ cm, Figure 7.21 resembles the corresponding plot for electron events. Therefore, it is possible to apply the gain correction technique we have been using on electron events to these γ-ray events.

The gain correction functions extracted from these time fitter fitted γ rays can be compared to the ones extracted from the time fitter fitted electrons. We found that the gain functions extracted from the γ rays are consistently higher than the electron ones in both running scenarios. This difference arises from the fact that γ rays have to travel a certain distance before converting to an electron. It is this converted electron vertex which the time fitter fits.

In Section 7.2.2, the extracted gain curves were fitted to fourth-order polynomials. By the definition of the gain correction function in Eqn.(7.3), it is an estimation of the amount of optical light attenuated in the SNO detector. Hence, we would expect

$$G^i_\alpha(R^{fit}_{PMT}) \propto \exp\left(\lambda R^{fit}_{PMT}\right) \qquad i = \mathrm{D_2O, NCD}; \alpha = N_{pe}, N_{hits} \tag{7.11}$$

where λ is an average attenuation length for optical photons propagating through the D_2O, acrylic vessel and the light water. We can therefore expect λ to be of the order of the optical light attenuation length in the D_2O. Because $\lambda R^{fit}_{PMT} \ll 1$, we can fit the gain function to a linear form:

$$G^i_\alpha(R^{fit}_{PMT}) = \sum_{i=0}^{1} a_i R^{fit,i}_{PMT}. \tag{7.12}$$

To correct for the shift of the gain correction function extracted from γ rays, we shift the linear fit of the gain correction function from electrons in R^{fit}_{PMT} to correspond to the γ-ray one. This shifting technique works as a geometrical correction because the γ-ray attenuation length is comparable to the spatial resolution of the time fitter. In Figure 7.22, the linear fit to the electron gain correction function in the pure D_2O running scenario was shifted to match the correction function extracted from γ-ray events for the different γ-ray candles. We found that there is an average R^{fit}_{PMT} shift of (57±7) cm amongst the three γ candle sets we used. A similar analysis on the NCD-installed scenario demonstrated that an average R^{fit}_{PMT} shift of (29±3) cm is needed to match the gain correction functions generated from the two different classes of events.

7.5.2 Energy Calibration and Spectral Reconstruction

In the last section, we have demonstrated the algorithm to extract the gain correction functions from γ-ray events. In this section, we shall apply these functions to construct energy spectra.

To demonstrate that the algorithm in the last section does reproduce the energy calibration curve and the detector resolution curve extracted from electron gain correction function, we used the gain correction functions extracted from electron events and γ-ray

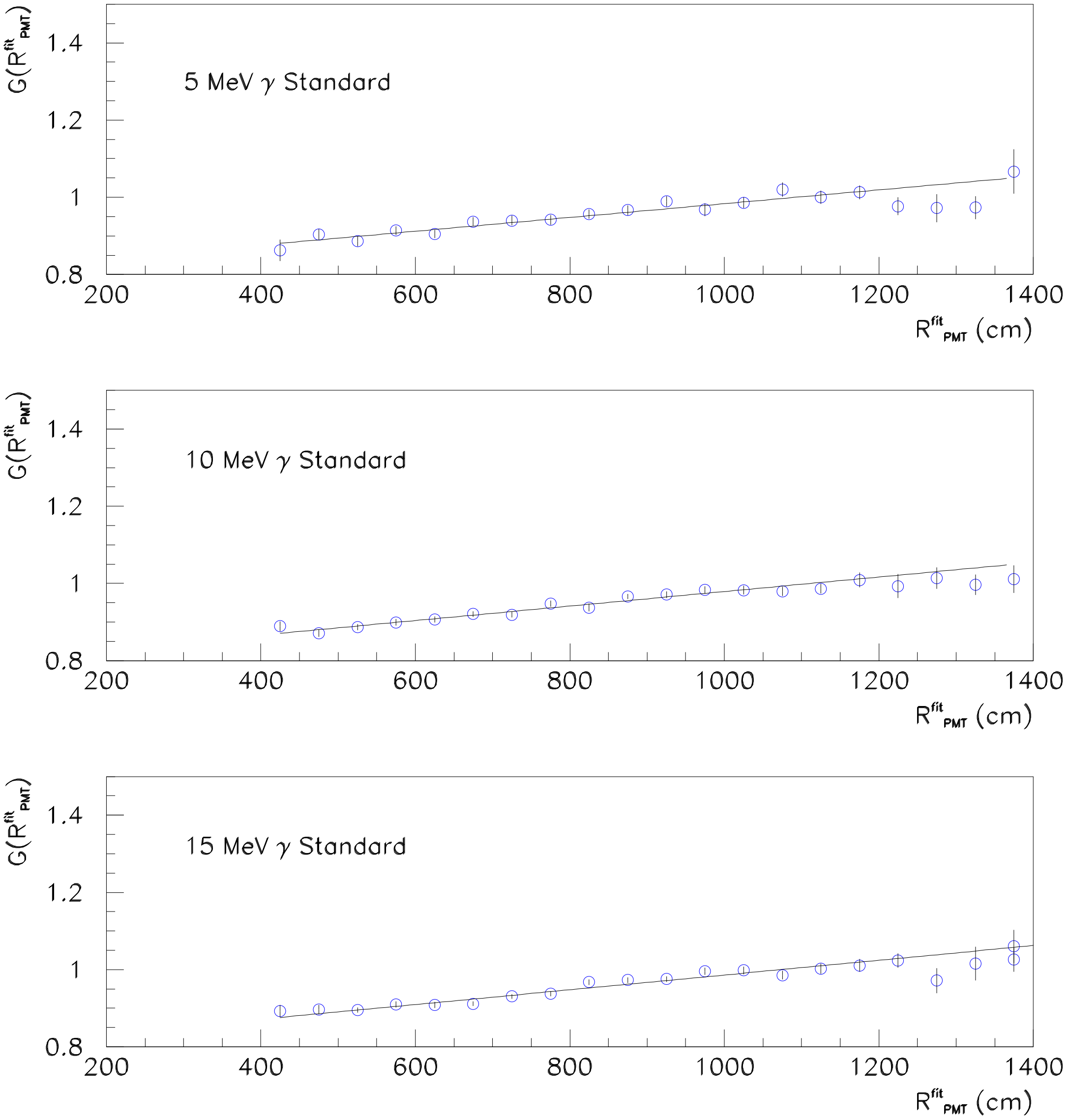

Figure 7.22: Matching the gain correction functions generated from electron events and from γ-ray events in the pure D_2O running scenario. The average R^{fit}_{PMT} shift for these three γ candles is (57±7) cm.

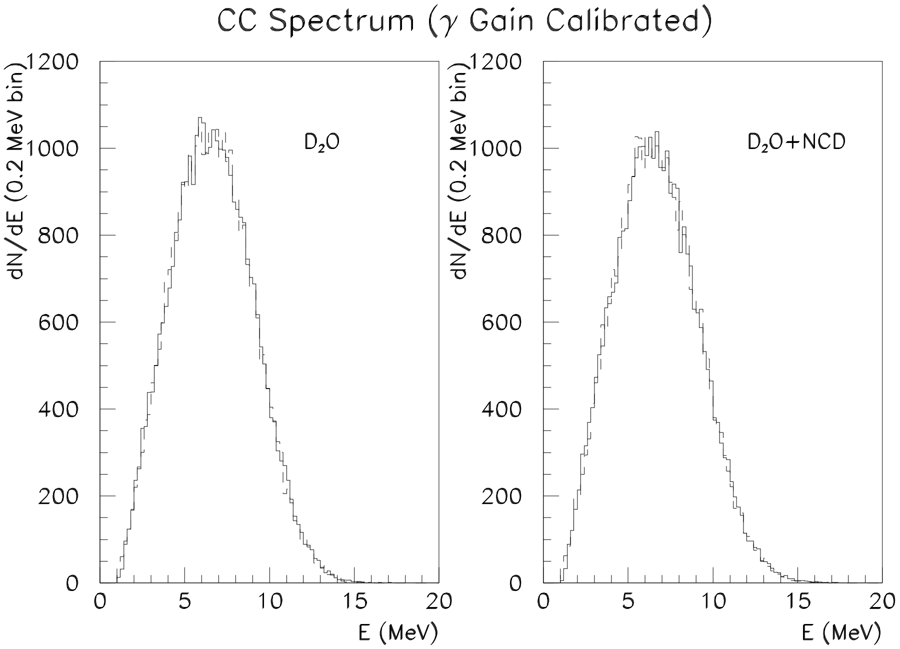

Figure 7.23: Reconstructed charged-current spectra. These spectra demonstrate that it is possible to use γ rays to calibrate the gain correction function. The solid histograms are the gain corrected and energy calibrated Monte Carlo spectra. The dashed histograms are theoretical spectra convoluted with the detector resolution function.

events to gain correct monoenergetic isotropic electrons generated evenly throughout the D_2O volume. Plots similar to Figure 7.12 were produced. When comparing the energy calibration curves extracted from using the two different classes of gain correction function, the difference between them is less than 0.5 photoelectron at 10 MeV.

Finally, we repeated this exercise for the charged-current energy spectrum. We used energy spectra corresponding to three years of full Standard Solar Model charged-current events reconstructed inside the D_2O volume. In Figure 7.23, the Monte Carlo N_{pe} spectrum was gain corrected and energy calibrated using the gain correction functions extracted from γ-ray events. This spectrum was then compared with the theoretical spectrum convoluted with the detector resolution. A Kolmogorov-Smirnov test showed that the probability for the null hypothesis is 0.83 and 0.70 for the pure D_2O and the NCD installed running scenarios.

In summary, we have demonstrated that it is possible to extract the gain correction functions from monoenergetic γ rays. One merely has to shift the functions in R_{PMT}^{fit} to correct for the distance the γ rays have to travel before converting to electrons.

Hitherto we have only considered using a gain correction function constructed from Monte Carlo events that were generated evenly within the D_2O volume. We found that this generalised gain correction function was adequate in correcting the Monte Carlo data. However, this situation is still somewhat idealised as we would not be able to generate any real, evenly distributed calibration data in the D_2O volume using our discrete calibration sources in SNO.

In a more realistic situation, gamma-ray sources are delivered to various locations within the SNO detector by the source manipulator system. By comparing the detector response at these locations to a "standard candle," one can then extract the gain correction function for each of these locations. This collection of gain correction functions, which is dependent on the reconstructed vertex position and the extracted R_{PMT} for the event, can then be used to gain correct the signals. Any possible asymmetry in the response of the real SNO detector can be more appropriately handled by this discrete set of gain correction functions.

Chapter 8

Multiple-Hit Effect in the SNO Photomultiplier Tube Array

> *. . . and now remains*
> *That we find out the cause of this effect,*
> *Or rather say, the cause of this defect,*
> *For this effect defective comes by cause:*
> *Thus it remains, and the remainder thus.*
>
> William Shakespeare
> Hamlet, Act ii, Sc. 2 (c.1600)

One of the most favourable parameters in analysing the signals from the SNO photomultiplier tube (PMT) array is the number of "fired" PMTs — N_{hits}. However, this parameter is intrinsically non-linear because of the multiple-hit effect. The reader is reminded that a PMT is fired when its anode charge output is equivalent to $\frac{1}{4}$ photoelectron level (page 184). Therefore, when multiple photons have contributed to the charge output of a PMT, it would be considered as only one PMT hit. One would expect this effect to have a bigger impact on the SNO detector's response as the energy of the event increases. The pT source we have developed is in the position to help the SNO collaboration to understand this effect. First of all, it has the highest energy output amongst all the calibration sources in SNO. Moreover, it is a monoenergetic source; therefore, it would not be necessary to unfold a complicated energy spectrum in order to understand the energy dependence of this effect. The optical calibration sources can help understanding this effect by varying the intensity of the optical light output. However, the nearly isotropic output of these sources cannot simulate the strong directional dependence of the Čerenkov cone. Therefore, we see that the pT source is in an advantageous position to complement the optical calibration in understanding this effect. In this chapter, we shall investigate how this multiple-hit effect would affect the linearity of SNO detector's energy response.

In the last chapter, we have developed an algorithm to correct for the event vertex positional dependence of SNO detector's energy response. However, a shortcoming of this gain correction technique is its inability to correct for the multiple-hit effect in each event. The gain corrected energy calibration line extracted from N_{hits} information has a ~3-4% systematic uncertainty in the calibrated energy near 10 MeV. This uncertainty arises from multiple hits not being correctly accounted for in extracting the gain correction function. This problem can be eliminated by using N_{pe}, which is linear in energy.

The calibrated charge spectrum N_{pe} is a broader distribution than the real generated photoelectron spectrum (N_{gen}) at a fixed energy. To first approximation, one can envision the energy spectrum reconstructed using the gain correction technique based on N_{pe} information as the real distribution of generated photoelectrons convolved with the single photoelectron spectrum of the PMT. As a result, any energy spectrum reconstructed using N_{pe} information will be broader than the corresponding one reconstructed using N_{hits} or N_{gen}.

To understand the systematic effects involving multiple hits, we investigated its dependence on energy and on position in both the D_2O and Neutral Current Detector (NCD) array installed scenarios. The Monte Carlo data sets we used in this study were generated using the same SNOMAN configuration as in last chapter.

8.1 Energy and Positional Dependence of the Multiple-Hit Effect

8.1.1 Energy Dependence

To understand the energy dependence of the multiple-hit effect, we generated electrons in the energy range of 2 to 25 MeV with a uniform distribution. The data set contained 30,000 isotropic electrons distributed evenly within the D_2O volume. In Figure 8.1, the real number of photoelectrons N_{gen} is plotted against the number of fired PMTs N_{hits} for this data set. In both running scenarios, it is clear that as the energy of the event increases, the bigger the spread in the deviation between N_{gen} and N_{hits} from linearity. The three-dimensional plots in Figure 8.2 demonstrate that the difference between the number of photoelectrons generated and the number of fired PMTs, Δ,

$$\Delta = N_{gen} - N_{hits}, \tag{8.1}$$

has a much broader distribution at higher energy.

Looking at Figure 8.1 more closely, one would realise that even at N_{hits}~100 (about 10 MeV), the magnitude of Δ can be as much as 10% of N_{hits}. This percentage increases substantially as energy increases.

We have also generated monoenergetic electron data sets at various discrete energies. In Figure 8.3, the distribution of Δ is shown for 5, 10, 15, 20-MeV isotropic electrons generated evenly within the D_2O volume. The Δ-histograms clearly demonstrate why using only the raw N_{hits} information to extract energy of an event is susceptible to a major systematic uncertainty. For instance, over 50% of the events have $\Delta > 0$ at an energy of 5 MeV. We define this proportion of events having non-zero Δ as $\delta_{>0}$:

$$\delta_{>0} = \frac{N_{\Delta>0}}{N_{trigger}} \tag{8.2}$$

where $N_{\Delta>0}$ is the number of events that registered a Δ greater than zero, and $N_{trigger}$ is the number of triggered events. In Table 8.1, we have summarised the energy dependence

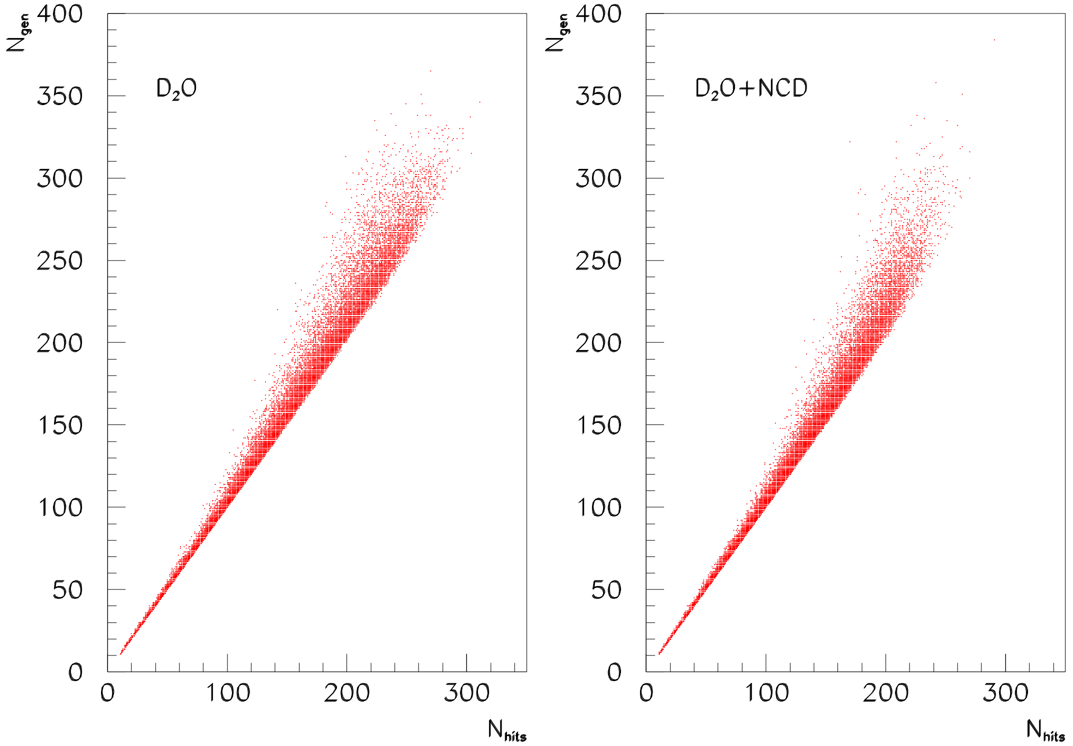

Figure 8.1: Real number of photoelectrons N_{gen} and N_{hits}. The data shown here represents 30,000 electrons generated with energy drawn uniformly in the range of 2 to 25 MeV. The electrons are evenly distributed in the D_2O volume, and have an isotropic angular distribution. It is clear that at higher N_{hits} the spread of N_{gen} becomes greater. This is an indication of an increasing number of PMTs receiving multiple hits.

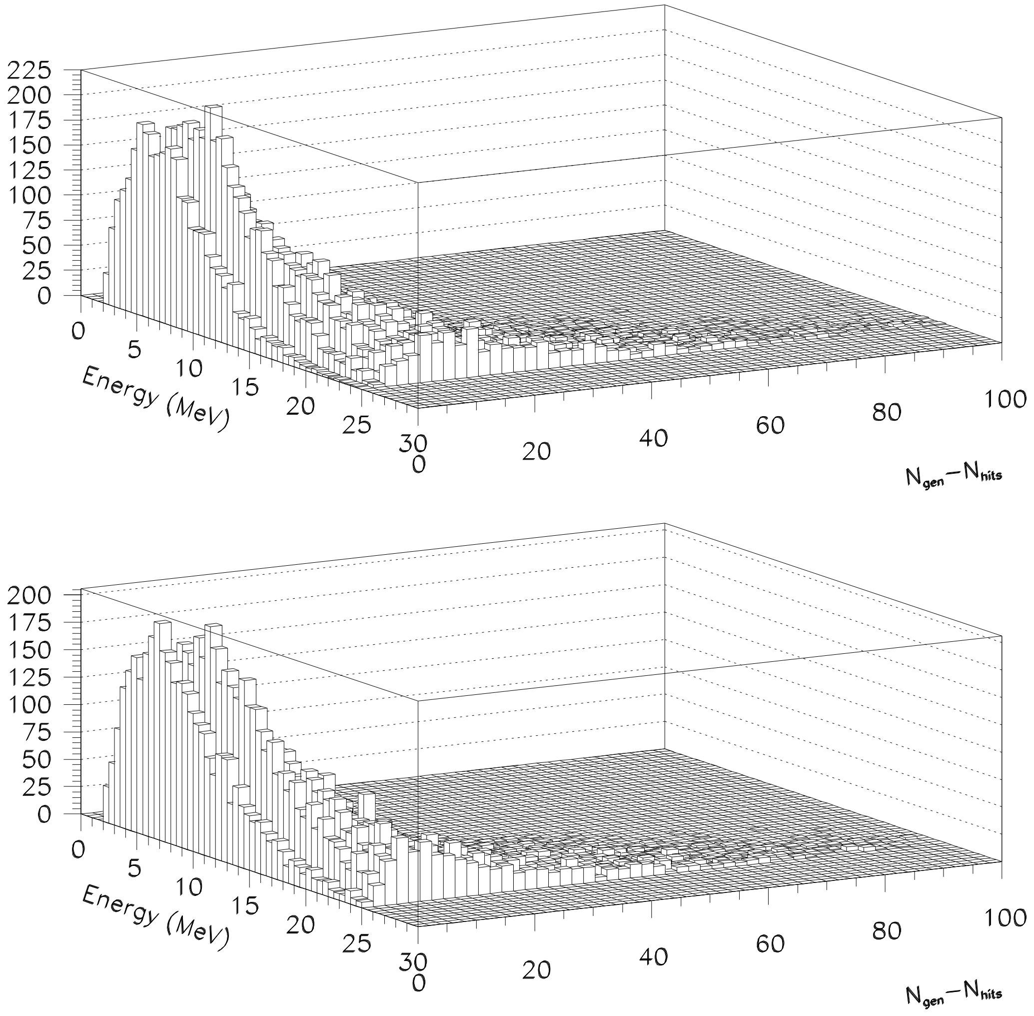

Figure 8.2: Energy dependence of the multiple-hit effect. The parameter, Δ, defined as N_{gen}-N_{hits} has a broader distribution as energy increases. The top panel shows the Δ distribution in the D_2O running scenario, whilst the bottom panel shows the NCD installed scenario. The data shown here represent 30,000 electrons generated with energy drawn uniformly in the range of 2 to 25 MeV.

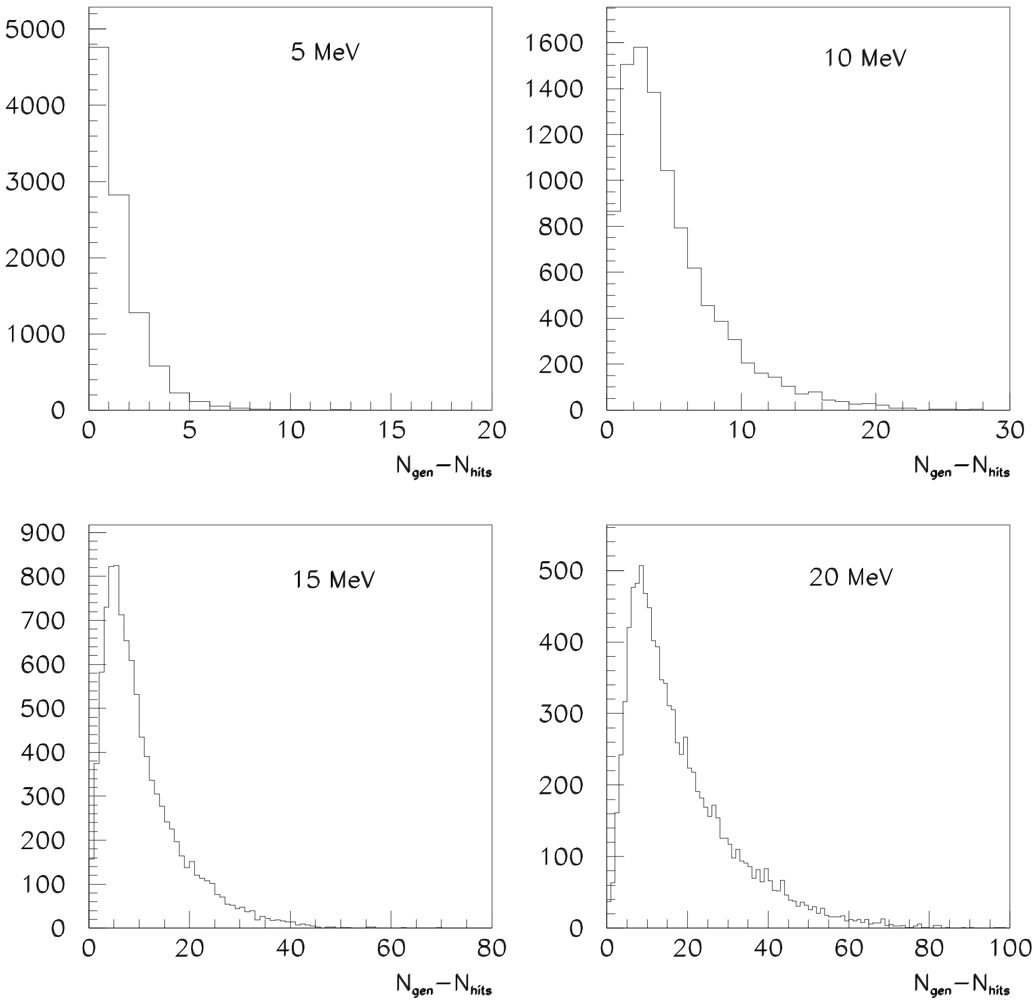

Figure 8.3: Distribution of Δ for 5, 10, 15 and 20-MeV electrons.

Energy (MeV)	D_2O		D_2O+NCD	
	$\delta_{>0}$	$\langle\Delta\rangle$	$\delta_{>0}$	$\langle\Delta\rangle$
5	0.517 ± 0.009	1.43 ± 0.01	0.475 ± 0.008	1.34 ± 0.01
10	0.912 ± 0.013	4.76 ± 0.04	0.863 ± 0.013	4.30 ± 0.04
15	0.984 ± 0.014	10.42 ± 0.08	0.967 ± 0.014	9.37 ± 0.09
20	0.996 ± 0.014	18.38 ± 0.08	0.992 ± 0.014	16.27 ± 0.13

Table 8.1: Energy dependence of the proportion of multiple-hit events and the mean Δ for electrons distributed evenly within the D_2O volume. The uncertainties quoted in this table are statistical uncertainties.

of $\delta_{>0}$ and the mean Δ for the monoenergetic electrons distributed evenly within the D_2O volume. We have verified that the N_{gen}-energy relation is linear; therefore, we can view $\langle\Delta\rangle$ as an estimate of N_{hits}'s deviation from linearity. Given that $N_{gen}\sim100$ at 10 MeV in the D_2O running scenario, average N_{hits} deviates from linearity by almost 5% at this energy.

8.1.2 Positional Dependence

Instead of using R_{PMT} as in last chapter, we used a refined parameter in this study of the positional dependence of the multiple hit effect. We define this parameter D_{PMT} as:

$$D_{PMT} = \frac{1}{N_{hits}} \sum_{i=1}^{N_{hits}} \left|\vec{r}_i - \vec{R}_v\right| \tag{8.3}$$

where $\vec{R}_v$ is the position of the event vertex generated by the Monte Carlo, the set $\{\vec{r}_i\}$ is the position of the i^{th} hit PMT. Therefore, D_{PMT} is the average distance between the event vertex and all the hit PMTs in the event.

The positional dependence of Δ is shown in Figure 8.4 for electrons in both run scenarios. The three-dimensional plots show that Δ has a much longer tail at small D_{PMT}. These events are the ones originating close to the acrylic vessel and directed outward towards the PMT array. This general observation is in agreement with a similar

Energy (MeV)	D_2O	
	$\delta_{>0}$	$\langle\Delta\rangle$
5	0.355±0.007	0.95±0.01
10	0.852±0.013	2.57±0.02
15	0.987±0.014	5.42±0.03

Table 8.2: Energy dependence of the proportion of multiple-hit events and the mean Δ for standard electron candles in D_2O. The uncertainties quoted in this table are statistical uncertainties.

analysis performed with the parameter R_{PMT} in the last chapter.

We want to compare $\langle\Delta\rangle$ in Table 8.1 to standard electron calibration "candles" in order to understand the significance of positional dependence. For our standard electron candles, we used 5, 10, and 15-MeV electrons generated at the centre of the SNO detector in the pure D_2O running scenario. In Table 8.2, we show the results of our analysis for the standard candles. Given the huge difference in $\langle\Delta\rangle$ between these standard candles and the evenly distributed cases in Table 8.1, it is apparent that one must handle the positional dependence of the signal with great care.

8.2 An Algorithm to Correct for the Multiple-Hit Effect

After a somewhat qualitative study in the previous sections on the energy and positional dependence of the multiple-hit effect, we shall describe in this section an algorithm which we have developed to correct for this effect.

Since it has been suggested in the last chapter that a quadratic fit of the energy-N_{hits} calibration curve is better than a linear fit in the "zeroth order approximation," it is natural to assume that there is a second-order component in the N_{hits} to N_{gen} conversion:

$$N_{gen} = N_{hits} + a_2 N_{hits}^2 \tag{8.4}$$

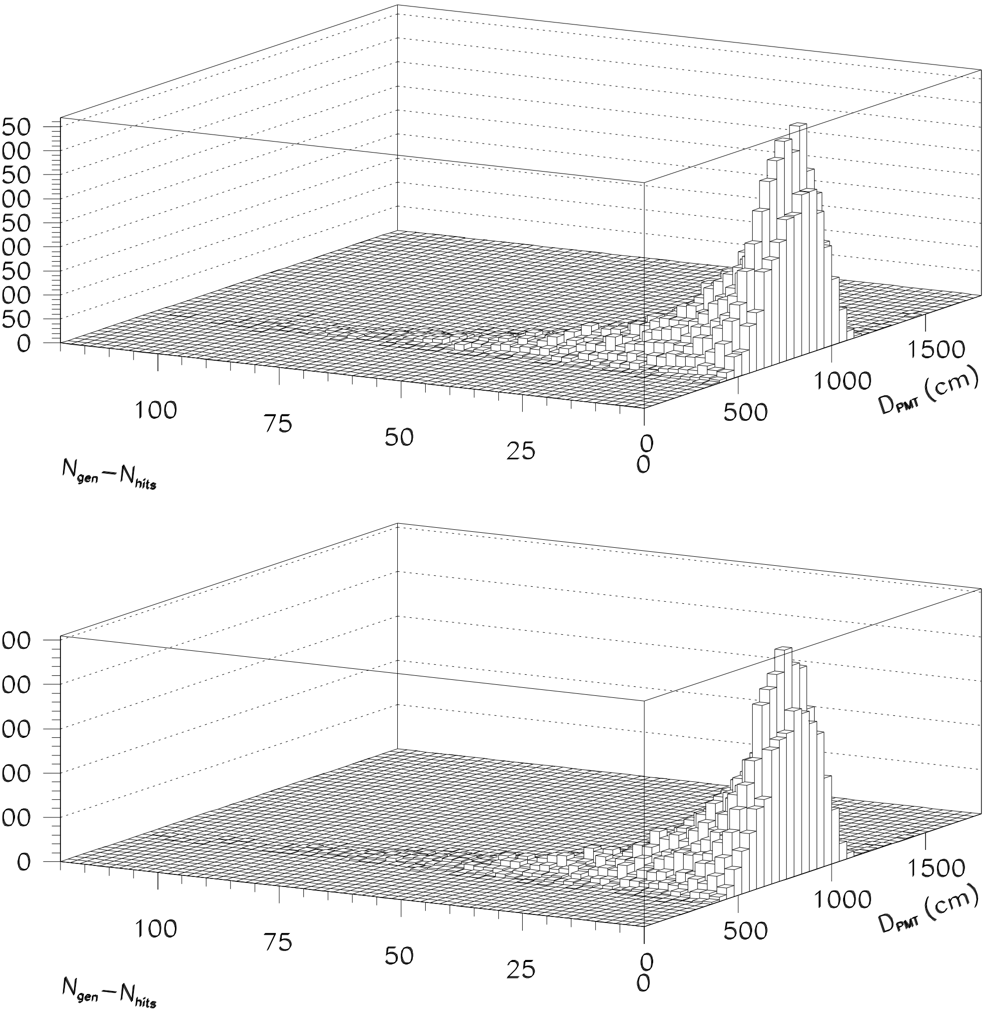

Figure 8.4: Positional dependence of the multiple-hit effect. The top panel shows the Δ distribution in the D_2O running scenario, whilst the bottom panel shows the NCD-installed scenario. Δ has a much longer tail at small D_{PMT}. These are the events originating close to the acrylic vessel and directed outward. The data shown here represent 30,000 electrons generated with energy drawn uniformly in the range of 2 to 25 MeV.

where a_2 is the second-order contribution which is dependent on the position of the event. We parameterise a_2 as a function of D_{PMT}:

$$a_2(D_{PMT}) \;=\; \beta_\circ + \frac{\beta_1}{(D_{PMT}-\beta_2)^2} \tag{8.5}$$

where $\{\beta_i\}$ are the parameters to be fitted. Naively speaking, this a_2 contribution should vary as $\sim D_{PMT}^{-2}$ because the number of PMTs that lie on a "ring" subtended by the Čerenkov cone goes as $\sim D_{PMT}^2$.

To generate the D_{PMT} dependence of a_2, we divided events in the 30,000-electron data set into 20-cm D_{PMT} bins. For each of these bins, we extracted the corresponding a_2 by fitting the N_{gen} distribution to the relationship in Eqn.(8.4). After extracting the a_2 function from all the bins, it was then fitted to Eqn.(8.5). This last fit for the two running scenarios is shown in Figure 8.5.

With the function a_2 determined for both the D_2O and the NCD-installed running scenarios, we can then correct for the multiple-hit effect on an event-by-event basis using the available N_{hits} and vertex information. We first ran the events in the 30,000-electron data sets through this correction mechanism. The corrected N_{hits} distributions are shown in Figure 8.6. The agreement between the multiple-hit corrected N_{hits} spectra and the corresponding Monte Carlo generated N_{gen} spectra is good. To further demonstrate the power of this correction algorithm, the distributions of the difference between the multiple-hit corrected N_{hits} and Monte Carlo generated N_{gen} for both running scenarios are shown in Figure 8.7. The sharp peaks at zero in this latter figure convince us further that this algorithm performs this multiple-hit correction to a high degree of accuracy.

So far, we have been using in our analysis the vertex position $\vec{R}_v$ generated by SNOMAN to avoid introducing any event fitter dependent effect. In the last chapter, we demonstrated that the simplest fitter of all—the time fitter—can reconstruct event vertex and electron direction reliably in both running scenarios. We wanted to verify that

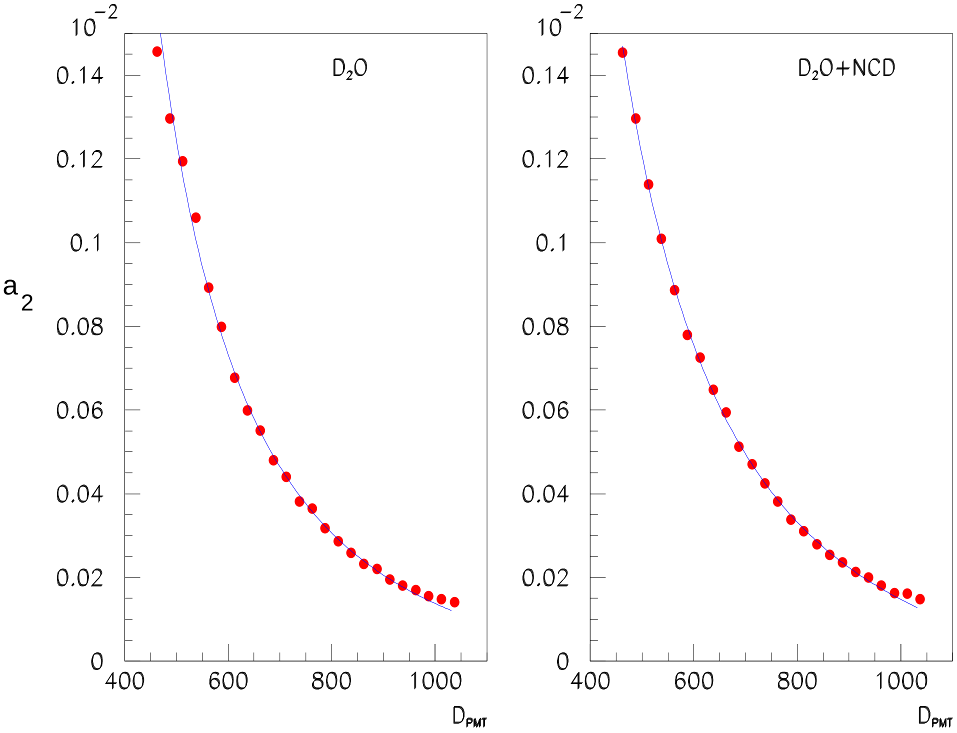

Figure 8.5: Fitting the second order contribution in N_{hits} non-linearity as a function of D_{PMT}. The function a_2 was fitted according to Eqn.(8.5).

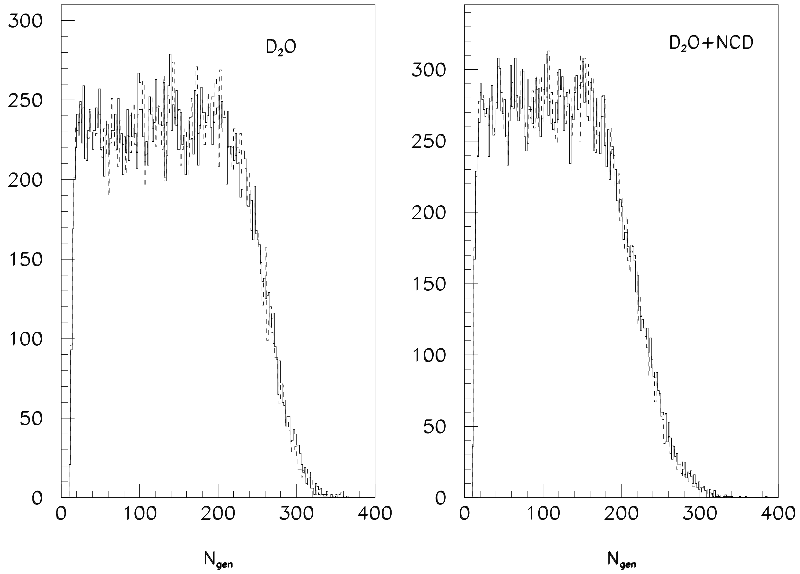

Figure 8.6: Comparing the multiple-hit corrected N_{hits} distributions to Monte Carlo generated N_{gen} distributions. N_{hits} from the 30,000-electron data set was corrected on an event-by-event basis. The Monte Carlo generated N_{gen} distributions are shown as the solid histograms, whilst the ones corrected from N_{hits} using the multiple-hit correction scheme are shown as dashed histograms.

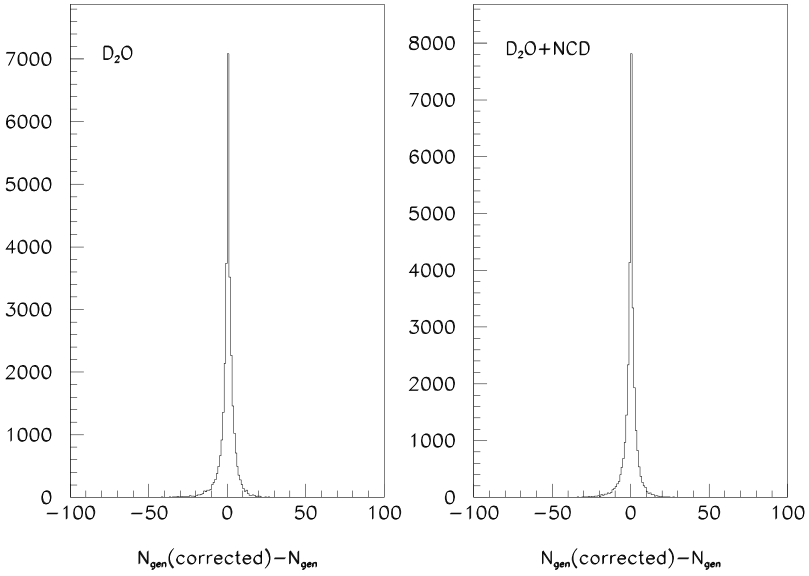

Figure 8.7: Difference between multiple-hit corrected N_{hits} distributions and Monte Carlo generated N_{gen} distributions.

the good agreement obtained in the multiple-hit correction analyses above will also hold for time fitter analysed events. We defined the time fitter analysed position parameter D_{PMT}^{fit} as

$$D_{PMT}^{fit} = \frac{1}{N_{hits}} \sum_{i=1}^{N_{hits}} \left| \vec{r}_i - \vec{R}_v^{fit} \right| \tag{8.6}$$

where $\vec{R}_v^{fit}$ is the event vertex fitted by the time fitter. We repeated the analysis by first extracting the corresponding a_2^{fit} in this scenario. The shape of the resulting a_2^{fit} functions looks similar to those in Figure 8.5, although the numerical values for the $\{\beta_i\}$ parameters differ somewhat. Finally, we found that there is not any degradation in the multiple-hit correction algorithm when the time-fitter analysed parameters were used.

Astute readers will realise that the good agreement between the multiple-hit corrected N_{hits} distributions and the N_{gen} distributions might be biased. This is because we corrected the N_{hits} distributions using a correction function extracted from the same data set. To verify the robustness of this correction scheme, we used the correction functions extracted from the 30,000-electron data sets to correct for monoenergetic electron N_{hits} spectra at 5, 10, 15, and 20 MeV. Each of these monoenergetic sets contains approximately 10,000 triggered events. We found that the multiple-hit correction scheme we have developed did an excellent job in correcting these monoenergetic electron data sets as well.

8.3 Multiple-Hit Effect in Gamma-Ray Events

As the energy of the gamma ray increases, the probability that it would be converted to electrons through Compton scattering decreases whilst that for pair production increases. Therefore, we would expect different Čerenkov photon hit patterns on the PMT array for electrons and gamma rays. The difference between the electron and the gamma ray hit patterns is small in the solar neutrino energy regime. But we should still ask ourselves

Energy (MeV)	D_2O	
	$\delta_{>0}$	$\langle\Delta\rangle$
5	0.374±0.007	1.16±0.01
10	0.836±0.013	4.00±0.03
15	0.970±0.014	9.94±0.08
20	0.994±0.014	17.16±0.08

Table 8.3: Energy dependence of the proportion of multiple-hit events and the mean Δ for gamma rays distributed evenly within the D_2O volume. The uncertainties quoted in this table are statistical uncertainties.

whether the multiple-hit correction technique we developed for electrons above would work for gamma-ray events as well.

In Table 8.3, $\delta_{>0}$ and $\langle\Delta\rangle$ for 5, 10, 15 and 20-MeV isotropic gamma rays distributed evenly within the D_2O volume are shown. Comparing these values with the corresponding ones for electrons in Table 8.1, we can see that multiple-hit effect appears to affect gamma-ray events to a slightly smaller extent than electron events at the same energy.

This difference in the influence of the multiple-hit effect on electron and gamma-ray events can arise from both the difference in the PMT hit pattern and the reduction in Čerenkov light output in gamma-ray events. One would expect the latter effect to have a bigger influence. Hence, we normalised $\langle\Delta\rangle$ by the average number of generated photoelectrons $\langle N_{gen}\rangle$ for both electron and gamma-ray events. In Figure 8.8, we show this quantity $\langle\Delta\rangle/\langle N_{gen}\rangle$ as a function of energy. The close agreement between the electron and the gamma-ray events indicates that the influence of multiple hits results primarily from the difference in their Čerenkov light output.

In the last chapter, we noted that gamma rays converted in the acrylic vessel have an enhanced Čerenkov light output because of acrylic's higher index of refraction. Given that these events originate closer to the PMT array, the probability that each hit PMT would receive multiple photons increases if the gamma rays are directed towards the array.

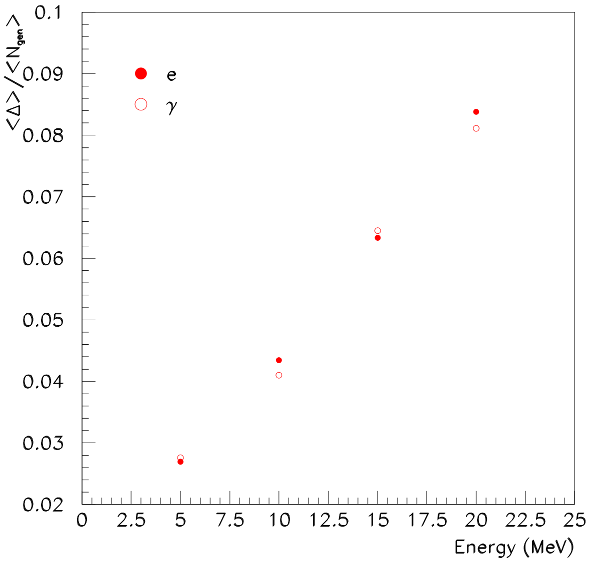

Figure 8.8: $\langle\Delta\rangle$ normalised by the average number of generated photoelectrons N_{gen} for monoenergetic electrons and gamma rays. It is clear from this plot that the influence of multiple hits on electron and gamma-ray events is correlated mainly with the difference in their Čerenkov light output.

In Figure 8.9(a), N_{gen} is plotted against D_{PMT} for 10,000 isotropic 20-MeV gamma ray events distributed evenly within the D_2O volume. The long tail at small D_{PMT} illustrates this enhancement. We placed a cut on this tail as shown in the figure. In Figure 8.9(b), the Δ distribution for events within this cut and for the whole data set are shown. It is clear that events within this cut dominate the histogram at large Δ. Finally, in Figure 8.9(c), we show how well the time fitter can reconstruct the events within this cut. Almost all these events were reconstructed outside the vessel. As we commented in the last chapter, this is expected since the vertices of the converted electrons originate in the acrylic vessel. Moreover, the time fitter systematically pulls the fitted vertex towards the PMT array.

We should apply the multiple-hit correction scheme we developed in the last section to gamma-ray events to check for its robustness. The time fitter was used to reconstruct

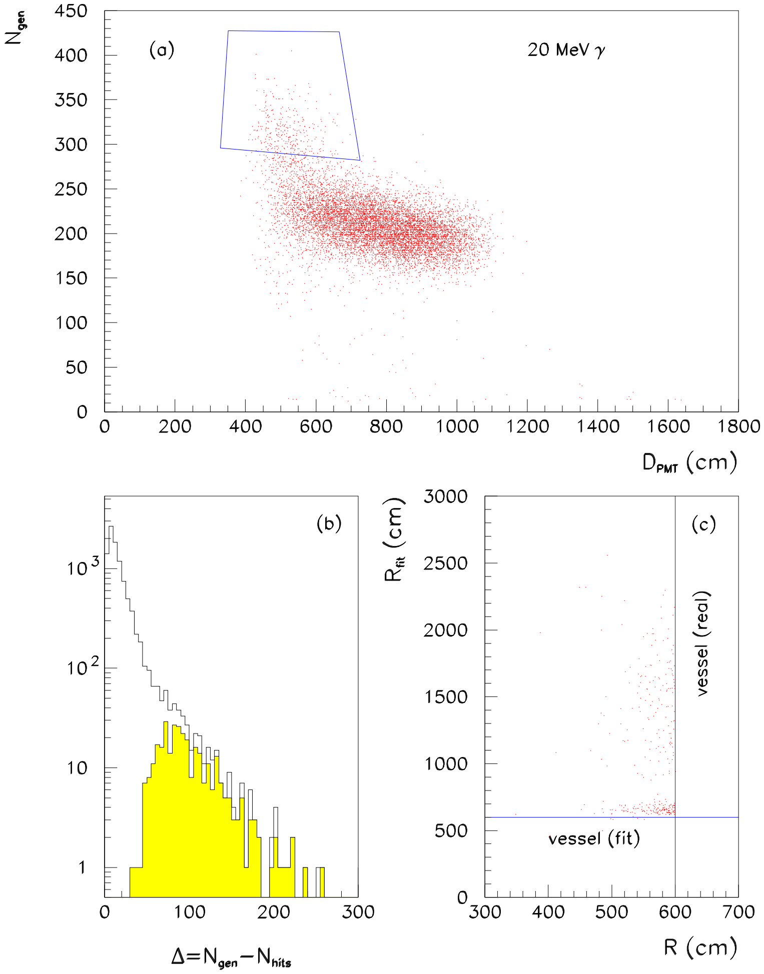

Figure 8.9: Positional dependence of N_{gen} for 20-MeV gamma rays. (a) N_{gen} is plotted against D_{PMT} for 10,000 isotropic 20-MeV gamma rays distributed evenly within the D_2O volume. The tail at small D_{PMT} indicates enhanced Čerenkov light output due to gamma-ray conversion in the acrylic vessel; (b) $\Delta = N_{gen} - N_{hits}$ is plotted for the whole data set and for the events within the cut shown in (a). The shaded histogram shows the distribution of Δ after this cut had been applied. It is clear that events within this cut dominate the histogram at large Δ; (c) The time fitter fitted radial distance (R_{fit}) is plotted against the origin of the gamma rays (R) for events within the cut. Almost all of the events within this cut were reconstructed outside the D_2O volume.

Energy (MeV)	$\mu_{N_{gen}}$	$\sigma_{N_{gen}}$
5	50.3	8.4
10	103.4	13.1
15	155.5	16.4

Table 8.4: N_{gen} statistics for 5, 10, and 15-MeV monoenergetic electron standard candle sets. The electrons were generated at the centre of the SNO detector. The resulting N_{gen} distributions were fitted to a normal distribution. The statistical uncertainty of the numbers is less than 0.2%.

these gamma-ray events. We then used the reconstructed information to calculate D_{PMT}^{fit}, and to correct the N_{hits} information for multiple hits using the correction function generated for the electron events in the last section. This usage of the electron correction function is to ensure that it is not necessary to perform a particle identification prior to this correction. In Figure 8.10, we show the multiple-hit corrected N_{hits} spectra along with Monte Carlo generated N_{gen} spectra. The agreement between them is good.

8.4 Applying Gain Correction to Multiple-Hit Corrected Events

As we mentioned earlier, the gain correction technique we developed in the last chapter broke down when trying to correct for the intrinsically non-linear entity N_{hits}. With the multiple-hit correction scheme above, we can now linearise the N_{hits} response.

First we need to generate the "standard candle" for the gain correction mechanism. We generated monoenergetic electron events from the centre of SNO with energies of 5, 10 and 15 MeV, and extracted the mean N_{gen} from these runs by fitting the spectra to a Gaussian distribution. In Table 8.4, we have summarised the extracted information.

Following the same procedure as we outlined in the last chapter, we generated the gain correction function $G^{i}_{N_{gen}^{fit}}(D_{PMT}^{fit})$ where N_{gen}^{fit} represents the multiple-hit corrected N_{hits} using the time-fitted D_{PMT}^{fit} for i=D_2O or NCD. Only events that were reconstructed with

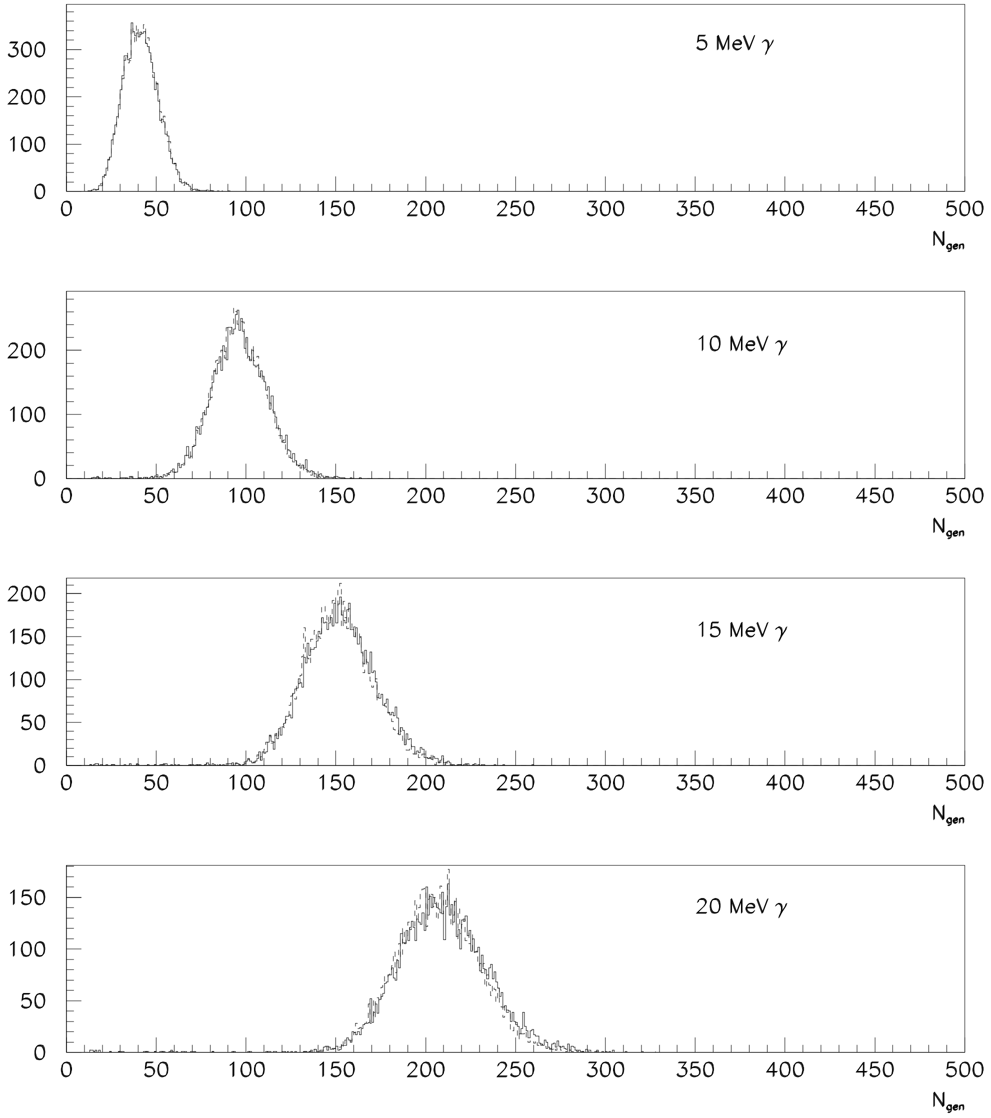

Figure 8.10: Reconstructing monoenergetic gamma-ray N_{gen} distribution in the D_2O running scenario. We used time fitter reconstructed D_{PMT}^{fit} to multiple-hit correct the events. The correction function used was the one generated with the electron data. The solid histograms are the Monte Carlo generated N_{gen} distributions, whilst the dashed histograms are the multiple-hit corrected ones based on N_{hits} information.

a vertex within the D_2O volume were used in extracting the gain correction function. In Figure 8.11, a plot showing the gain correction functions extracted using different candle sets demonstrates that the non-linearity associated with the gain correction functions extracted with only N_{hits} information (Figure 7.9) has been corrected for.

As we argued in the last chapter, we would expect

$$G^{i}_{N^{fit}_{gen}}(D^{fit}_{PMT}) \propto \exp\left(\lambda D^{fit}_{PMT}\right) \qquad i = \mathrm{D_2O,\ NCD} \tag{8.7}$$

where λ is an average attenuation length for optical photons propagating through the D_2O, acrylic vessel and the light water. Hence, we fitted the gain correction functions in Figure 8.11 to a linear relationship given that $\lambda D^{fit}_{PMT} \ll 1$.

To combine the multiple-hit correction and the gain correction, N_{hits} information was first processed by the multiple-hit algorithm on an event-by-event basis. The multiple-hit corrected output for each event was then processed by the gain correction mechanism. In Figure 8.12, these two-tier corrected energy spectra are shown along with the corresponding real energy spectra convoluted with the detector resolution function for the NCD-installed scenario.

We extracted the energy calibration line and the energy resolution of the detector by running monoenergetic electron events through the two-tier correction system. These events were generated with an isotropic angular distribution and a uniform distribution in position within the D_2O volume. The energy calibration and the energy resolution functions are shown in Figure 8.13. In the figure, the energy calibration is linear. There is a significant improvement in the energy resolution in the NCD-installed scenario when comparing the two-tier corrected spectra with the "zeroth order" N_{hits} resolution. In Figure 8.14, we compare these two resolution functions in the NCD-installed scenario. As a comparison, the "zeroth order" N_{hits} and the two-tier corrected resolution in the D_2O running scenario are also shown. When comparing the "zeroth order" N_{hits} resolution

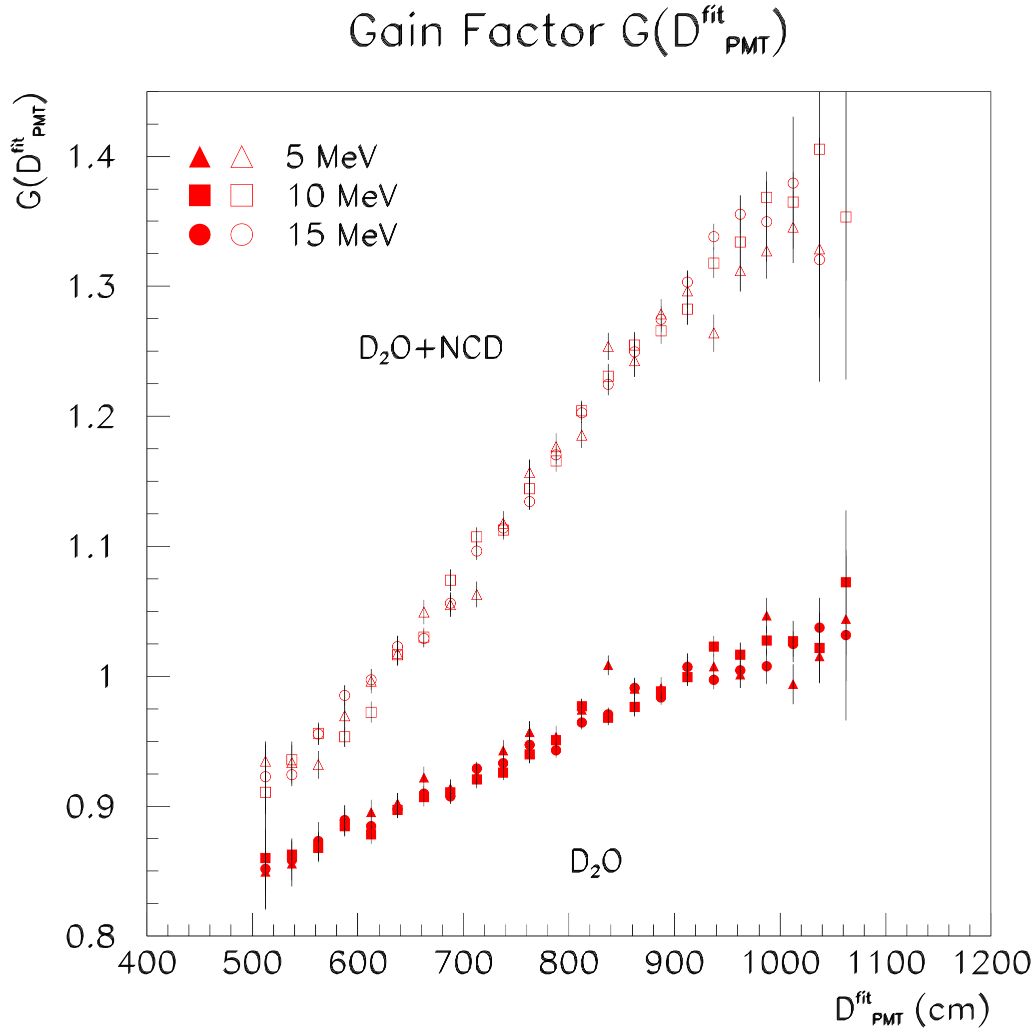

Figure 8.11: Gain correction functions extracted using multiple-hit corrected N_{hits} using 5, 10 and 15-MeV standard electron candles. Only events that were reconstructed with a vertex within the D_2O volume were used in extracting the gain correction functions. The good agreement amongst the gain correction functions extracted using different standard candles convinced us that the non-linearity associated with N_{hits} that we observed previously have been correctly dealt with.

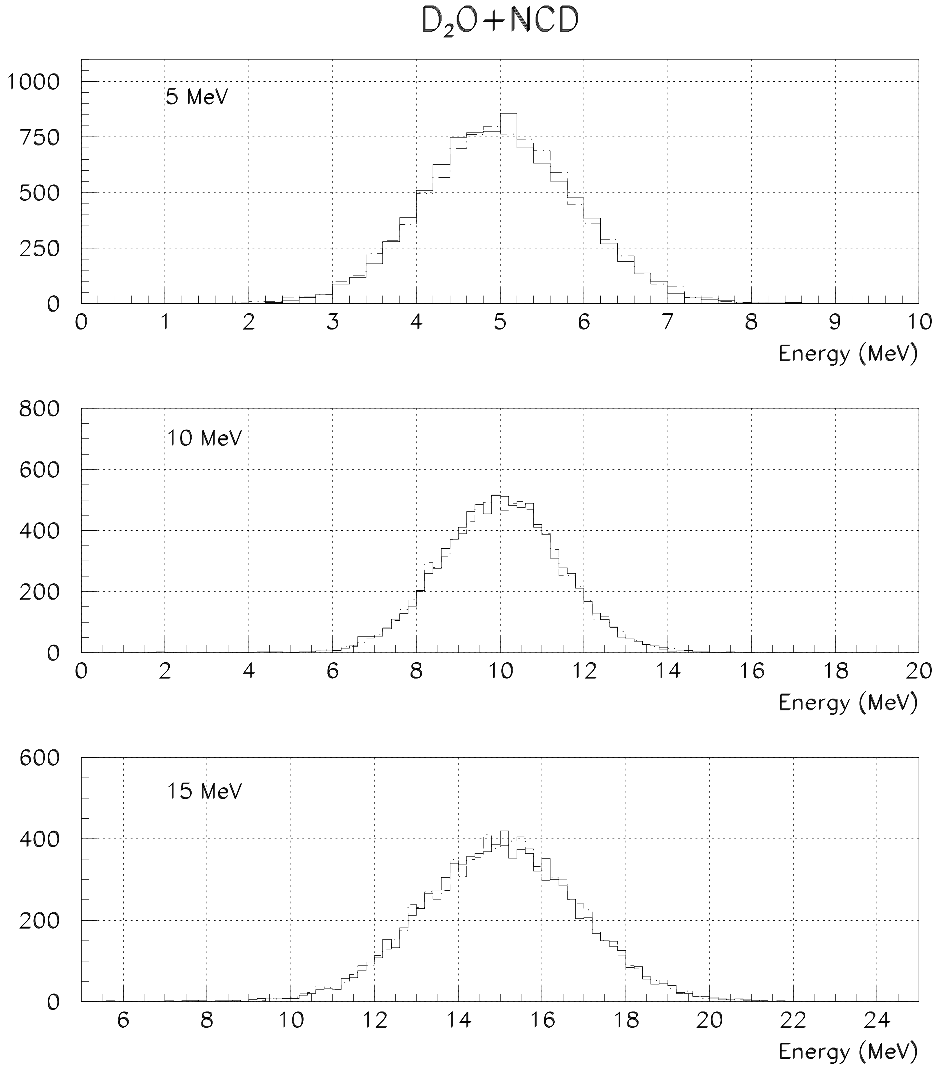

Figure 8.12: Comparing the two-tier correction scheme with theoretical expectation in the NCD installed running scenario. The solid histograms are the two-tier corrected distribution, and the dashed histograms are generated by convoluting the detector resolution function with a theoretical energy line.

and the two-tier corrected resolution in the D_2O running scenario, it is clear that the former has a marginally better resolution. This is counter-intuitive as more information was used in processing the signals in the latter case. We shall investigate this "anomaly" in the next section.

An improvement in the energy resolution by the two-tier correction scheme has a significant impact on SNO data analysis. A previous analysis by Skensved [120] showed that the SNO analysis threshold might be as high as 5.6 MeV when the NCD array is in place. This threshold is set at the point where the "background wall" (see Section 2.2.2) and the CC spectrum intersects. With this two-tier correction scheme we developed, the energy resolution has significantly improved in the NCD running scenario. This would lead to a narrower tail from the low energy background wall. We estimated that the analysis threshold might be lowered to ~5.3 MeV when this analysis technique is employed under the NCD running scenario.

8.5 The N_{hits} Resolution Anomaly

In the last section, we found that the N_{hits} resolution in the "zeroth order" approximation is *better* than the two-tier corrected resolution. This is somewhat counter-intuitive as the two-tier correction scheme linearises the energy response. Therefore, photon counting is done correctly in the two-tier corrected quantities. We shall try to understand this "anomaly" in this section.

We shall study the results of a very simple Monte Carlo experiment. In this experiment, we have a certain number of bins (number of available PMT N_{PMT}) to accept objects (Čerenkov photons) randomly thrown at them. A total of N°_{gen} objects are thrown. Not all of these objects will land inside a bin, and there is a fixed probability (photocathode quantum efficiency p_{qe}) that an object will land inside a bin. We set p_{qe}

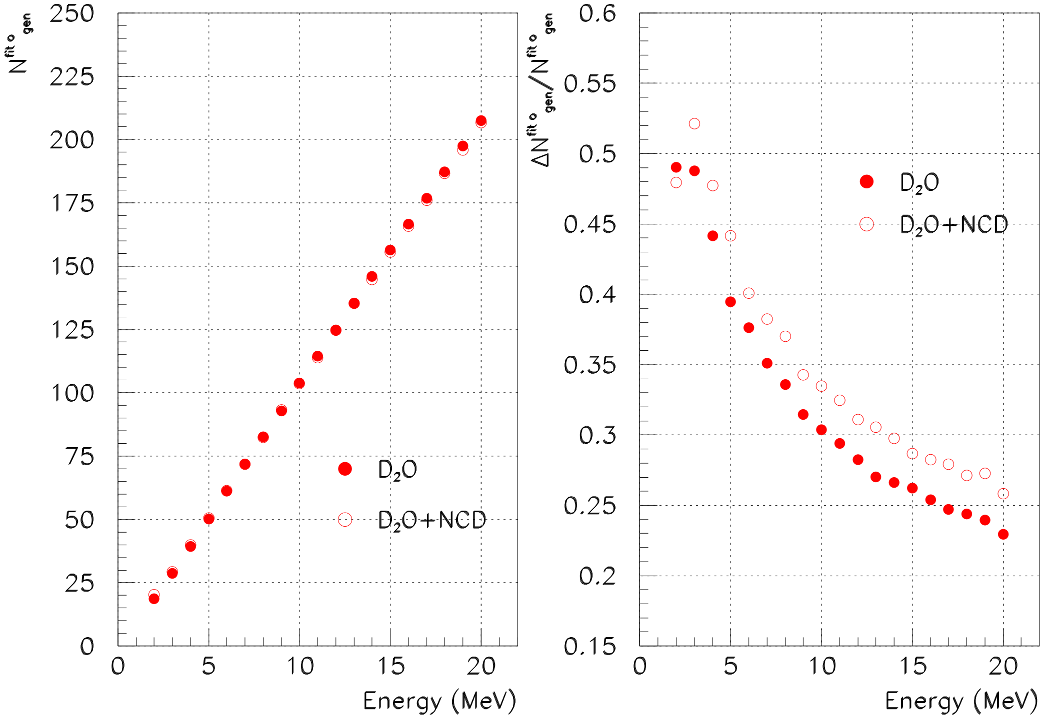

Figure 8.13: Energy calibration curve and detector resolution using two-tier corrected information. The energy calibration line is now linear, and there is a significant improvement for the energy resolution in the NCD-installed scenario. The "improvement" in energy resolution at $E \leq 3$ MeV is an artifact of the 10-hit hardware threshold.

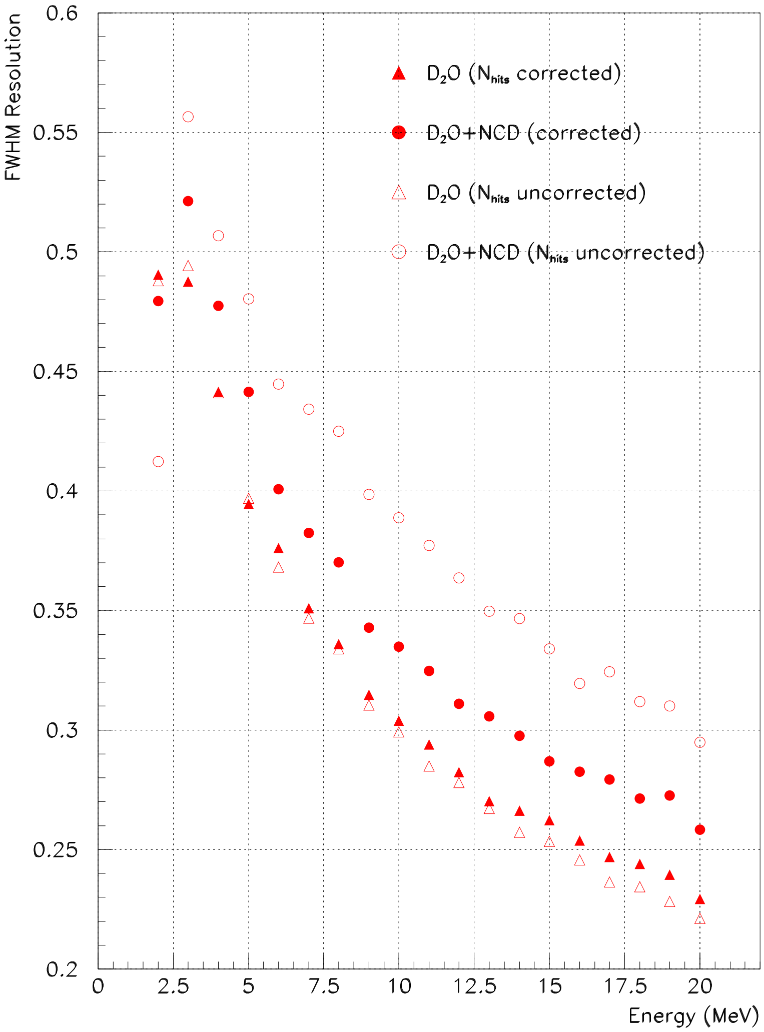

Figure 8.14: Comparing the energy resolution in the "zeroth order approximation" and the two-tier corrected electron events. The "improvement" in energy resolution at $E \leq 3$ MeV is an artifact of the 10-hit hardware threshold.

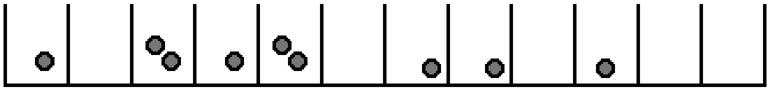

Figure 8.15: A simple Monte Carlo analysis to understand the first two moments in N_{hits} distribution. In the configuration above, the number of available bins N_{PMT}=12, the number of filled bins N_{hits}=7, and the total number of detected objects N_{gen}=9.

N°_{gen}	$\langle N_{gen} \rangle$	$\sigma_{N_{gen}}$	$\sigma_{N_{gen}}/\langle N_{gen} \rangle$
100	33.33	4.71	0.141
200	66.66	6.67	0.100
300	100.0	8.17	0.082

Table 8.5: Expected mean, standard deviation and fractional width for N_{gen} in the simple Monte Carlo experiment to understand the N_{hits} resolution anomaly. N°_{gen} is the total number of "throws" generated. We have assumed a quantum efficiency p_{qe} of $\frac{1}{3}$.

to $\frac{1}{3}$. What we want to determine from this experiment is the dependence of the mean and the standard deviation of the number of occupied bins (N_{hits}) and the number of detected objects (N_{gen}) on the number of available bins N_{PMT}. It is clear that N_{hits} and N_{gen} are two different distributions. The diagram in Figure 8.15 shows the configuration of this Monte Carlo experiment. This simple Monte Carlo configuration can be compared to a "ring" of PMTs that lie right at Čerenkov cone angle, and these PMTs are ready to accept Čerenkov photons in the absence of any light scattering in the D_2O.

The distribution of the number of detected objects N_{gen} follows a binomial distribution. We have summarised the values of the mean $\langle N_{gen} \rangle$ and standard deviation $\sigma_{N_{gen}}$ for the cases of N°_{gen} =100, 200 and 300 in Table 8.5. We have verified that the results of our Monte Carlo experiment agree with these expressions for the N°_{gen} cases we considered.

To better understand the N_{hits} anomaly, we plotted the two ratios, $\langle N_{hits} \rangle / \langle N_{gen} \rangle$ and $\sigma_{N_{hits}}/\sigma_{N_{gen}}$, against the number of available bins N_{PMT}. Given that $\langle N_{gen} \rangle$ is a linear

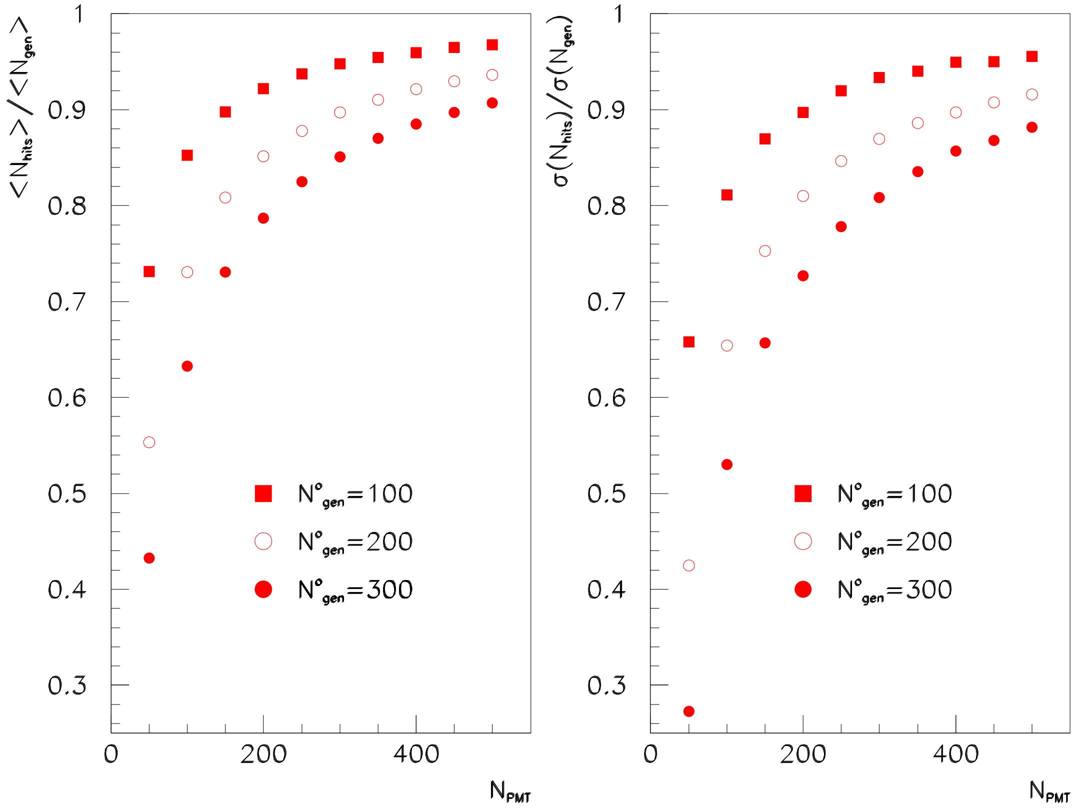

Figure 8.16: Relative deviation from linearity for $\langle N_{hits}\rangle$ and $\sigma_{N_{hits}}$ in the simple Monte Carlo experiment to understand the N_{hits} resolution anomaly.

quantity, we want to determine the relative deviation from linearity for $\langle N_{hits}\rangle$ and $\sigma_{N_{hits}}$ by inspecting these ratios. This is shown in Figure 8.16.

It should be clear that as $N_{PMT}\rightarrow\infty$, these ratios should approach unity. Of course, this theoretical limit could not be reached for signals with a strong directionality, such as the Čerenkov light cone, in a finite-size detector. However, if one looks at these ratios closely, it is surprising to learn that even for the case of $N^{\circ}_{gen}=100$ with N_{PMT}=500, i.e. a factor of 5 difference in the number of generated photons to the number of available bins, the ratios $\langle N_{hits}\rangle/\langle N_{gen}\rangle$ and $\sigma_{N_{hits}}/\sigma_{N_{gen}}$ are about 4% and 5% from unity.

Another interesting fact that is obvious from this figure is that the relative deviation from linearity for $\langle N_{hits} \rangle$ and $\sigma_{N_{hits}}$ are different for the same N_{PMT}. In fact,

$$\frac{\langle N_{hits} \rangle}{\langle N_{gen} \rangle} > \frac{\sigma_{N_{hits}}}{\sigma_{N_{gen}}} \tag{8.8}$$

in all the cases we have considered. What this means is that the "resolution" for N_{hits} will be better than N_{gen} even though we have done all the counting correctly in the latter case. The reader is reminded that N_{hits} and N_{gen} are two different distributions. This is the primary reason why the N_{hits} resolution is "better" than the two-tier corrected resolution in the D_2O running scenario as we found in the last section. The two-tier correction scheme did improve the resolution in the NCD-installed scenario because the severe degradation in resolution in this scenario is primarily caused by the positional and directional dependence of the detector response. The two-tier correction corrects for these dependencies and significantly improves the resolution.

To further illustrate this last point, we have plotted the two-tier corrected full-width-at-half-max (FWHM) resolution $R_{2-tier}(E)$, the Monte-Carlo generated N_{gen} FWHM resolution $R_{Ngen}(E)$, and the N_{hits} FWHM resolution $R_{Nhits}(E)$ as functions of energy for isotropic, monoenergetic electrons evenly distributed in a pure D_2O run scenario in Figure 8.17. When one inspects this plot, one would find that

$$R_{Ngen}(E) > R_{2-tier}(E) > R_{Nhits}(E). \tag{8.9}$$

This clearly states that the two-tier correction scheme does improve the N_{gen} resolution R_{Ngen}.

One can conclude from this simple Monte Carlo analysis that even though the N_{hits} resolution appears to be "better" than the N_{gen} resolution, one should be really careful in interpreting its true significance. Whilst N_{hits} is a narrower distribution, it is N_{gen} which represents the true photon counting statistics and contains maximum amount of

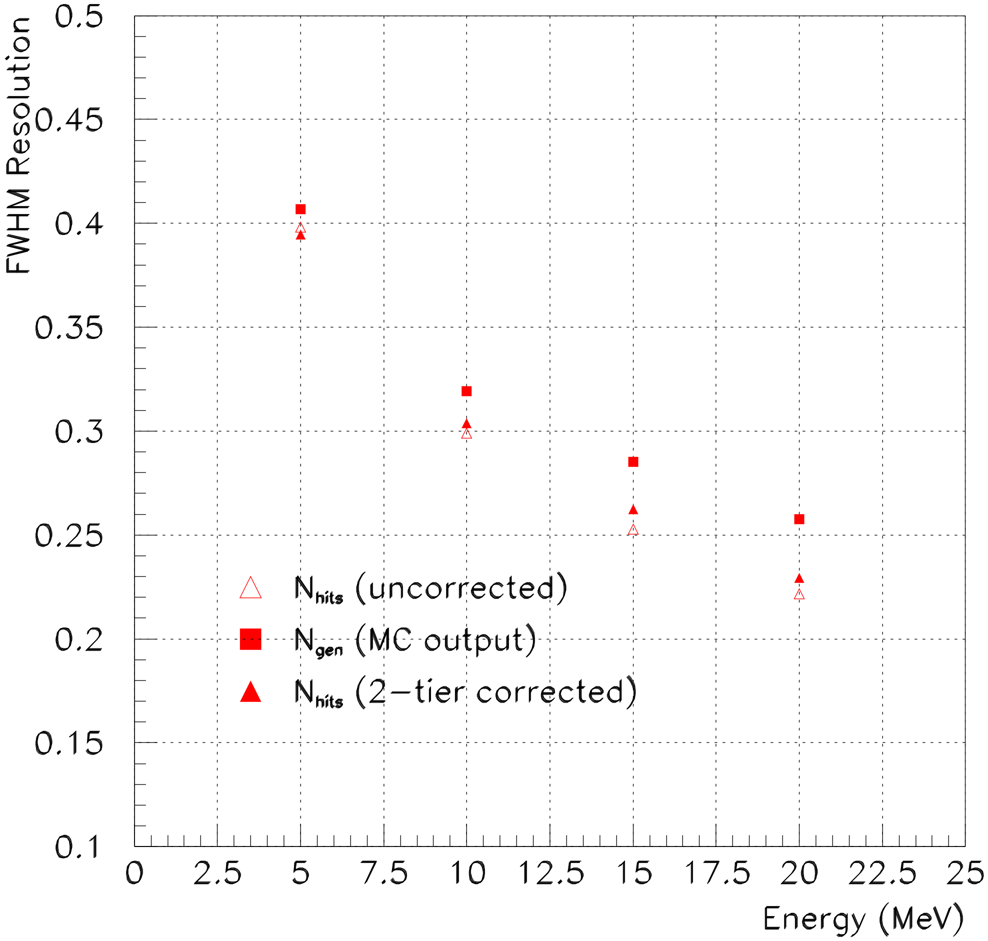

Figure 8.17: Comparing the two-tier corrected detector resolution to Monte Carlo generated N_{gen} resolution.

statistical information. It is the incorrect photon counting statistics inherent to N_{hits} which contributes to the "degradation" in the two-tier corrected resolution R_{2-tier} in the pure D_2O run scenario in Figure 8.14.

Chapter 9

Conclusions

I've studied now Philosophy
And Jurisprudence, Medicine—
And even, alas! Theology—
From end to end with labour keen;
And here, poor fool! with all my lore
I stand, no wiser than before.

JOHANN WOLFGANG VON GOETHE
Faust, Pt. 1, "Night" (1808)

You never know what is enough unless you know what is more than enough.

WILLIAM BLAKE
The Marriage of Heaven and Hell (1790-93)

In this study, we have solved the technical problems in energy calibrating the Sudbury Neutrino Observatory (SNO) detector using monoenergetic gamma-ray sources. These problems involve two broad categories: the construction of a compact high energy gamma-ray source, and the implementation of monoenergetic gamma-ray sources to understand the systematics of the SNO detector response. In the following, we shall summarise the details of the achievements in these two areas.

We built a functional 19.8-MeV gamma-ray source using the $^3\mathrm{H}(p,\gamma)^4\mathrm{He}$ (pT) reaction. We demonstrated that this pT source met all the physical and operational requirements for calibrating the SNO detector. This is the first time a self-contained, compact and portable high energy (E_γ >10 MeV) gamma-ray source of this type has ever been constructed. This work evolved from designing a $^2\mathrm{H}(\mathrm{p},\gamma)^3\mathrm{He}$ prototype source to the actual construction and testing of a pT source. Both of these sources consist of three components—the proton source, the proton acceleration beam line and a solid, high purity scandium tritide (or deuteride) target in a sealed assembly. A continuous (i.e. direct current) beam of protons and hydrogen molecular ions are generated by the home-built proton source, and are subsequently accelerated towards the scandium target up to an energy of 30 keV.

The ion beam current was measured by a calorimetric method and by a Faraday cup outfitted with a secondary electron suppression scheme. Beam current measured by both methods agreed with each other. The mass composition of the beam was also measured, albeit in a small H_2 partial pressure range of 0.3×10^{-3} to 0.6×10^{-3} mbar.

We have developed techniques to fabricate very high quality scandium deuteride and tritide targets. The tritiated target, fabricated in collaboration with Ontario Hydro Technologies in Toronto, Canada, had a Sc:^{3}H atomic ratio of 1:2.0±0.2. A tritiated target like this one is essential in neutron generators for use in oil-logging and mining industries. Since the early 1990s, there has not been any North American firm producing a solid tritiated target for commercial applications.

In our testing of the pT source, 19.8-MeV gamma rays from the pT reaction were observed and found to be sufficient for calibrating the SNO detector. The neutron production rate by the pT source is also low enough that the neutron background would not mask the gamma-ray signal during calibration.

A measurement of the gamma-ray angular distribution in the pT reaction was made at a beam energy of 29 keV. In this measurement, three large BaF_2 crystals (14.5-cm diameter by 17.5-cm long) were used. We fitted the angular distribution data to the functional form of $W(\theta) = A + B\sin^2\theta$. We set an upper limit for the ratio A/B at 0.35 at the 90% confidence level. Our results are consistent with the picture that the pT reaction proceeds primarily through E1 capture of p-wave protons at this energy. We should point out that the beam energy at which the measurement was made was the lowest ever attempted, and was more than an order of magnitude lower than any previous measurements. Because one would expect the s-wave contribution to the cross section to increase as beam energy decreases, our results set an upper limit on A/B at higher beam energies.

The operational lifetime of the pT source was 98.8 hours. A thin conducting layer was deposited on the high voltage insulator in the ion acceleration line. This caused a high voltage breakdown across the insulator. The deposit was originated from target material sputtered off by the ion beam. A second pT source has been constructed with minor engineering changes to reducing this deposition effect. This latter source will be used primarily for energy calibration at the SNO detector. We plan to use this calibration data in SNO to determine the gamma-ray angular distribution to a much better accuracy than the measurement reported in this thesis. We also plan to run the pT source in a number of operating conditions in order to understand its beam characteristics better. The first pT calibration run in SNO is expected to take place by the end of 1998.

At nuclear physics research facilities, calibration of detectors at energies above 10 MeV has always been a cumbersome process, as a particle beam from the accelerator has to be used to generate the radiation for calibration. This proof-of-principle experiment of the pT source opens up the window for more convenient calibration standards in the future. One area in which we could see improvement in the pT source is to implement a beam analyser to reduce the beam power on the target, and to reduce the neutron output of the pT source. This feature was not instrumented in this project because of stringent constraint on the physical size of calibration sources which can be deployed in the SNO detector.

We have done an extensive study on the energy response of the SNO detector using the SNO Monte Carlo program SNOMAN. In this investigation, we studied the detector's photomultiplier tube (PMT) array response to electrons and gamma rays of various types of energy distribution in two different settings: the pure D_2O and the Neutral Current Detector (NCD) array installed scenarios.

When the NCD array is in place, it reduces the number of detected Čerenkov photons by about 15%. The positional dependence of the SNO detector response is also stronger. However, we have demonstrated in this thesis that when this position dependence is corrected by the methods we developed, the NCD array does not introduce any non-linear systematic artifact. In addition, there is no significant degradation of the event reconstruction ability.

We have identified a systematic feature of enhanced Čerenkov light output for γ rays converted in the acrylic vessel. A γ-ray calibration near the acrylic vessel is necessary to get the correct γ-ray response of the SNO detector.

We have investigated the problem of using γ rays to calibrate the "gain correction" algorithms mentioned above. In this analysis, γ-ray calibration events were reconstructed by the time fitter. The resulting correction function extracted from this reconstruction has to be corrected for the γ ray attenuation length before it is useful for correcting electron signals in SNO. Our results indicate that one can accurately reconstruct energy spectra with this technique.

We have demonstrated that using only the number of fired PMT (N_{hits}) information from the data stream to perform the energy calibration may lead to a significant non-linearity. This is primarily a direct consequence of the multiple photon hits on a PMT. We worked out an algorithm which would correct for this non-linear effect. We repeated the gain correction analysis using the multiple-hit corrected N_{hits} information, and demonstrated dramatic improvement in the detector energy resolution in the NCD installed scenario. This will allow the SNO collaboration to set the solar neutrino data analysis threshold to ~5 MeV in the pure D_2O scenario, and to ~5.3 MeV in the NCD installed scenario, given the target levels of radioactive background. In summary, these correction algorithms we developed are necessary for establishing an energy scale accurately. Therefore, these algorithms are important tools in looking for spectral distortion in the observed neutrino energy spectrum as any spectral distortion is evidence of new physics beyond the standard electroweak model of particle physics.

Bibliography

[1] A. Pais, *Inward Bound*, p.158, Oxford University Press, Oxford, 1986.

[2] *ibid.,* p. 307.

[3] C. Sutton, *Spaceship Neutrino*, p. 17, Cambridge University Press, Cambridge, 1992.

[4] *ibid.,* p. 18.

[5] Ref. [1], p. 315.

[6] C. L. Cowan *et al.,* Science **124**, 103 (1956).

[7] S. L. Glashow, Nucl. Phys. **22**, 579 (1961); S. Weinberg, *Phys. Rev. Lett.* **19**, 1264 (1967); A. Salam, *Elementary Particle Theory; Relativistic Groups and Analyticity*, Proceedings of the Eigth Nobel Symposium, edited by Svartholm (Almquist and Wiksell, Stockholm, 1968).

[8] S. P. Mikheyev and A. Yu. Smirnov, Sov. J. Nucl. Phys. **42**, 913 (1986); Nuovo Cimento **9C**, 17 (1986); L. Wolfenstein, Phys. Rev. **D17**, 2369 (1979).

[9] C. F. von Weizsäcker, Physik Z. **38**, 176 (1937); C. F. von Weizsäcker, Physik Z. **39**, 663 (1938); G. Gamow, Phys. Rev. **53**, 595 (1938); H. A. Bethe and C. L. Critchfield, Phys. Rev. **54**, 248 (1938); H. A. Bethe, Phys. Rev. **55**, 434 (1939).

[10] J. N. Bahcall and M. H. Pinsonneault, with an Appendix on the Age of the Sun by G. J. Wasserburg, Rev. Mod. Phys. **67**, 781 (1995).

[11] J. Christensen-Dalsgaard, D. O. Gough, and M. J. Thompson, Astrophys. J., **378**, 413 (1991).

[12] J. N. Bahcall and M. H. Pinsonneault, Rev. Mod. Phys. **64**, 885 (1992).

[13] S. Turck-Chièze and I. Lopes, Astrophys. J. **408**, 347 (1993).

[14] C. R. Proffitt, Astrophys. J. **425**, 849 (1994).

[15] A. Kovetz and G. Shaviv, Astrophys. J. **426**, 787 (1994).

[16] J. N. Bahcall and R. Ulrich, Rev. Mod. Phys. **60**, 297 (1988).

[17] S. Turck-Chièze, S. Cahen, M. Cassé and C. Doom, Astrophys. J. **335**, 415 (1988).

[18] I. J. Sackmann, A. I. Boothroyd, W. A. Fowler, Astrophys. J. **360**, 727 (1990).

[19] V. Castellani, S. Degl'Innocenti, G. Fiorentini, L. M. Lissia, and B. Ricci, Phys. Lett. **B324**, 425 (1994).

[20] J. Christensen-Dalsgaard, Europhysics News **25**, 71 (1994).

[21] X. Shi, D. N. Schramm, D. S. P. Dearborn, Phys. Rev. **D50**, 2414 (1994).

[22] J. N. Bahcall and A. Glasner, Astrophys. J. **437**, 485 (1994).

[23] J. N. Bahcall and A. Ulmer, Phys. Rev. **D53**, 4202 (1996).

[24] R. W. Kavanagh, T. A. Tombrello, J. M. Mosher, and D. R. Goosman, Bull. Am. Phys. Soc., **14**, 1209 (1969)

[25] B. W. Fillipone, A. J. Elwyn, C. N. Davids, and D. D. Koetke, Phys. Rev. **C28**, 2222 (1983).

[26] C. W. Johnson, E. Kolbe, S. E. Koonin and K. Langanke, Astrophys. J., **392**, 320 (1992).

[27] B. T. Cleveland *et al.*, Nucl. Phys. B (Proc. Suppl.) **38**, 47 (1995).

[28] Y. Suzuki. Talk given at the 4th International Conference on Solar Neutrinos, Heidelberg, Germany, 1997.

[29] Y. Suzuki, Nucl. Phys. B (Proc. Suppl.), **38**, 54 (1995).

[30] D. Vignaud *et al.,* to appear in the Proceedings of the IV International Workshop on Theoretical and Phenomenological Aspects of Underground Physics.

[31] S.R. Elliott *et al.*, *Preliminary Results from the Russian-American Gallium Experiment Cr-neutrino Source Measurement*, to appear in the Proceedings of the IV International Workshop on Theoretical and Phenomenological Aspects of Underground Physics.

[32] N. Hata and P. Langacker, Phys. Rev. **D50**, 632 (1994).

[33] S. Parke, Phys. Rev. Lett., **74**, 839 (1995).

[34] J.N. Bahcall, Ap. J. **467**, 475 (1996).

[35] P. Langacker, University of Pennsylvania Report UPR-0640T (1994).

[36] K.M. Heeger and R.G.H. Robertson, Phys. Rev. Lett., **77**, 3720 (1996).

[37] B. Kayser, Phys. Rev. **D24**, 110 (1981).

[38] S. J. Parke, Phys. Rev. Lett., **57**, 1275 (1986).

[39] N. Hata, U of Pennsylvania Report UPR-0605T.

[40] J. N. Bahcall, *Neutrino Astrophysics*, Cambridge University Press, Cambridge, 1989.

[41] T. Goldbrunner in *Paticles and Cosmology*, ed. E.N. Alexeev, V.A. Matveev, Kh.S. Nirov, and V.A. Rubakov, p. 258, World Scientific, 1996.

[42] The ICARUS Collaboration, *ICARUS II, A Second-Generation Proton Decay Experiment and Neutrino Observatory at the Gran Sasso Laboratory*, Vol. I and II, LNGS-9 (1994).

[43] K. Lande in *Proc. 22nd Int. Conf. on Cosmic Ray Physics* (1997).

[44] S.R. Bandler, R.E. Lanou, H.J. Maris, T. More, F.S. Porter, G.M. Seidel, R.H. Torii, Phys. Rev. Lett., **68**, 2429 (1992).

[45] World Wide Web home page at http://sg1.hep.fsu.edu/~hellaz/

[46] T.L. Jenkins, *A Proposed Experiment for the Detection of Solar Neutrinos*, Case University proposal, unpublished (1966).

[47] F. Reines, Proc. Roy. Soc., **A301**, 159 (1967).

[48] E. Pasierb, H.S. Gurr, J. Lathrop, F. Reines, and H.W. Sobel, Phys. Rev. Lett., **43**, 96 (1979).

[49] H.H. Chen, Phys. Rev. Lett., **55**, 1534 (1985).

[50] J.N. Bahcall and E. Lisi, Phys. Rev. **D54**, 5417 (1996).

[51] J.N. Bahcall, Phys. Lett, **13**, 332 (1964).

[52] J.J. Simpson and J.-X. Wang, *Determination of NC/CC During the Pure D_2O Stage of Operation*, SNO internal report, SNO-STR-98-001, unpublished (1998).

[53] P.J. Doe, J.V. Germani, A.W.P. Poon, R.G.H. Robertson, T.D. Steiger, J.F. Wilkerson, T.J. Bowles, A. Hime, M.M. Fowler, P.M. Thornewell, J.B. Wilhelmy, and J.M. Wouters, *Construction of an Array of Neutral-Current Detectors for the Sudbury Neutrino Observatory*, SNO internal report, SNO-STR-95-023, unpublished (1995).

[54] G.T. Ewan *et al., Sudbury Neutrino Observatory Proposal*, SNO report SNO-87-12, October 1987.

[55] J.R. Leslie,*Sudbury Neutrino Observatory Calibration Design Criteria*, DC-17-360-01, unpublished, March 1992.

[56] R.M. Chasteler and H.R. Weller, Nucl. Instr. and Meth. **A 344**, 429 (1994).

[57] J.H. Weinlein, M.L. O'Neal, and F.M. Bacon, Nucl. Instr. and Meth. **B 56/67**, 904 (1991).

[58] L.S. Erhardt, M.Sc. thesis, Queen's University at Kingston, Canada, unpublished (1994).

[59] D. Waller, M.Sc. thesis, Queen's University at Kingston, Canada, unpublished (1997).

[60] V. Uras, M.Sc. thesis, Queen's University at Kingston, Canada, unpublished (1992).

[61] T. Radcliffe, private communication (1994). See also Erhardt [58].

[62] W.A. Fowler, G.R. Caughlan and B.A. Zimmerman, Annu. Rev. Astron. Astrophys., **5**, 525 (1967); W.A. Fowler, G.R. Caughlan and B.A. Zimmerman, Annu. Rev. Astron. Astrophys., **13**, 69 (1975); M.J. Harris, W.A. Fowler, G.R. Caughlan and B.A. Zimmerman, Annu. Rev. Astron. Astrophys., **21**, 165 (1983); G.R. Caughlan, W.A. Fowler, M.J. Harris and B.A. Zimmerman, Atomic Data and Nuclear Data Tables, **32**, 197 (1985).

[63] World Wide Web home page of the U.S. Nuclear Reaction Data Network, http://www.dne.bnl.gov:80/~burrows/usnrdn/.

[64] G.M. Griffiths, M. Lal, and C.D. Scarfe, Can. J. Phys. **41**, 724 (1963).

[65] G.J. Schmid, R.M. Chasteler, C.M. Laymon, H.R. Weller, R.M. Prior, and D.R. Tilley, Phys. Rev. **C52**, R1732 (1995).

[66] J.E. Perry, Jr., and S.J. Bame, Jr., Phys. Rev. **99**, 1368 (1955).

[67] K.I. Hahn, C.R. Brune, and R.W. Kavanagh, Phys. Rev. **C51**, 1624 (1995).

[68] G.M. Griffiths, Ph.D. thesis, University of British Columbia, 1953 (unpublished).

[69] H.V. Argo, H.T. Gittings, A. Hemmendinger, G.A. Jarvis and R.F. Taschek, Phys. Rev. **78**, 691 (1950).

[70] D.S. Gemmell and G.A. Jones, Nucl. Phys. **33**, 102 (1962).

[71] W.E. Meyerhof, M. Suffert, and W. Feldman, Nucl. Phys. **A148**, 221 (1970).

[72] J.B. Warren, and G.M. Griffiths, Phys. Rev. **92**, 1084 (1953).

[73] R. Schrack, D. Kohler, N.G. Puttaswamy and W.E. Meyerhof, Phys. Lett., **18**, 327 (1965).

[74] W. Del Bianco and G. Kajrys, Can. J. Phys., **58**, 1496 (1980).

[75] J.B. Warren *et al.*, Can. J. Phys. **32**, 563 (1954).

[76] R.F. Christy and I. Duck, Nucl. Phys. **24**, 89 (1961).

[77] J.F. Ziegler, *The Stopping and Range of Ions in Matter version 96.01*, IBM Research, 1996; J.P. Biersack and J.F. Ziegler, *TRIM*, IBM Research, 1989 (unpublished).

[78] W.R. Leo, *Techniques for Nuclear and Particle Physics*, Springer-Verlag, 1992.

[79] Donald C. McGilvery and Richard J.S. Morrison, Department of Chemistry, Monash University, Clayton, Victoria, Australia, 1988.

[80] M F Physics, Inc., Colorado Springs, CO, USA, private communication, (1994).

[81] E.R. Graves *et al.,* Rev. Sci. Instr., **20**, 579 (1949).

[82] L.M. Jones *et al.,* J. Vac. Sci. Technol., **17**, 1225(1980).

[83] H.L. Adair *et al.,* Nucl. Instr. Meth., **200**, 99 (1982).

[84] T. Yanagi *et al.,* Nucl. Instr. Meth., **A234**, 6 (1985).

[85] K. Sumita, Nucl. Instr. Meth.,**A282**, 345 (1989).

[86] J.H. Singleton and L.N. Yannopoulos, J. Vac. Sci. Technol., **12**, 414 (1975).

[87] J.C. McGuire and C.P. Kempter, J. Chem. Phys. **33**, 1584 (1960).

[88] P. Frisch, IBM Research, private communication, 1994.

[89] N.P. Kherani, Ph.D. thesis, University of Toronto, Canada, unpublished (1994).

[90] *St172 Advanced Porous Getters*, SAES Getters S.p.A., October 1989.

[91] G.F. Knoll, *Radiation Detection and Measurement*, John Wiley & Sons, 1989.

[92] *GEANT*, CERN program library long writeup W5013 (1994).

[93] S. Pai, W.F. Piel, D.B. Fossan, and M.R. Maier, Nucl. Instr. and Meth., **A278**, 749 (1989).

[94] L. DeBraeckeleer, M. Felton, and A. Poon, Nuclear Physics Laboratory Annual Report, University of Washington, 33 (1995); L. DeBraeckeleer, M. Felton, and A. Poon, Nuclear Physics Laboratory Annual Report, University of Washington, 4 (1996).

[95] N.P. Kherani, Ontario Hydro Technologies test plan TL2.400.036 (1989); M. Hooper, N.P. Kherani, A.W.P. Poon, Ontario Hydro Technologies test plan TL2.400.036 ammendment (1996).

[96] N.P. Kherani and W.T. Shmayda, *Bulk Getters for Tritium Storage* in *Proc. Cdn. Nucl. Soc. 7th Annual Conference*, Toronto, 232 (1986).

[97] N.P. Kherani, W.T. Shmayda and A.G. Heics, Z. Phys. Chem. **164**, 1421 (1989).

[98] N.P. Kherani, private communication (1994).

[99] R.J. Komar, Ph.D. thesis, Queen's University at Kingston, Canada, unpublished (1992).

[100] Particle Data Group, Phys. Rev. **D54**, 1 (1996).

[101] E. Storm and H.I. Israel, Nucl. Data Tables, **A7**, 565 (1970).

[102] D.M. Drake, L.R. Nilsson, and J. Faucett, Nucl. Instr. Meth. **188**, 313 (1981).

[103] Harshaw catalogue GE 102, Harshaw/Filtrol (1984).

[104] F. James, *MINUIT Reference Manual*, CERN program library long writeup D506 (1994).

[105] P.R. Bevington, *Data Reduction and Error Analysis for the Physical Sciences*, McGraw-Hill, New York (1969).

[106] J.F. Ziegler and J.M. Manoyan, Nucl. Instr. and Meth., **B35**, 215 (1988).

[107] C. Wong, J.D. Anderson and J.W. McClure, Nucl. Phys. **71**, 106 (1965).

[108] M.E. Anderson and R.A. Neff, Nucl. Instr. and Meth., **99**, 231 (1972).

[109] T. Lauritsen and F. Ajzenberg-Selove, Nucl. Phys. **78**, 1 (1966).

[110] J.R. Calarco, B.L. Berman, and T.W. Donnelly, Phys. Rev. **C27**, 1866 (1983).

[111] C.C. Garner and J.D. Anderson, Phys. Rev. **125**, 626 (1962).

[112] G. Feldman, M.J. Balbes, L.H. Kramer, J.Z. Williams, H.R. Weller and D.R. Tilley, Phys. Rev. **C42**, R1167 (1990).

[113] The SNOMAN authors, *The SNOMAN User's Manual, Version 2.09*, 1996

[114] M.D. Lay, D.L. Wark, and N. West, *It's Alive — The Birth of SNOMAN*, SNO internal report STR-91-077, unpublished (1991).

[115] *ZEBRA*, CERN program library long writeups Q100/Q101, 1994.

[116] W.R. Nelson, H. Hirayama, and D.W.O. Rogers, *The EGS4 Code System*, SLAC report SLAC-265 (1985).

[117] C.E. Waltham, private communication, 1996.

[118] M. Lay, *Energy Response and PMT Backgrounds in SNO*, SNO internal report STR-96-015, unpublished (1996).

[119] J.V. Jelley, *Čerenkov Radiation*, Pergamon Press, London (1958).

[120] T.J. Bowles, P.J. Doe, A. Hime, R.G.H. Robertson, T.C. Spencer, P.M. Thornewell, J.B. Wilhelmy, and J.F. Wilkerson, *Neutral-Current Detection in the Sudbury Neutrino Observatory*, page 60, Los Alamos National Laboratory FIN-94-ER-E324, January 1992.

[121] A. Owens, N. Gehrels, S.M. Pascarelle, and B.T. Teegarden, IEEE Trans. Nucl. Sci., **38**, 221 (1991).

Appendix A

Technical Drawings of the pT Source

In this appendix, all the technical drawings that are relevant to the construction and the assembly of the pT source are displayed. In these drawings, we follow the general practise at machine shops in North America to display all the linear dimensions in inches.

Figure A.1 is the assembly drawing of the pT source. Drawings that are referred to by this assembly drawing can be found in subsequent figures. For a description of the design of the pT source, the reader is referred to Section 3.4.1.

For the pT source that was used in the measurements made in this thesis, the tritiated target was secured in place by the target mounting cap shown in Figure A.7. To reduce the deposition of beam sputtering products on the high voltage insulator (MDC part number DEG-150 in the assembly drawing), a new design of the mounting cap was used in the new pT source for energy calibration at the SNO detector. The drawing of this new design is shown as Figure A.13.

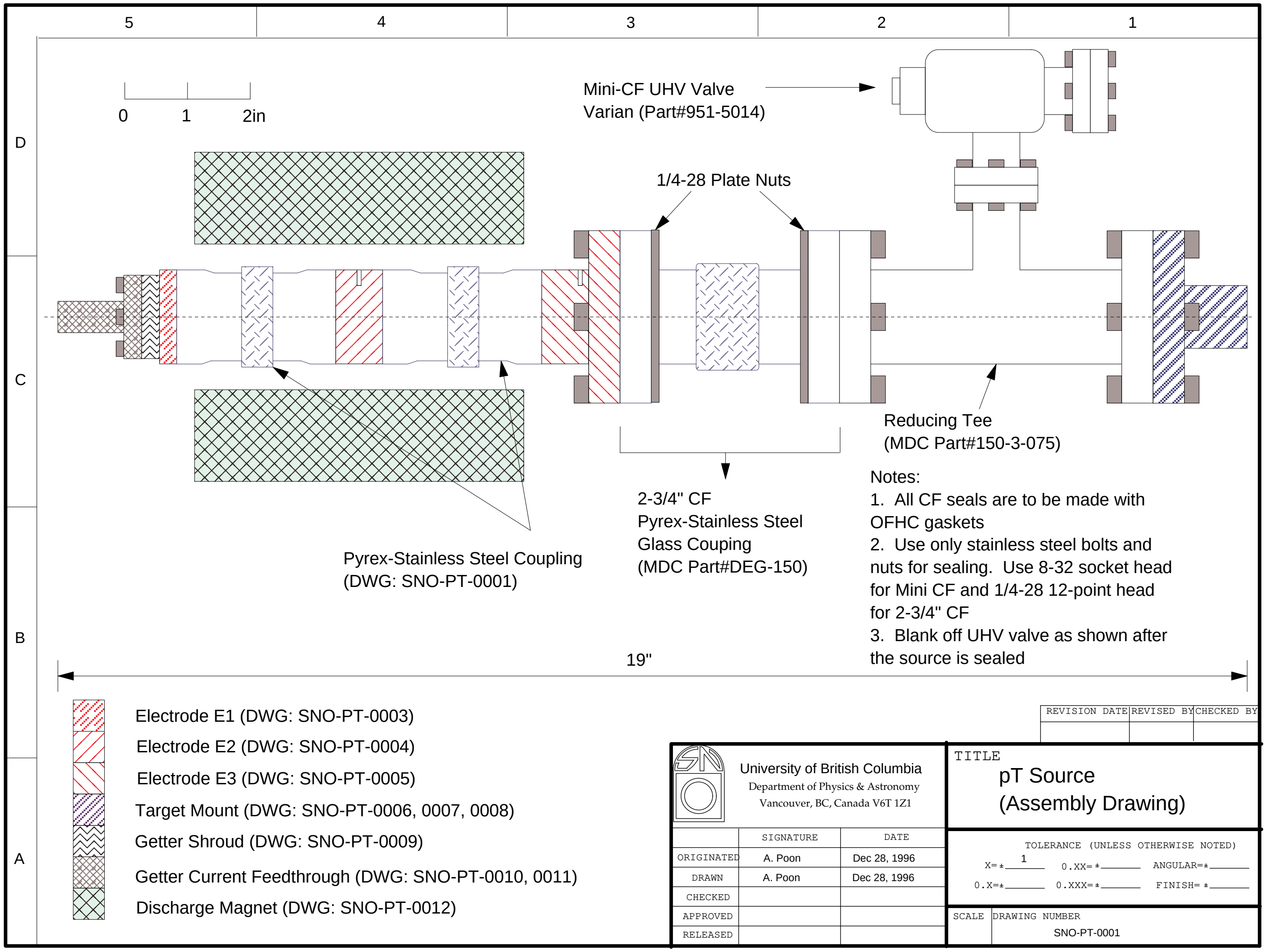

Notes:
1. All CF seals are to be made with OFHC gaskets
2. Use only stainless steel bolts and nuts for sealing. Use 8-32 socket head for Mini CF and 1/4-28 12-point head for 2-3/4" CF
3. Blank off UHV valve as shown after the source is sealed

Figure A.1: Assembly drawing of the *pT* source. Mechanical drawings of the parts can be found in subsequent figures.

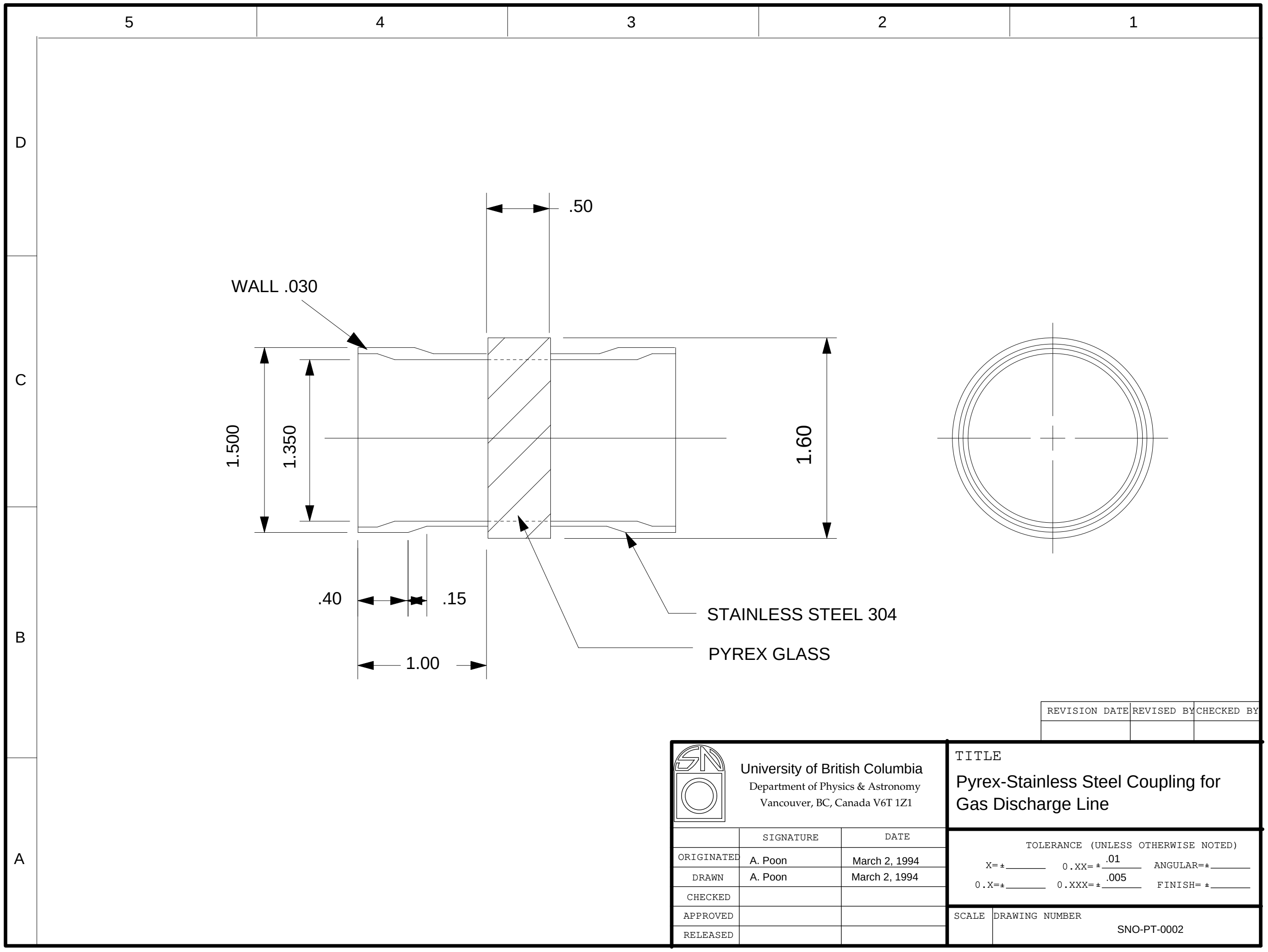

Figure A.2: Technical drawing of the Pyrex-stainless steel coupling used in the gas discharge line. (SNO-PT-0002).

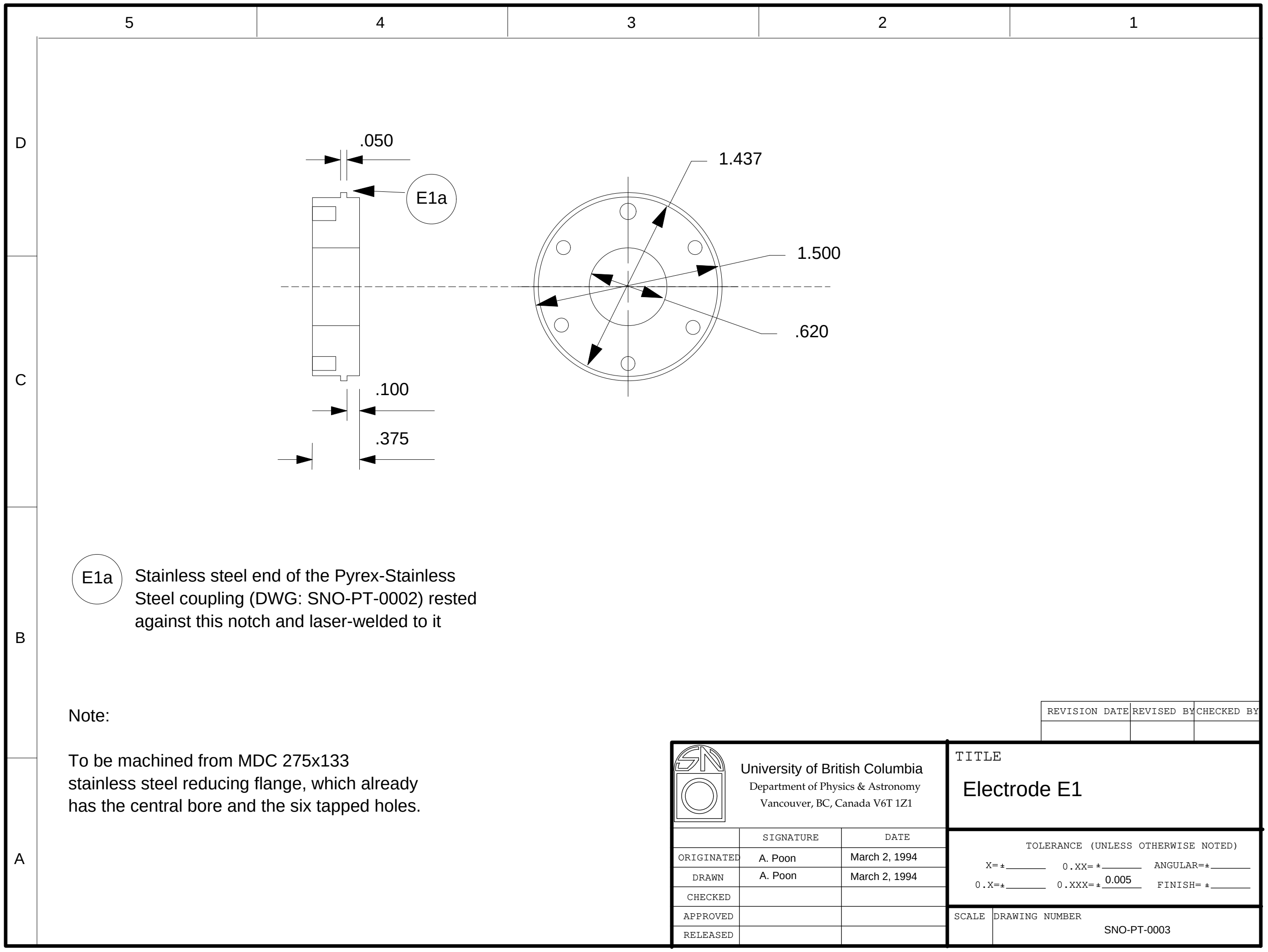

E1a Stainless steel end of the Pyrex-Stainless Steel coupling (DWG: SNO-PT-0002) rested against this notch and laser-welded to it

Note:

To be machined from MDC 275x133 stainless steel reducing flange, which already has the central bore and the six tapped holes.

REVISION DATE	REVISED BY	CHECKED BY

University of British Columbia
Department of Physics & Astronomy
Vancouver, BC, Canada V6T 1Z1

	SIGNATURE	DATE
ORIGINATED	A. Poon	March 2, 1994
DRAWN	A. Poon	March 2, 1994
CHECKED		
APPROVED		
RELEASED		

TITLE
Electrode E1

TOLERANCE (UNLESS OTHERWISE NOTED)
X=± 0.XX=± ANGULAR=±
0.X=± 0.XXX=± 0.005 FINISH=±

SCALE
DRAWING NUMBER
SNO-PT-0003

Figure A.3: Technical drawing of the electrode E1 in the gas discharge line. (SNO-PT-0003).

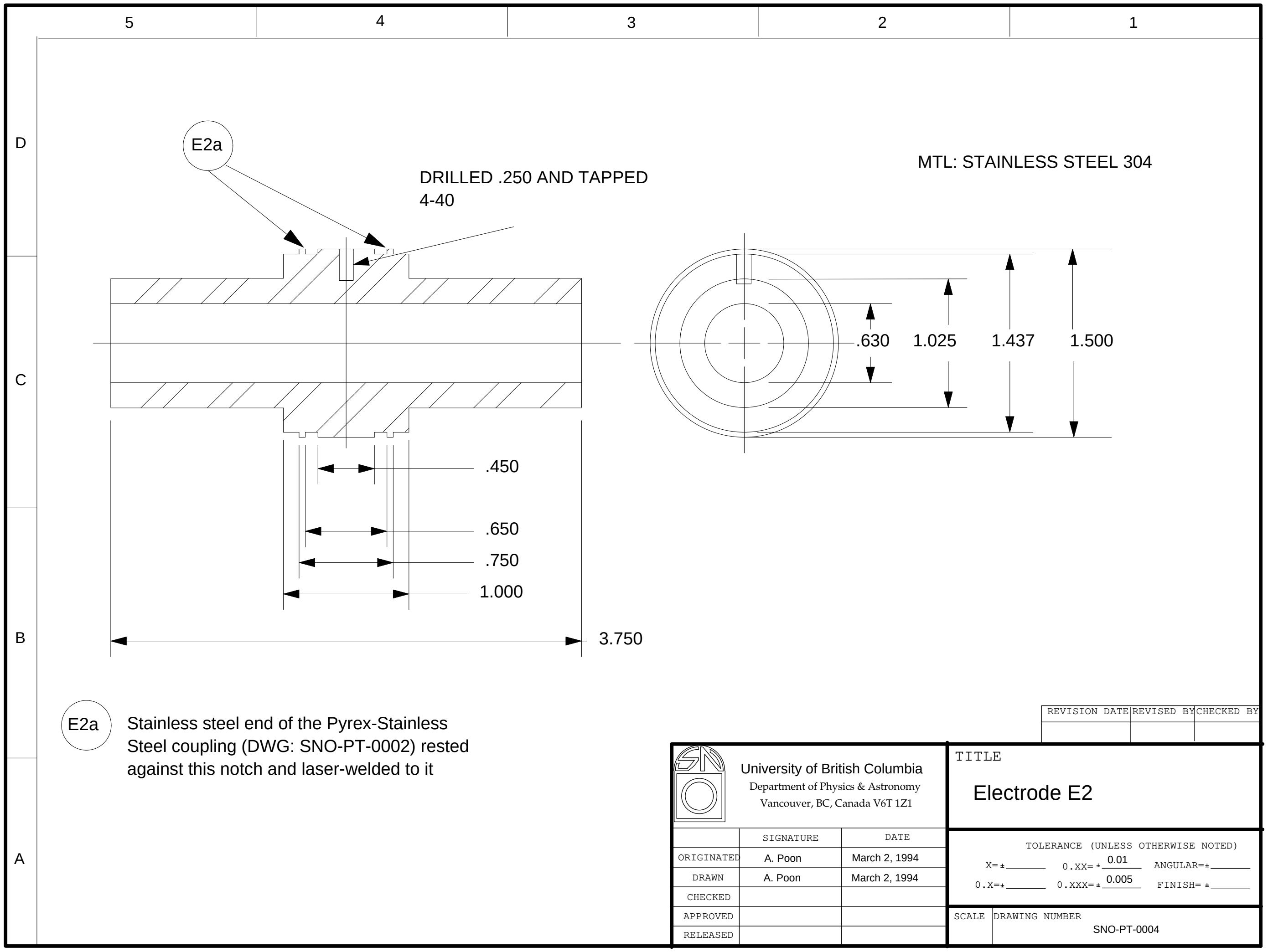

E2a Stainless steel end of the Pyrex-Stainless Steel coupling (DWG: SNO-PT-0002) rested against this notch and laser-welded to it

University of British Columbia
Department of Physics & Astronomy
Vancouver, BC, Canada V6T 1Z1

	SIGNATURE	DATE
ORIGINATED	A. Poon	March 2, 1994
DRAWN	A. Poon	March 2, 1994
CHECKED		
APPROVED		
RELEASED		

TITLE
Electrode E2

TOLERANCE (UNLESS OTHERWISE NOTED)
X=± ______ 0.XX=± 0.01 ANGULAR=± ______
0.X=± ______ 0.XXX=± 0.005 FINISH= ± ______

SCALE
DRAWING NUMBER SNO-PT-0004

Figure A.4: Technical drawing of the electrode E2 in the gas discharge line. (SNO-PT-0004).

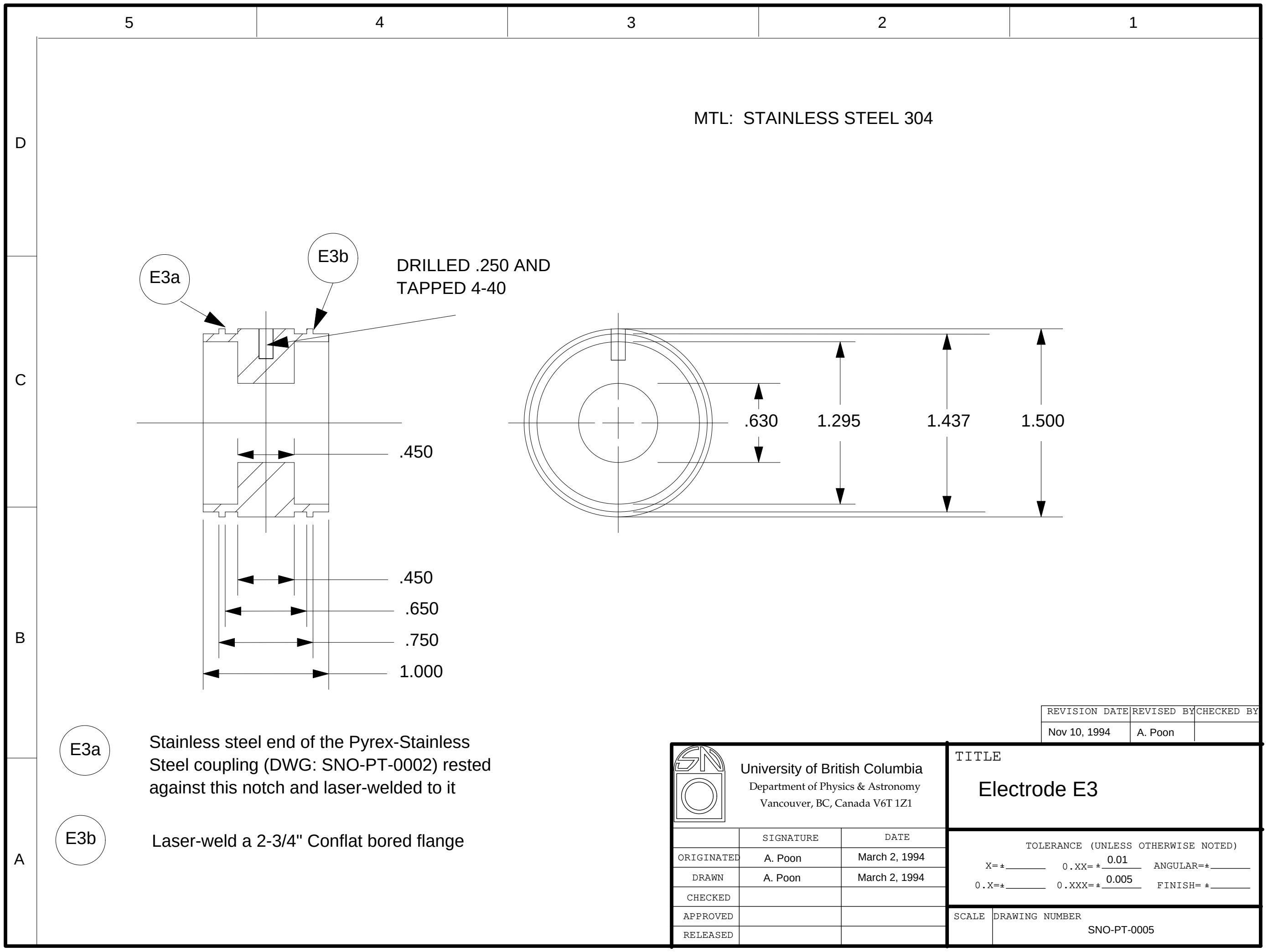

Figure A.5: Technical drawing of the electrode E3 in the gas discharge line. (SNO-PT-0005).

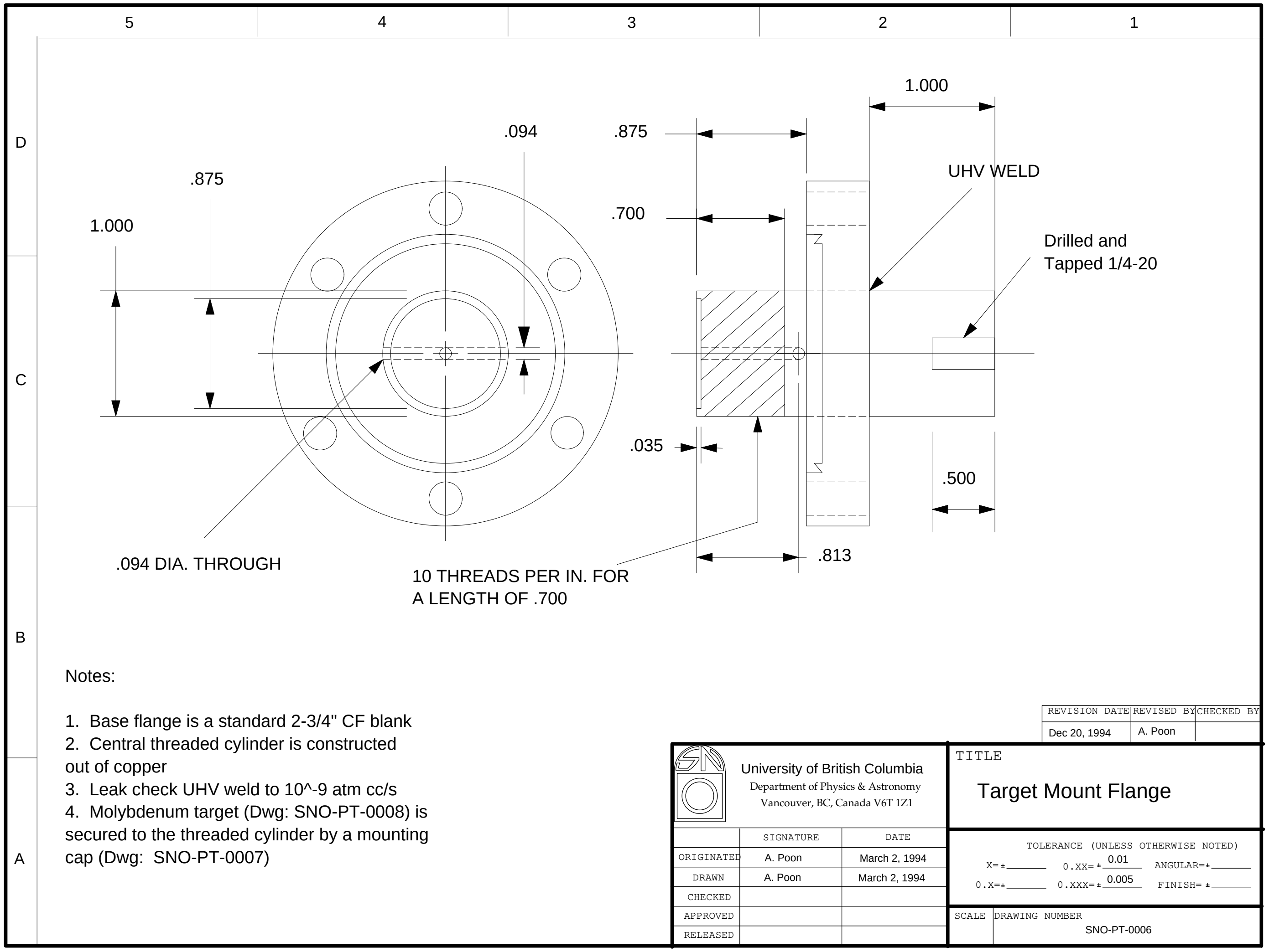

Notes:

1. Base flange is a standard 2-3/4" CF blank
2. Central threaded cylinder is constructed out of copper
3. Leak check UHV weld to 10^-9 atm cc/s
4. Molybdenum target (Dwg: SNO-PT-0008) is secured to the threaded cylinder by a mounting cap (Dwg: SNO-PT-0007)

University of British Columbia
Department of Physics & Astronomy
Vancouver, BC, Canada V6T 1Z1

	SIGNATURE	DATE
ORIGINATED	A. Poon	March 2, 1994
DRAWN	A. Poon	March 2, 1994
CHECKED		
APPROVED		
RELEASED		

Figure A.6: Technical drawing of the target mount flange. (SNO-PT-0006).

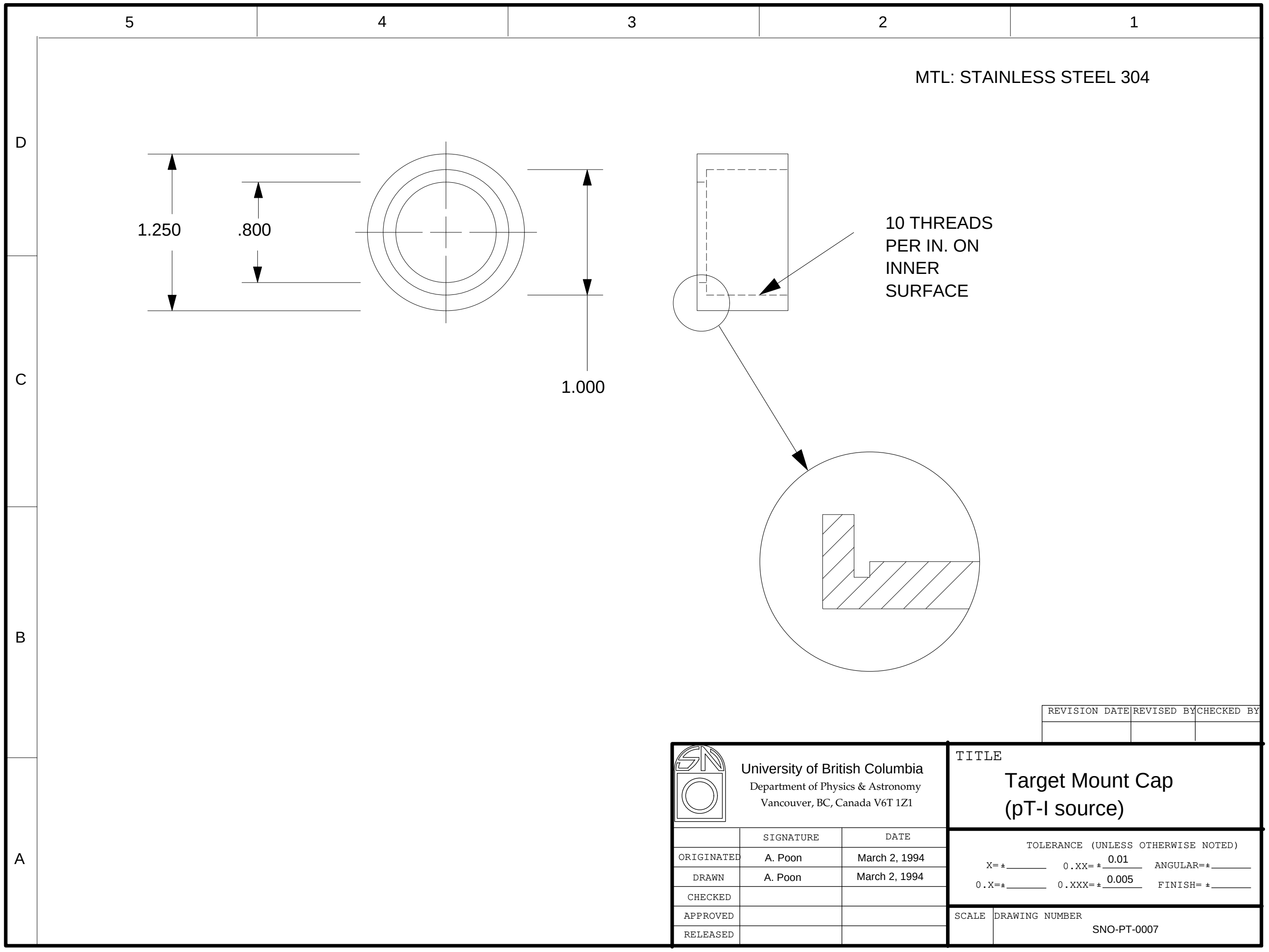

Figure A.7: Technical drawing of the target mounting cap in the *pT* source. This design was used in the *pT* source. A new design (Figure A.13, SNO-PT-0013) has been installed in the new *pT* source. (SNO-PT-0007).

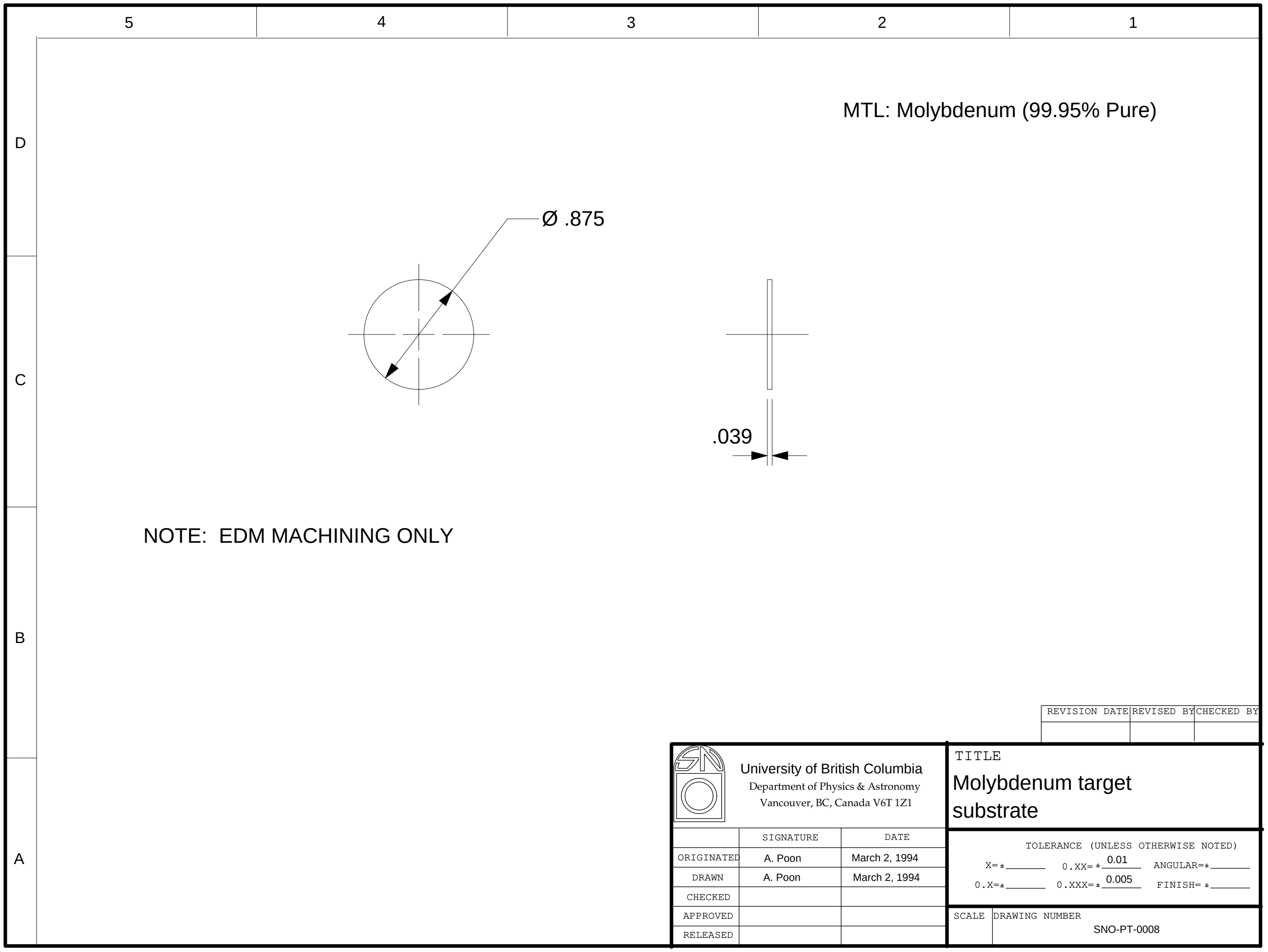

University of British Columbia
Department of Physics & Astronomy
Vancouver, BC, Canada V6T 1Z1

	SIGNATURE	DATE
ORIGINATED	A. Poon	March 2, 1994
DRAWN	A. Poon	March 2, 1994
CHECKED		
APPROVED		
RELEASED		

TITLE
Molybdenum target substrate

TOLERANCE (UNLESS OTHERWISE NOTED)
X=± ______ 0.XX=± 0.01 ANGULAR=± ______
0.X=± ______ 0.XXX=± 0.005 FINISH=± ______

SCALE
DRAWING NUMBER SNO-PT-0008

Figure A.8: Technical drawing of the molybdenum target substrate. (SNO-PT-0008).

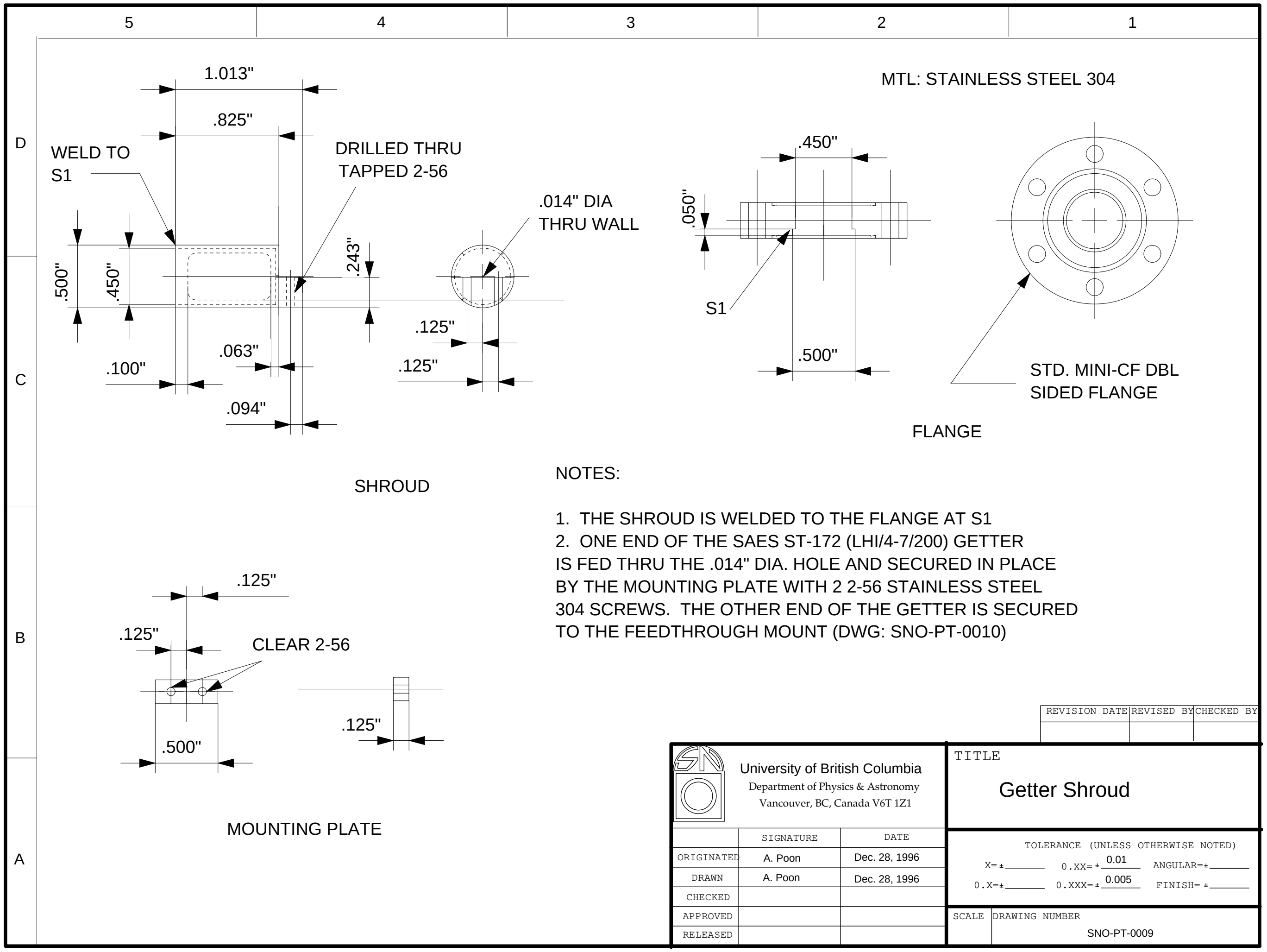

NOTES:

1. THE SHROUD IS WELDED TO THE FLANGE AT S1
2. ONE END OF THE SAES ST-172 (LHI/4-7/200) GETTER IS FED THRU THE .014" DIA. HOLE AND SECURED IN PLACE BY THE MOUNTING PLATE WITH 2 2-56 STAINLESS STEEL 304 SCREWS. THE OTHER END OF THE GETTER IS SECURED TO THE FEEDTHROUGH MOUNT (DWG: SNO-PT-0010)

REVISION DATE	REVISED BY	CHECKED BY

University of British Columbia
Department of Physics & Astronomy
Vancouver, BC, Canada V6T 1Z1

	SIGNATURE	DATE
ORIGINATED	A. Poon	Dec. 28, 1996
DRAWN	A. Poon	Dec. 28, 1996
CHECKED		
APPROVED		
RELEASED		

TITLE
Getter Shroud

TOLERANCE (UNLESS OTHERWISE NOTED)
X= ±_____ 0.XX= ± 0.01 ANGULAR= ±_____
0.X= ±_____ 0.XXX= ± 0.005 FINISH= ±_____

SCALE
DRAWING NUMBER SNO-PT-0009

Figure A.9: Technical drawing of the getter shroud. (SNO-PT-0009).

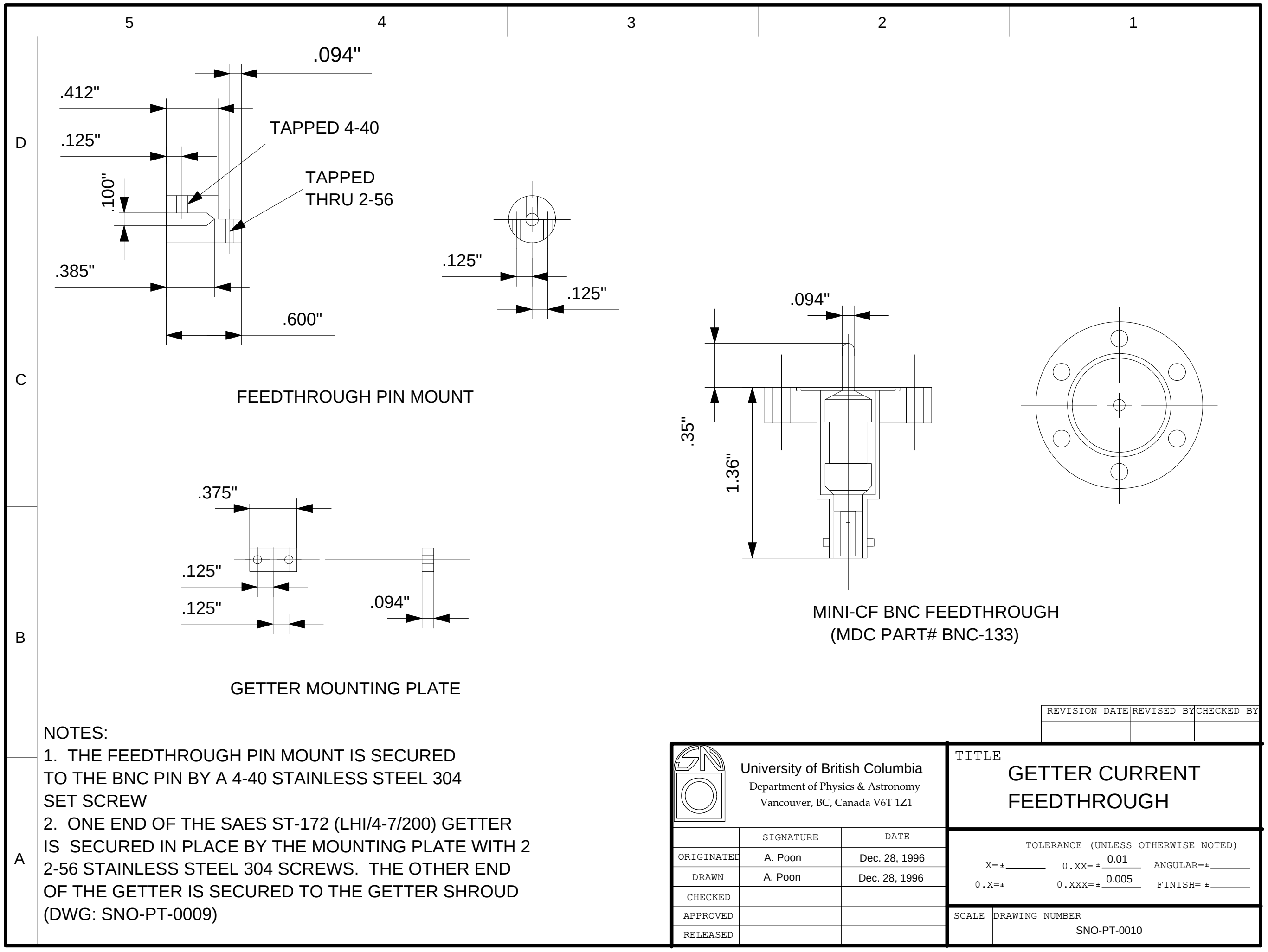

NOTES:
1. THE FEEDTHROUGH PIN MOUNT IS SECURED TO THE BNC PIN BY A 4-40 STAINLESS STEEL 304 SET SCREW
2. ONE END OF THE SAES ST-172 (LHI/4-7/200) GETTER IS SECURED IN PLACE BY THE MOUNTING PLATE WITH 2 2-56 STAINLESS STEEL 304 SCREWS. THE OTHER END OF THE GETTER IS SECURED TO THE GETTER SHROUD (DWG: SNO-PT-0009)

University of British Columbia
Department of Physics & Astronomy
Vancouver, BC, Canada V6T 1Z1

TITLE
GETTER CURRENT FEEDTHROUGH

	SIGNATURE	DATE
ORIGINATED	A. Poon	Dec. 28, 1996
DRAWN	A. Poon	Dec. 28, 1996
CHECKED		
APPROVED		
RELEASED		

TOLERANCE (UNLESS OTHERWISE NOTED)
X=± ______ 0.XX=± 0.01 ANGULAR=± ______
0.X=± ______ 0.XXX=± 0.005 FINISH= ± ______

SCALE
DRAWING NUMBER SNO-PT-0010

Figure A.10: Technical drawing of the current feedthrough to the getter. (SNO-PT-0010).

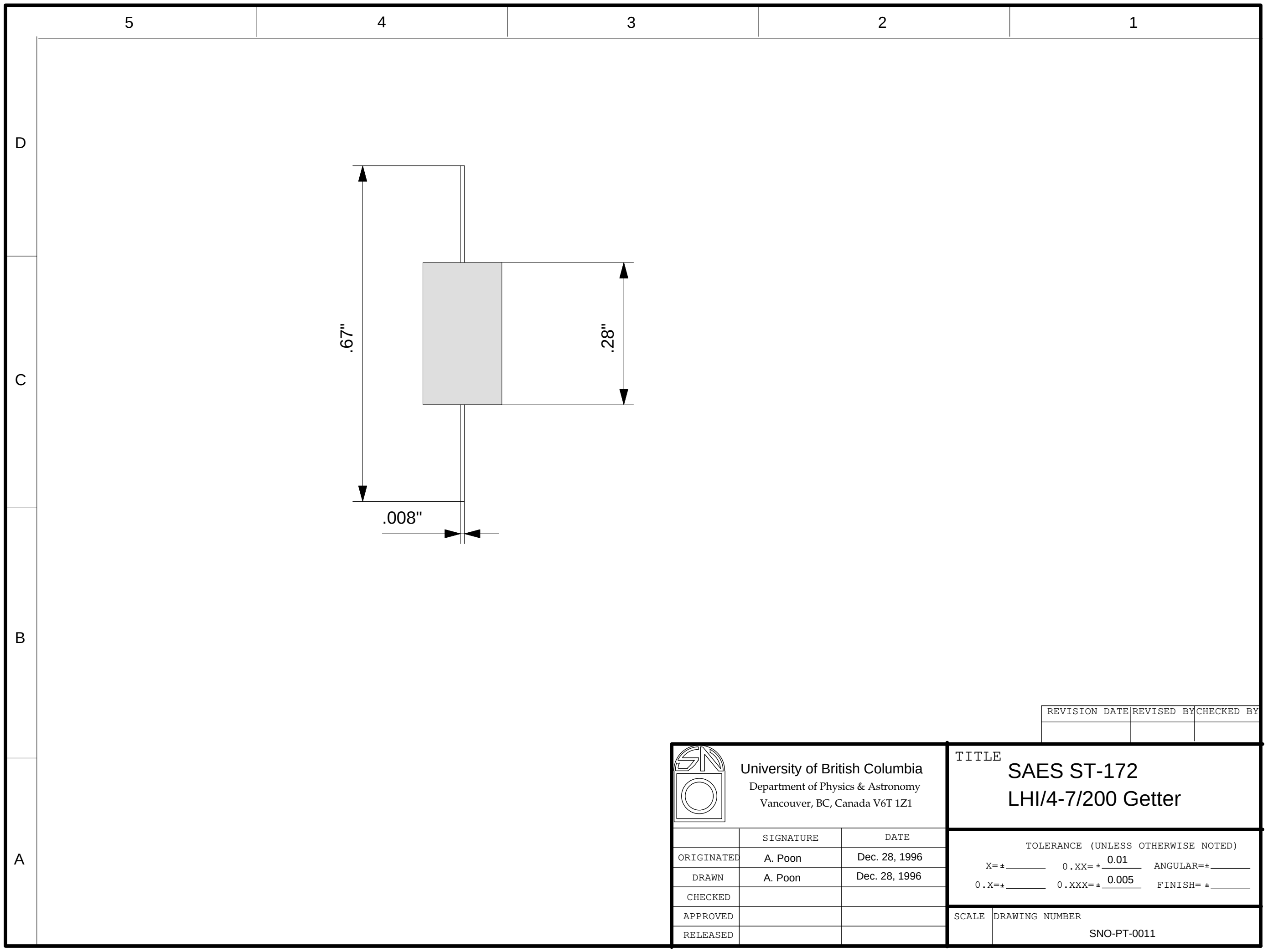

REVISION DATE	REVISED BY	CHECKED BY

University of British Columbia
Department of Physics & Astronomy
Vancouver, BC, Canada V6T 1Z1

	SIGNATURE	DATE
ORIGINATED	A. Poon	Dec. 28, 1996
DRAWN	A. Poon	Dec. 28, 1996
CHECKED		
APPROVED		
RELEASED		

TITLE SAES ST-172
LHI/4-7/200 Getter

TOLERANCE (UNLESS OTHERWISE NOTED)
X=± 0.XX=± 0.01 ANGULAR=±
0.X=± 0.XXX=± 0.005 FINISH=±

SCALE DRAWING NUMBER SNO-PT-0011

Figure A.11: Technical drawing of the getter used in the pT source. This getter is manufactured by SAES Getters, Inc. (SNO-PT-0011).

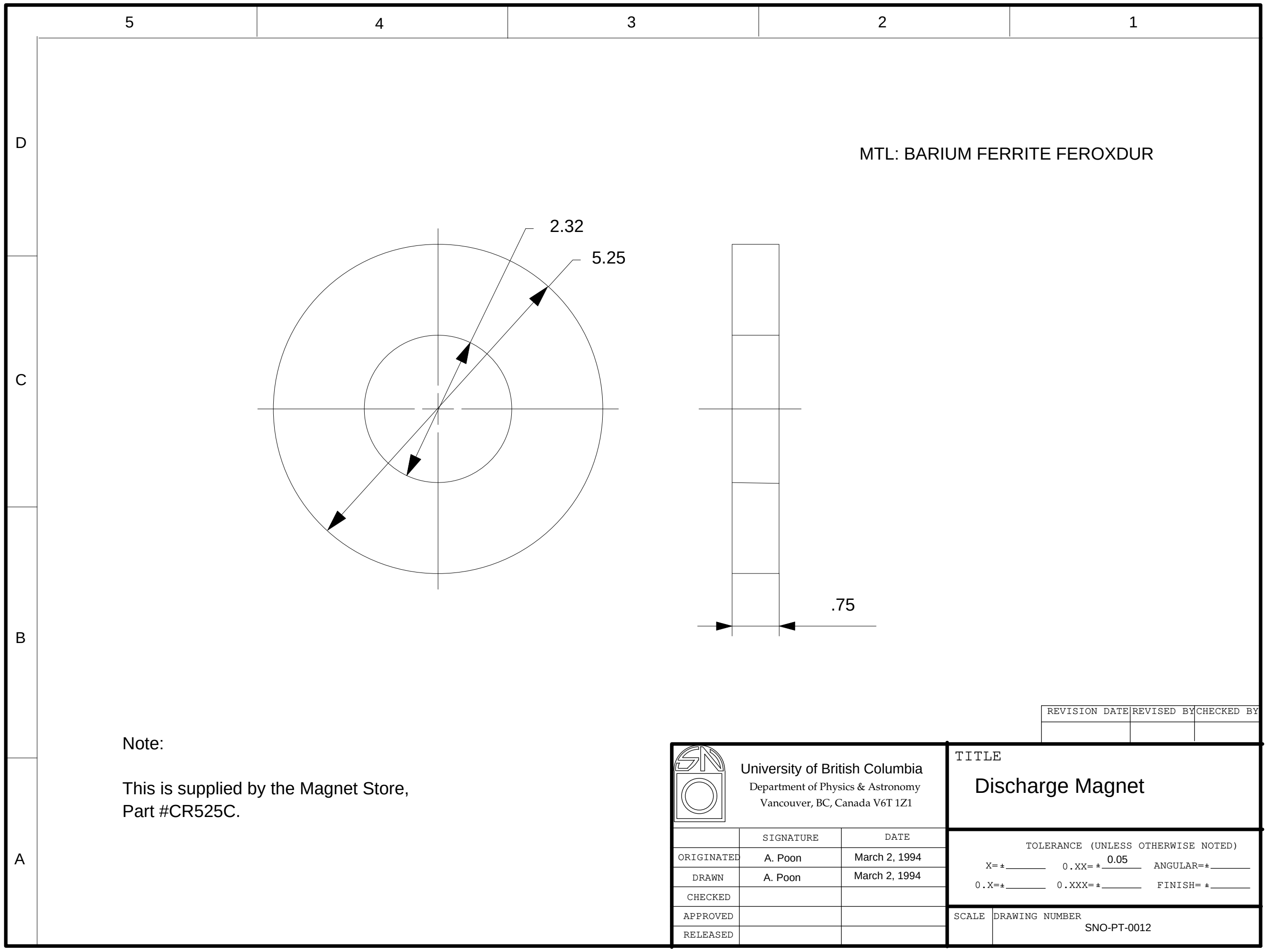

MTL: BARIUM FERRITE FEROXDUR

Note:

This is supplied by the Magnet Store,
Part #CR525C.

REVISION DATE	REVISED BY	CHECKED BY

University of British Columbia
Department of Physics & Astronomy
Vancouver, BC, Canada V6T 1Z1

	SIGNATURE	DATE
ORIGINATED	A. Poon	March 2, 1994
DRAWN	A. Poon	March 2, 1994
CHECKED		
APPROVED		
RELEASED		

TITLE
Discharge Magnet

TOLERANCE (UNLESS OTHERWISE NOTED)
X=±
0.XX=± 0.05
ANGULAR=±
0.X=±
0.XXX=±
FINISH=±

SCALE
DRAWING NUMBER SNO-PT-0012

Figure A.12: Technical drawing of the ceramic discharge magnet. The magnets used in the *pT* source are supplied by the Magnet Store, Castle Rock, Colorado, USA. (SNO-PT-0012).

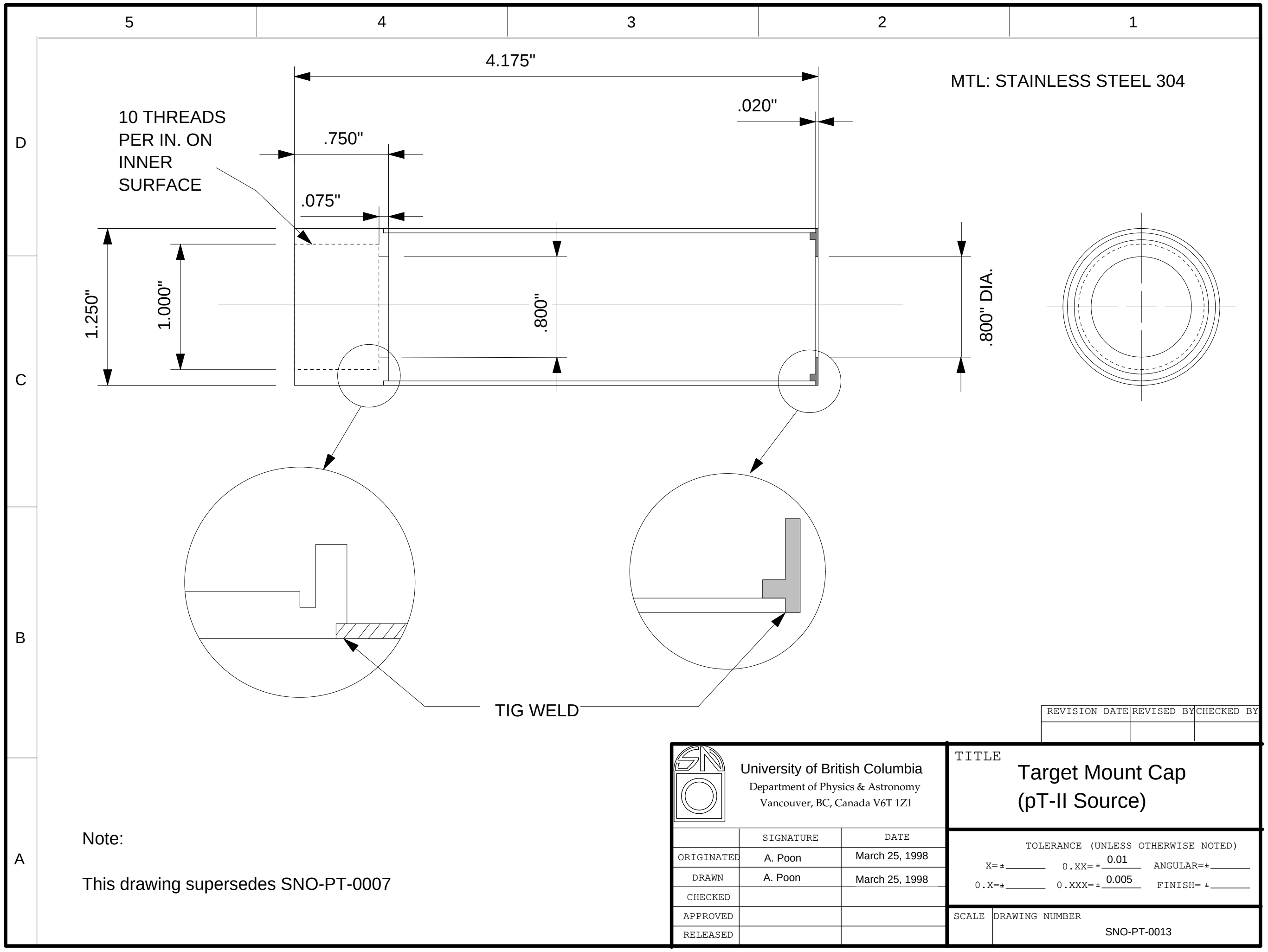

Note:

This drawing supersedes SNO-PT-0007

Target Mount Cap
(pT-II Source)

	SIGNATURE	DATE
ORIGINATED	A. Poon	March 25, 1998
DRAWN	A. Poon	March 25, 1998
CHECKED		
APPROVED		
RELEASED		

0.XX=± 0.01
0.XXX=± 0.005

DRAWING NUMBER SNO-PT-0013

Figure A.13: Technical drawing of the target mounting cap in the new pT-II source. (SNO-PT-0013).

Appendix B

Reliability of GEANT at Low Energy

In this thesis, we have used GEANT [92] to simulate the energy response of gamma-ray detectors. GEANT is a computer program commonly used in particle physics experiments to simulate the response of very complicated detectors at very high energies. In this appendix, we shall investigate whether GEANT can be relied upon at lower energy. We carried out this investigation by running GEANT simulations for a variety of detectors. The results of these simulations were compared to experimental results or other numerical calculations in the literature.

B.1 Photopeak Efficiency in Germanium Detectors

We began our investigation by looking at the photopeak efficiencies of germanium detectors. Germanium detectors have very high resolution and we could understand the GEANT calculated photopeak efficiency without having to worry too much about the effects resolution introduces to the determination of the photopeak efficiency.

Owens *et al.* [121] calculated the photopeak efficiencies, and first and second escape peak efficiencies for germanium detectors of various sizes. Their calculations were carried out using the UCSD MONTE Monte Carlo code. Their Monte Carlo calculations were tested against experimental measurement and found to be in agreement to within the quoted experimental uncertainties, which are typically a few percent.

In Figure B.1, we show the basic model geometry we used in our GEANT Monte Carlo calculations. This geometry is similar to the one used in Owens *et al.* with a few minor

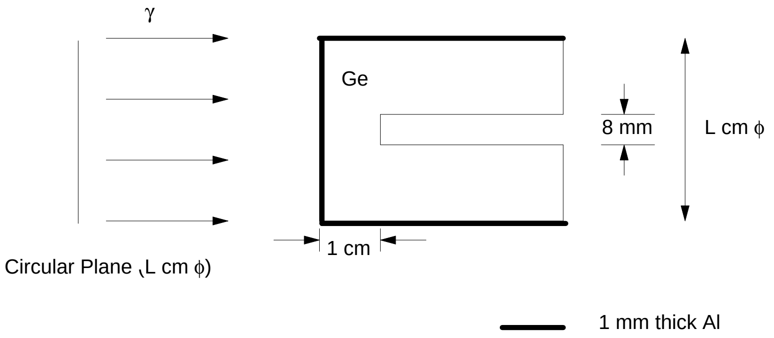

Figure B.1: The model geometry considered in calculating the photopeak efficiency in germanium detector using GEANT. This geometry is similar to that in the analysis by Owens *et al.* [121].

differences. In our model geometry, we had a homogeneous 1-mm thick aluminum shell to simulate the aluminum vacuum cryostat-beryllium window assembly in Owens *et al.* We have excluded in our model geometry a thin mylar film, which acted as an infra-red shield by covering the front face of the germanium crystal in Owens *et al.* Finally, we have also excluded a 0.5 mm thick lithium contact which lined the central core of the germanium detector, and a 0.1-mm thick implanted boron dead layer.

In our GEANT calculations, a parallel gamma-ray beam was directed towards the germanium detector. All secondary electrons and gamma rays were tracked by GEANT until a lower tracking threshold of 10 keV was reached. We calculated the intrinsic interaction efficiencies ε_i (i.e. the probability that an interaction would take place given a quantum incident on the detector) and the photopeak efficiencies ε_p for 500 keV gamma rays in germanium crystals of different sizes. A summary of our GEANT calculated efficiencies is provided in Table B.1. Results from Owens *et al.* are also shown in the table.

Comparing our GEANT calculated ε_i and ε_p to those in Owens *et al.*, the agreement

L	This work		Owens *et al.* [121]	
(cm)	ε_i	ε_p	ε_i	ε_p
4	0.7935	0.2504	0.7824	0.2482
5	0.8608	0.3268	0.8534	0.3271
6	0.9058	0.3972	0.9007	0.3985
7	0.9347	0.4570	0.9319	0.4602
8	0.9539	0.5039	0.9527	0.5136

Table B.1: Calculated intrinsic and photopeak efficiencies of germanium detectors for 500-keV γ rays. The intrinsic interaction efficiencies ε_i, i.e. the probability of an interaction taking place, and the photopeak efficiencies ε_p calculated by our GEANT program and by Owen *et al.* using the UCSD MONTE Monte Carlo program are listed here. L is the diameter and the length of the germanium detector depicted in Figure B.1. The statistical uncertainty in our GEANT calculation is 0.3%.

between the two calculations is good. However, we note that our calculated intrinsic efficiencies are consistently ~1% higher. This can arise from the fact that we used a simplified geometry. This small discrepancy can also arise from the differences in particle transport algorithms between GEANT and UCSD MONTE.

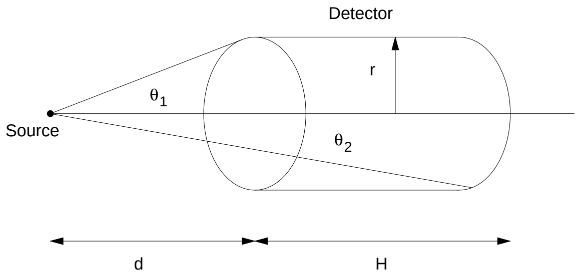

Figure B.2: Definition of variables in calculating gamma-ray absolute efficiency of a cylindrical detector

B.2 Comparing the Absolute Efficiency and Detector Response Function

Let us consider an isotropic, monoenergetic, point gamma-ray source situated at a distance d from a cylindrical detector of radius r and length H as shown in Figure B.2. The absolute efficiency ε_{abs}—the probability that an emitted quantum is detected by the detector is given by

$$\begin{aligned} \varepsilon_{abs} \;=\; & \tfrac{1}{2}\Big\{\textstyle\int_0^{\theta_2} d\theta \left[1-\exp\left(-\frac{H}{\lambda\cos\theta}\right)\right]\sin\theta + \\ & \textstyle\int_{\theta_2}^{\theta_1} d\theta \left[1-\exp\left(-\frac{1}{\lambda}\left(\frac{r}{\sin\theta}-\frac{d}{\cos\theta}\right)\right)\right]\sin\theta\Big\}, \end{aligned} \tag{B.1}$$

where λ is the attenuation length, and

$$\theta_1 = \arctan\left(\frac{r}{d}\right), \tag{B.2}$$

$$\theta_2 = \arctan\left(\frac{r}{d+H}\right). \tag{B.3}$$

For 5.5 and 20-MeV gamma rays incident on a NaI crystal [100],

$$\frac{1}{\lambda} = \begin{cases} 0.127\,\mathrm{cm}^{-1} & 5.5\ \mathrm{MeV} \\ 0.160\,\mathrm{cm}^{-1} & 20\ \mathrm{MeV}. \end{cases} \tag{B.4}$$

To verify that GEANT calculates the absolute efficiency correctly, we programmed a 12.7-cm diameter by 12.7-cm long NaI crystal into GEANT. We then ran Monte Carlo simulations for isotropic, monoenergetic, point gamma-ray sources at various distance d from the detector as depicted in Figure B.2.

In Figure B.3, we compare the GEANT calculated absolute efficiencies with those calculated with the linear attenuation model in Eqn.(B.1). The agreement is good to within ±0.6% at 20 MeV.

So far we have been calculating various detector efficiencies. We want to establish the reliability of GEANT in calculating the detector response function as well. Komar [99] developed a Monte Carlo program to understand the response of a 12.7-cm diameter by

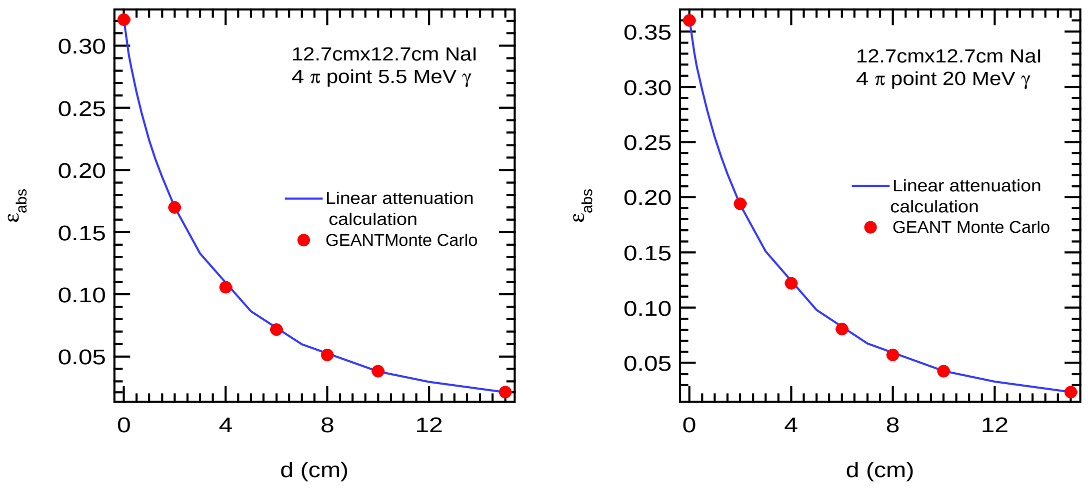

Figure B.3: Comparing GEANT and linear attenuation model calculated absolute efficiencies for a NaI detector. The detector is a 12.7 cm by 12.7 cm NaI crystal. The attenuation model was calculated using Eqn.(B.1).

7.62-cm long bismuth germanate (BGO) detector. Results from his calculations agreed with calibration data of the actual BGO detector. We ran a GEANT program with a BGO crystal of the same dimensions as the one in Komar. In Figure B.4, we compare our GEANT-calculated response function to that in Komar for a 10.76 MeV point gamma-ray source located 30 cm from the BGO detector. Once again, the agreement is good. It should be pointed out that the spectral shape calculated by Komar reproduced the measured spectra with high accuracy.

Good agreement between our GEANT programs and different independent calculations and experimental studies of various detector characteristics convince us that GEANT can be relied upon for the energy regime we are interested in.

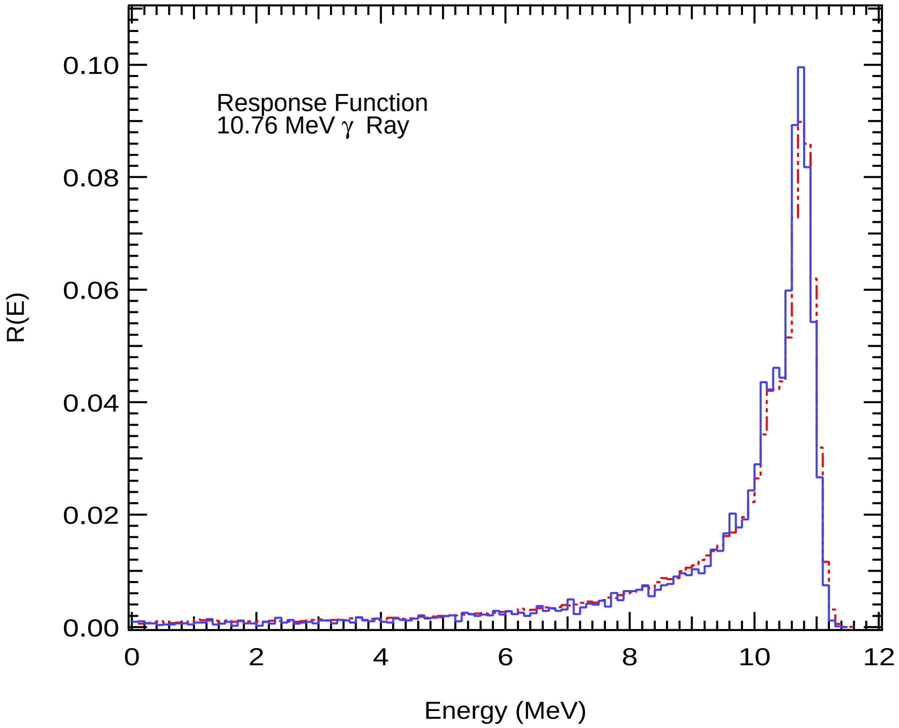

Figure B.4: GEANT calculated response function for a point 10.76-MeV gamma-ray source located 30 cm from a 12.7-cm diameter by 7.62-cm length BGO detector. The dashed histogram is the GEANT calculated spectrum, and the solid histogram is calculated by Komar [99].